



HAL
open science

Pulsed Laser Deposition of Substituted thin Garnet Films for Magnonic Applications

Lucile Soumah

► **To cite this version:**

Lucile Soumah. Pulsed Laser Deposition of Substituted thin Garnet Films for Magnonic Applications. Materials Science [cond-mat.mtrl-sci]. Université Paris Saclay (COMUE), 2019. English. NNT : 2019SACLS042 . tel-02102550

HAL Id: tel-02102550

<https://theses.hal.science/tel-02102550>

Submitted on 17 Apr 2019

HAL is a multi-disciplinary open access archive for the deposit and dissemination of scientific research documents, whether they are published or not. The documents may come from teaching and research institutions in France or abroad, or from public or private research centers.

L'archive ouverte pluridisciplinaire **HAL**, est destinée au dépôt et à la diffusion de documents scientifiques de niveau recherche, publiés ou non, émanant des établissements d'enseignement et de recherche français ou étrangers, des laboratoires publics ou privés.

Pulsed laser deposition of substituted thin garnet films for magnonic applications.

Thèse de doctorat de l'Université Paris-Saclay
préparée à l'Université Paris-Sud

École doctorale n°564 Physique de l'Île-de-France (PIF)
Spécialité de doctorat: Physique

Thèse présentée et soutenue à Palaiseau, le 28 Janvier 2019, par
Mlle Soumah Lucile

Composition du Jury :

M. Chumak Andrii *Rapporteur*

Professeur à l'Université Technique de Kaiserslautern (Center for Optics and Materials Science-OPTIMAS)

M. Gubbiotti Gianluca *Rapporteur*

Directeur de Recherche à l'Université de Pérouges (Istituto Officina dei Materiali – IOM)

Mme Popova Olena *Examinatrice*

Ingénieur de Recherche à l'Université de Versailles Saint-Quentin-en-Yvelines (Groupe d'Etudes de la Matière Condensée- GEMaC)

Mme Dagens Béatrice *Présidente*

Directeur de Recherche à l'Université Paris Saclay (Centre de Nanosciences et de Nanotechnologies- C2N)

Mme Thevenard Laura *Examinatrice*

Chargée de recherche à l'Université Pierre et Marie Curie (Institut des Nanosciences de Paris –INSP)

M Prellier Wilfrid *Examineur*

Directeur de Recherche à l'Ecole Nationale Supérieure des Ingénieurs de Caen (Laboratoire de cristallographie et science des matériaux - CRISMAT)

M. Anane Abdelmadjid *Directeur de thèse*

Maître de Conférences à l'Université Paris Sud (Unité Mixte de Recherche CNRS-Thales)

M. Bortolotti Paolo *Co-directeur de thèse*

Ingénieur de Recherche chez Thales Recherche Technologie (TRT)

M. Cros Vincent *Invité*

Directeur de Recherche à l'Université Paris Sud (Unité Mixte de Recherche CNRS-Thales)

Table of contents

<i>I Remerciements.</i>	5
<i>II Abstract/Résumé</i>	8
<i>III Introduction.</i>	10
III-A Yttrium Iron Garnet (YIG) and Bismuth doped YIG(BiYIG).	11
III-A.1 General properties of YIG.....	11
III-A.2 Effect of Bi doping.....	17
III-A.3 Case of thin films.....	21
III-B FMR and magnetization dynamic.	24
III-B.1 Dynamic of the magnetic moment.....	24
III-B.2 Spin waves in short.....	29
III-B.3 Magnetic losses.....	31
<i>IV Spintronics with magnetic insulators.</i>	34
IV-A Spin current in a metal.	35
IV-A.1 Definition and origin in metals.....	35
IV-A.2 Spin relaxation in a NM.....	38
IV-B Spin current in a MI/NM bilayer	40
IV-B.1 Spin pumping.....	40
IV-B.2 Spin Transfer Torque.....	41
IV-C Spin Hall Effect (SHE) metals and magnetoresistive effects in NM/MI bilayer.	43
IV-C.1 SHE and ISHE.....	43
IV-C.2 Experimental interest of SHE metal for MI/NM bilayer.....	43
IV-D Spintronic effects with a NM(SHE)/MI.	44
IV-D.1 Spin Hall Magnetoresistance (SMR).....	44
IV-D.2 Inverse Spin Hall Effect.....	46
IV-D.3 Anomalous Hall Effect.....	46
<i>V MI for spintronics.</i>	48
V-A Materials for spintronics.	49
V-A.1 Parameter for an efficient spintronic bilayer.....	49
V-A.2 FM metals with low magnetic damping : an alternative to MI.....	50
V-A.3 Ultrathin MI for spintronics.....	52
V-B Why use of a MI?	55
V-C Recent advances in YIG spintronics.	57
V-C.1 Magnon-spintronics with YIG.....	57
V-C.2 Recent advances in insulating based magnon-spintronics.....	61
<i>VI Experimental work.</i>	65
VI-A Thin films elaboration	66
VI-A.1 Pulsed laser deposition technique.....	66
VI-A.2 Sputtering.....	68
VI-B Characterization techniques.	69
VI-B.1 X-Ray characterization technique.....	69
VI-B.2 Atomic Force Microscopy (AFM).....	76
VI-B.3 SQUID magnetometry	77

VI-B.4	Ferromagnetic resonance (FMR) measurement.	78
VI-B.5	Magnetoresistive effects.	82
VI-C	Magneto-optical measurement. _____	84
VI-C.1	Kerr microscopy.	84
VI-C.2	Faraday rotation measurement.	88
VII	Thin films characteristics.	91
VII-A	Growth conditions. _____	92
VII-A.1	Generalities about the growth.	92
VII-A.2	Growth conditions.	94
VII-B	Structural properties. _____	99
VII-B.1	Out-of-plane structure.	99
VII-B.2	In-plane structure.	101
VII-B.3	Discussion.	103
VII-C	Magnetic properties. _____	105
VII-C.1	Determination of the magnetic anisotropy.	105
VII-C.2	Magneto-optical properties.	111
VII-C.3	Dynamical magnetic properties.	112
VII-D	Discussion on the magnetic anisotropy in BiYIG films. _____	123
VII-D.1	Anisotropy terms.	123
VII-D.2	Origin of the different anisotropy in our films.	124
VII-D.3	Conclusion on the origin of the anisotropy.	126
VIII	Spintronic applications with BiYIG.	128
VIII-A	Effect of Pt on the magnetic characteristics of BiYIG films. _____	129
VIII-A.1	Magnetic anisotropy with Pt on in-plane magnetized sample.	129
VIII-A.2	Effect of Pt on BiYIG films with PMA.	130
VIII-A.3	Discussion on the origin of the change in anisotropy.	131
VIII-B	Inverse Spin Hall Effect measurement. _____	135
VIII-B.1	Spin pumping.	135
VIII-B.2	ISHE.	136
VIII-C	SMR measurements. _____	138
VIII-D	Anomalous Hall Effect in Pt/BiYIG. _____	142
VIII-E	Spin wave emission using a charge current. _____	144
VIII-E.1	Auto-oscillation observation.	144
VIII-E.2	Spin wave emission from auto oscillation.	145
IX	Conclusion and Outlook.	148
IX-A	Conclusion. _____	149
IX-B	Outlook. _____	151
IX-B.1	Magnon-spintronics applications.	151
IX-B.2	New magnetic insulators for spintronics.	151
Annexe	152
A.	Commutation rules for the spin dynamic equation. _____	153
B.	Calculation of the relaxed structure lattice parameter with a uniform and homogeneous strain model. _____	154
C.	Derivation of the domain wall energy from the Kaplan et Gehring model. _____	156
D.	Derivation of ΔH_0 in homo for in-plane FMR. _____	158

E.	Brillouin Light Scattering (BLS) characterisation of BIYIG with and without Pt capping. __	159
<i>X</i>	<i>Résumé en français.</i>	163
X-A	Introduction. _____	164
X-B	Caractérisation. _____	165
X-C	Applications. _____	169
X-D	Conclusion et perspectives. _____	170
	<i>References</i>	171

I Remerciements.

Après avoir lu les remerciements de la thèse de Martin me voilà rassurée sur le fait que je n'ai pas de limite de pages. Je vais donc pouvoir dire librement tout le bien que je pense des gens autour de moi en restant concise... ça sera l'ultime challenge de cette thèse.

First of all I need to reward the jury members that took good care of correcting the typography and the physics in this PhD manuscript. Thanks for your careful reading of my work, your questions and all of your comments which made the manuscript more complete and clearer.

Je vais donc maintenant pouvoir passer au français parce que comme dirait mon grand-père 'quand même parler français c'est important !'

Je vais commencer par le début...merci Jean Marie grâce à qui j'ai pu rejoindre le labo malgré une performance lamentable à l'oral de l'EDPIF, je suis vraiment contente que l'on ait fini par faire des manip ensemble, merci aussi pour tout l'intérêt que tu portes au BiYIG même si tu le cache avec pudeur☺.

Ensuite il faut remercier Cécile et Éric qui ont sauvé mes échantillons de PLD dans des situations les plus extrêmes, et ceux, jusqu'à la dernière année☺. Je veux aussi remercier des gens que je ne connais pas : R. Bernard et de H. Molcepres qui ont permis à un merveilleux YIG de pousser dans le bâti avant mon arrivée et ont bien préparé le terrain pour ma thèse.

Merci à Sophie C. et Florian pour m'avoir épaulé en litho en pulvé et à la machine café dans mes pics de stress.

Merci à Richard et Raphael pour m'avoir aidé à remplir le SQUID même si j'étais une grande fille.

Merci à Jamal, le roi du grenat, pour toutes ces connaissances partagées, ta bienveillance et ta patience. La ville de Brest doit également te remercier car tu l'as rendu super fun à chaque fois que j'y étais (j'en ai même oublié la pluie ou les retards de train de trois heures). Merci à Nathan pour avoir bien pris soin de moi sur la manip Faraday et pour avoir mis du vernis à paillettes sur tous mes échantillons☺.

Merci à Nico pour n'avoir JAMAIS perdu patience avec mes bugs de programme LabVIEW bordelique (c'est moins le bordel maintenant) je t'attends en Suède, le ciel y est très clair pour voir les étoiles, les aurores boréales et...il y a du chocolat Daims aussi☺.

Merci à la team YIG : Olivier pour m'avoir mis la pression dès mon arrivée en s'étonnant que je trouve le temps pour aller nager. Tu m'as aussi bien aidé avec tes petits tips origin qui m'ont sauvé bien du temps pour la rédaction de thèse. Merci Martin pour ton grand cœur bien caché (et tes répliques bien cash aussi) et ta bienveillance. Merci pour ton aide sur les manip et pour les bons moments qu'on a passé au states même 'without the alligatoooooooooooooors' vient me voir la Suède c'est super ! Merci Hugo pour ton talent de crêpière et tes oupsiiiiiiiiii, l'avenir de AL5207 est entre tes mains gros fais gaffe quand tu le prends avec une pince ☺ !!!

Merci Eloïse, la reine de Labenne, pour ta pêche, ton sourire, ta joie de vivre, je te souhaite une super thèse à l'ESPCI, je ferai des pancartes moi aussi lorsque le temps sera venu...

Cette thèse aurait été sacrement fade sans mes camarades de bureau : Karim qui n'a jamais vu que je rédigeais ma thèse, Soph qui se cuit au soleil, et Regina son super sourire, ses ballons, ses scoubidoues qui suffisent à faire rayonner tout un bureau.

Merci à Benoit pour être si casual et pour avoir partagé tes goûts littéraires. Merci Quentin, best partner pour les manip (au pire on s'en fout non ?) et qui deviendra un jour le roi du démineur, prends soin de mes échantillons je sais que tu leur apporteras tout l'amour dont ils

ont besoin☺. Merci à David qui m'accompagne à la mer, à la montagne, à la piscine et à l'escalade (on a tous besoin d'un David en fait !). Merci à Johanna ma sport Buddy qui ne dit jamais non à une petite activité à midi...tu vas me manquer mais grâce à Hermann tu ne seras jamais très loin de moi☺. Merci à Angès, Julie et Pierre pour leur bienveillance. Merci à Dédé pour sa bonne humeur et sa gentillesse. Merci à Vincent C. pour toujours avoir été intéressé par mes travaux, pour sa foi à voir des skyrmions dans le BiYIG... je t'enverrai des bonbons c'est promis. Merci à Maxence sa motivation pour aller à la piscine et sa bonne humeur.

Merci à Henri qui m'a bien éclairé et aidé sur ma vie future dans le THz. On se recroisera très certainement en conf !

Merci à Richard L. pour toujours chercher Éric mais finir dans mon bureau à discuter de cibles et à Lilia pour m'avoir fait découvrir le monde des céramiques.

Merci à FNVD et F. Petroff pour avoir géré une phobique administrative comme moi et m'avoir envoyé au bilan de groupe de recherche...trop facile de présenter la thèse dans l'amphi après....

Merci à Anne, Nathalie et Christine qui m'ont rendu l'administratif presque pas effrayant (normal je n'y touchais pas !).

Un grand merci à tous ces gens bienveillants de TRT et de l'UMR qui m'ont toujours aidé, écouté, assisté à mes présentations etc... c'est grâce à tous ces échanges que cette thèse a été un vrai plaisir.

Un spécial thanks a Piotr qui sait que je peux progresser maintenant.

Et évidemment grosse dédicace a mon super voisin Willou, pour qui je pourrai écrire des lignes et des lignes, this collaboration was NOT worthless GROS, la preuve même dans le monde de l'ultrafast, tu vas me manquer... Stockholm n'attends que toi et Mathou☺. Mathou je t'attends pour un ride en Suède c'est tout aussi bien qu'à Grenoble...ou presque

Merci à François Lesin qui m'a fait découvrir l'escalade et a Gi ma besta de Fontainebleau...je reviendrai en été pour les beaux cailloux de Fontainebleau soyez en certain. Il n'y a pas que la piscine dans la vie il y a la grimpe aussi!

Merci à mes beŞtas de Lyon : Drey, Fran, Flo, Geo et Ju. Docteur Lulu n'aurait peut-être été qu'un reportage Strip tease sans votre soutien et votre amooooooooooooour. Je vous attends en Suède très bientôt.

Merci à ma marraine Lucile qui continue à prendre soin de moi en dehors de l'ECAM même avec un bébé et un mari...merci aussi a toutes mes poules de l'ECAM.

Merci à Vivi et ses cartes postales toujours plus moches qui égayent ma vie depuis bientôt 10 ans....

Merci à Vincent pour être mon aide psychologique et matérielle avant les partiels de L3 ET avant ma soutenance de thèse. Merci à Sarah et Natoch mes copines de tous les instants depuis maintenant 6 ans. Merci à french Alex, mon besta d'Uppsala que j'attends pendant Valborg pour revivre notre jeunesse. La Team Pierre et Marie Curie : curieux et fiers de l'être ouais ouais !

Merci à Paolo, pour la réponse a ta question j'ai plus de longueurs à la piscine que d'échantillons à mon actif un mythe s'effondre (ou pas ?)... tu étais un jätte bra co-encadrant et tu seras un jätte jätte bra directeur de labo mais n'oublie pas de déléguer ☺.

Merci à ma famille suédoise qui a toujours été d'un grand soutien et d'une chaleur telle que je ne crains même plus de passer l'hiver à Stockholm.

Merci à ma famille dont je suis très fière car ces trois années ont été un petit challenge pour nous tous! Je vous aime, vous m'avez permis de m'épanouir et d'aller vers ce que j'aimais. Me

voilà bien grande maintenant et pour une fois je peux le dire avec confiance 'Ne vous inquiétez pas ça ira très bien pour moi'.

Voici venu le temps de dire merci à mon encadrant de thèse (et ça me fait bien rire qu'il ait dut lire toute une page avant de trouver son paragraphe). D'abord ne stresse pas j'ai trop bien rangé toutes mes datas☺. Ensuite merci d'avoir supporté avec patience et calme : mes coups de stress, mes crises de nerfs, mes doutes existentiels sur mes résultats...j'imagine qu'il n'est pas facile de gérer un pétard tous les jours...rassure toi la tempête est passée ! J'espère que tu auras des milliards et des milliards de thésards qui seront tout aussi heureux que moi, et aussi (ce n'est pas très très compatible mais bon) que tu trouveras du temps pour te remettre à l'escalade. J'ai eu énormément de plaisir à travailler avec toi, tu m'as appris pleins de trucs et tu m'as aussi beaucoup fait mûrir, et même si je ne suis pas toujours super sûre de moi l'm on my way! Je sais que l'on restera en contact mais j'espère que l'on continuera à travailler ensemble parce que travailler avec toi c'est trop cool (Tu noteras que j'ai bien fait de passer en français juste pour cette dernière phrase !). Encore une fois un BIG merci et longue vie au BiYIG.

Enfin merci à mon pojkvän Alex que je vais enfin pouvoir retrouver! Comme dirait Kyo on a parcouru le chemin on a tenu la distance, je suis tellement soulagée d'arrêter de polluer la planète à coup de vols Norwegian et de ne plus devoir me battre avec le micro de l'ordi because you hear me very badly. Il est vrai que je laisse la France et plein de belles choses (en dehors des chips et du fromage) derrière moi mais l'avenir avec toi ça ne me fait pas peur. J'ai confiance, tout sera beau et lumineux (au moins de Juin à Aout) avec toi et tout le monde viendra nous voir ! Älskär dig min lilla bulle.

Voilà, je crois que j'ai fini...merci à vous qui avez lu ces lignes (car ce n'est pas par hasard que vous les avez lu non ?!) et merci à vous si vous osez aller plus loin que ces deux pages de remerciement...le BiYIG c'est super cool je vous promets allez faites un effort....

II Abstract/Résumé

In magnetic materials it is possible to excite magnetic moments; this excitation can be uniform (ferromagnetic resonance) or can propagate within the material (spin waves). Dynamics of the magnetic materials can cover from GHz to THz frequency range depending on magnetic properties which makes it relevant for technological applications. However detection and generation of magnetization precession is usually done by RF antennas which makes spin waves based devices not compact enough compared to the electronic ones. During the last decades it has been shown that charge current and magnetization dynamics can be coupled by spin angular momentum transfer between metals and magnetic materials. This gave the rising of a new field: magnon-spintronics, combining spin to charge conversion and spin wave based technology.

To propagate spin waves low magnetic losses materials are necessary. Among magnetic materials it is the Yttrium Iron Garnet (YIG), first synthesized in 1956, that presents the lowest reported magnetic damping. This property makes this material crucial for any applications involving magnetization dynamics:

- Since the 60's bulk YIG spheres are used in tunable RF resonator or filters because of the high quality factor of the material.
- In the 80's μm -thick YIG films were the first medium used to propagate RF generated spin waves due to its low attenuation length.

However the YIG is an insulating material which made its application limited to the field magnonic up to recently.

- In 2010 the first evidence of spin angular momentum transfer at the Pt/YIG interface is observed. This allowed generating and detecting electrically spin waves in μm -thick YIG films which opened the field of electronic to insulating materials.
- During the last decade efforts have been focused on obtaining thinner YIG films (nm thickness) while keeping magnetic losses as low as possible. This allowed to increase the torque (arising from the spin angular momentum transfer) and to observe auto oscillation of the magnetization.

Because YIG has very low uniaxial anisotropy nm-thick YIG films presents in-plane magnetic easy axis due to shape anisotropy. Ultrathin magnetic materials with low losses and different magnetic anisotropies would be however desirable for magnon-spintronic applications.

Changing magnetic properties in YIG can be done by doping or substitution. This has been done since the 70's and allow to obtain magnetic insulators with tunable magnetic anisotropy, magnetostriction, magnetization.... Doping YIG with Bi at the Yttrium dodecahedral lattice site allows obtaining a material with high uniaxial anisotropy and magneto-optical coefficient. Therefore BiYIG μm thick films grown by Liquid Phase Epitaxy have been used in magnetic bubble memory materials and for photonic applications. In those films the dynamical quality of the material was not relevant and therefore not reported.

In this Ph.D. thesis the goal was to grow a material of low thickness with good dynamical properties that could offer itself as an alternative to the YIG for spintronic applications which will open then new perspectives for magnon-spintronics applications. The material developed

was the partially doped (from 25 to 50%) Bismuth YIG, it has been grown by Pulsed Laser Deposition in order to obtain nanometer thicknesses films.

In the first part of the Ph.D. (Chapter III to IV) the theory necessary to understand the experimental results and the motivation of the work are presented. In the second part (V to VIII) experimental work is presented with the main results in terms of materials properties and of spintronic applications.

This Ph.D. evidences that Bismuth YIG films presenting low magnetic losses and perpendicular magnetic anisotropy can be elaborated. In these films it is also possible to transfer spin angular momentum and detection or generation of magnetization dynamics is now possible using charge current only. This material already opened new perspectives for the magnon-spintronics community and complete the panel of magnetic insulators relevant within this field.

III Introduction.

This Ph.D. thesis aims at studying magnetic insulators (MI) thin films that can thereafter find applications in the fields of spintronics and magnonics. Therefore both static (easy magnetic axis, magneto-optical coefficient, magnetic moment...) and dynamic (Gilbert damping, FMR linewidth...) magnetic properties of thin films will be studied.

The materials of interest here derive from Yttrium Iron Garnet (YIG) known since the 50's for its dynamical magnetic properties.

This introduction aims at giving a presentation on two key points of this Ph.D: materials' properties and physical processes involved into the dynamics of the magnetic moments.

III-A Yttrium Iron Garnet (YIG) and Bismuth doped YIG(BiYIG).

This section gives an introduction on materials used in this Ph.D. and thin films in general. Both YIG and BiYIG materials are well-studied materials since decades: structural, magnetic, magneto-optical and dynamical characteristics of those materials are well documented. Those properties, intrinsic to the material are presented in the two first parts of this section. Thin films materials have usually different properties than the bulk one. Those are presented in the last part of the section.

III-A.1 General properties of YIG.

The bulk YIG has been first synthesized in France in 1956 by Bertaut and Forrat¹. Because of its outstanding dynamical properties it gathered immediately a huge interest from the scientific community² and has been '*to ferromagnetic resonance what the fruitful fly is to genetics*'³.

The different characteristics of this material, making it so relevant for the magnetism community, are presented in the following section.

III.A.1.1 Structure and magnetic properties.

The YIG chemical formula is $Y_3Fe_5O_{12}$; it belongs to the family of garnets. Garnets have a cubic unit cell, within this unit cell there are 8 sub lattices of atomic formula: $\{X\}_3\{Y\}_2\{Z\}_3O_{12}$. In one unit cell of garnet there are:

- 24 {X} dodecahedral atomic sites with 8 oxygen neighbors (Y^{3+} for the YIG).
- 16 [Y] tetrahedral atomic sites with 6 oxygen neighbors (Fe^{3+} for the YIG).
- 24 (Z) octahedral atomic sites with 4 oxygen neighbors (Fe^{3+} for the YIG).

The lattice parameter of the YIG at room temperature is 12.376 Å. The picture of the YIG structure is given in Figure III-1.

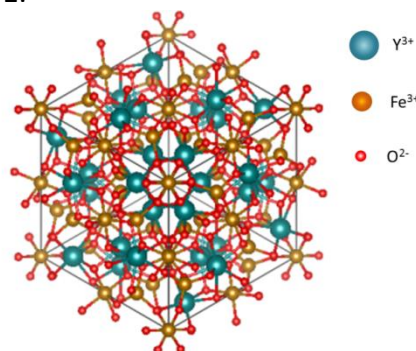


Figure III-1 YIG structure

III.A.1.2 Magnetic moment.

The YIG is a ferrimagnetic material in which the different Fe^{3+} ions located at both

tetrahedral and octahedral lattice sites are antiferromagnetically coupled through O^{2-} ions via the superexchange interaction. There are three types of interactions in YIG which define the total magnetic moment:

- Fe^{3+} ions at the tetrahedral position with their nearest tetrahedral neighbor.
- Fe^{3+} ions at the octahedral position with their nearest octahedral neighbor.
- Fe^{3+} ions at the tetrahedral position with their nearest octahedral neighbor.

The strength of these interactions depends on both the distance and the angle of the Fe-O-Fe bonds. Both distances and angles between the different ions can be found in the literature⁴. Using the two sub lattices model for ferromagnetic materials⁵ it is possible to express the total magnetic moment of the YIG (M_{YIG}) :

$$M_{YIG} = M(Fe^{3+})_{tetra} - M(Fe^{3+})_{octa} \quad III-1$$

Where $M(Fe^{3+})_{tetra(octa)}$ is the magnetic moment of the tetrahedral (octahedral) sub lattice. $M(Fe^{3+})_{tetra(octa)}$ can be derived by using the molecular field theory⁶ with a fit (shown in Figure III-2) of the temperature dependence of M_{YIG} where all different interactions need to be taken into account.

The total magnetic moment at room temperature for the YIG is $140 \text{ kA}\cdot\text{m}^{-1}$.

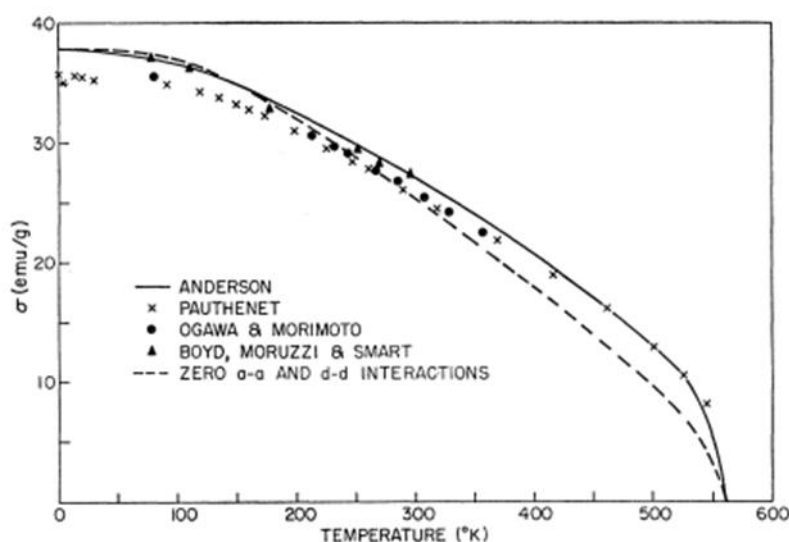


Figure III-2 Spontaneous magnetization (in emu/g) of YIG vs temperature. The solid curve corresponds to experimental measurements. Data points are extracted from other papers. The dotted curve is the molecular field solution. The curve is extracted from ref 6.

III.A.1.3 Exchange stiffness.

The exchange stiffness parameter (A in $\text{J}\cdot\text{m}^{-1}$) is quantifying the strength of the magnetic interaction in the crystal. It is also related to the magnetic domain wall energy (σ in $\text{J}\cdot\text{m}^{-2}$) and the effective anisotropy of the material (K_{eff} in $\text{J}\cdot\text{m}^{-3}$) by:

$$\sigma = 4 \sqrt{AK_{eff}} \quad III-2$$

The exchange stiffness can be computed from the spin wave theory^{6,7} using the spin wave dispersion relation. For the YIG: $A=1.96\cdot 10^{-12} \text{ J}\cdot\text{m}^{-1}$. This value seems to be underestimated as recent results⁸ gave $A=3.7(\pm 0.4)\cdot 10^{-12} \text{ J}\cdot\text{m}^{-1}$.

III.A.1.4 Magnetic anisotropy.

In bulk YIG the magnetocrystalline anisotropy is parameterized using a cubic anisotropy with an easy axis along the (100) direction. The value of the cubic anisotropy constant K_1 is $K_1 = 610 \text{ J} \cdot \text{m}^{-3}$ ⁹. As it will be seen in Section III.A.2.3 and III.A.3.2 it is a very weak value when compared to other terms that originates from doping, strain or shape effects. This can be explained by two reasons:

- a weak spin orbit coupling (SOC) in YIG due to orbital moment quenching of the magnetic Fe^{3+} ions.
- the high symmetry of the cubic YIG structure.

Another anisotropy source can arise due to an external stress σ applied on the material along a specific axis: the magneto elastic anisotropy K_{MO} . It depends on the axis along which the strain is applied: for a stress applied along the [hkl] crystalline axis it is written as:

$$K_{MO} = -\frac{3}{2}\sigma\lambda_{hkl} \quad \text{III-3}$$

λ_{hkl} is called the magnetostriction and σ is the strain energy density.

The magnetostriction in bulk YIG can be measured by exciting the magnetic moment of the material using ferromagnetic resonance (FMR) (detailed in the section III-B) while applying an external stress along the different cubic crystalline axis. This causes a shift in the FMR resonant conditions which is related to λ_{hkl} ¹⁰. In this Ph.D. due to the substrate and the material orientation only the magnetostriction value in the [111] cubic axis is used, for the bulk YIG: $\lambda_{111} = -2.4 \cdot 10^{-6}$. This value is rather weak compared to the one of highly magnetostrictif material such as TbFe_2 alloys : $\lambda > 1200 \cdot 10^{-6}$ (for polycrystalline TbFe_2 ¹¹) or even to simple elements such as Cobalt $\lambda = -62 \cdot 10^{-6}$ (for polycrystalline Co ¹¹).

III.A.1.5 Magneto-optical properties.

In a magnetized material optical constant and magnetic moment are related via the dielectric tensor¹². One consequence is the Faraday (Kerr) effect: a linearly polarized light transmitted (reflected) through a magnetized material will experience a rotation of its polarization plane if the propagation direction is parallel to the magnetic moment of the material. The angle of rotation (θ_F) is called the Faraday angle and it is wavelength dependent.

III.A.1.5.1.1 *Microscopic Origin of magneto-optical effects.*

Origins of Kerr or Faraday effects are the electric-dipole transitions. A transition between two electronic levels can be induced by photon absorption if this latter satisfies the *dipole transition selection rules* (Figure III-3 top left). Faraday (Kerr) effect occurs if the energy of the absorbed photon is dependent on both the magnetization of the material and the light polarization.

As a consequence the degeneracy of the electronic energy levels needs to be lifted on both the orbital and the spin values^{13,14}. This is illustrated in the Figure III-3 :

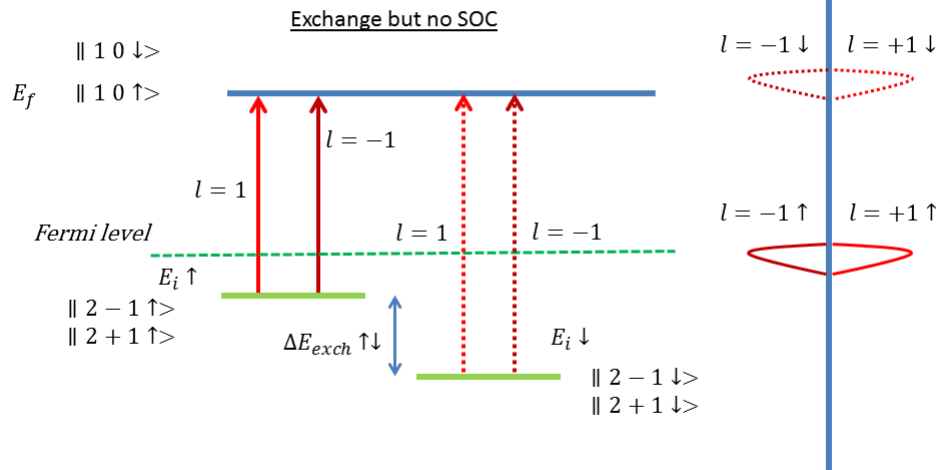
- If only exchange interaction lifts the degeneracy the energy of the absorbed photon depends only on the magnetic moment of the material and not on the polarization of the light (Figure III-3(a))

- If only SOC interaction lifts the degeneracy the energy of the absorbed photon will depends only on the polarization of the light and not on the magnetization of the sample (Figure III-3(b))

Thus, magneto-optical effect requires both exchange and SOC interactions (Figure III-3 (c)) for the absorption energy to be dependent on both the polarization of the light and the magnetization of the material.

(a)

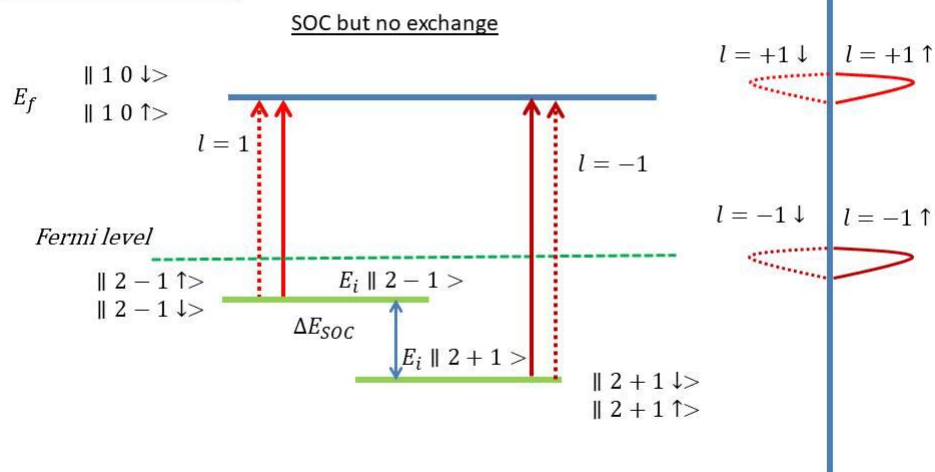
Selection rules:
 $\Delta s = 0$
 $\Delta l = \pm 1$
 $E_i - E_f = \hbar\omega$



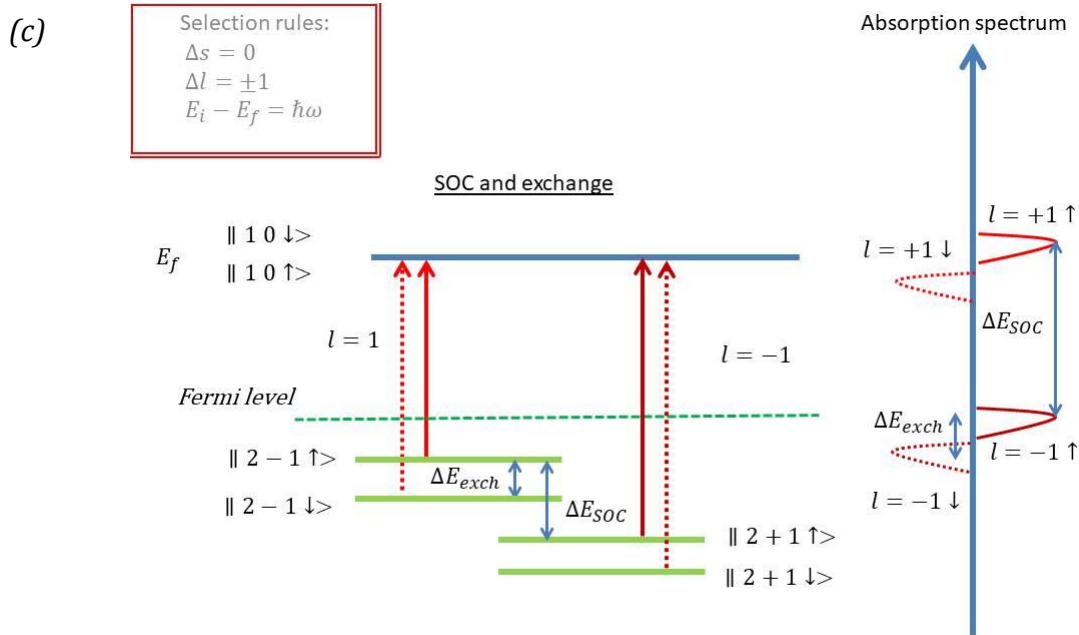
→Energy depends only on M and not on the light polarisation

(b)

Selection rules:
 $\Delta s = 0$
 $\Delta l = \pm 1$
 $E_i - E_f = \hbar\omega$



→Energy depends only not on M and but on the light polarisation



→Energy depends on both M and the light polarisation

Figure III-3- (adapted from ref 14) Electronic dipole transition for the case of electronic split due to (a) exchange energy only (b) SOC only (c) both SOC and exchange energy. On the right is displayed the energy corresponding to the different transition. Red dotted (continuous) light corresponds to a photon absorption by a spin down (spin up) electron.

III.A.1.5.1.2 YIG magneto-optical properties.

The YIG is known for its high figure of merit (FOM): it is defined as the ratio $\frac{\theta_F}{\alpha_{att}}$ with α_{att} being the attenuation losses in cm^{-1} . The FOM of the YIG at 633 nm and 1310 nm (laser and telecommunication wavelength) is respectively 0.5 and 1.63 which makes it suitable for applications in photonic circuits^{15,16,17}.

For YIG the exchange energy is due to superexchange between Fe^{3+} ions that are coupled via O^{2-} ions. The SOC comes from the mixing between electronic orbitals of the ground state and the excited states of Fe^{3+} ions located at the tetrahedral and octahedral atomic sites¹³. This effects lifts up the L_z degeneracy of the electronic ground state. In Figure III-4 we present a schematic representation of the different electronic transitions in YIG taken from Wittekoek *et al*. The magnitude of the Faraday Rotation (FR) for the different absorption is given by the strength of those transitions.

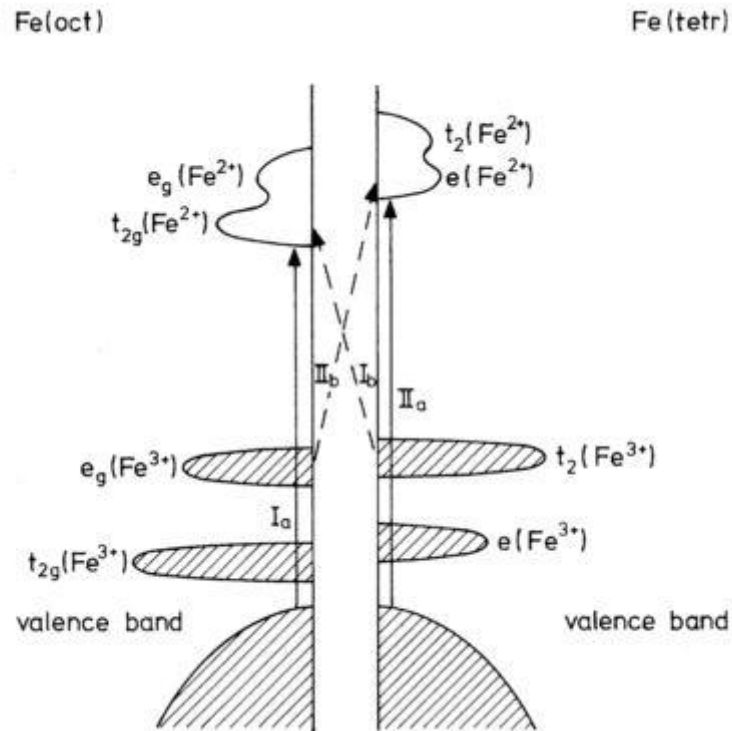


Figure III-4-Scheme of the different transitions between the electronic levels of the Fe³⁺ electrons giving rise FR from ref17. The solid (dashed) arrows corresponds to oxygen to iron (octahedral to tetrahedral iron) charge transfer transitions.

The FR is correlated with the strength of electronic transitions and the magnetization therefore it is different for irons located at the octahedral and the tetrahedral atomic sites as a result:

$$\theta_F = A_{tetra} \mathcal{M}(Fe^{3+})_{tetra} + A_{octa} \mathcal{M}(Fe^{3+})_{octa} \quad III-4$$

Values of the different coefficient can be found in the literature¹⁸.

III.A.1.6 Dynamics.

YIG's properties make it an ideal material for ferromagnetic resonance studies:

- It's a cubic material (highly isotropic).
- It's an insulator (conduction electrons as a loss of magnetic energy are not present).
- All magnetic ions (iron) have the same valence: 3+.
- Due to orbital quenching of the crystal field they have almost no orbital momentum and are weakly coupled to the Yttrium ions of the lattice.

Magnetic relaxation have been thoroughly studied in the YIG during the 60's³ and more general studies on relaxation processes for magnetic insulators based on this material can also be found in ref².

In the absence of chemical impurities the linewidth in YIG is arising from coupling between the uniform precession mode (FMR) and the spin wave mode having the same energy of the FMR mode³. Those spin wave modes scatter with thermal magnons that can couple to the phonons of the lattice to keep the temperature of the lattice equal to that of the spins.

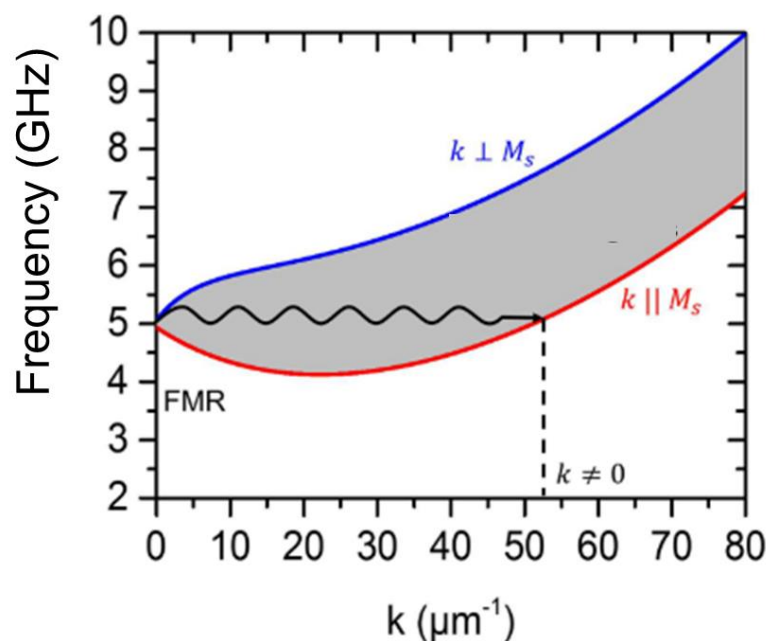


Figure III-5- Two magnons scattering process: the red and blue curves corresponds to magnons dispersion curve propagating \perp and \parallel to the magnetization direction. The FMR frequency is degenerated with a magnon of $\mathbf{k} \neq \mathbf{0}$ and can scatter to create this magnon. The dispersion relation are the one of YIG thin films with $M \parallel$ to the film plane.

This main relaxation process is called the two magnons scattering: the magnon of the FMR mode at $k=0$ annihilates to create another one at $k \neq 0$. It is illustrated in the Figure III-5. The typical value for the Gilbert damping in YIG associated to this relaxation process only is of $\alpha = 10^{-5}$ which is the lowest value reported for bulk materia³.

III-A.2 Effect of Bi doping.

Considering the complexity of the garnet structure many substitutions can be done, one of them is to replace Y^{3+} by Bi^{3+} . Effects of Bi doping on the garnet's properties have gathered a lot of interest in the context of materials for magnetic bubble memory application^{19,20}.

Due to its large ionic radius ($r_{Bi^{3+}}=1.132 \text{ \AA}^{21}$) and its valence Bi^{3+} atoms are substituent to the Y^{3+} atoms at the dodecahedral lattice site: the chemical formula is then $Bi_xY_{3-x}Fe_5O_{12}$ ($Bi_xY_{3-x}IG$). Because of the difference between Y and Bi ionic radii ($r_{Y^{3+}}=1.017 \text{ \AA}^{22}$) the lattice constant of the BiYIG linearly increases with the doping in Bi²⁰. The increase of this lattice constant makes the $x=3$ phase (i.e. full substitution of Y by Bi) thermodynamically unstable, no reference for bulk BiIG can be found and only out of equilibrium growth methods, such as Pulsed Laser Deposition (PLD), allow crystallizing BiIG films²³⁻²⁵.

Liquid Phase Epitaxy (LPE) technique allowed to grow μm thick BiYIG films up to 66% Bi doping¹⁹. In this Ph.D. thesis the highest doping level achieved is 50%, therefore for intrinsic properties of the BiYIG we will present the one of partially doped BiYIG LPE grown films (and not to the one of a bulk structure).

III.A.2.1 Structure.

BiYIG films are grown on lattice mismatched garnet substrate which modifies the original structure of the material if it would exist as bulk: the garnet-parent cubic structure is distorted due to misfit induced epitaxial strain of the film. The lattice parameter of the original (relaxed) structure is calculated by assuming that the deformation is elastic (see Annexe I.B). From the experimental results it is possible to extrapolate a linear dependence of the relaxed BiYIG lattice parameter $a_{Bi_xY_{3-x}IG}$ with Bi content^{26,27}:

$$a_{Bi_xY_{3-x}IG} = a_{YIG} + 0.0828x \quad III-5$$

It is presented in Figure III-6.

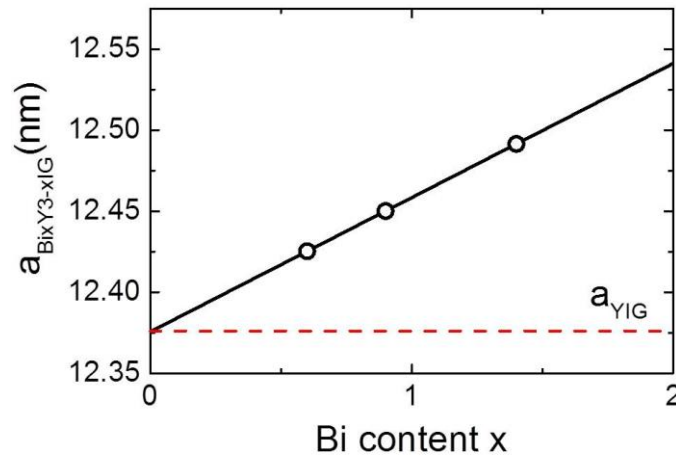


Figure III-6 Evolution of the lattice constant of $BixY_{3-x}IG$ with the doping rate x using the coefficient from ref27 the three points correspond to the doping rate of 0.7, 1 and 1.5 used in this Ph.D.

III.A.2.2 Magnetic moment.

Bi^{3+} is non-magnetic ions and are therefore not directly affecting the magnetization value of the garnet.

However Bi^{3+} ions are involved in the superexchange interaction through both structural (unit cell deformation that changes the $Fe^{3+}-O^{2-}-Fe^{3+}$ angles) and electronic (mixing between the Oxygen and Bismuth electronic orbitals) mechanisms^{28,29}. This leads to a linear increase of the Curie temperature T_c with the Bi content x : $\frac{\Delta T_c}{x} = 34K$ ²⁰. Consequently, for a given temperature, the magnetic moment of the BiYIG compared to the YIG one unit cell is slightly enhanced.

Moreover Bi^{3+} ionic radii is greater than Y^{3+} ^{20,21} thus, the total volume of the unit cell is larger for BiYIG than YIG²⁴ hence the magnetic moment per unit volume is slightly smaller than of YIG structure.

Those two phenomena compensate each other at room temperature and consequently the magnetization of BiYIG and YIG are similar, as can be seen in Figure III-7.

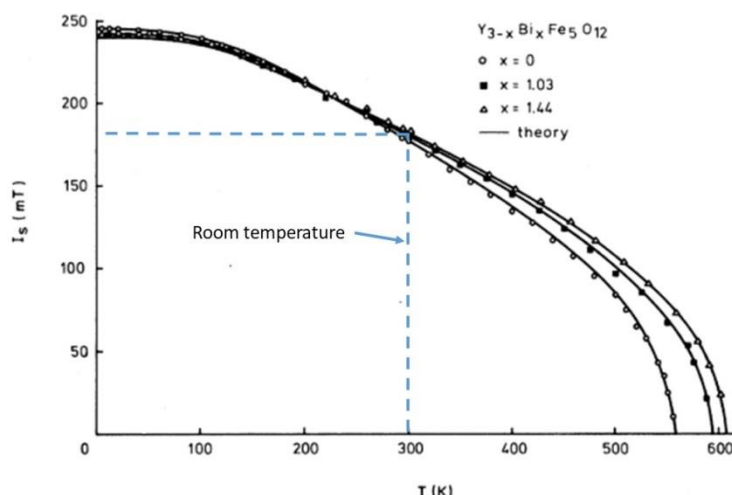


Figure III-7 Evolution of the magnetization for BiYIG and YIG LPE grown films from ref 20. The room temperature is indicated in blue: the magnetization field I_s of YIG and doped YIG is around 170 mT (magnetization field for YIG).

III.A.2.3 Exchange stiffness.

Brillouin Light Scattering (BLS) measurements performed on single crystal $\text{Bi}_x\text{Y}_{3-x}\text{IG}$ evidenced that the exchange stiffness (D_{ex}) is increasing with the Bi content x (for x varying between 0 to 0.92) in the film²⁸. The exchange stiffness constant A is defined from D_{ex} by⁸:

$$A(T) = \frac{D_{ex}M_s(T)}{2} \quad \text{III-6}$$

The Bismuth content x doesn't affect the magnetization of the film at room temperature (see above Section) the increase of D_{ex} with x leads then to an increase of A . This increase is attributed to the same mechanisms leading to the decrease of the Curie temperature in BiYIG (see above Section)^{16,28,29}.

III.A.2.4 Magnetic anisotropy.

Partially doped garnet films can present another anisotropy term compared to undoped structures. It is called the growth induced anisotropy and has a major impact for the case of BiYIG films.

III.A.2.4.1 Growth induced anisotropy.

This growth induced anisotropy term K_{growth} is due to preferential occupation of the dodecaedral site by Bi^{3+} atoms.

Bi^{3+} ions have 24 dodecahedral atomic sites available in one unit cell. Among those 24 possibilities 6 are non-equivalent (due to different number of iron and oxygen neighbors)³⁰, and it is the non-random distribution of Bi^{3+} among those positions that gives rise to uniaxial magnetic anisotropy³¹⁻³⁴. The distribution of the Bi^{3+} ions within the available sites depends on the orientation of the substrate^{31,35} and on the growth parameter (for the case of LPE films

the supercooling temperature plays a crucial role in the magnitude of the $K_{growth}^{31,34}$. A model has been developed by Callen to explain this preferential site ordering^{30,31}.

The magnitude and the sign of K_{growth} depends on both the substituted atoms ($K_{growth} > 0$ for Bi^{3+} or $K_{growth} < 0$ for Pr^{3+})²⁶ and the substitution rate.

For the case of Bi substitution it is positive and the value can reach up to $2 \cdot 10^4 Jm^{-3}$ for some LPE grown BiYIG films¹⁹. Worth to mention that this term is about 30 times larger than the cubic anisotropy K_1 in YIG and is then a relevant anisotropy term.

III.A.2.4.2 Magnetostriction.

The magnitude of the magnetostriction coefficient has been measured using the same procedure as for bulk YIG and has been shown to be linearly dependent on the Bi content and for the case of μm -thick films²¹

$$\lambda_{111}(Bi_xY_{3-x}IG) = \lambda_{111}(YIG)(1 + 0.68x) \quad III-7$$

This increase of the magnetostriction is due to SOC induced by a mixing between the 6p Bi^{3+} orbitals with the 3d and 2p ones from Fe^{3+} and O^{2-} . It is then directly related to the Bi content x ³⁶.

III.A.2.4.3 Magneto cristalline.

The doping in Bi^{3+} is also slightly modifying the magnetocrystalline anisotropy:

$$K_1(Bi_xY_{3-x}IG) = K_1(YIG)(1 + 0.08x) \quad III-8$$

This increase has the same SOC origin as the one of the magnetostriction.^{19,36}

III.A.2.5 Magneto-optical properties

BiYIG has been widely recognized for its high FR coefficient at visible wavelength range (from 0.6 to 2.4 μm)^{16,21,36,37}. Thus, highly doped BiYIG films have found applications for photonics^{38,39} and the increase of magneto-optical coefficient in BiYIG with Bi content can be explained by two main causes¹⁷:

- doping in Bi acts on the strength of the superexchange between Fe^{3+} and increases the magnitude of the splitting due to exchange interaction.
- it enhances the splitting due to SOC⁴⁰ via $Bi^{3+}-O^{2-}-Fe^{3+}$ ligands which splits further the excited states of the Fe^{3+} ions.

The doping in Bi doesn't introduce new transitions but enhances the efficiency of the one already present for the YIG¹⁷. For a given wavelength, the dependence of the FR of BiYIG with Bi content in the film is linear for instance @ 630 nm the magnitude of the FR coefficient for $Bi_xY_{3-x}IG$ LPE grown films related to the Bi content x is measured to be : $\frac{\theta_F}{x} = -2.54^\circ/\mu m$ ²¹. For garnet of composition $Bi_xR_{3-x}Fe_5O_{12}$ with R being a rare earth element (Tm, Lu, Gd) the average increase in FR is $\frac{\theta_F}{x} = -2^\circ/\mu m$ ²⁰. Those materials are promising for integrated photonic application due to their low magneto optical losses and high FR at telecom wavelength⁴¹.

III.A.2.6 Magnetization Dynamics.

Few reports of the BiYIG dynamical properties can be found from films grown by LPE. Some works report a low magnetic damping for BiYIG materials⁴²⁻⁴⁴ comparable to the one obtained for YIG but no significant efforts have been made to understand the correlation between Bi content and magnetic damping.

III-A.3 Case of thin films.

Intrinsic properties of BiYIG and YIG have been presented but thin films materials have usually different properties than the bulk ones. General properties specific to the state of thin films are presented in this section.

III.A.3.1 Structure.

Thin films can have different structures which are: single crystalline, polycrystalline or amorphous. For the case of PLD growth method, films' structure depends on the growth parameters and the lattice parameter of the target material and the substrate.

BiYIG films presented in this Ph.D. thesis are grown on lattice matched garnet substrates (less than 2% misfit between the substrate and the target lattice parameter) having the same structural symmetry (cubic unit cell) as the target (see Part VII.A.1.1). In the optimized growth conditions, we could grow single crystallized BiYIG films oriented in the same (111) growth direction as the substrate. As mentioned for LPE grown films, the substrate-target lattice misfit induces an in-plane strain and leads to an elastic deformation of the original cubic unit cell. In this conditions, the lattice parameters of the film and the substrate are the same in the plane of the film and the growth is said to be pseudomorphic.

It is then important to distinguish the structural properties of the relaxed structure (a_0) and the one of the strained film, distorted when compared to the original structure. As detailed in the Annex I.B, the elastic theory allows obtaining a_0 from the in-plane (a_{film}^{\parallel}) and the out-of-plane (a_{film}^{\perp}) lattice parameter of the strained film. The undistorted lattice is written:

$$a_0 = a_{film}^{\parallel} - \frac{\mu - 1}{1 + \mu} (a_{film}^{\perp} - a_{film}^{\parallel}) \quad III-9$$

Where μ is the Poisson coefficient of the material. Moreover, the pseudomorphic growth imposes $a_{film}^{\parallel} = a_{substrate}$ in and out-of-plane.

All our thin films present those pseudomorphic growth characteristics, thus Equation III-9 will be extensively used to derive the lattice parameters of the relaxed structure.

III.A.3.2 Magnetic properties.

III.A.3.2.1 Magnetization.

The total magnetic moment of our thin films should be the same as the bulk crystal if the stoichiometry in iron ions is preserved. SQUID magnetometry shows indeed that within 5%, this is the case.

III.A.3.2.2 Magnetic anisotropy

The magnetic energy E_m in the absence of an external field applied is defined by:

$$E_m = -K_{shape} \cos(\theta)^2 + K_u \sin(\theta)^2 \quad III-10$$

With the angle θ defined as in the Figure III-8. The different energy terms are the shape and uniaxial anisotropy (respectively K_{shape} and K_u). Thus the positive uniaxial anisotropy favors an out-of-plane easy magnetic axis.

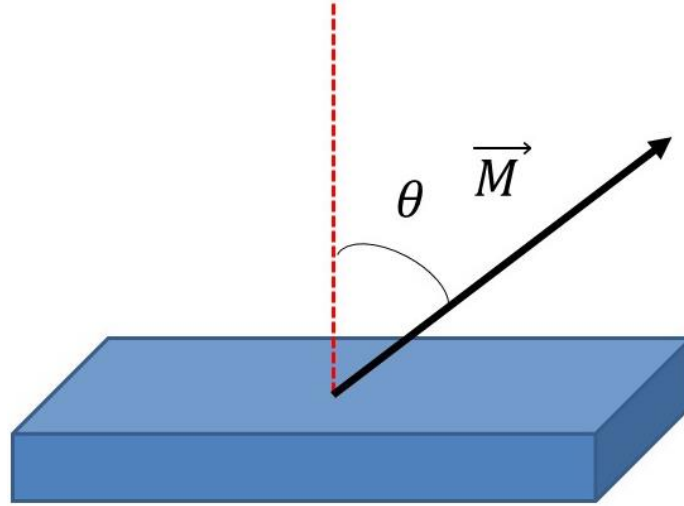


Figure III-8-Scheme of the magnetization direction for a magnetic film.

For the case of thin films the anisotropic shape of the film gives rise to a demagnetization energy term that favors in-plane magnetization (see Section III.B.1.4). This term is also called shape anisotropy and is proportional to the magnetic moment of the material.

$$K_{shape} = \frac{-\mu_0 M_s^2}{2} \quad III-11$$

To induce out-of-plane magnetic anisotropy in thin films, it is then necessary to compensate this shape anisotropy. For the case of YIG (and BiYIG) thin films: $K_{shape} \sim -12 \text{ kJ} \cdot \text{m}^{-3}$ it is then a very important contribution to the magnetic energy for YIG thin films.

In thin films under epitaxial strain the total uniaxial magnetic anisotropy K_u contains a magneto elastic anisotropy induced by magnetostriction. In BiYIG μm -thick films the magnetostriction is a bit higher than for bulk and has been measured to be ⁴⁵:

$$\lambda_{111}(x) = -2.89 \cdot 10^{-6}(1 + 0.75x) \quad III-12$$

It is possible to estimate the magneto elastic anisotropy energy induced by strain σ from Equation III-9 using the substrate/relaxed structure misfit (Δa) (see Annexe I.B).

$$\sigma = \frac{E}{1-\mu} \left(\frac{\Delta a}{a_0} \right) = \frac{E}{1-\mu} \frac{(a_0 - a_{substrate})}{a_0} \quad III-13$$

With $E = 2.055 \cdot 10^{11} \text{ J} \cdot \text{m}^{-3}$ and $\mu = 0.29$ the Young modulus and the Poisson coefficient (that can be found in the literature for the YIG and the BiYIG²¹). If we assume 2% of misfit (highest misfit value achieved in our films), the magnitude of the magneto elastic term is $K_{MO} \sim 1.6 \text{ kJ} \cdot \text{m}^{-3}$. This term is higher than the intrinsic magnetocrystalline anisotropy but remains below (about a factor of 8) than the shape anisotropy term.

If we sum up energy terms arising for the special case of thin films the dominant term remains the shape anisotropy favoring an in-plane easy axis of the magnetization. To induce perpendicular magnetic anisotropy (PMA) in our films an additional anisotropy term is required. This term can be the growth induced anisotropy or the magneto elastic term.

III.A.3.3 Magneto optics.

There are no deep studies on the dependence of the magneto-optical coefficient behavior with the thickness of the films for tenth of nm-thick PLD grown films. One study on hundreds of nm-thick films grown by PLD claimed that θ_F was decreasing with the film thickness²⁵ but this was due to a degradation of the quality of the films (cracks and electronic deficiencies for Fe^{3+} ions).

III.A.3.4 Dynamical properties.

Dynamical properties of nm-thick garnet films reported in the literature are not as good as the bulk material one. State of the art PLD grown YIG thin films have Gilbert damping of $\alpha = 2.3 * 10^{-4}$ and inhomogeneous contribution $\mu_0 \Delta H_0 = 0.14 \text{mT}$ ⁴⁶ which is one order of magnitude larger than the value of the bulk. There are no clear understanding of this difference in the dynamical properties between the thin films and the bulk material.

III-B FMR and magnetization dynamic.

In this section, we will discuss the general properties of magnetization dynamics in magnetic materials and then we derive the fundamental equations describing this motion. In a second part we present the Ferromagnetic Resonance (FMR) technique which is the experimental tool used in this Ph.D. thesis, to measure the magnetic losses as well as the magnetic anisotropy of the investigated YIG and BiYIG films.

III-B.1 Dynamic of the magnetic moment.

In this part, we describe the dynamic of the magnetic moment starting from the case of a single spin and then extend it to the case of a magnetic material.

III-B.1.1 From the single spin to the magnetic moment.

A single spin creates an external field $\mu_0 \mathbf{H}$. It is coupled to its magnetic environment through the Zeeman term, and its Hamiltonian is then:

$$\mathcal{H}_t = \mu_0 \frac{g\mu_B}{\hbar} \mathbf{S} \cdot \mathbf{H} \quad III-14$$

With g , \hbar and μ_B : the Landé factor of the electron, the reduced Planck constant (in J.s) and the Bohr magneton (in A.m²).

From the Ehrenfest theorem the time evolution of the operator $\langle \mathbf{S} \rangle$ that gives the expected value of the spin \mathbf{S} is written:

$$\frac{d}{dt} \langle \mathbf{S} \rangle = \langle \frac{\partial \mathbf{S}}{\partial t} \rangle + \frac{1}{i\hbar} \langle [\mathbf{S}, \mathcal{H}_t] \rangle \quad III-15$$

It is possible to show that $\langle \frac{\partial \mathbf{S}}{\partial t} \rangle = 0$ due to conservation of the spin norm \mathbf{S}^2 .

Using commutation rules (shown in Annexe I.A) it is possible to simplify the Equation III-15 to:

$$\frac{d}{dt} \langle \mathbf{S} \rangle = \frac{g\mu_b\mu_0}{i\hbar} \langle \mathbf{S} \rangle \times \langle \mathbf{H} \rangle \quad III-16$$

By writing the magnetic moment of the spin \mathbf{m} it gives:

$$\mathbf{m} = -\gamma \mathbf{S} \quad III-17$$

Where $\gamma = \frac{g\mu_B}{\hbar}$ is the gyromagnetic ratio of the electron (rad.s⁻¹T⁻¹). For magnetic materials with SOC the Landé factor is not the one of a single electron $g \rightarrow g_L$, hence the gyromagnetic ratio is changed.

The magnetization vector of a spin assembly in a volume V can be derived from the magnetic moment of single spins within this assembly:

$$\mathbf{M} = \frac{\sum \mathbf{m}}{V} \quad III-18$$

And the Equation III-16 can be generalized to the magnetization of a solid:

$$\frac{d}{dt}\mathbf{M} = -\mu_0\gamma\mathbf{M} \times \mathbf{H} \quad \text{III-19}$$

Equation III-19 is the Landau-Lifshitz equation which governs the evolution of a magnetic moment in a solid under an external field $\mu_0\mathbf{H}$: the motion of the magnetic moment is due to the torque applied by the external field.

It is possible to show that the Equation III-19 corresponds to a circular motion of the magnetic moment around the external field axis. The frequency of precession is called the Larmor frequency (ω_L in $\text{rad}\cdot\text{s}^{-1}$) and is written as:

$$\omega_L = \gamma\mu_0 H \quad \text{III-20}$$

So far we described the motion of the magnetic moment under an external field without any other source of energy provided in the system. We will now see how the magnetization vector behaves if the field $\mu_0\mathbf{H}$ is time dependent and introduce then the FMR phenomena.

III.B.1.2 FMR.

We will now treat the case an external field $\mu_0\mathbf{H}$ which is time dependent and restrict ourself to small perturbations : $\mu_0\mathbf{H}(t) = \mu_0(\mathbf{H}^0 + \mathbf{h}(t))$.

To get an analytical solution for the magnetic moment \mathbf{M} it is necessary to linearize the Equation III-19 by considering the case of small oscillations for the magnetic moment: $\mathbf{M}(t) = \mathbf{M}^0 + \mathbf{m}(t)$. Because \mathbf{M}^0 and \mathbf{H}^0 are not time dependent, the Equation III-19 after linearization becomes:

$$\frac{\partial \mathbf{m}}{\partial t} = -\gamma\mu_0(\mathbf{M}^0 \times \mathbf{h}(t) + \mathbf{m}(t) \times \mathbf{H}^0) \quad \text{III-21}$$

The geometry of the system is shown in Figure III-9: the magnetic moment $\mathbf{M}(t)$ precesses around its equilibrium axis (\mathbf{H}^0), the amplitude of the precession is given by $\mathbf{m}(t)$.

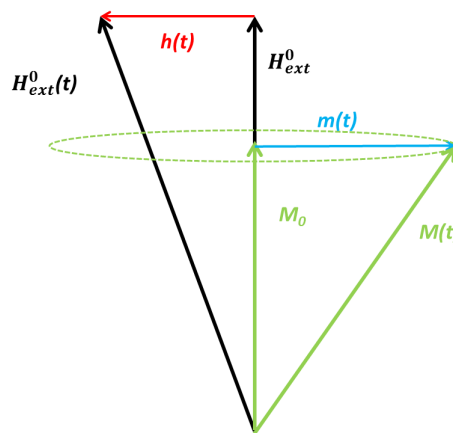


Figure III-9 Scheme of the magnetic direction vectors in the case of the linearisation of the Equation III-21 under the assumption that $\mathbf{M}^0 \parallel \mathbf{H}^0$.

The solution for such motion is found by writing: $\mathbf{m}(t) = \mathbf{m}e^{\hat{i}\omega t}$ and $\mathbf{h}(t) = \mathbf{h}e^{\hat{i}\omega t}$. The magnetic moment $\mathbf{m}(t)$ can be expressed from the external field excitation:

$$\mathbf{m}(t) = \vec{\chi}_p \mathbf{h}(t) = \begin{bmatrix} \chi & i\chi_a & 0 \\ -i\chi_a & \chi & 0 \\ 0 & 0 & 0 \end{bmatrix} \mathbf{h}(t) \quad III-22$$

$\vec{\chi}_p$ is the Polder tensor that relates the magnetic moment to the external field, the different terms that are contained in the tensor are:

$$\chi = \frac{\omega_M \omega_H}{\omega_H^2 - \omega^2} \quad III-23$$

$$\chi_a = \frac{\omega_M \omega}{\omega_H^2 - \omega^2} \quad III-24$$

with $\omega_M = \gamma \mu_0 M^0$ and $\omega_H = \gamma \mu_0 H^0$.

In the simple case of an isotropic infinite material the motion of the magnetic moment \mathbf{m} is gyrotropic and in the plane perpendicular to the direction of \mathbf{M}_0 (Figure III-9).

For the resonant frequency of excitation $\omega = \omega_{res} = \omega_H$ the system is in resonance and $\chi_a \rightarrow \infty$. In practice this corresponds to the absorption of rf energy by the magnetic degrees of freedom.

We saw that for a specific excitation the system can absorb energy we will see how this energy is dissipated.

III.B.1.3 Magnetic losses.

The dissipation of the magnetic energy can be introduced phenomenologically by adding another term in the Equation III-19 :

$$\frac{d\mathbf{M}}{dt} = -\gamma \mu_0 \mathbf{M} \times \mathbf{H} + \frac{\alpha}{\|\mathbf{M}\|} \mathbf{M} \times \frac{d\mathbf{M}}{dt} \quad III-25$$

The parameter α in Equation III-25 is unit-less and is called the Gilbert damping, it accounts for magnetic losses. For ferromagnetic metals (FM) $\alpha \geq 10^{-3}$ and for magnetic insulators this value can be considerably lower $\alpha \sim 10^{-5}$ (for YIG) due to the absence of conduction electrons-magnons interactions (see Section III-B.2).

Worth to note here that the norm of the magnetization vector norm is conserved even after introduction of magnetic losses:

$$\frac{d\mathbf{M}^2}{dt} = \left(\frac{d\mathbf{M}}{dt} \right) \cdot \mathbf{M} = (-\mu_0 \gamma \mathbf{M} \times \mathbf{H}) \cdot \mathbf{M} + \frac{\alpha}{\|\mathbf{M}\|} \left(\mathbf{M} \times \frac{d\mathbf{M}}{dt} \right) \cdot \mathbf{M} = 0 \quad III-26$$

This means that magnetic losses are just pushing back the magnetic moment to its equilibrium position but the total magnetic 'quantity' is preserved. Other dissipation processes can give rise to non-conservation of \mathbf{M} length⁴⁷.

The result in term of solution for the equation of motion compared to the lossless case III-19 is the introduction of an imaginary part in the tensor $\vec{\chi}_p$ and ω_{res} . In the resonant conditions, matrix elements of permeability tensor have finite values (contrary to the lossless case). The infinite divergence of $\mathbf{m}(t)$ is replaced by a Lorentzien shape peak corresponding to absorption of the rf power for $\omega = \omega_{res}$. The width of this peak is related to the α parameter:

$$\mu_0 \Delta H_{res} = \frac{2\alpha \omega_{res}}{\gamma} \quad III-27$$

From FMR experiments it is possible to determine the dissipation parameter α .

So far the coupling between the magnetization vector and its environment was all contained in the Zeeman term under the term $\mu_0 \mathbf{H}^0$. For real magnetic materials it corresponds to an effective field felt by the precessing magnetization and depends on the materials' magnetic properties as detailed in the next section.

III.B.1.4 Effective Field.

In an external magnetic field a magnetic material is 'reacting' to minimize its energy. Hence there is a difference between the field applied $\mu_0 \mathbf{H}_{ext}$ and the field 'felt' by the magnetization of the material: $\mu_0 \mathbf{H}_{eff}$.

The total energy of a magnetic material under an external magnetic field is composed of different terms:

$$E_T = E_{Zeeman} + E_{anisotropy} + E_{magnetostatic} + E_{exch} \quad III-28$$

We describe the different energy terms that are defining the total magnetic energy within the picture and the geometry given in Figure III-10.

- Due to the external field the magnetic moment of the material will tend to align with the film due to the Zeeman energy term:

$$E_{Zeeman} = -\mu_0 \int \mathbf{m}(V) \mathbf{H}_{ext} dV = -\mu_0 M H_{ext} \cos(\theta) \quad III-29$$

- Depending on the type of the magnetic material (ferro, antiferro, ferri) spins will tend to align parallel or antiparallel to each other in order to minimize the exchange interaction energy. Any deviation from the equilibrium situation will cause an increase in the exchange energy. The macroscopic expression of this latter is:

$$E_{exch} = -A \int \frac{|\nabla \mathbf{M}|^2}{\|\mathbf{M}\|^2} dV \quad III-30$$

Where A is the exchange stiffness (in $\text{J}\cdot\text{m}^{-1}$) (mentioned in Section III.A.1.3).

- A magnetic material of a finite size which is polarized presents magnetic dipoles (+ and – in Figure III-10) on its surfaces, those are coupled with each other and create a dipolar field (blue arrows in Figure III-10). Depending on the shape and the size of the sample the strength of interaction is not the same along all directions. The stabilization of those dipoles is at the cost of the magnetostatic energy:

$$E_{magnetostatic} = -\frac{\mu_0}{2} \mathbf{H}_D \cdot \mathbf{M} \quad III-31$$

with $\mu_0 \mathbf{H}_D = \mu_0 (-\vec{N} \cdot \mathbf{M})$ the demagnetizing field and \vec{N} is the shape tensor which depends on the shape of the material. For the simple case of ultrathin films

considered as infinite in the (x,y) plane $\vec{N} = \begin{pmatrix} 0 & 0 & 0 \\ 0 & 0 & 0 \\ 0 & 0 & 1 \end{pmatrix}$. Therefore

$\mathbf{H}_D = -M_s \cos(\theta_z) \mathbf{u}_z$ and the expression of the magnetostatic energy for thin films is:

$$E_{magnetostatic} = -\frac{\mu_0}{2} M_s^2 \cos(\theta_z)^2 \quad III-32$$

with θ_z the angle between \mathbf{M} and the out-of-plane direction of the film.

- The magnetic moment of the electronic spin \mathbf{S} interacts with the orbital momentum of the atom \mathbf{L} : this is called the spin orbit coupling (SOC). As a consequence, the direction of the effective magnetic field within the material doesn't depend only upon the spin-spin exchange interaction (which is isotropic) but also on the arrangement, the position and the spacing of atoms. That's why the energy to align the magnetic moment along the different crystallographic axis of the material can be different. This is called the magnetocrystalline anisotropy. For the simplest case of a uniaxial symmetry it is written:

$$E_{ani} = K_u \sin(\theta_u)^2 \quad III-33$$

with θ_u the angle between the magnetic moment and the anisotropy axis and K_u the corresponding anisotropy constant.

In our case, we have three sources of anisotropy (see Section III.A.1.4 and III.A.2.3):

- the magnetocrystalline anisotropy: K_1 .
- the growth induced anisotropy: K_{growth} .
- the magneto elastic anisotropy: $K_{magneto-elastic} = K_{MO}$.

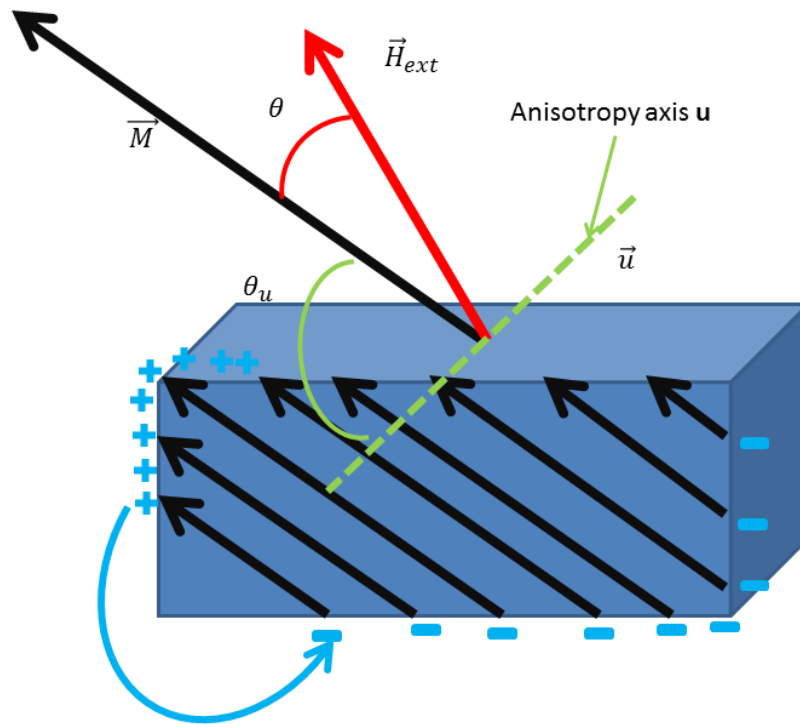


Figure III-10-Illustration of a magnetic material under an external magnetic field

In the presence of all these energy terms, the effective field felt $\mu_0 H_{eff}$ by the magnetization submitted to an external magnetic field $\mu_0 \mathbf{H}_{ext}$ can be derived from the following expression:

$$\mu_0 \mathbf{H}_{eff} = -\nabla_M \mathbf{E}_T \quad III-34$$

In this Ph.D. work, FMR experiments are performed on magnetic thin films for which the magnetic energy terms are :

- The magnetostatic energy.
- The uniaxial anisotropy (for an anisotropy axis directed in the out-of-plane direction).

Due to the anisotropy of $\mu_0 \mathbf{H}_{eff}$ (contrary to $\mu_0 \mathbf{H}_{ext}$) the resonant conditions will be modified.

III.B.1.5 Resonant conditions for a ferromagnetic thin film.

The equation of motion for the magnetic moment of a magnetic material is then:

$$\frac{1}{\gamma} \frac{d\mathbf{M}}{dt} = -\mathbf{M} \times (\mu_0 \mathbf{H}_{eff}) + \frac{\alpha}{\|\mathbf{M}\|\gamma} \mathbf{M} \times \frac{d\mathbf{M}}{dt} \quad III-35$$

This equation can be linearized as the Equation III-21 and the resonant conditions become dependent on the direction of the external field with respect to the main anisotropy axis of the material: the out-of-plane direction:

- For $\mathbf{H}_{ext} \parallel$ film plane:

$$\frac{\omega_0^2}{\gamma^2} = \mu_0^2 H_{ext} (H_{ext} - (\frac{2K_u}{M_s} - M_s)) \quad III-36$$

- For $\mathbf{H}_{ext} \perp$ film plane:

$$\frac{\omega_0}{\gamma} = \mu_0 (H_{ext} + (\frac{2K_u}{M_s} - M_s)) \quad III-37$$

With $M_s = \|\mathbf{M}\|$ the norm of the magnetization vector and $K_u = K_{MO} + K_{growth}$ the total uniaxial anisotropy term. It can be noticed that the term K_1 is neglected in the expression of the anisotropy because as we saw in III.A.1.4 and III.A.2.3 it is considerably smaller than the other terms.

We saw that in a magnetic material all spin can precess together in the resonant conditions: this is the FMR phenomena. It is also possible that those spins are precessing coherently but not uniformly this is called a spin wave. We present briefly this phenomena in the next Section.

III-B.2 Spin waves in short.

There are different kind of precession for the magnetic moment:

- uniform which is the FMR.
- non-uniform but coherent which is the spin wave and will be described in this part.
- non uniform and non-coherent.

In an external magnetic field the Hamiltonien of the spin system is written:

$$\mathcal{H} = g\mu_b \sum_i \mathbf{S}_i \mathbf{H}_{ext} - 2J \sum_{i,j} \mathbf{S}_i \mathbf{S}_j \quad III-38$$

Where $g, \mu_b, \mathbf{S}_i, J$ and \mathbf{H}_{ext} are respectively the Landé factor, the Bohr magneton, the vector of the i^{th} spin, the exchange integral and the external field. The first term corresponds to the Zeeman energy and the second term to the exchange energy between all neighbouring spins. The ground state of such a system corresponds to the alignment of all spins in the same direction. If we consider the first excited state depending on the strength of the exchange energy term it might be not desirable to reverse one single spin but to adopt instead the spin distribution of Figure III-11(b).

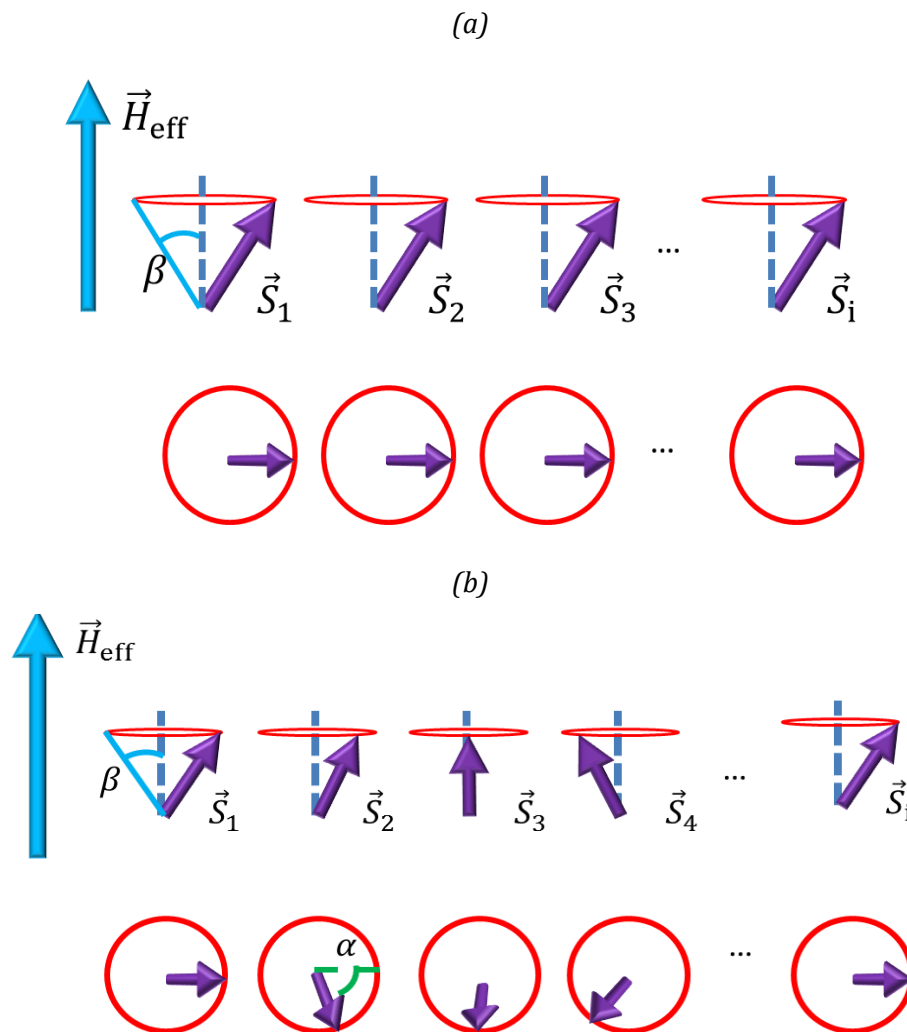


Figure III-11 Illustration of (a) the uniform precession due to FMR and (b) the non-uniform precession due to a spin wave

The first excited state corresponds to the following situation:

- all spins are doing the same angle β with the external field $\mu_0 \mathbf{H}_{ext}$ (opening of the red cone in Figure III-11 (b))
- each spin is slightly shifted of a phase angle α with respect to its first neighbour (in green Figure III-11 (b)).

The magnetic precession in the material is not uniform but coherent and this configuration is called a spin wave. The spin wave corresponds to an excited state of:

- energy $\epsilon = \hbar\omega$
- angular momentum \hbar
- wavelength λ which is the distance between two parallel spins
- propagation direction vector $\mathbf{k} = \frac{2\pi}{\lambda} \mathbf{u}_k$ (\mathbf{u}_k being the unit vector of propagation of the spin wave).

A quanta of spin waves is called a magnon.

The spin wave dispersion relation depends on:

- the orientation of the effective field with respect to spin wave propagation direction

- the ratio between between the spin wave wavelength and the exchange interaction constant of the material Λ .

The exchange constant is defined by different parameters of the material:

$$\Lambda = \sqrt{\frac{A}{\mu_0 M_s^2}} \quad \text{III-39}$$

A and $\mu_0 M_s^2$ being respectively the exchange stiffness ($J \cdot m^{-1}$) and the demagnetizing anisotropy term ($J \cdot m^{-3}$). Different spin wave dispersion relation have to be considered depending on the spin wave. The two types of spin waves are defined by the following way:

- $\frac{\lambda}{\Lambda} \gg 1$ corresponds to the case of **dipolar spin waves**. The exchange term is neglected in the magnetic energy terms. In this regime for thin films the expression of the spin wave dispersion relation changes depending on the orientation of \mathbf{k} with respect to the external field.
- $\frac{\lambda}{\Lambda} \approx 1$ corresponds to the case of **exchange spin wave**. Due to the very short value of λ those spin waves are not guided within the material. No boundary conditions due to finite dimension of the material have to be taken into account. The expression of the spin wave dispersion relation is not depending on the orientation of \mathbf{k} with respect to the external field.
- $\frac{\lambda}{\Lambda} > 1$ corresponds to the case of **dipole-exchange spin wave**. Both the exchange and the dipolar energy needs to be taken into account. This regime allow to connect the spin wave dispersion relation from the exchange and dipolar regime.

A more complete review on the subject can be found in ref ⁴⁷ but for the purpose of this Ph.D. this very short introduction on the concept of spin waves is enough.

Now we saw the different type of precession for the magnetic moment in a magnetic material we will now focus on how the magnetic energy can be dissipated within the magnetic material.

III-B.3 Magnetic losses.

In the Equation III-25 a phenomenological term, the Gilbert damping, corresponding to energy dissipation by the system has been introduced. It is in theory directly related to the linewidth of the resonant peak (Equation III-27). However to describe the evolution of ΔH_{res} with f_{res} from FMR experimental values another frequency independent term: the inhomogeneous broadening ΔH_0 needs to be introduced. The expression of the linewidth is then:

$$\mu_0 \Delta H = \mu_0 \Delta H_0 + \frac{\alpha 2\pi f_{res}}{\gamma} \quad \text{III-40}$$

From the expression of the magnetic losses we will define mechanisms behind each relaxation term starting with the inhomogeneous broadening term ΔH_0 .

III.B.3.1 Relaxation processes involved in ΔH_0 .

The broadening of the linewidth due to the term ΔH_0 has an extrinsic origin only and is coming from inhomogeneities or defaults within the magnetic material. Those defaults can enhance the linewidth due to different reasons:

- **A spread of the magnetic properties:** as magnetic properties of the material are defining the resonant field in FMR experiments, local variations of those properties lead to different values of the resonant field. Summing up all those different single contributions, slightly shifted between each other leads to a broadening of the resonance linewidth which is not frequency dependent. This is illustrated in Figure III-12.

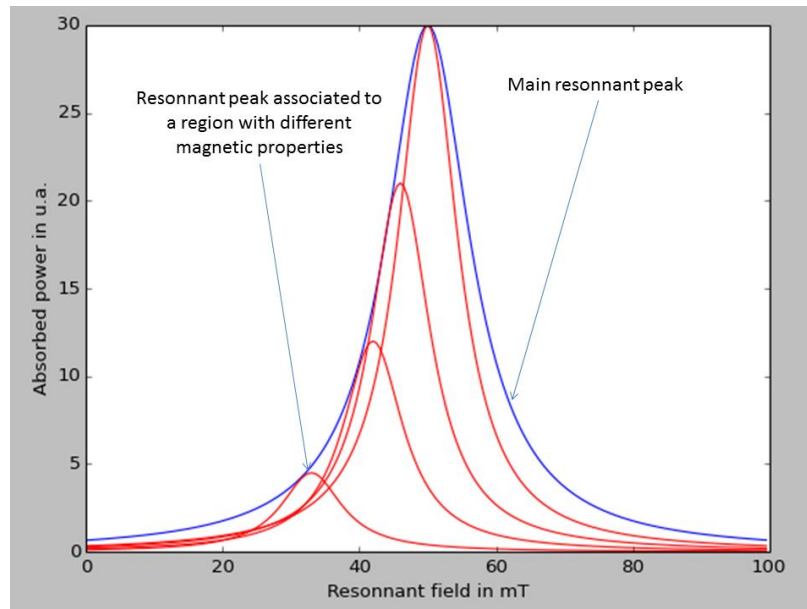


Figure III-12-FMR resonant peaks of a sample presenting magnetic inhomogeneities. The main resonant peak is the sum of several peaks corresponding to regions with slightly different magnetic properties.

- **The scattering of FMR mode due to the presence of magnetic inhomogeneities.** Those inhomogeneities act as scattering centers for the spin wave. If the energy is conserved the FMR mode (spin wave of $k = 0$) can scatter into an higher mode (spin wave of $k \neq 0$). For this scattering process to happen it is necessary that magnons with the same energy as the FMR mode exist (see Figure III-5 in Section III.A.1.6. This gives restriction on the scattering condition (geometry of excitation, frequency of FMR mode...)).

III.B.3.2 Relaxation processes involved in α .

We detail now relaxation processes that are contained in the parameter α , they have both extrinsic and intrinsic origins and are summed up in the Figure III-13. They are due to the material properties (intrinsic mechanism) or to the imperfections of the material (extrinsic).

- **FMR precession-lattice coupling through ionic impurities** is due to extrinsic properties of the material such as magnetic impurities or off-stoichiometry. In a magnetic material the precession of \mathbf{M} leads to electronic transitions that have a finite life time. Those transitions require energy absorption (coming from the magnetization precession) which is thereafter released to other degrees of freedom such as phonons.
- **The Kasuya-Le Crau mechanism**⁴⁸ where FMR mode couples to the phonons of the lattice to create a magnon (this process requires restriction on the dispersion relation of both magnons and phonons of the system). It is an intrinsic relaxation process.

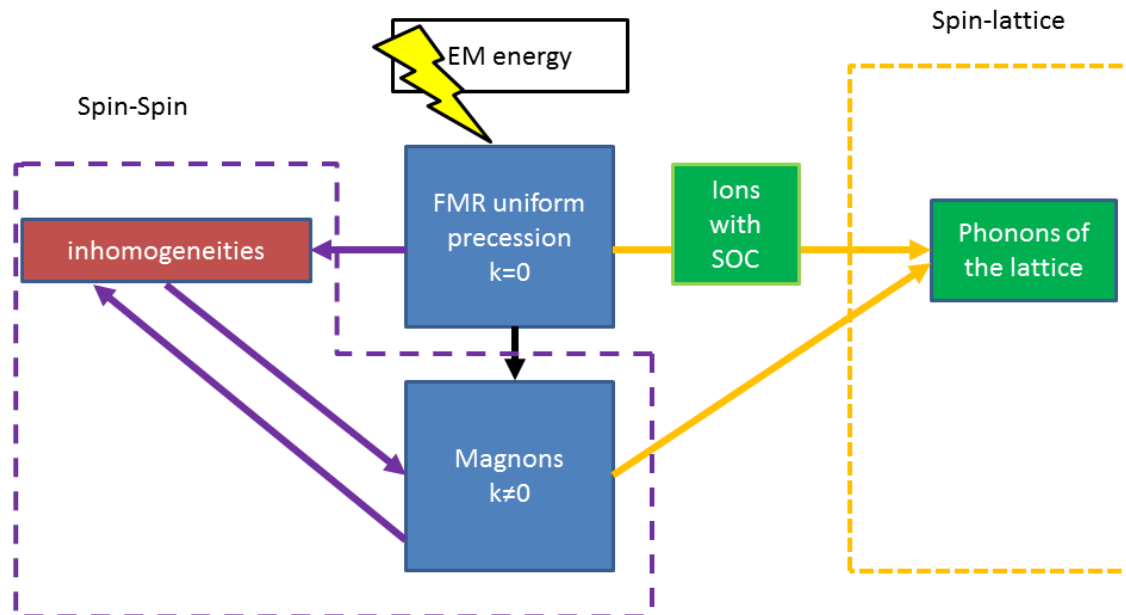


Figure III-13-Scheme of the different relaxation processes inducing losses

- **The spin pumping mechanism** occurs for the case of a metal/magnetic material bilayer. For this situation the angular momentum of electrons from the FMR mode is transferred to the electrons of the normal metal. Electrons in the normal metal become spin polarized but angular momentum corresponding to FMR precession is lost. This phenomenon is known to increase the Gilbert damping and is more detailed in the part IV-D.2.

Magnetic dynamics will be a key point in this Ph.D. and it is then important to be able to distinguish between the different relaxation mechanisms in order to know which parameter (Gilbert damping or inhomogeneous broadening) we are extracting from FMR measurements.

IV Spintronics with magnetic insulators.

This Chapter is dedicated to the field of spintronics and the use of magnetic insulators within this subject. We present first the main concepts necessary to understand spintronics and then we focus on spintronic effects that can be observed in insulating materials.

IV-A Spin current in a metal.

In this Section we introduce the concept of spin current for metallic materials and describe its dynamic.

IV-A.1 Definition and origin in metals.

In any material electrons carry both a charge and a spin. As it is possible to define an electric current corresponding to the motion of electronic charges it is also possible to define a spin current. The spin density current is expressed through the tensor \vec{j}_s :

$$\vec{j}_s = \begin{bmatrix} j_{sx}^x & j_{sx}^y & j_{sx}^z \\ j_{sy}^x & j_{sy}^y & j_{sy}^z \\ j_{sz}^x & j_{sz}^y & j_{sz}^z \end{bmatrix} \quad IV-1$$

Where j_{sl}^m corresponds to the spin density polarized along the axis l for an electron flow in the direction m . In reality due to magnetic anisotropy there are preferential spatial axes for the orientation of the electronic spin. In that case only one axis of polarization (let's say z) can be considered:

$$\mathbf{j}_s = \begin{bmatrix} j_{sz}^x \\ j_{sz}^y \\ j_{sz}^z \end{bmatrix} \quad IV-2$$

Values of s_z are the eigenvalues of the spin in this basis (so $\pm \frac{1}{2}$), in the following we will simply write $\mathbf{j}_\downarrow(\mathbf{j}_\uparrow)$ for spin polarized along the $+z(-z)$ direction.

The spin current \mathbf{j}_s is written:

$$\mathbf{j}_s = -\frac{\hbar}{2e}(\mathbf{j}_\uparrow - \mathbf{j}_\downarrow) \quad IV-3$$

The charge current \mathbf{j}_c is related to the spin density vector by:

$$\mathbf{j}_c = (\mathbf{j}_\uparrow + \mathbf{j}_\downarrow) \quad IV-4$$

For the sake of simplicity in the writing we define a spin current (\tilde{j}_s) having the same dimension as the charge current:

$$\tilde{j}_s = \frac{2e}{\hbar}(\mathbf{j}_s) = -(\mathbf{j}_\uparrow - \mathbf{j}_\downarrow) \quad IV-5$$

Similarly to the flux of electric current, the flux of up or down spin can be related to the gradient of the chemical potential μ for the up or down spin population by:

$$\mathbf{j}_{\uparrow(\downarrow)} = \frac{\sigma_{\uparrow(\downarrow)} \nabla \mu_{\uparrow(\downarrow)}}{e} \quad IV-6$$

Where $\sigma_{\uparrow(\downarrow)}$ and $\mu_{\uparrow(\downarrow)}$ are the conductivity (in $S \cdot m^{-1}$) and the chemical potential (in Joules) of the up (down) polarized electrons. Hence in a metal there are different possibilities to induce a spin current:

- a difference in the conductivity between the up and down spin: $\sigma_\uparrow \neq \sigma_\downarrow$.
- a difference in the chemical potential for the up and down spin: $\mu_\downarrow \neq \mu_\uparrow$.

The first type is called a spin polarized current and the second one a pure spin current.

IV.A.1.1 Spin polarized current.

The spin polarized current is coming from a difference in conductivity between up and down electrons. The conductivity is written:

$$\sigma_{\uparrow(\downarrow)} = e^2 D_{\uparrow(\downarrow)} N_{\uparrow(\downarrow)}(E_F) \quad IV-7$$

With $D_{\uparrow(\downarrow)}$ and $N_{\uparrow(\downarrow)}(E_F)$ being respectively the diffusion coefficient (in $\text{m}^3 \cdot \text{s}^{-2}$) of up (down) polarized electrons and the number of up (down) conduction electrons at the Fermi level. The expression of $D_{\uparrow(\downarrow)}$ is related to the Fermi velocity $v_{\uparrow(\downarrow)}^F$ and the mean free path $\lambda_{\uparrow(\downarrow)}^F$ of the up (down) electrons at the Fermi level:

$$D_{\uparrow(\downarrow)} = \frac{\lambda_{\uparrow(\downarrow)}^F}{3} N(E_F)_{\uparrow(\downarrow)} (v_{\uparrow(\downarrow)}^F)^2 \quad IV-8$$

In 3d transition metals with unfilled d band such as Co or Fe due to exchange energy the band structure is shifted for up and down electrons (Figure IV-1(a)) therefore the velocity and the number of up and down electrons at the Fermi level (related to the diffusion coefficient) are not the same leading to: $\sigma_{\downarrow} \neq \sigma_{\uparrow}$.

A charge current due to an electronic chemical potential gradient $\nabla\mu$ in these conditions is written:

$$\mathbf{j}_c = -\frac{\frac{\sigma_{\uparrow} + \sigma_{\downarrow}}{e} \nabla\mu}{2} \quad IV-9$$

Because of the difference in mobility between up and down electrons this will also leads to a spin current:

$$\tilde{\mathbf{j}}_s = \frac{2e}{\hbar} (\mathbf{j}_s) = -\frac{1}{2} \left(\frac{\sigma_{\uparrow} - \sigma_{\downarrow}}{e} \right) \nabla\mu \quad IV-10$$

The spin current is called spin polarized current and is related to a charge current.

IV.A.1.2 Pure spin current.

In a Normal Metal (NM) there is no difference in conductivity for the up and down spin, because the electronic band structure is symmetric with respect to the spin polarization (see Figure IV-1(b)). Consequently $\sigma_{\uparrow} = \sigma_{\downarrow} = \frac{\sigma}{2}$ and only a difference in the chemical potential gradient between up and down channel can lead to a spin current. In that case the spin current is called a *pure spin current* and is written:

$$\tilde{\mathbf{j}}_s = \frac{2e}{\hbar} (\mathbf{j}_s) = -\frac{\sigma}{2e} \nabla(\mu_{\uparrow} - \mu_{\downarrow}) \quad IV-11$$

Indeed if we calculate the charge current:

$$\mathbf{j}_c = \mathbf{j}_{\uparrow} + \mathbf{j}_{\downarrow} = \frac{\sigma}{2e} (\nabla\mu_{\uparrow} + \nabla\mu_{\downarrow}) \quad IV-12$$

Due to conservation of the number of charge carrier we have $\nabla\mu_{\uparrow} = -\nabla\mu_{\downarrow}$ hence the total charge current is zero (there is no flow of electrons) but there is a spin current which is called a *pure spin current* Figure IV-1(d).

The difference in chemical potential between up and down channel is called a *spin accumulation* μ_s and is written:

$$\mu_s = \mu_{\uparrow} - \mu_{\downarrow} \quad IV-13$$

The spin accumulation is a scalar quantity but can also be written as a vector $\boldsymbol{\mu}_s$ in that case the direction of the vector corresponds to the spin polarization direction (that we said to be the z axis in the beginning).

The spin accumulation allows expressing the pure spin current in a similar way as the charge current:

$$\tilde{\mathbf{j}}_s = \frac{2e}{\hbar} (\mathbf{j}_s) = -\frac{\sigma}{2e} \nabla \mu_s \quad IV-14$$

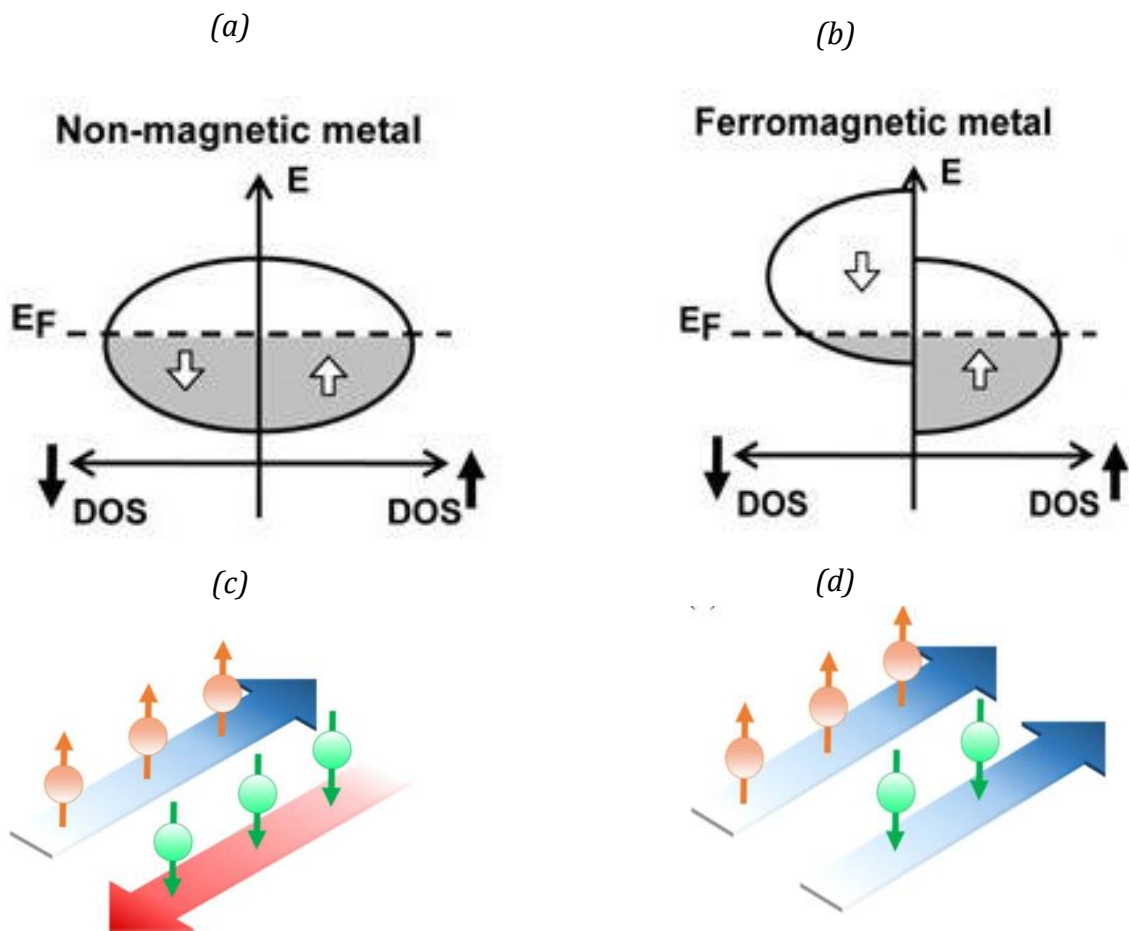


Figure IV-1-Scheme of the electronic band structure for a normal metal (a) and a ferromagnetic material (b) from ref¹⁵. E_f and DOS stand respectively for the Fermi energy and the Density of States. Due to the shift of the energy band a net spin polarization is observed for the situation (b). Illustration of a pure spin current (c) and a spin polarized current(d) from ref⁴⁹.

We defined here the notion of spin current and the two types of spin current that could occur in metals depending on their electronic band structure. In this Ph.D. thesis, spintronic

phenomena are observed with NM where only pure spin current can be found. We focus now on those materials and on the dynamic of spin current in those NM.

IV-A.2 Spin relaxation in a NM.

In a NM like Pt at the thermodynamic equilibrium state, electrons at the Fermi level with up and down spin have the same chemical potential (due to symmetry of the electronic band structure):

$$\mu_{equ}(E = E_F) = \mu_{\uparrow equ} = \mu_{\downarrow equ} \quad IV-15$$

The return to equilibrium of μ is done by spin flip: the characteristic distance corresponding to this relaxation is called the spin diffusion length (λ_{sd}). The evolution in space of the spin accumulation can be derived from the spin current gradient:

$$\nabla \tilde{j}_s = \frac{\sigma}{e2} \nabla (\nabla \mu_s) \quad IV-16$$

Moreover the spin current dynamic is described by the Valet and Fert⁵⁰ diffusion model:

$$\nabla \tilde{j}_s = \frac{\sigma \mu_s}{e D_{sf} \tau_{sf}} \quad IV-17$$

This model is taking into account two phenomena that rule the spin current dynamic:

- an increase of spin accumulation due to a spin current.
- a decrease of spin current due to spin flip.

The quantities τ_{sf} and D_{sf} are the spin flip time and the spin dependent charge diffusion coefficient. They are related to the λ_{sd} by $\lambda_{sd} = \sqrt{D_{sf} \tau_{sf}}$.

In terms of chemical potential the spin diffusion equation is then written:

$$D_{sf} \nabla^2 \mu_s = \frac{\mu_s}{\tau_{sf}} \quad IV-18$$

The profile of chemical potential along the NM thickness is given by Equation IV-19 the solution is an exponential decay over the sample thickness x :

$$\mu_s(x) = A e^{\frac{x}{\lambda_{sd}}} + B e^{-\frac{x}{\lambda_{sd}}} \quad IV-19$$

Where parameters A and B are determined by the boundary conditions.

For the NM that we consider (Pt) the spin diffusion length is about 2nm, in our Pt/BiYIG bilayer the thickness of the NM is always greater than λ_{sd} : this situation corresponds to the case of Figure IV-2. The NM accumulates spin on one end and relaxes exponentially back to the equilibrium value for the chemical potential due to spin flip.

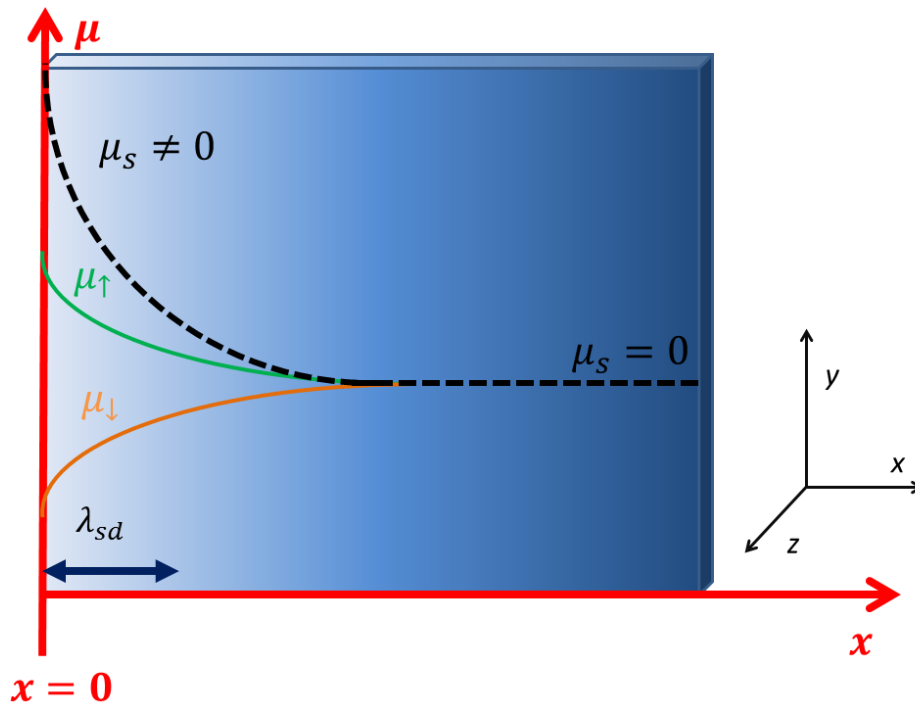


Figure IV-2-Profile of the chemical potential in a NM presenting an exponential decrease along the NM thickness. The spin up and down channel present different profile therefore a spin accumulation is created in $x=0$. The two profile (up and down spin) recover exponentially (almost) the same value after few λ_{sd} .

In NM the spin accumulation is a non-equilibrium state for the spin chemical potential and the relaxation toward the equilibrium for spin population occurs via the creation of a diffusive spin current. Thus in NM the spin accumulation is at the origin of a spin current. The following section presents how to create this spin accumulation in a MI/NM bilayer.

IV-B Spin current in a MI/NM bilayer

We now treat the case of a NM/MI bilayer and we will see how spin flow can occur between the two materials.

It is possible to generate a spin accumulation at the NM/MI interface from the MI this effect is called spin pumping. On the other side one can also transfer spin angular momentum in the MI from a spin accumulation in the NM this effect is called spin transfer torque.

IV-B.1 Spin pumping.

The spin pumping corresponds to the transfer of angular momentum from the MI electrons to the NM electrons due to precession of the MI's magnetic moment.

Precession of the magnetic moment in the FMR resonant condition is an out of equilibrium state for the MI. In the FMR resonant condition the chemical potential of the magnon population is then modified: $\mu_{magnon} = \mu_{equ} + \delta\mu_{FMR}$ (Figure IV-3). At the NM/MI interface the $\delta\mu_{FMR}$ in the MI is transferred as a spin accumulation in the NM. This latter will relax through the spin diffusion current in the NM according to the process described previously (Figure IV-2).

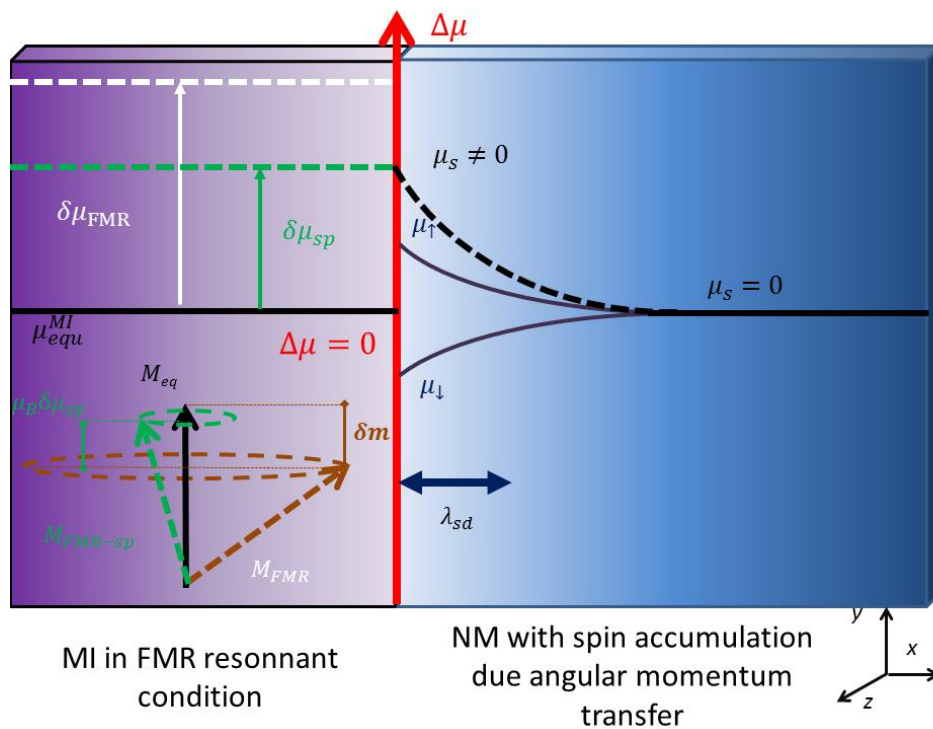


Figure IV-3-Spin accumulation in NM due to spin pumping in the MI. The precession of the magnetic moment in the FMR resonant condition in the MI leads to a modification of the magnon chemical potential in the MI $\delta\mu_{FMR}$. A part of $\delta\mu_{sp}$ is transferred via spin angular momentum in the NM. A spin accumulation is created in the NM at the NM/MI interface.

The transfer of chemical potential imbalance $\delta\mu$ can be seen as transfer of angular momentum from electrons of the MI to electrons of the NM. The NM is 'pumping' angular

momentum (or magnon) from the MI during the precession of the magnetic moment (Figure IV-3).

Experimentally this can be seen as an enhancement of the FMR peak linewidth: some magnetic energy is lost by the MI in the NM due to the spin pumping and will relax in the NM. The magnetic losses are increased compared to the case of MI without any NM on the top, the linewidth of the system is then written:

$$\Delta H_{pp} = \Delta H_{MI} + \Delta H_{sp} \quad IV-20$$

Where the first term corresponds to the losses of the MI layer, only, and the second one to NM/MI bilayer.

The frequency dependence of the magnetic losses is then written:

$$\Delta H = \Delta H_0^{MI} + \Delta H_0^{sp} + \frac{(\alpha_{MI} + \alpha_{sp})2\pi f_{res}}{\mu_0 \gamma} \quad IV-21$$

The damping enhancement due to spin pumping is directly linked to the amount of spin angular momentum that can be transferred from the MI in the FMR resonant conditions to the NM.

The NM/MI interface is seen as a discontinuity for the spin flow, as a consequence a part of the spin current is reflected back in the MI and another one is transferred. The effective spin mixing conductance ($G_{\uparrow\downarrow}$) characterizes the amount of spin that can be transferred at the interface. There are different ways to evaluate experimentally this parameter⁵¹⁻⁵³, in this thesis we will use the enhancement of the magnetic damping due to spin pumping $\Delta\alpha_{sp}$:

$$G_{\uparrow\downarrow} = \frac{4\pi M_s t}{g_{eff} \mu_B} \Delta\alpha_{sp} \quad IV-22$$

Where M_s , t , g_{eff} and μ_B are respectively the magnetic moment at saturation, the thickness of the sample, the effective Lande factor and the Bohr magneton.

IV-B.2 Spin Transfer Torque.

The transfer of spin accumulation (due to spin current) from the NM to in the MI is also possible and is called the Spin Transfer Torque (STT) phenomena.

Let us first consider the case of an NM/FM (the MI is replaced by a FM) bilayer in which a pure spin current, spin polarised along a direction σ flows from the NM to the FM. Moreover we suppose that σ is transverse to \mathbf{M} , the magnetization direction of the FM. In this conditions the eigenstate of the spin in the two systems: NM ($|\uparrow\rangle_{NM}$ or $|\downarrow\rangle_{NM}$) and the FM ($|\uparrow\rangle_{FM}$ and $|\downarrow\rangle_{FM}$) are different.

Eigenstates of the NM (or the FM) can also be linearly decomposed in the basis of the FM (NM) eigenstate. This decomposition contains a part transverse and a part parallel to the magnetization of the FM (NM).

For spin polarized electrons of the NM coming from the pure spin current the part transverse to the magnetization of the FM is absorbed as angular momentum and the part parallel to the magnetization of the FM is reflected back in the NM.

This transfer of spin angular momentum from the NM to the FM can be seen as a torque and is called STT. It is written⁵³:

$$\boldsymbol{\tau}_{STT} = -\frac{\gamma J_s}{M_s t_{FM}} \mathbf{m} \times (\mathbf{m} \times \boldsymbol{\sigma}) \quad IV-23$$

Where γ , M_s , J_s and t_{FM} are respectively the gyromagnetic factor, the saturation magnetic moment of the FM, the spin current density transmitted from the NM to the FM (which depends for a given charge current sent in the NM on the $G_{\uparrow\downarrow}$ and the θ_{SHE}) and the thickness of the FM. Note that \mathbf{m} corresponds to the dynamic part of the magnetization (the green component in Figure III-9), it is perpendicular to the static magnetic moment (and most of the time to the external field) and arises from thermal fluctuation of the magnetic moment in the FM.

The STT acts on the magnetic moment of the FM and can eventually lead to magnetic switching of the FM if it is efficient enough⁵⁴. This STT term is also involved in the LLG equation and acts on the magnetic moment dynamic:

$$\frac{d\mathbf{m}}{dt} = -\gamma \mathbf{m} \times \boldsymbol{\mu}_0 \mathbf{H}_{eff} + \alpha \mathbf{m} \times \frac{d\mathbf{m}}{dt} - \boldsymbol{\tau}_{STT} \quad IV-24$$

As $\boldsymbol{\tau}_{STT}$ is perpendicular to the magnetic moment of the FM (cross product of IV-23) it has the same geometry as the losses term: $\times \frac{d\mathbf{m}}{dt}$. Depending on the sign of J_s it can modulate the magnetic losses of the FM⁵⁵. For a full compensation of the α it even leads to auto induced oscillations^{56,57} of the magnetic moment in the FM.

The situation is similar if we consider a MI instead of a FM (even though electrons of the MI are not conduction electrons) and the transfer of spin angular momentum by the mean of STT remains the same⁵⁸.

In this part we introduced the concept of spin angular momentum transfer between a MI and a conducting material. Now the magnetic moment of the MI is somehow connected to a conducting material where charge current can be sent: it is one step more to implement MI in spintronic.

However in this overall picture it is the spin current (and not the charge current) in the NM that has a major role for the MI so the question remains on how to induce this spin current. This will be treated in the next section with the concept of Spin Hall Effect (SHE) and SHE materials which are very useful for spintronic with MI.

IV-C Spin Hall Effect (SHE) metals and magnetoresistive effects in NM/MI bilayer.

The SHE is very convenient as it allows the spin to charge conversion and electrical detection of magnetic states. It is then very important for insulating materials. We first present SHE and then different experiments based on this phenomena involving MI. Those experiments are directed on our Pt/BiYIG bilayer (in Chapter VIII).

IV-C.1 SHE and ISHE.

For some NM, due to high spin orbit coupling (SOC), the spin current $\tilde{\mathbf{j}}_s$, the charge current \mathbf{j}_c and the polarization direction of the spin current $\boldsymbol{\sigma}$ are related via a cross product:

$$\tilde{\mathbf{j}}_s = \theta_{SHE} (\boldsymbol{\sigma} \times \mathbf{j}_c) \quad IV-25$$

This is called the direct Spin Hall Effect (SHE) and has been discovered in 1971 by Dyakonov and Perel⁵⁹.

The parameter θ_{SHE} is called the spin Hall angle, its sign and magnitude changes depending on the material and it is expressed in %. The estimation of θ_{SHE} for the same material varies among the literature ($\theta_{SHE}(Pt)$ values for instance varies from 0.37⁶⁰ to 11%⁶¹).

This phenomenon has its reciprocal effect called Inverse Spin Hall Effect (ISHE): if we consider a spin current induced by spin accumulation in a SHE NM (Equation IV-14) it will also induce a charge current in the SHE NM:

$$\mathbf{j}_c = -\theta_{SHE} (\boldsymbol{\sigma} \times \tilde{\mathbf{j}}_s) \quad IV-26$$

Origins of the SHE and ISHE are both intrinsic (electronic band structure of the electrons in the NM) and extrinsic (involving scattering with SOC). Materials with high θ_{SHE} are usually heavy metals as they have high SOC.

It is then very interesting to use SHE metals for NM/MI bilayer as the spin current in the NM can be directly controlled using charge current.

IV-C.2 Experimental interest of SHE metal for MI/NM bilayer.

For SHE metals spin and charge current are coupled through θ_{SHE} , consequently a pure spin current from a NM (to distinguish from a spin polarized current of the FM) can be electrically detected in its transverse direction (due to the cross product).

We saw that for NM/MI bilayer spin accumulation at the interface can lead to spin current from the NM to the MI (SHE and STT) and from the MI to the NM (in the FMR resonant conditions). If the NM that is used is a SHE metal it is then possible to detect this spin current electrically. Moreover we also saw that spin current in NM and magnetic state in a MI can be correlated: it is then possible to probe the magnetization of an insulator using a charge current using a NM (SHE)/MI bilayer.

Now we presented the different concepts that are necessary to understand how the magnetic state of an insulator can be electrically detected in a NM(SHE)/MI bilayer. We will present the different magnetoresistive effects based that can be observed in those bilayers.

IV-D Spintronic effects with a NM(SHE)/MI.

Spintronic effects involving NM (SHE)/MI bilayer are presented here, those effects will be measured in Chapter VIII using our ultrathin BiYIG films as the MI bilayer.

IV-D.1 Spin Hall Magnetoresistance (SMR).

In SHE metal/MI bilayer the resistance of the SHE metal can vary with the direction of the magnetic moment \mathbf{M} of the MI. This is called the SMR effect. The origin of SMR is the dependence of the STT τ_{STT} to magnetization of the MI \mathbf{M} (see Equation IV-23).

Let us now consider a NM SHE/MI bilayer (from now the SHE is Pt and MI BiYIG) in which a charge current \mathbf{J}_c is sent in the Pt top layer in the geometry of the Figure IV-4.

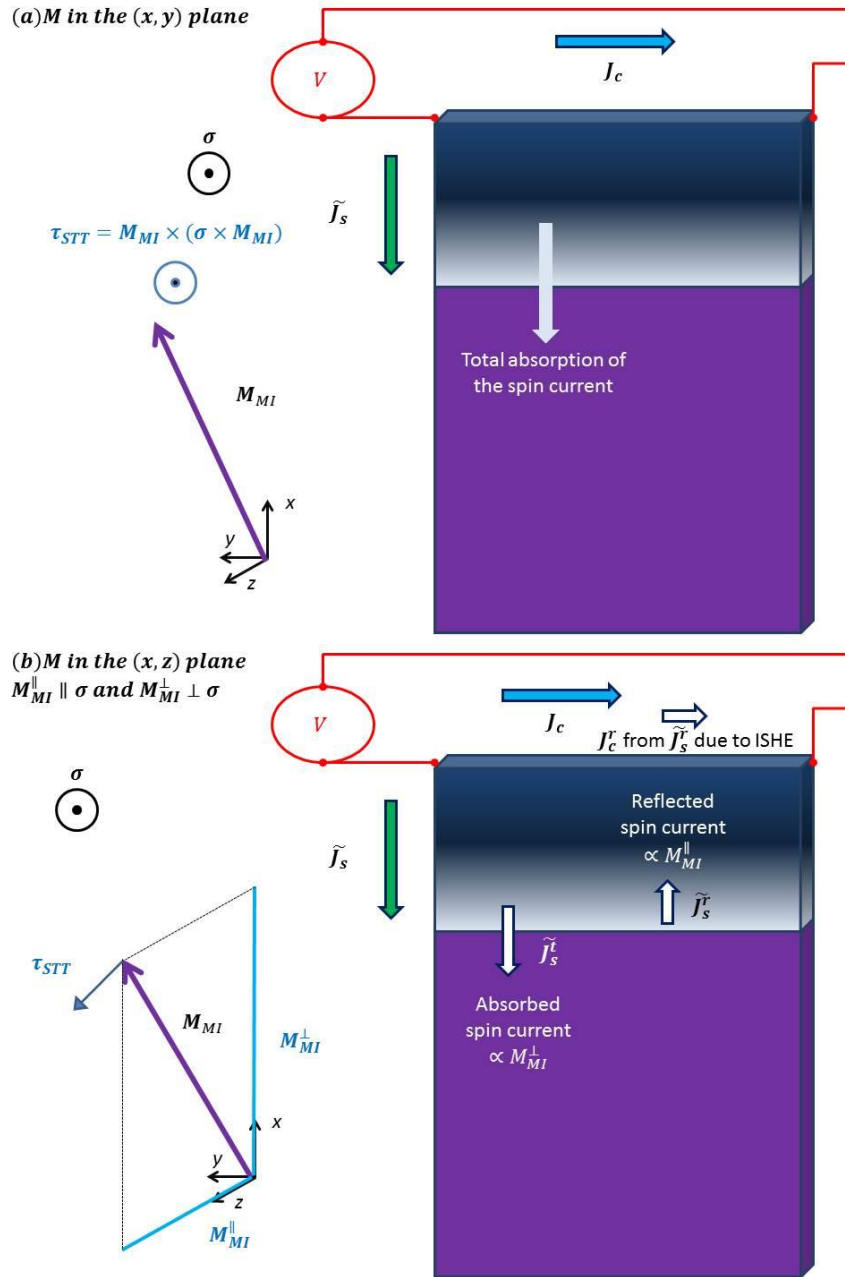


Figure IV-4-SMR effect for $M_{MI} \parallel \sigma$ (a) and for $M_{MI} \perp \sigma$ (b)

Due SHE it creates a spin current \tilde{J}_s flowing from the NM SHE to the MI, polarized along σ . Through STT, this spin polarized current can be totally transferred to M_{MI} as spin angular momentum (Figure IV-4(a)) or reflected at the interface (Figure IV-4(b)), depending on the direction of M_{MI} compared to σ . This corresponds to the cross product of Equation IV-23:

- τ_{STT} is minimized if $M \parallel \sigma$ and the reflection of \tilde{J}_s is maximal.
- τ_{STT} is maximized if $M \perp \sigma$ and the reflection of \tilde{J}_s is minimal.

The reflected spin current \tilde{J}_s^r in the NM SHE top layer is converted into a transverse charge current (J_c^r) via ISHE which leads to an increase of the total current in the NM SHE: $J_c^t = J_c + J_c^r > J_c$. As the applied charge current J_c remains the same, the resistance of the NM SHE has to drop due to the presence of J_c^r .

This magnetoresistive effect is then characterized by:

- High resistive state of the NM SHE when $\mathbf{M} \perp \boldsymbol{\sigma}$.
- Low resistive state of the NM SHE when $\mathbf{M} \parallel \boldsymbol{\sigma}$.

The dependence of the NM SHE resistance with respect to \mathbf{M}_{MI} is called the SMR effect.

IV-D.2 Inverse Spin Hall Effect.

We saw in the part IV-B.1 that the precession of the magnetic moment due to FMR in a MI can induce a spin accumulation and a spin current due to spin pumping in a NM top layer. If now the NM is a SHE metal it is possible to convert this spin current into a transverse charge current due to ISHE. Consequently in a SHE NM/MI, the FMR precession of the magnetic moment can be electrically detected in the SHE NM top layer.

This experiment is called ISHE measurement and is a direct evidence of spin angular momentum transfer from the MI to the SHE NM.

IV-D.3 Anomalous Hall Effect.

The Anomalous Hall Effect (AHE) has been first observed in FM metals. In a FM magnetized along $\mathbf{m} = \frac{M_s}{\|M_s\|}$ an initial charge current \mathbf{J}_c^i sent in the FM creates a transverse charge current \mathbf{j}_c^{AHE} due to the AHE (see Figure IV-5). The expression of the AHE current is then:

$$\mathbf{j}_c^{AHE} = \theta_{AHE}(\mathbf{m} \times \mathbf{J}_c^i) \quad \text{IV-27}$$

With θ_{AHE} the anomalous angle (proportional to the magnetic induction) which is the analogue of the spin hall angle for SHE metals. In FM the AHE is due to SOC that induces a spin dependent scattering of electrons.

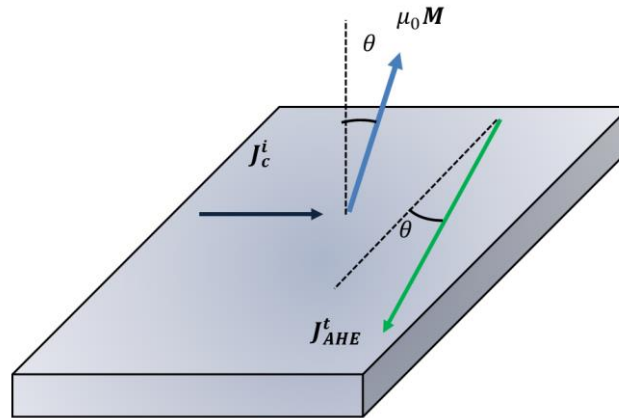


Figure IV-5-Geometry of the AHE in a FM magnetized along a direction \mathbf{M} in which an external charge current \mathbf{J}_c^i is applied: apparition of a transverse current due to AHE

For the case of a SHE NM/MI bilayer if an initial charge current \mathbf{J}_c^i is sent in the NM an anomalous charge current \mathbf{J}_c^{AHE} can be measured in the NM⁶²⁻⁶⁴. \mathbf{J}_c^{AHE} is transverse to both:

- the magnetic moment of the MI \mathbf{M}
- the initial charge current \mathbf{J}_c^i sent in the SHE NM

Contrary to the case of the FM the charge current doesn't flow in the magnetic material this effect is then called non local AHE⁶⁵ and has different origins:

- **Proximity induced magnetism in the NM.** The MI polarizes the NM SHE metal due to proximity effects (the NM is behaving like a FM).

- **Spin dependent scattering of J_c^i at the NM/MI interface.** At the MI/NM interface due to the magnetic moment M of the MI the scattering of the initial charge current J_c^i is spin dependent, thus J_c^i becomes a spin polarized charge current J^s . J^s is polarized in the direction of M . J^s is then converted by ISHE into a charge current J_c^{AHE} perpendicular to both J_c^i and M (Figure IV-6(a)).
- **Spin dependent scattering of J_s^{SHE} at the NM/MI interface.** Due to SHE J_c^i is also converted into J_s^{SHE} polarized along $\sigma \parallel M$. Spin dependent scattering of the pure spin current J_s^{SHE} at the NM/MI interface creates a charge current J_c^{AHE} in the same direction as J_s^{SHE} (Figure IV-6(b)).

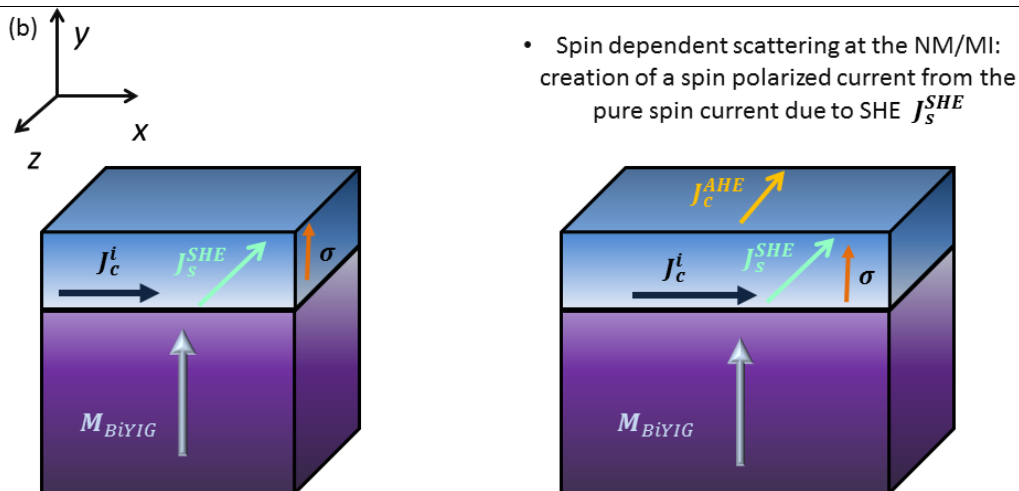
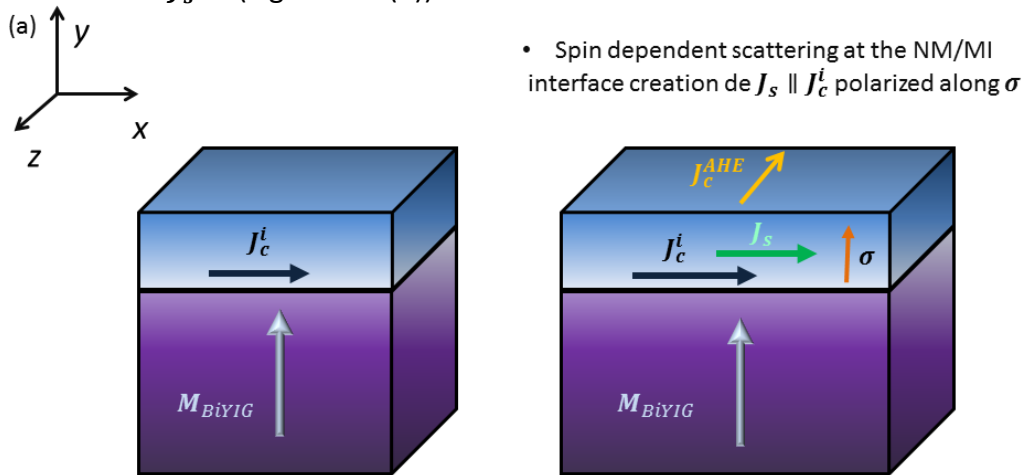


Figure IV-6 Different origins of the AHE in a NM SHE/MI bilayer

After introducing spintronic concepts we showed that NM SHE/MI bilayer allow to open the field of spintronics to insulating materials. We then presented few magnetoresistive effects that could be observed in those bilayers. The next chapter is then dedicated to state of the art of MI materials for spintronic applications.

V MI for spintronics.

We have now presented two magnetic insulators the YIG and the BiYIG and introduced some spintronic effects in which MI could be used. We will now give the state of the art of MI for spintronics.

To begin with we will present the alternative in terms of material to MI for spintronic applications: Ferromagnetic Metals (FM) with low magnetic losses. In a second part we present recent advances in the elaboration of MI for spintronics and magnonic applications. In the last part we present some magnon-spintronics phenomena that are involving those MI.

V-A Materials for spintronics.

Bilayers discussed for spintronic applications contain two parts: a spin to charge converter and a magnetic material. A wide range of materials with different properties can fulfill those requirements which makes the spectrum of spintronic materials quite large (metals, insulators, semi conducting materials can be used for spintronic applications).

The spin to charge converter material can be a metal with high SOC presenting SHE (Section IV-C.1) but topological insulators^{66,67} and 2D materials represents valid alternatives. In those materials, the spin to charge conversion can be understood by Rashba-Edelstein effect.

The magnetic material in the spintronic device can be either an insulator or a FM.

The choice of each material has to be carefully done as it will impact the geometry of the device, the observed spintronic effect and the efficiency of the device.

In the following Section, we consider the general case of a spin to charge converter / magnetic material bilayer. We first consider which are the parameters affecting the overall performance of the device and then review the alternatives available for the type of magnetic materials.

V-A.1 Parameter for an efficient spintronic bilayer.

In the spin to charge converter/ magnetic material (MM) bilayer the efficiency is given by the conversion between charge current and angular momentum transfer at the interface of the two materials. This depends on:

- **The efficiency of the spin to charge conversion.** For SHE materials it corresponds to θ_{SHE} (see Section IV-C.1) for the case of spin to charge conversion relying on the Rashba effect (topological insulators or 2D materials) the spin to charge conversion is measured in terms of inverse Edelstein Length λ_{IEE} (in meters)⁶⁸.
- **The magnitude of τ_{STT} acting in the magnetic layer.** A given spin current J_s sent in the MM is inversely proportional to M_s and t_{MM} which are respectively the magnetic moment and the thickness of the MM (See Equation IV-23). Moreover τ_{STT} appears in the LLG equation (see Equation IV-24) and has the same symmetry as the losses term $\alpha \mathbf{m} \times \frac{d\mathbf{m}}{dt}$. Thus for τ_{STT} to affect the dynamic of the magnetic moment low magnetic losses are desirable.
- **The spin transparency of the interface.** It is given by the $G_{\uparrow\downarrow}$ parameter that defines how much spin angular momentum can be transferred from one material to another (Equation IV-22).

From now we will let aside the Rashba Edelstein effect and consider only SHE materials as spin to charge converter and focus on alternatives concerning the MM in the bilayer which can be conducting or insulating. We present those two alternatives by keeping in mind that an efficient NM SHE/ MM bilayer requires for the MM:

- ✓ low magnetic damping.
- ✓ low thickness.
- ✓ high spin mixing conductance.
- ✓ low magnetic moment at saturation.

V-A.2 FM metals with low magnetic damping : an alternative to MI.

We consider first the case of a FM as the MM in the spin to charge converter/MM bilayer. The main advantage of using a metal instead of an insulator for the MM is the spin mixing conductance which is about an order of magnitude larger compared to insulating materials⁶⁹. The drawback of is the increase of α as conduction electrons are a source a relaxation process of the magnetization dynamic (FMR and spin wave modes). In FM the α value is at least one order of magnitude larger than in MI which reduces the τ_{STT} efficiency. Consequently for FM materials reducing the magnetic damping is the main goal.

Among all single element FM Fe has the lowest intrinsic damping⁷⁰. Values of α from 0.002 to 0.004 are reported for thin epitaxial films of iron (below 50 nm thick) elaborated by sputtering or MBE^{70,71}($1.9 \cdot 10^{-3}$ for Fe films doped with Vanadium in which the SOC is reduced⁷²). Those films were grown on common substrates (MgO, GaAs) which have proven to be compatible with standard industrial processes.

It is also possible to reduce the magnetic damping in metallic systems by engineering the energy band diagram of FM metals. A spin wave that scatters on an electron obeys to the momentum and energy conservation rule as illustrated in the Figure V-1:

- $q_{SW} + k_{e-}^i = k_{e-}^s$
- $\epsilon_{SW} + \epsilon_{e-}^i = \epsilon_{e-}^s$

The spin wave in FM has typically an energy of the order of 10^{-12} eV (GHz frequency) and a momentum of the order of 10^7 m^{-1} . For conduction electrons that are at the Fermi level the typical energy is the order of 1eV and the wave vector is about 10^{12} m^{-1} . As a consequence during the scattering process the energy and the wave vector of the electron will not be significantly modified. However the spin wave carries an angular momentum \hbar which can flip the electron spin (Figure V-1).

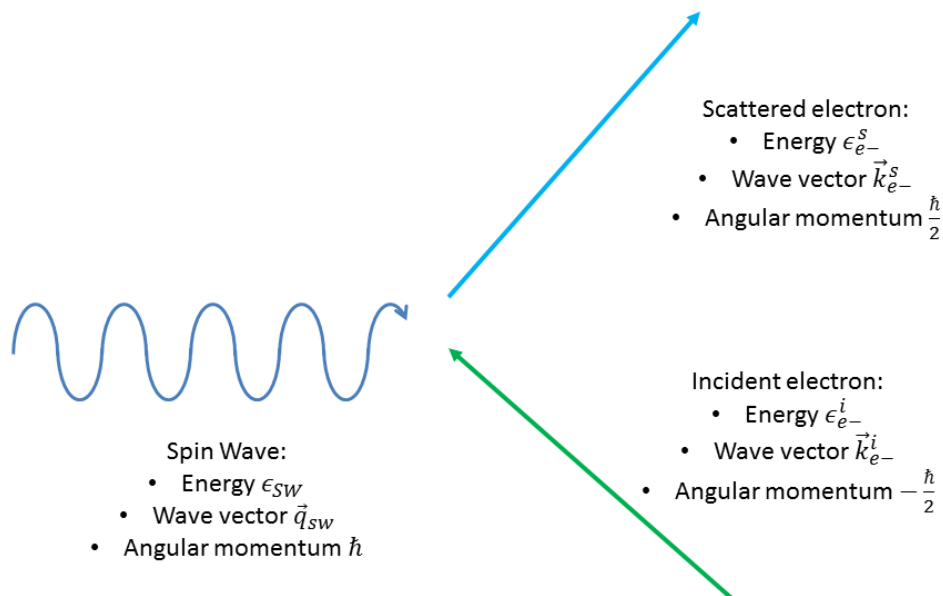


Figure V-1- Conservations laws for the scattering of a spin wave

Thus the scattering of the spin wave on conduction electrons corresponds to a spin flip of a conduction electron which keeps the same energy and wave vector. This phenomenon is

possible only if there are available states for spin up and spin down electrons at the Fermi level.

On the basis of these considerations the relaxation due to conduction electrons can be reduced by having zero available state in the minority electrons band at the Fermi level. In this condition the scattering of majority electrons is not possible. This type of materials are called half metals, an example of half metallic materials are Heusler alloys such as $\text{Co}_2\text{Fe}_x\text{Mn}_{1-x}\text{Si}$. As shown in the Figure V-2(a) in $\text{Co}_2\text{Fe}_x\text{Mn}_{1-x}\text{Si}$ alloys α can be modified with the Fe concentration. In this alloy, a modification of the Fe concentration changes the position of the Fermi energy (ϵ_{Fermi}) in the density of state diagram (Figure V-2(b)). Low magnetic damping values are observed when the ϵ_{Fermi} position is in a zone where no minority states are available (Figure V-2(a)).

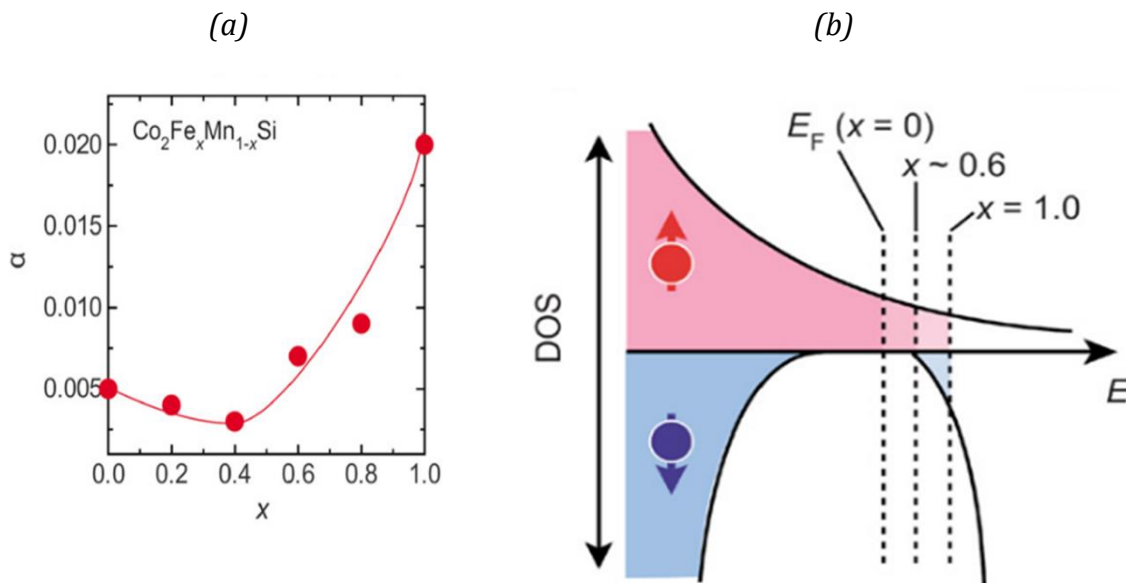


Figure V-2- from ref⁷³ (a) Evolution of the measured damping in $\text{Co}_2\text{Fe}_x\text{Mn}_{1-x}\text{Si}$ with the Fe concentration and (b) scheme of the density of state of the alloy: the Fermi level can be tuned with the Fe doping. The lowest value of the Gilbert damping in the alloy corresponds to a Fermi level position where the density of state for minority spin is zero.

In Heusler alloys, the predicted α values are comparable to what is obtained for state of the art YIG thin films ($0.6 \cdot 10^{-4}$ for Co_2MnSi alloys⁷⁴), which makes them very promising as FM with low damping values. However experimental measurements are far from theoretical expectations and the lowest values measured for those kind of materials are of the order of 10^{-3} ^{73,75-77} (in Figure V-2(a) the lowest damping obtained is $\alpha = 3 \cdot 10^{-4}$ which is far from the predicted value of $0.6 \cdot 10^{-4}$).

In $\text{Co}_{1-x}\text{Fe}_x$ alloys it is also possible to move ϵ_{Fermi} in a energy range where no minority states are available⁷⁸⁻⁸⁰ and to decrease the magnetic losses. For polycrystalline $\text{Co}_{25}\text{Fe}_{75}$ films grown on MgO substrates by sputtering⁷⁸ the magnetic damping value reported was $\alpha = 2.1 \cdot 10^{-3}$ and for single crystalline $\text{Cr}/\text{Co}_{25}\text{Fe}_{75}/\text{MgO}$ sputtered films⁸⁰ $\alpha = 7 \cdot 10^{-4}$ (which is close to values obtained for YIG ultrathin films^{55,81,82}). However those FM have so far not been used in spintronic.

To conclude on the elaboration of FM with low values of magnetic damping we can highlight that, in most of cases there is one order of magnitude difference between α from MI and FM. Thus they are still far away from insulators in terms of dynamical quality. Moreover the lowest

magnetic damping values in FM are obtained for materials with easy in-plane magnetic axis. PMA in FM metals can also be achieved by different ways: stacking several ultrathin layers and using interface anisotropy⁸³, interlayer diffusion and mixing of the different materials^{84,85}, doping alloys with heavy elements to introduce SOC⁸⁶...in any cases this leads to a significant increase of the damping parameter (about one order of magnitude) due to increase of SOC and the presence of conduction electrons. Low damping PMA FM ($\alpha < 5 \cdot 10^{-3}$) are then not reported so far.

V-A.3 Ultrathin MI for spintronics.

We now focus on MI materials. In those materials we already know that the spin transparency will not be as good as the one of FM therefore we need to develop other strategies to optimize them for spintronic applications.

The STT efficiency can be improved by using ultrathin MI with low magnetic damping. In this context the MI chosen for spintronic applications has been the YIG^{46,56,62,87-90} due first to its dynamical quality but also because the growth of YIG μm -thick films have already been developed since the 60's.

Depending on the spintronic phenomenon that is measured, different range of MI thicknesses can be considered and depending on the magnetic property desired different kind of doping for the YIG or growth substrates can be considered.

We present here first YIG grown on Gallium Gadolinium Garnet (GGG) (YIG//GGG) thin films and their magnetic properties, in a second part we focus on doped YIG or YIG grown on different substrate than GGG in which the magnetic anisotropy can be tuned.

V.A.3.1 YIG//GGG.

Regarding the growth of YIG films the most common choice in terms of substrate is the Gallium Gadolinium Garnet (GGG), which has lattice parameter (12.383 Å) very close to the bulk YIG one (absolute misfit <0.06%) and a garnet cubic structure.

Liquid Phase Epitaxy (LPE) is the oldest method that has been employed to grow YIG or doped YIG thin films with thicknesses varying from few microns to hundreds of nm⁹¹. Magnetic properties of μm thick LPE grown films are close to the bulk YIG: $M_s = 140 \text{ kA/m}$ and $\alpha = 6 \cdot 10^{-5}$ ⁹⁰⁻⁹³. However to get STT efficient enough, it is desired to reduce further these thicknesses. A recent work from Beaulieu et al.⁹⁴, showed that it is possible to obtain 18 nm YIG films using LPE, though the damping value reported in those films ($3 \cdot 10^{-4}$) is higher than the one usually measured in thicker films.

Sputtering or PLD growth techniques are the most commonly used to elaborate YIG films with thicknesses below 100 nm: typical thicknesses obtained are from 5 to 50 nm thick⁹⁵⁻⁹⁹. The magnetic moment is most of the time the same as the one of the bulk (within 10%) and the Gilbert damping ($\alpha = 3 \cdot 10^{-4}$ for the state of the art ultrathin films) is higher than typical values obtained for thicker LPE films^{81,96,100-102}. So far one work on PLD grown YIG//GGG films obtained by recrystallization reports damping values below 10^{-4} ($\alpha = 6 \cdot 10^{-5}$)¹⁰² but the general observation is that reducing the thickness affects the magnetic damping. There are no clear understanding of why.

However even with one order of magnitude above the bulk value those ratio of thicknesses-damping are sufficient to observe STT induced phenomena in nm-thick films^{56,57,103} as we will see in the following.

To sum up YIG ultrathin films have generally magnetic damping values of few 10^{-4} which are suitable for STT based devices^{52,55,103}. However as mentioned in III.A.1.4 the YIG has a weak magnetocrystalline anisotropy; hence due to the shape anisotropy the magnetic easy axis of the film is in-plane. Garnet thin films with out-of-plane anisotropy are the focus of the next section.

V.A.3.2 Tuning YIG's magnetic properties.

For garnet thin films the magnetic anisotropy can be tuned using epitaxial strain and/or doping of the original YIG structure (see section III.A.1.4 and III.A.2.3). Films mentioned are below 100 nm thickness and are grown by PLD or sputtering.

In undoped YIG the magnetic anisotropy can be induced with magnetostriction using other garnet substrates (Neodinium Gallium Gadolinium Garnet (NdGG), Yttrium Aluminium Garnet (YAG), substituted Gallium Gadolinium Garnet (sGGG)) than the (almost) perfectly matched GGG. Thin films grown under epitaxial strain on those various substrates are distorted and out-of-plane misfit of different sign and magnitude can be obtained (up to 3% with the YAG¹⁰⁴). This leads to different sign and magnitude of the magneto elastic anisotropy term (K_{MO} see Annexe I.B) due to magnetostriction^{97,98,100,105,106}. Hence epitaxial strain can tune the uniaxial anisotropy through K_{MO} .

When reported dynamical properties of YIG on non GGG substrates are close to the one obtained for the best ferromagnetic metals¹⁰⁶ ($\alpha > 7 \cdot 10^{-4}$) and higher than YIG//GGG ones. However the magnitude of K_{MO} never reaches the value of the K_{shape} hence, no PMA can be observed on strained YIG films, changing the substrate of growth allows only a slight tuning of the magnetic anisotropy which remains in-plane.

It is also possible to dope the original YIG structure on the various atomic sites, this leads to different effects:

- changing the lattice parameter²¹
- modifying the total magnetic moment due to super exchange¹⁰⁷
- introducing growth induced anisotropy for the case of partial doping^{34,35}

Various doping for thin films have been reported to obtain PMA in ultrathin garnet films. Tensile strain can lead to PMA in strained $Tm_3Fe_5O_{12}$ //sGGG^{63,108} (TmIG) as illustrated in Figure V-3. XRD scan in the in-plane direction shows a strained film structure (Figure V-3(b)) and a positive out-of-plane misfit between the substrate and the film (Figure V-3(a)). Hysteresis loops in the out-of-plane direction shows a clear out-of-plane easy axis for those films (Figure V-3(c)). For those films the damping values are closer to the one obtained for the best FM metals than the one of ultrathin YIG//GGG films ($\alpha = 10^{-3}$)¹⁰⁸.

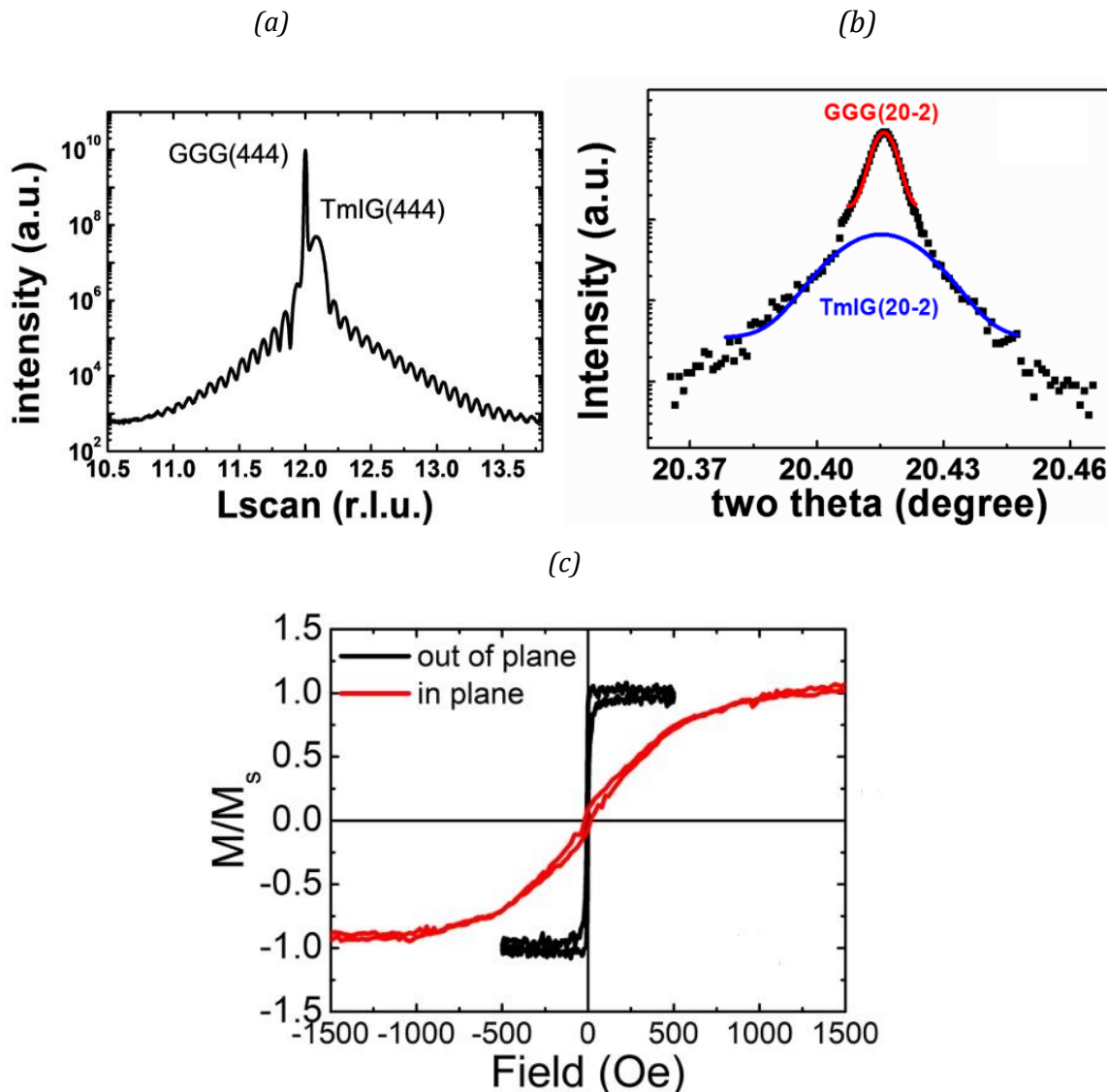


Figure V-3 from ref¹⁰⁹ (a) out-of-plane XRD scan of 24.5 nm thick TmIG//GGG showing out-of-plane misfit between the film and the substrate (b) in-plane XRD scan showing epitaxial strain of the TmIG film (c) hysteresis loop showing PMA of the TmIG//GGG structure

Partial doping of the structure is also possible ($\text{Sm}_x\text{Y}_{3-x}\text{IG}$ or $\text{Mn}_x\text{Y}_{3-x}\text{IG}$ ^{98,110}) it allows tuning the uniaxial anisotropy using the epitaxial strain stress but not PMA is observed. Values of linewidth reported are at least one order of magnitude higher than the one of the YIG//GGG¹¹⁰.

To conclude on MI for spintronics, in most cases these are there are iron garnet films (only one report on hexaferrite¹¹¹). They can be grown over a broad range of thicknesses and can present very different dynamical and static magnetic properties depending on the growth method the substrate and the doping. Therefore it is a highly flexible MI which makes it ideal for spintronic applications.

Now we reviewed the different options in terms of MM for spintronics, we will quickly justify the use of ultrathin (tenth of nanometer thicknesses) MI with low losses for spintronics.

V-B Why use of a MI?

So far we saw qualitatively that both insulators and metals have pro and count if we want to use them in spintronic bilayers. We will now compare their efficiency with qualitative numbers to show why MI are relevant in spintronics. In another part we will introduce another field magnon-spintronics which requires those low losses insulators films.

Let us consider a spintronic phenomenon involving the dynamic of the magnetic moment such as damping compensation in a NM SHE/FM bilayer. The threshold current required to achieve the auto-oscillation regime is dependent on the magnetic material's properties^{55,58,112}:

$$I_{th} \propto \frac{\alpha t_{FM} M_S^{FM}}{G_{\uparrow\downarrow}} \quad V-1$$

We compare here the threshold current for a Pt/MM bilayer using values of Table V-1 where the magnetic material is:

- a low damping metallic ferromagnet (Heusler alloy Co₂MnSi) .
- a ultrathin YIG film.

	$G_{\uparrow\downarrow}(\text{m}^{-2})$	$t_{FM}(\text{nm})$	α	$M_S(\text{kA/m})$
Pt/Co ₂ MnSi from ¹¹³	$15 \cdot 10^{18}$	20	$8 \cdot 10^{-3}$	697
Pt/YIG from ¹⁰³	$3.6 \cdot 10^{18}$	20	$2.05 \cdot 10^{-3}$	140

Table V-1 Relevant characteristics for comparing their spin torque efficiency of Pt/Co₂MnSi and Pt/YIG

The expected threshold current to induce auto-oscillations is about 4 times larger for the case of a metallic FM than for a MI($\frac{I_{th}^{YIG/Pt}}{I_{th}^{Co/Pt}} \approx 0.25$). To obtain damping compensation insulating based bilayers are then more interesting than the metallic based one, therefore insulators are relevant for spintronics especially when it comes to magnetization dynamic.

Furthermore in low magnetic losses materials spin waves can propagate over long distances (typically few μm in YIG^{112,114–116}) which is another interesting aspect of those MI and makes them highly desirable within the field of magnon-spintronics.

Spin waves, or magnons are quanta of magnetic energy (see Section III-B.2) and can be used to carry or process data. Using spin waves as information carrier presents many advantages:

- they can travel over macroscopic distances without any Joule heating
- they allow to perform wave based computing
- depending on the material used they can expand from GHz to THz regime

The field of science that deals with spin waves is called magnonics. It is not a new topic of research and many patents for spin wave based devices such as interferometers or wave guides have been deposited during the 80's. Due to its low magnetic losses the material used for those devices was μm -thick YIG films grown by LPE. However in this technology excitation and generation of spin waves was done by inductive methods which made magnonic devices not compact enough compared to the CMOS based electronics and the technological appeal for magnonics decreased after few years.

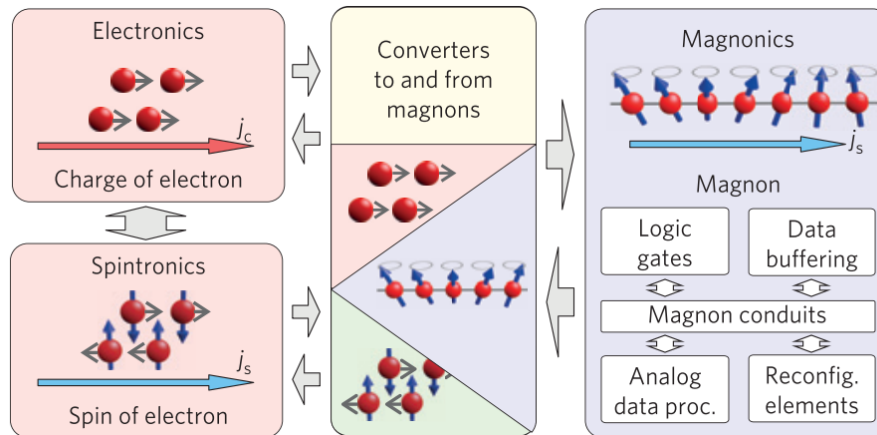


Figure V-4-Magnon-spintronics scheme from ref¹⁷

However spin to charge conversion opened recently new prospects for magnonics. In 2010 Kajiwara et al⁹⁰ were the first to evidence a spin current at an SHE metal/MI interface and they showed that detection and excitation of a spin wave using charge current in a Pt/YIG bilayer is possible. This first experimental proof has been followed by many others and it is now well established that it is possible to create¹⁰³ or detect¹¹⁸ magnon using charge current in NM SHE/YIG bilayer. This allows then to couple the field of electronic and magnonic as illustrated in the Figure V-4 and gives the field of magnon-spintronics. In this picture, spin waves are used to perform data computing based on interferences processes^{117,119,120}. In this context nm thick YIG films become interesting:

- they can be easily patterned (because they are thin enough).
- they present Gilbert damping values that allow spin waves to propagate on few μm length¹¹².
- the charge current based STT when used with a NM SHE top layer is efficient.
- the magnetic anisotropy and consequently the spin wave dispersion relation can be tuned in those films using strain or doping.

Thus YIG ultrathin films and more generally ultrathin MI with low magnetic losses are potentially more interesting than FM presenting high magnetic losses in the context of magnon-spintronics. Worth to point out that they also have few drawbacks like their high sensitivity to temperature variation (their T_c is low) and their low magnetization which limits their frequency operation range.

We briefly discussed the research field for which ultrathin MI with low losses can be used. Now we will present the most relevant phenomena that are observed using ultrathin MI with NM SHE top layer.

V-C Recent advances in YIG spintronics.

In this section, we review the state of the art for MI within the field of magnon-spintronics. In the first part we present spintronics effects involving YIG films of various thicknesses (few μm to tenth of nm), deposited through PLD, sputtering or LPE. In the second part we present the recent advances concerning the development of new ultrathin MI in the context of spintronic applications with the new effects that those materials allow to observe. This section does not aim to be exhaustive, it will just give a snapshot of the large variety of devices and physical phenomena in the field of YIG magnon-spintronic.

V-C.1 Magnon-spintronics with YIG.

The use of MI in spintronics started in 2010, when Kajiwara et al ⁹⁰ evidenced for the first time experimentally the existence of pure spin currents at a SHE NM/MI interface using a $5\mu\text{m}$ thick LPE grown YIG film and a Pt top layer. Since then many experiments involving spin current such as SMR, ISHE or AHE in a NM SHE/YIG bilayer have been realized using many different SHE metals^{62,95,96,121–125}. We cite here few of these works in which physical processes behind the experimental observations are explained in the Section IV-D.

V.C.1.1 Evidence of spin current between YIG and SHE metal.

We present two effects that evidence the presence of spin current between YIG and SHE metals: the ISHE and the AHE.

It is possible to convert magnons into DC charge current with ISHE in a NM SHE/YIG bilayer (explained in Section IV-D.2). The bilayer lies on rf-transmission line that provides a rf excitation of 3.5GHz, the in-plane external field is swept until the resonance condition for the YIG film is reached: in this condition a DC current (ISHE voltage) can be measured in the NM SHE top layer. Figure V-5 presents ISHE voltage measured using two different types of NM SHE: Ta and Pt. Because θ_{SHE} of Ta and Pt have opposite sign the DC voltage sign is reversed for the two structures. The difference in the ISHE voltage magnitude is attributed the thickness difference between the two NM ($V_{ISHE} \propto \frac{1}{t_{NM}}$)¹²².

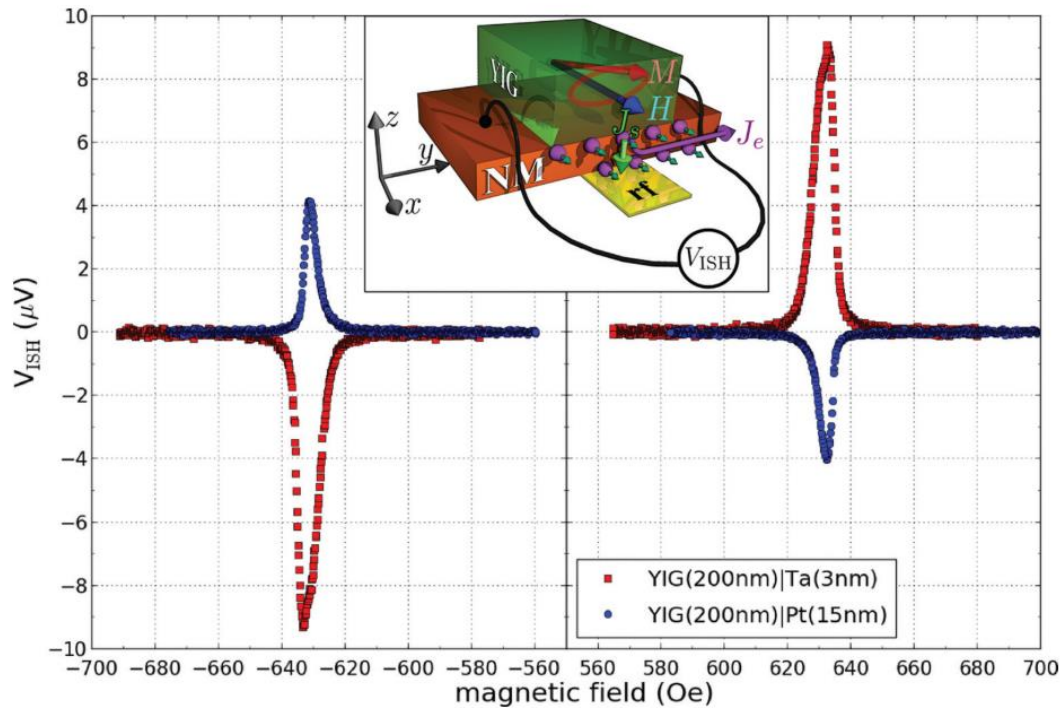


Figure V-5-ISHE measured on Pt/YIG and Ta/YIG bilayer from ref¹²².

It is also possible to measure AHE in Pt/YIG bilayers⁶² as presented in the Figure V-6. The geometry of the experimental set up is shown in Figure V-6(a): the transverse resistivity ρ_{trans} is measured, in the plane of the Pt layer and perpendicular to the charge current J_c . The magnitude of the external field $\mu_0 H$ varies along the out-of-plane direction from -3 to 3T. As shown in Figure V-6(b,c,d) a jump in ρ_{trans} is observed when $\mu_0 H$ is sufficient to saturate the YIG in the out-of-plane direction. The linear contribution in the graph of Figure V-6(bc,d) is attributed to the ordinary Hall Effect in Pt and needs to be removed to observe the AHE effect contribution (α_{AHE}) of the YIG. The sign of the ordinary Hall effect in Pt changes for very low thicknesses (Figure V-6(d)).

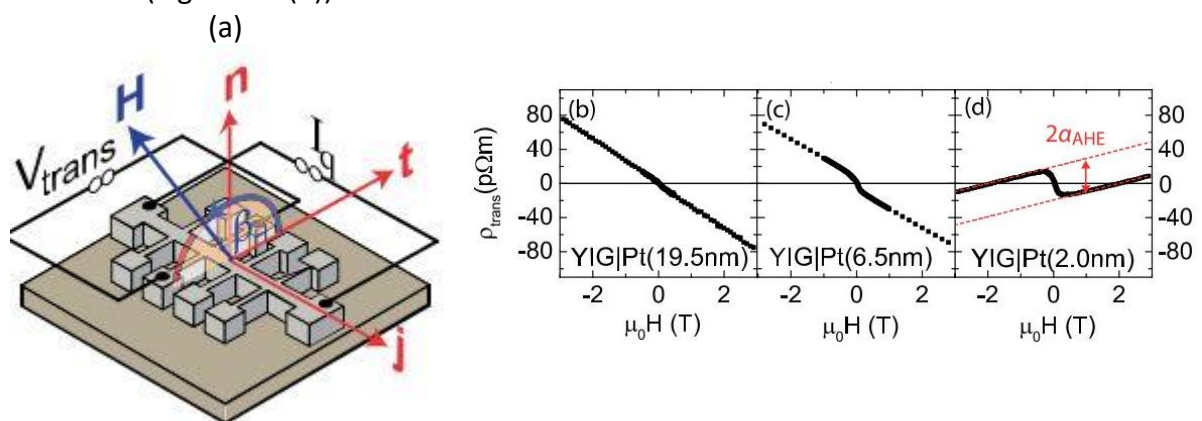


Figure V-6 AHE in Pt/YIG from ref⁶² (a) Scheme of the measurement set up and (b,c,d) AHE measurement for Pt/BiYIG with three different thicknesses of Pt

Since the YIG is in-plane magnetized the applied field in the out-of-plane direction to saturate it is quite large (200 mT). Hence the AHE contribution can only be observed when the contribution of the ordinary Hall Effect in Pt is large (indeed it is proportional to the external

field applied in the out-of-plane direction). This makes the α_{AHE} signal barely noticeable from the ordinary Hall Effect for the case of bilayers with the thickest Pt top layer. In this experiment we see that in-plane magnetic anisotropy is not the best magnetic configuration to observe AHE. PMA would be more favorable to observe clear AHE signal at low $\mu_0 H$ values in which the ordinary Hall Effect in Pt is neglectable.

V.C.1.2 Magnon-spintronics with YIG.

Evidencing the existence of a spin current in a spin to charge converter/YIG bilayer does not specially require the use of nm thick with low magnetic damping. Those films become essential to observe STT based auto-oscillations of the magnetic moment^{56,57,103} in which the STT need to compensate the magnetic losses of the material.

The Figure V-7(a) displays an experimental set up used to detect STT induced auto oscillations in a Pt/YIG microdisk. A charge current J_c and an external field $\mu_0 H$ are applied in the x and y direction respectively. Due to SHE a spin current J_s is polarized in the y direction and applies a STT on M_{YIG} . Thermal fluctuation of the magnetic moment can lead to auto-oscillation when the magnitude of the STT compensates the magnetic losses of the YIG. This auto-oscillation corresponds to the precession of M_{YIG} at the FMR frequency and can be detected inductively using an antenna (Figure V-7(a)).

The damping compensation is achieved for $I > I_{th}$ (see Equation V-1). Because YIG films are thin enough and present low α value the current density necessary to induce auto oscillation ($J_{th} \approx 10^{11} A.m^{-2}$) is low enough no too damage the Pt top layer.

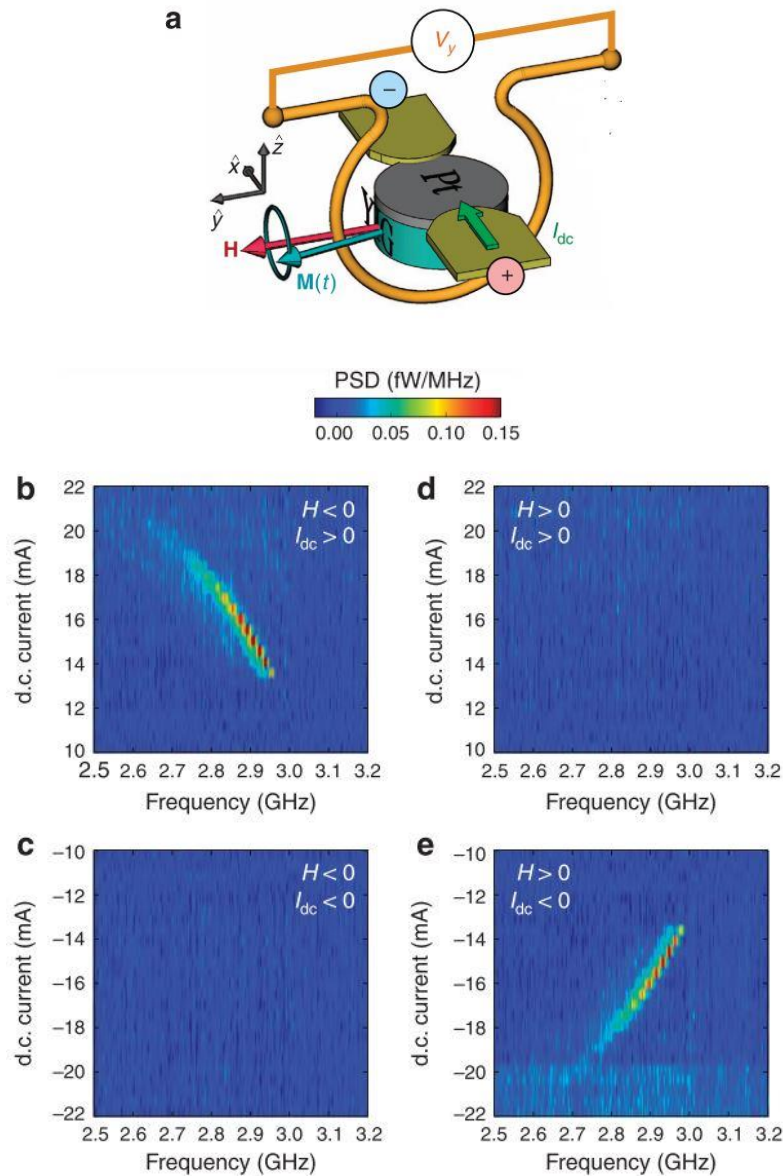


Figure V-7 Auto-oscillations in a Pt/YIG microdisk from ref¹⁰³. Scheme of the set up (a) and power spectral density (PSD) of the magnetic signal. In the favorable configuration for damping compensation (b) and (e) auto-oscillations can be generated above the critical current. Due to Joules heating induced by the current the $M_{YIG} \downarrow$ and the FMR resonant frequency is decreasing.

Figure V-7(b, c, d and e) display the intensity of the current detected by induction at different frequencies for several geometrical configurations. In the sign convention used in this study, auto-oscillations requires H and I having opposite signs (Figure V-7(a) and (e)). When H and I have the same sign the τ_{STT} term will add to the magnetic losses term instead of compensating them and no auto-oscillations can be observed (Figure V-7(b) and (c)).

In YIG films it is also possible to propagate spin waves over μm distances, there are different techniques available to detect spin waves in those films (induction, optical techniques, ISHE...). The major advantages of ultrathin YIG films as spin wave propagation medium is that they can

be easily patterned contrary to their μm - thick counterpart however because of the higher magnetic damping, one could expect that the spin wave would decay too rapidly in those films. In the ref¹¹² (see Figure V-8) authors have studied the propagation of spin wave in a 20 nm-thick YIG waveguide. The spin wave is generated by an rf excitation from an antenna and a static external field is applied perpendicularly to the waveguide. BLS technique images the propagation of a Damon-Eschbach wave ($k_{\text{sw}} \perp \mu_0 H$) of different modes (1 and 3) that can propagate over few μm distances (Figure V-8(b)). It was also possible to detect inductively (using another antenna) the propagation of those waves up to 70 μm distances. Due to low film thicknesses the patterning of the waveguide could be ‘easily’ done using ion milling technique without affecting the dynamical properties of the film.

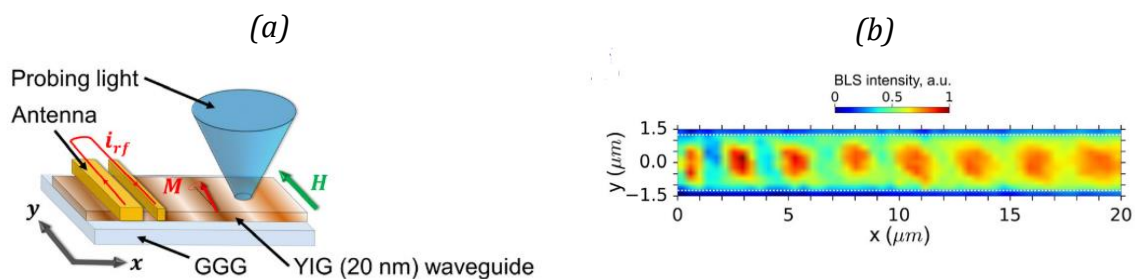


Figure V-8-Imaging using μ –BLS of the spin wave propagation in 20 nm thick YIG waveguide from ref¹¹²(a)scheme of the experimental: the spin wave is generated inductively by a rf antenna, the laser spot of the BLS set up is focused at different position of the waveguide. Due to the scattering of the light on magnons (see Annexe I.E for BLS details) it is possible to obtain the spatially phase resolved image of the spin wave in the waveguide (b).

In these YIG nm-thick film $\alpha=3 \cdot 10^{-4}$, this shows that even though they present not as good dynamical properties as the μm -thick YIG films the nm-thick films are still suitable as a spin wave propagation medium.

Now we presented typical phenomena that can be observed in YIG and in YIG ultrathin films with low magnetic losses we will now focus on new MI that have been developed for spintronic and magnonic applications. Those materials are ultrathin MI that can be an alternative for the YIG.

V-C.2 Recent advances in insulating based magnon-spintronics.

So far we showed that YIG ultrathin films grown by PLD are both a platform for spin wave propagation and spintronic effects, they are now recognized and widely used within the field of magnon-spintronic.

The scientific community is now making efforts to find new materials alternatives to YIG in order to observe for instance new spintronic phenomena or allow new geometries for magnon-spintronics devices. We give here two examples of what was recently achieved in terms of materials development as an alternative for the YIG and present the new effects or geometry that have been realized with those.

V.C.2.1 Inverted YIG/SHE metal structures.

In order to build up spintronic devices working with perpendicularly magnetized insulators it is necessary to be able to grow MI films with good magnetic properties on NM SHE sublayer. In those devices the spin current induced (by charge current) on the bottom SHE layer flows in the perpendicular direction in the MI and a transverse charge current could be detected on the top SHE layer.

The growth of YIG on SHE NM bottom layer has been successfully realized using Pt or Au^{56,87,126}. In YIG grown on Pt thin films STT induced auto-oscillations could be observed⁵⁶ which makes those films promising for magnon-spintronics applications.

In sandwiched structure Pt/YIG/Pt it is possible to inject and detect the charge current in the bottom and top NM SHE layer. A scheme of measurement of this first insulator based spin valve is illustrated in Figure V-9(c). A charge current is injected in the bottom layer ($J_{injected}$), and a charge current is measured in the top layer ($J_{induced}$) along the same direction. An external field $\mu_0 H$ is applied perpendicularly to the charge current. The variation of $J_{induced}$ with the intensity of $\mu_0 H$ is shown in Figure V-9(d).

In the Figure V-9(d) the detected voltage is dependent upon the magnetic direction of M_{YIG} :

- If $M_{YIG} \perp J_{injected}$ (low value of $\mu_0 H$ in Figure V-9(d)) $M_{YIG} \parallel \sigma_i$. There are no spin current absorption by the YIG (see IV-B.2) and $J_{injected}^S$ accumulates at the YIG/bottom SHE layer interface. This creates magnon accumulation in the YIG side which will relax in the top layer SHE layer and induce a spin current in the NM SHE. Because of SHE in the top layer a charge current is detected in the NM top layer. This all process is illustrated in the Figure V-9(a) and it corresponds to the increase of voltage observed in the Figure V-9(d) at low values of $\mu_0 H$.
- If $M_{YIG} \parallel J_{injected}$ (high value of $\mu_0 H$ in Figure V-9(d)) $M_{YIG} \perp \sigma_i$ there will be absorption of the spin current by the YIG (see IV-B.2), no spin accumulation and no magnons in YIG are created. This is illustrated in Figure V-9(b)

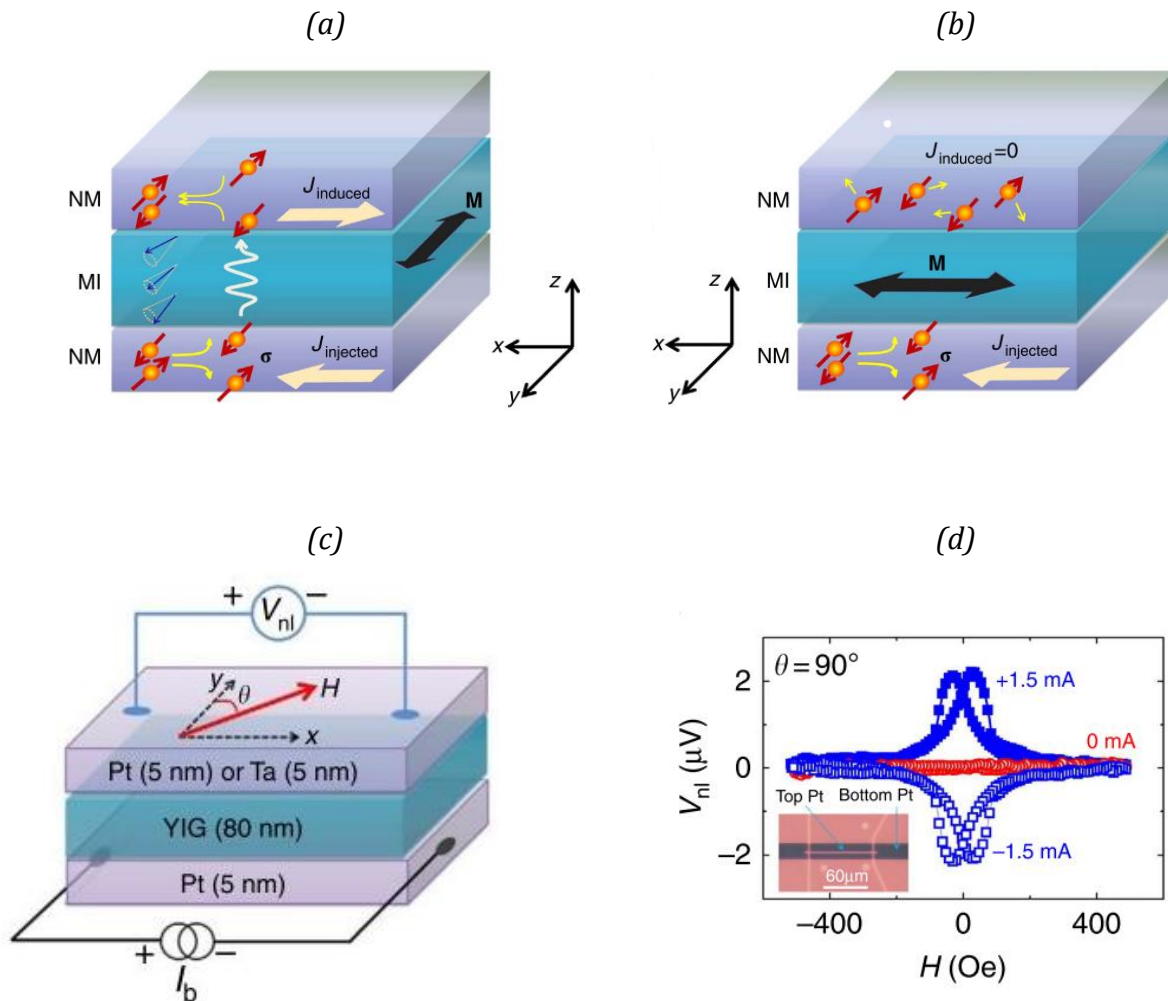


Figure V-9 (a) Magnon valve made of Pt/YIG/Pt (or Ta) from ref¹²⁷. (a)-(b) Scheme of the different configurations possible giving rise to the detection or not of a transverse voltage in the top layer of NM. (c) Sketch of the experimental set up used for measurements. (d) Evolution of the voltage detected in the top NM layer with the external field

The structure of those trilayers is similar to the one that are used for STT MRAM nanopillar which is a promising result to start implementing insulators within STT MRAM technology. Moreover growing YIG with good properties on non garnet structures is also important if one want to implement this material in the present technology that is based on Si substrates.

V.C.2.2 Ultrathin insulators with PMA.

Modifying the insulating materials' magnetic properties is highly desirable as it can:

- Give more flexibility concerning the geometry of the spintronic devices
- Allow an easier detection for some spintronic phenomenas (AHE)
- Allow the observation of new spintronic phenomenas
- Modify the spin wave dispersion relation.

Therefore doped YIG in which PMA was stabilized due to epitaxial strain such as TmIG have been elaborated (see Section V.A.3.2) but other insulating materials with high uniaxial anisotropy such as BaFe₁₂O₁₉ have been developed for the same purpose. In those films switching of the magnetic moment by STT has been demonstrated^{111,128,129}.

The Figure V-10 shows the STT induced magnetic switching in a Pt/TmIG Hall cross. The experimental set up is illustrated in Figure V-10(a): a charge current J_c is injected in the Pt top layer and the transverse voltage V_{trans} is detected. Due to AHE of TmIG it is possible to detect electrically the up or down direction of M_{TmIG} with V_{trans} . STT induced magnetic switching requires an in-plane external field for symmetry breaking^{69,111} therefore an external field ($\mu_0 H_x$) is applied parallel to J_c .

In the Figure V-10(b) the AHE resistance (deduced from V_{trans}) vs J_c is plotted, an external field of $\mu_0 H_x = 50$ mT is also applied. We see that for an applied current $J_c > 1.8 \cdot 10^{11} \text{A/m}^2$ the STT helped with $\mu_0 H_x$ is sufficient to flip M_{TmIG} . This corresponds to the abrupt change in R^{AHE} of the Figure V-10(b).

The current switching of the magnetic moment in PMA insulators is very promising as it could allow implementing insulating materials in magnetic tunnel junction structures and opening the field of STT MRAM devices to insulators. Therefore PMA insulators are very relevant for the spintronic community.

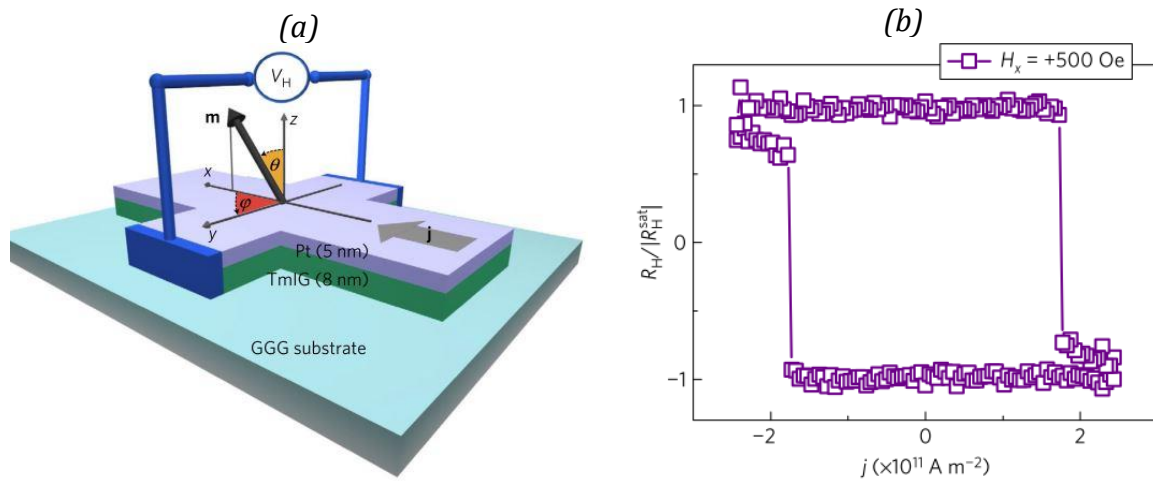


Figure V-10 STT induced magnetic switching in a Pt/PMA insulator(TmIG). (a) Scheme of the experimental set up : an Hall Cross is patterned in the Pt/TmYiG. A charge current is sent in the x direction and a the transverse AHE voltage is detected along the y direction, an external field $\mu_0 \mathbf{H}_x$ is applied parallel to the charge current (not shown here).(b) Evolution of the transverse resistivity vs the applied current for $\mu_0 \mathbf{H}_x = 50 \text{mT}$. For high sufficient current the magnetic moment of the TmIG is switched in the other direction.

This Ph.D. work falls in the second direction: development of PMA ultrathin films for magnon-spintronic applications. Keeping in mind that our material will be a spin wave propagating medium (so low magnetic losses are required) the goal is to offer an alternative to YIG thin films in terms of magnetic anisotropy. This new ultrathin insulator has to also be suitable for spintronics application in order to be relevant for the magnon-spintronic community.

Now we presented the state of the art and the objective of the material developed in this Ph.D. we present the experimental work involved for those thin films elaboration and characterization.

VI Experimental work.

In this Chapter we detail the different experimental set up and present methods used for the elaboration and the characterization of our thin films.

VI-A Thin films elaboration

In this section we present the different techniques that were used for the elaboration of thin films and bilayers that are studied in this Ph.D. thesis.

VI-A.1 Pulsed laser deposition technique.

The main growth process used for our thin films' elaboration is the Pulsed Laser Deposition (PLD) technique. This technique allows crystallizing very complex crystalline structure by ablating material from a polycrystalline target using a highly energetic pulsed laser under a controlled O₂ atmosphere and temperature. To ensure a good thermal contact we stick the sample with silver paste. The temperature of the substrate is measured from outside the chamber with a pyrometer.

Prior to the growth, the substrate (GGG or sGGG (111)) is heated at 700⁰C under 0.4 mbar of O₂ pressure during 15 minutes. Potential organic contaminants are burned and the surface of the substrate is cleaned.

After the cleaning procedure the growth can start: the O₂ pressure is 0.25 mbar and the substrate temperature is set to the one required for the growth. To ablate the material of the polycrystalline target (BiYIG) we use a high energy (~0.1 to 0.5 mJ/m²) YAG laser and a frequency tripler ($\lambda=355\text{nm}$) focused (spot of 4.2 mm²) on the target. The target is ablated over a square region of 1x1 cm². The frequency and the fluency of the laser pulse are defining the amount of matter ablated from the target for a given time. In our case the typical fluency of the laser is 0.2 mJ/m² and the pulse rate is 2.5 Hz. Due to energy of the pulses species are ionized and form a plasma beam (called a plume). The shape and the color of the plasma vary with the growth conditions (material, laser pulses energy, pressure in the chamber...). The typical plume obtained for our BiYIG sample is shown in Figure VI-1. Our growth rate varies from 2 to 3 Å/s and the typical growth time is 5 to 20 min.

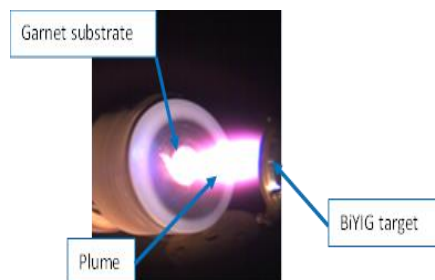


Figure VI-1 Typical plume obtained during growth of BiYIG

At the end of the growth process the sample is cooled down to room temperature (about 30 minutes) under 300 mbar of O₂ to provide enough oxygen to the structure during the cooling procedure. The Figure VI-2 illustrates schematically the growth procedure.

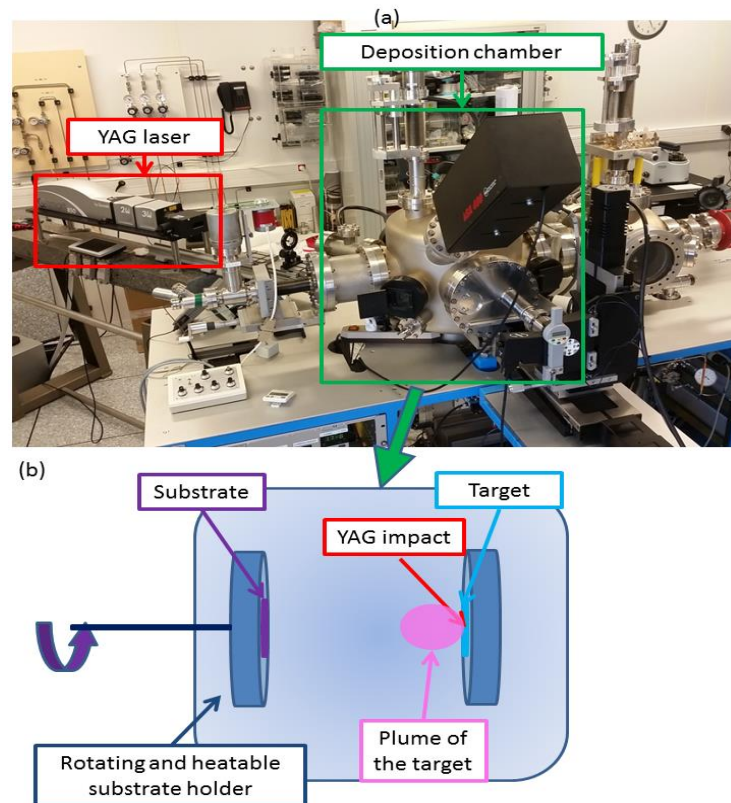


Figure VI-2-PLD set up. Picture (a) and scheme (b)

Many parameters can affect in different ways the growth.

The temperature gives kinetic energy to the ionized species to arrange when they land on the surface of the substrate thus, it is a key parameter for the growth. Too low temperature can lead to no crystallization of the desired material but too high temperature can lead to re-evaporation of some volatile species (Bi) from the surface during the growth.

The O_2 pressure has two main roles during the growth:

- O^{2-} ions necessary to elaborate a stoichiometric garnet film are taken from the background atmosphere
- O_2 atoms within the chamber are also modifying the trajectory and the energy of species ejected from the target due to collisions. Too high O_2 pressure can then prevent species from the target to reach the substrate.

Finally the distance between the target and the substrate defines the amount and the energy of ionic species that arrives on the target.

In PLD the growth is performed out of equilibrium with all atomic species ejected at the same time. This technique allows crystallizing very complex structure (such as iron garnet). However, the main drawback of PLD is the poor homogeneity of the sample realized ($10 \times 10 \text{ mm}^2$ at most for our PLD). Efforts to palliate this problem have recently allowed obtaining industrial scale PLD systems with 300 mm^2 wafer capabilities.

VI-A.2 Sputtering.

To transfer pure spin current using charge current in insulators such as garnets it is necessary to deposit few nanometers of a SHE metal on the top of the PLD grown film, this is done by sputtering. A scheme of the sputtering process is given in Figure VI-4.

To transfer angular momentum from metallic electrons to the magnetic insulator and vice versa the quality of the NM SHE/MI interface is critical. As sputtering and PLD chamber are not connected, the surface of the garnet sample can be exposed to contaminants present in the air before the sputtering deposition process. Thus, it is necessary to clean the surface of the garnet thin film: this is done by bombarding the surface with oxygen-argon (25%, 75%) plasma that breaks chemical bonding of organic contaminants from the atmosphere without affecting the surface of the garnet.

Sputtering is performed at room temperature in a chamber under an atmosphere of 10^{-3} mbar of Argon (Ar). Due to the AC voltage applied between the target and the substrate an electric field will ionize Ar atoms and create plasma (see Figure VI-4). Ar^+ ions are bombarding the target and atoms are ejected, they travel within the plasma from the target to the substrate. A magnetron located under the target is generating magnetic field lines that focus the Ar^+ beam on the target.

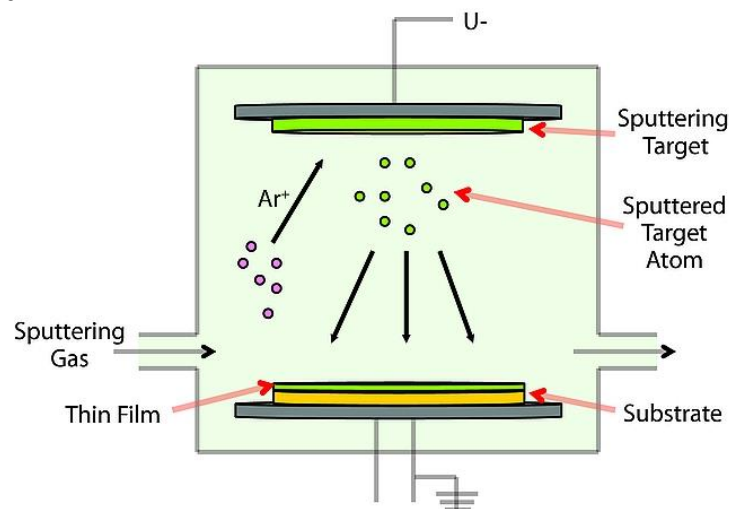


Figure VI-4-Scheme of the sputtering process

VI-B Characterization techniques.

After deposition of thin films we perform structural and magnetic characterization using different experimental techniques.

VI-B.1 X-Ray characterization technique.

Crystalline structures are ordered on the atomic scale therefore they are diffracting X-Ray light in which $\lambda \sim \text{\AA}$. X-Ray Diffraction (XRD) and X-Ray Reflectivity (XRR) techniques are used to obtain structural properties and thickness of our deposited thin films. The diffractometer used for our characterization is an Emyrean diffractometer with $K\alpha_1$ monochromator ($\lambda = 1.54056 \text{ \AA}$).

VI.B.1.1 XRD technique.

In a single crystal, families of atomic planes are regularly spaced at a distance d . An incident X-Ray beam of a single wave length λ is reflected successively on the different atomic planes (as shown in Figure VI-5) and those reflected beams will interfere with each other.

Constructive interferences occur for a specific incident angle of the beam θ with the family of atomic plane (which does not necessarily correspond to the surface of the crystal as shown in Figure VI-5 (b)). The diffraction condition is:

$$2d_{hkl}\sin(\theta) = n\lambda \quad \text{VI-1}$$

The orientation of the family of atomic planes within the crystal is given by three numbers (h,k,l) . The family of plane (h,k,l) is orthogonal to the vector $[h,k,l]$.

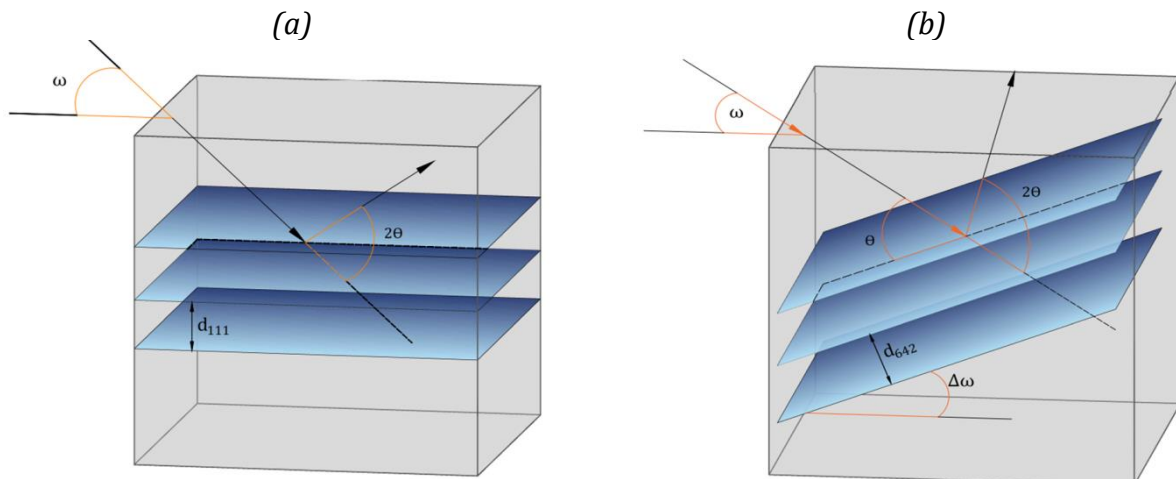
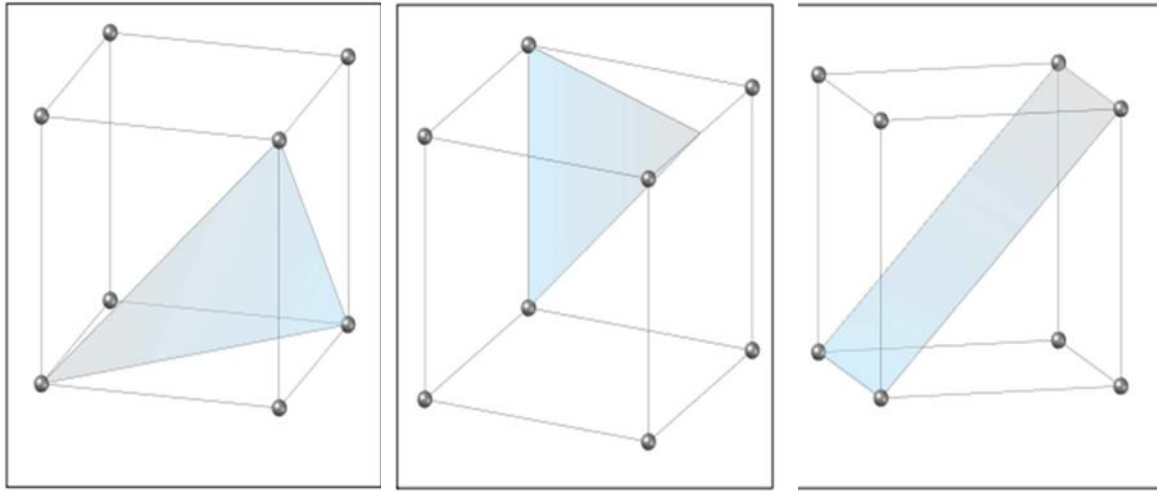


Figure VI-5 Incident X-Ray beam geometry for planes parrallels (a) and oblique (b) to the sample surface.

For our cubic garnet substrates, the (111) family plane is parallel to the sample surface and the [111] vector is normal to the surface. The two planes perpendicular to the out-of-plane (111) lying in the thin film plane are $(\bar{1}10)$ and $(2\bar{1}\bar{1})$.

The Figure VI-6 shows for a cubic garnet structure the (111), $(\bar{1}10)$ and $(2\bar{1}\bar{1})$ family of plane.



(111) family of plane

$(2\bar{1}\bar{1})$ family of plane

$(\bar{1}10)$ family of plane

Figure VI-6 Three different family of atomic planes involved for a growth along the (111) direction.

Depending on the crystal structure (cubic, rhombohedral...) the distance between two lattice unit cell along the three direction of space $(\mathbf{x}, \mathbf{y}, \mathbf{z})$ can be derived from d_{hkl} . For the case of a cubic structure the lattice unit cell a is written:

$$d_{hkl} = \frac{a}{\sqrt{(h^2 + k^2 + l^2)}} \quad \text{VI-2}$$

In our thin films, due to epitaxial strain (Section III.A.3.1), the initial cubic structure is distorted and we need to define two new lattice parameters:

- $a^\perp = 4\sqrt{3}d_{111}$ the unit cell lattice distance along the (111) out-of-plane direction.
- $a^\parallel = d_{(2\bar{1}\bar{1})}\sqrt{6} = \sqrt{2}d_{(\bar{1}10)}$ the unit cell distance spacing along the $(\bar{1}10)$ (or $(2\bar{1}\bar{1})$) in-plane direction.

To fully characterize the structure we rotate the sample holder (or the instrument) around the three spatial directions $(\mathbf{x}, \mathbf{y}, \mathbf{z})$ with the following angle: $(2\theta, \omega, \phi, \chi)$ (see Figure VI-7) We define those angles by the following way:

- ω is the angle between the incident beam and the surface of the sample.
- 2θ is the angle between the incident beam and the detector. Consequently the angle between the atomic plane and the surface of the sample is defined as $\theta = \omega + \Delta\omega$
- χ is the angle between the sample holder and the (yz) plane.
- ϕ is the angle in the (xy) plane.

plane (or the number of planes equivalent planes to (h,k,l)). This scan is used to conclude about an epitaxial relation between the substrate and the film.

VI.B.1.2 2D reciprocal space mapping:

The reciprocal space mapping (RSM) technique gives information about both in-plane and out-of-plane lattice parameters of the film. RSM scans are performed by doing several $(2\theta - \omega)$ scans for different $\Delta\omega$ values. The analysis of RSM scans requires the use of the reciprocal space that we briefly introduce below.

The angular positions of the incident and refracted beam defined with $(2\theta, \omega)$ can be transformed in reciprocal lattice unit vectors $(\mathbf{q}_\perp, \mathbf{q}_\parallel)$. The reciprocal lattice vector corresponding to the incident and diffracted beam are $(\mathbf{k}_i, \mathbf{k}_r)$ with:

- $\mathbf{k}_i = \frac{1}{\lambda} \mathbf{u}_i$ for the incident beam.
- $\mathbf{k}_r = \frac{1}{\lambda} \mathbf{u}_r$ for the refracted beam.

We also need to define the \mathbf{q} vector: $\mathbf{q} = \mathbf{k}_i - \mathbf{k}_r = \frac{2\sin(\theta)}{\lambda} (\mathbf{u}_i - \mathbf{u}_r)$ (see Figure VI-8).

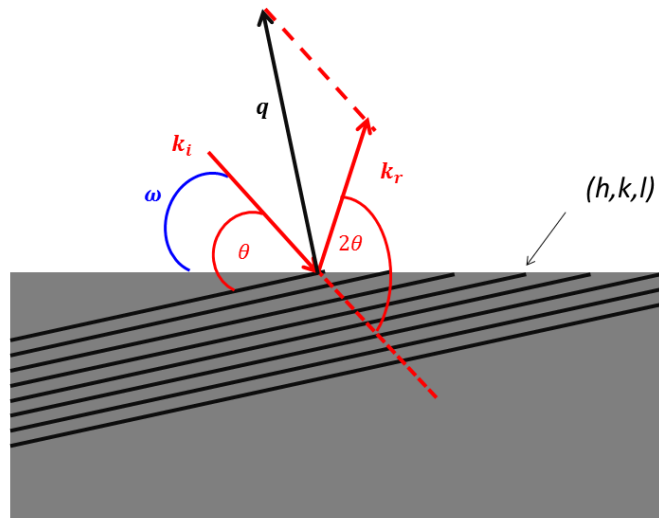


Figure VI-8 Illustration of the reciprocal lattice vector in the real space

Consequently in the diffraction conditions:

- $(\mathbf{u}_i, \mathbf{u}_r) = 2\theta_{hkl}$
- $\|\mathbf{q}\| = \frac{1}{d_{hkl}} = \|\mathbf{q}_{hkl}\|$.

In the reciprocal space a diffraction on a family of atomic plane (h,k,l) is characterized by its \mathbf{q}_{hkl} .

For our thin films grown in the (111) out-of-plane direction we perform RSM on (642) plane. This latter can be linearly decomposed in two planes perpendicular to each other: $(642) = (444) + (20\bar{2})$ which are respectively perpendicular (the plane (444)) and parallel (the plane $(20\bar{2})$) to the thin film plane. In the reciprocal space we define a basis of two vectors perpendicular to each other: $(\mathbf{q}_\perp, \mathbf{q}_\parallel)$ with $\mathbf{q}_\perp = \mathbf{q}_{d_{444}}$ and $\mathbf{q}_\parallel = \mathbf{q}_{d_{20-2}}$. In this basis, as illustrated in the Figure VI-9(a) the decomposition of \mathbf{q}_{642} is written:

$$\mathbf{q}_{642\perp} = \sin(\theta) \cos(\theta - \omega) \mathbf{q}_{d_{444}} = \sin(\theta) \cos(\Delta\omega) \mathbf{q}_{d_{444}} \quad \text{VI-3}$$

$$\mathbf{q}_{642\parallel} = \sin(\theta) \sin(\theta - \omega) \mathbf{q}_{d_{20-2}} = \sin(\theta) \sin(\Delta\omega) \mathbf{q}_{d_{20-2}} \quad \text{VI-4}$$

If the film presents an epitaxial relation with the substrate the reciprocal vector should be the same along the in-plane direction which is written:

- $q_{642\parallel\text{film}} = q_{642\parallel\text{substrate}}$ in the reciprocal space.
- $\sin(\Delta\omega_{\text{substrate}}) = \sin(\Delta\omega_{\text{film}})$ in the real space.

This corresponds to the different graphs in the Figure VI-9(b) and (c).

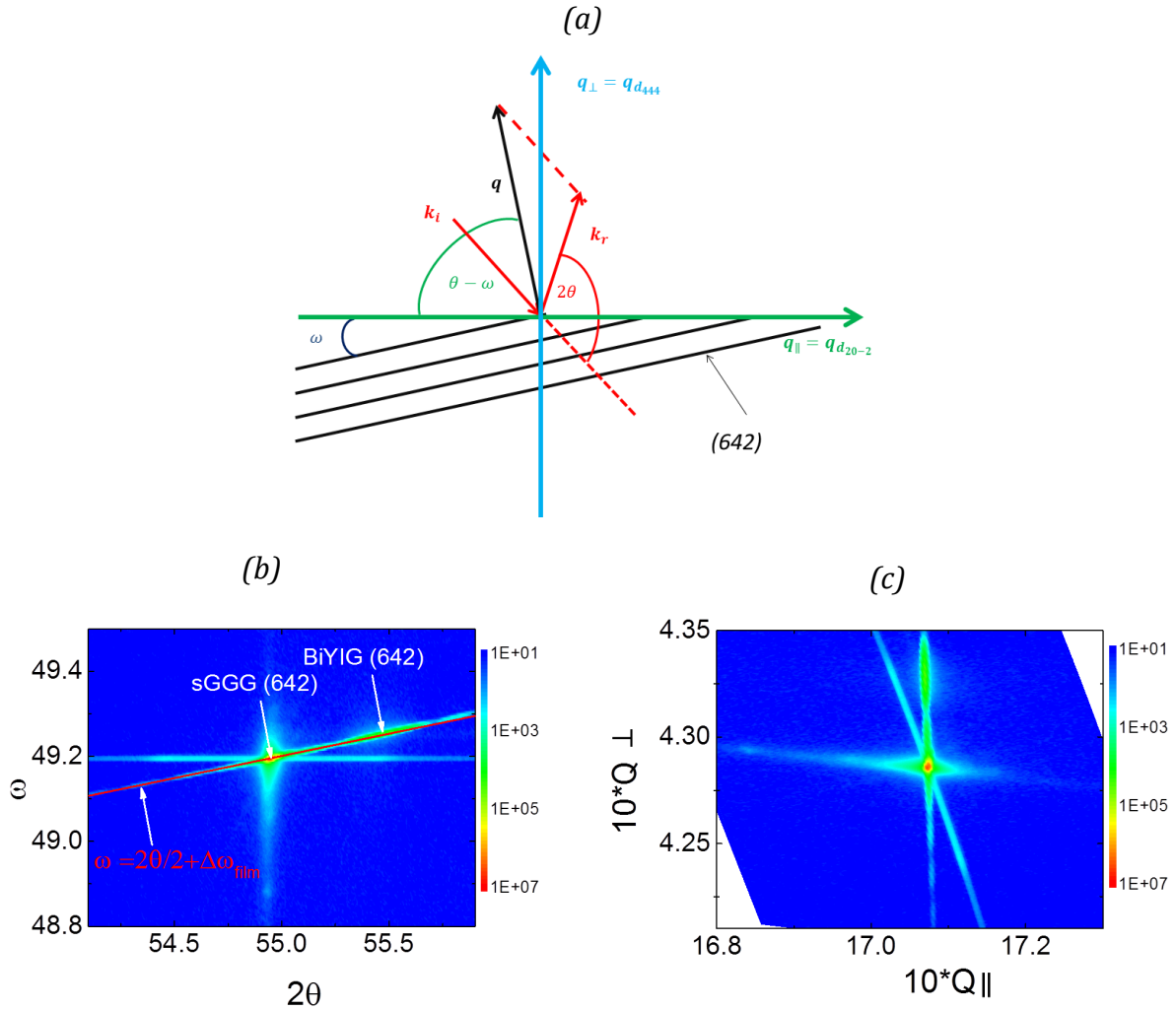


Figure VI-9 (a) Scheme of the projection of the (642) plane on the $(\mathbf{q}_{\parallel}, \mathbf{q}_{\perp})$ axis. 2D reciprocal space map along the (642) plane of an epitaxially strained film $\text{Bi}_1\text{Y}_2\text{IG/sGGG}$ (22 nm thick) in the $(2\theta, \omega)$ basis (b) and the $(\mathbf{q}_{\parallel}, \mathbf{q}_{\perp})$ one (c). In the $(2\theta, \omega)$ basis peaks of the substrate and of the film are aligned along the slope $\omega(2\theta) = \frac{2\theta}{2} + \Delta\omega_{\text{film}}$. In the $(\mathbf{q}_{\parallel}, \mathbf{q}_{\perp})$ they are aligned along the \mathbf{q}_{\parallel} axis. This corresponds to the conditions of a pseudomorphic growth.

The Figure VI-9(b) and (c) shows a RSM scan of a pseudomorphic growth displayed in both the $(2\theta, \omega)$ basis (Figure VI-9 (b)) and the $(q_{\perp}, q_{\parallel})$ one (Figure VI-9 (c)). A pseudomorphic growth in the real space $((2\theta, \omega)$ basis) corresponds to the relation $\Delta\omega_{\text{substrate}} = \Delta\omega_{\text{film}} = \text{cste}$, the diffraction peak of the substrate and the film are aligned along a line of equation $\omega(2\theta) = \frac{2\theta}{2} + \Delta\omega_{\text{film}}$ (dotted line in Figure VI-9 (b)). Conversion of the $(2\theta, \omega)$ basis in the reciprocal

space ($q_{\perp} q_{\parallel}$) basis gives an alignment of the film and the substrate peaks along q_{\parallel} (Figure VI-9 (c)).

VI.B.1.3 X-Ray Reflectivity

The X-Ray reflectivity (XRR) technique is used to obtain the thickness of films sub 100 nm. In XRR scans the incident beam penetrates within the total film thickness and is reflected at the substrate/film interface (Figure VI-10(e)). Due to the difference of refractive index between the two materials (n_{film} and $n_{\text{substrate}}$), interferences coming from these reflections allow to get the thickness of the film but also the electronic density, the roughness at the surface and the interface film/substrate.

In the Figure VI-10, we show a typical XRR scan in the linear (a) and log (b) scale. The graph can be decomposed into three different parts:

- the incident angle is below the critical angle θ_c , the XRD beam does not penetrate in the thin film ($\theta < \theta_c$) (see Figure VI-10(c)) and is fully reflected on the surface. The intensity of the collected signal is maximal: $I=I_0$ (see Figure VI-10(a)).
- the beam starts to penetrate in the thin film $\theta = \theta_c$ (see Figure VI-10(d)) half of the beam is lost from reflection at the surface. This corresponds to a drop of intensity: $I(\theta_c) = \frac{I_0}{2}$ (see Figure VI-10(a)).
- the beam penetrates in the film ($\theta > \theta_c$) and is reflected at the substrate/film interface, multiple reflection are interfering (see Figure VI-10(e)) to give maximum and minimum of intensity regularly spaced of δ (see Figure VI-10(b)). This spacing is related to the thickness of the film.

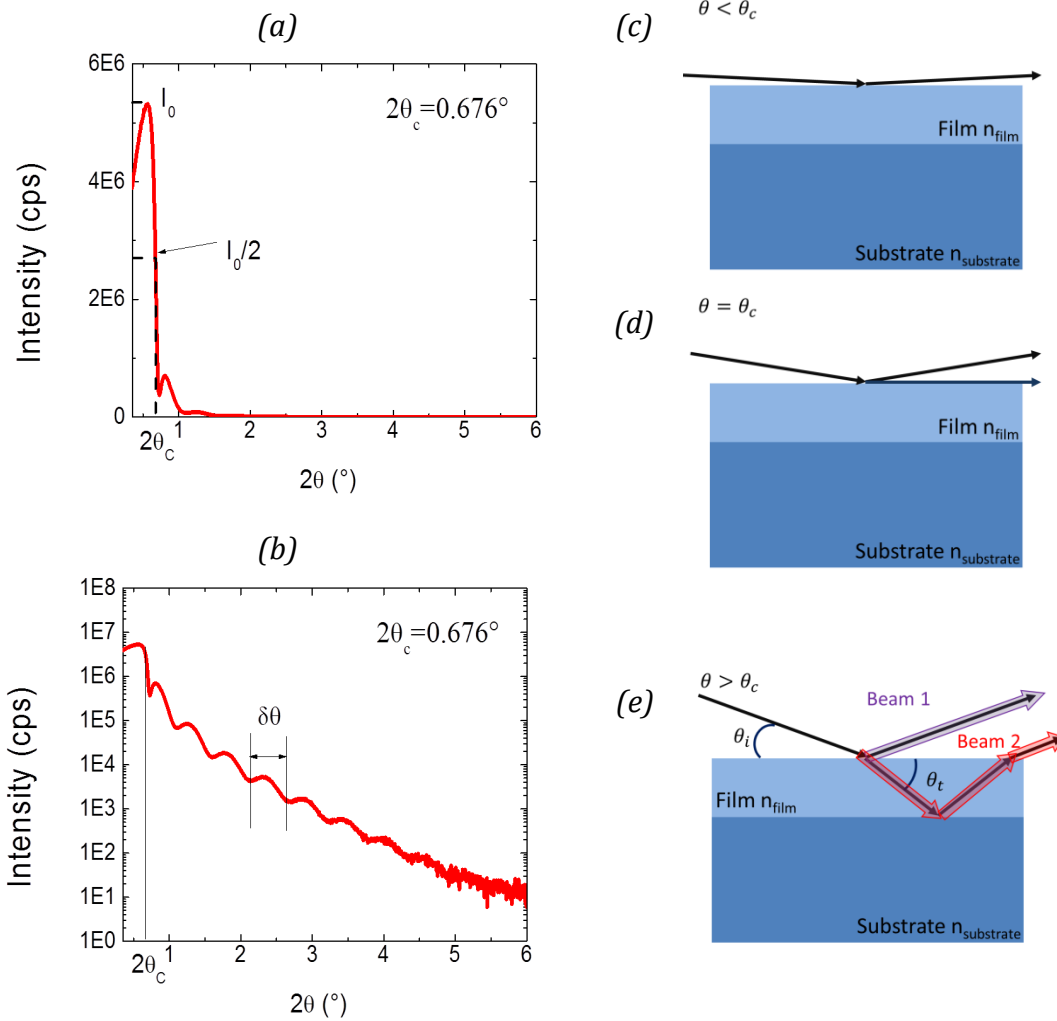


Figure VI-10-(a) Reflectivity scan in linear (a) and log (b) scale. Configuration of the X-Ray incident beam depending on the incident angle for an angle below (c), equal (d) and above (e) the critical angle.

To obtain the film thickness from a curve like Figure VI-10(b)) we use the Snell Descartes reflection law. The X-Ray beam penetrating within the film satisfies the angular relation:

$$\cos(\theta_i) = \cos(\theta_t) n_{film} \quad VI-5$$

Where θ_i and θ_t are respectively angle between the incident and transmitted beam and the thin film surface normal (see Figure VI-10(c-e)) and $n_{film} = 1 - \delta + i\beta$ the complex refractive index of the film (δ and β are the dispersion and absorption coefficient of the thin film, they are related to the electronic density and the mass density of the material).

In practice $n_{film} \rightarrow 1$ consequently $\cos(\theta) \sim 1 - \frac{\theta^2}{2}$ therefore when $\theta_i = \theta_c$ the beam starts to penetrate the sample and $\theta_t = 0$ the equality of VI-5 gives the relation $\theta_c \sim \sqrt{2\delta}$. The critical angle θ_c is then related to the dispersion coefficient of the film.

When the beam penetrates within the all film multiple reflection of the beam at the air/film and film/substrate interfaces will interfere, the phase difference ϕ between two beams (see Figure VI-10(e)) is:

$$\phi = \frac{1}{\lambda} \cdot \frac{2t}{\sin(\theta_t)} = \frac{4\pi}{\lambda} \cdot t \frac{n_{film}}{\sin(\theta_i)} \quad \text{VI-6}$$

A maximum of intensity is obtained for $\phi = \phi^m$ an integer, from the angular position between two maximas ($\delta\theta$ in Figure VI-10(b)) it is then possible to obtain the film thickness after approximating $\sin(\theta) \sim \theta$:

$$\delta\theta = \frac{\lambda}{2t_{film}} \quad \text{VI-7}$$

By averaging on many fringes it is possible to obtain the thickness of the film within 1 nanometer accuracy.

The decrease of the intensity is linked to the imaginary part β of the refraction index and can be used to obtain the substrate/film roughness using a complete fit of the reflectivity pattern.

VI-B.2 Atomic Force Microscopy (AFM).

The AFM technique is used to extract information on films' surface topography. Our AFM scans are performed with a Bruker Atomic Force Microscope in the tapping mode.

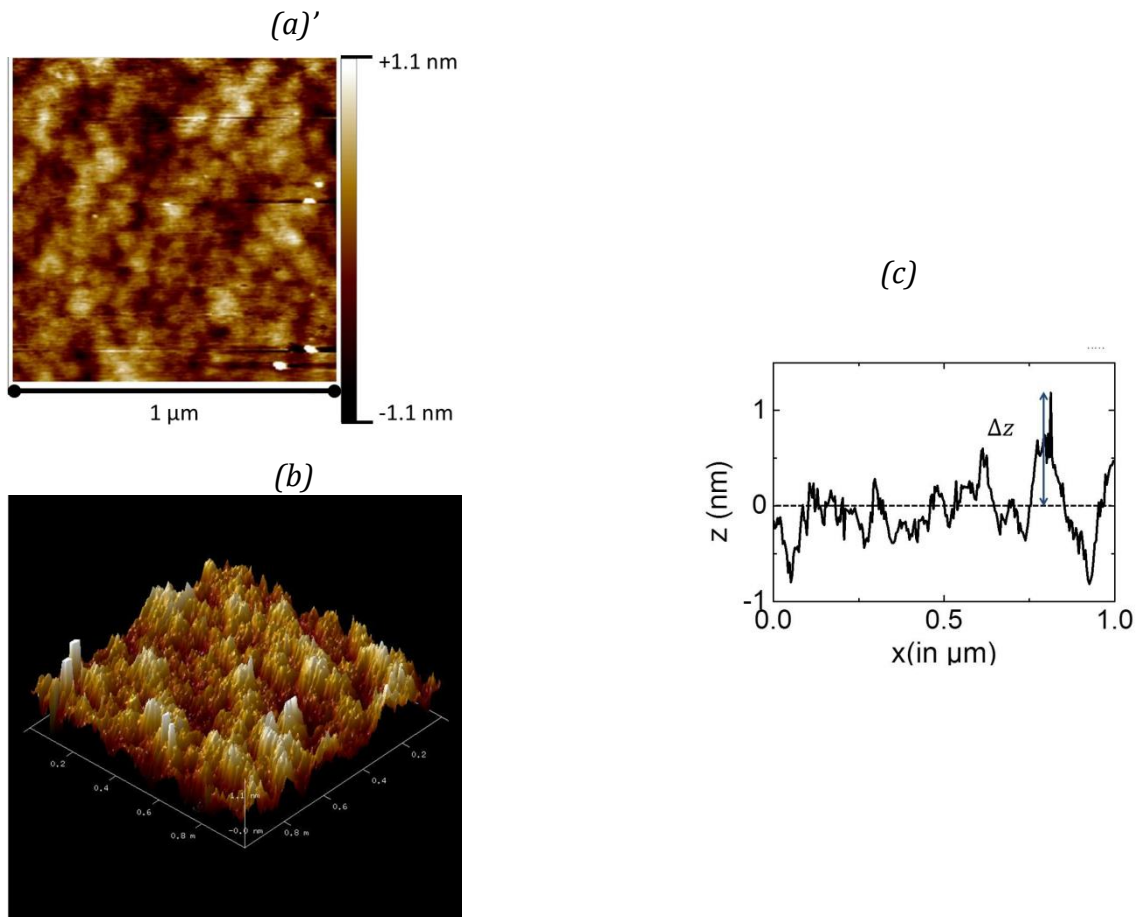


Figure VI-11 AFM picture of $1 \times 1 \mu\text{m}^2$ surface of YIG(20nm)/sGGG. From the 2D scan (a) it is possible to extract 1D profile for a certain position (c) and simulate the 3D image of the surface (b). From the Equation VI-9 the overall roughness of the film is $R_q = 0.385 \text{ nm}$

AFM scans gives information about the roughness R_q of our samples which can be defined along a single line by:

$$R_q = \sqrt{\frac{1}{L} \int_0^L |z^2(x)| dx} \quad \text{VI-8}$$

with $z(x)$ the height variation at the position (x) (see Figure VI-11 (c)) and L is the length over which we evaluate the roughness of the sample.

For the 2D scan (Figure VI-11(a)) the formula becomes:

$$R_q = \sqrt{\frac{1}{L_x L_y} \int_0^{L_x} \int_0^{L_y} |z^2(x, y)| dx dy} \quad \text{VI-9}$$

with $z(x,y)$ the height variation at the position (x,y) and L_x, L_y are the length over which we evaluate the roughness of the sample. It is this formula we refer to when mentioning the sample roughness.

3D images can be generated from 2D images as shown in Figure VI-11(b) to get a more realistic picture of the surface.

VI-B.3 SQUID magnetometry

To extract the saturation magnetization (M_s) of our magnetic thin films we use a Quantum Device SQUID. The M_s is measured from the saturated state of the thin film, obtained by applying a static external magnetic field $\mu_0 H_{ext}$ (the maximum field is 5.5T).

Garnet substrates used for the growth (GGG and sGGG) are paramagnetic and have a linear response to the external field: this contribution has to be subtracted in order to derive M_s . Thus an 'high enough' external field is applied ($\mu_0 H_{ext} = 50 \text{ mT}$ along the easy magnetic axis and $\mu_0 H_{ext} > \mu_0 (M_s + H_{Ku})$ for the hard magnetic axis) to saturate the magnetic material. After saturation ($\| \mu_0 H \| > \| \mu_0 H_{sat} \|$ in Figure VI-12 (a) and (b)) the magnetic contribution of the film is constant and $M = M_s$ and the linear response of the paramagnetic substrate to the external field can be fitted, the linear fit is then subtracted from the initial curve Figure VI-12(a) to observe the hysteretic behavior characteristic of magnetic materials (Figure VI-12(b)).

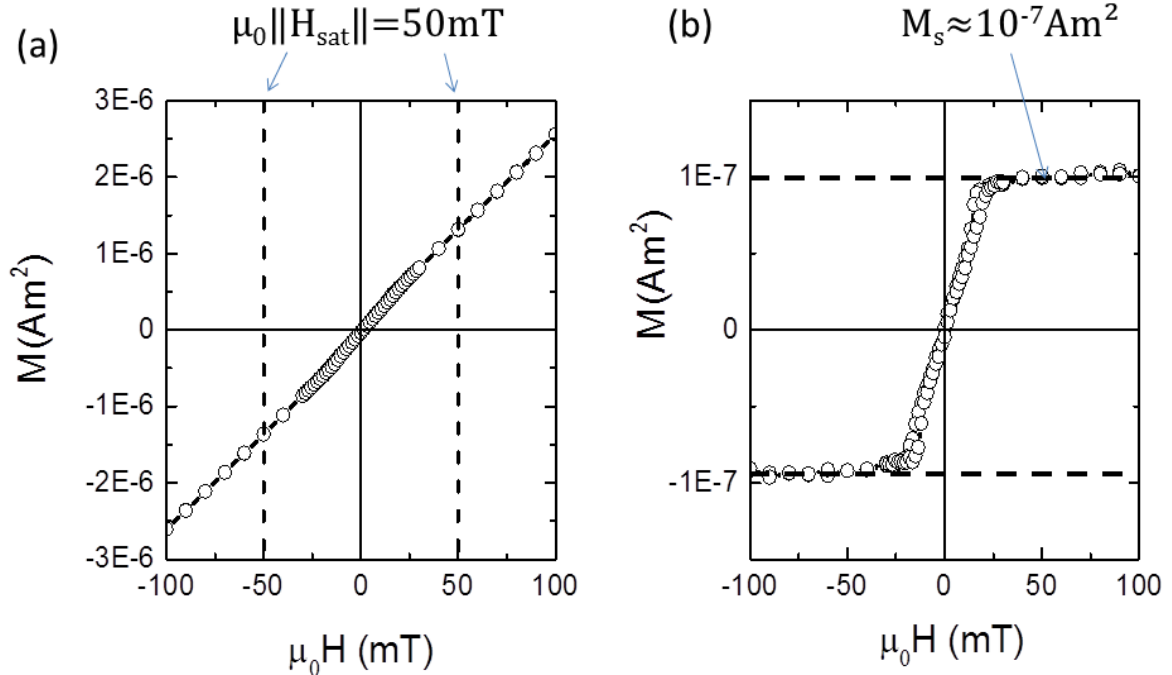


Figure VI-12 Typical SQUID curve of a 50 nm BiYIG//sGGG sample before (a) and after (b) subtraction of the substrate's linear contribution. The static field is applied in the easy direction of magnetization and the fit is performed with experimental points: $M^{\text{fit}} = M(\mu_0 \parallel \mathbf{H} \gg \mu_0 \parallel \mathbf{H}_{\text{sat}} \parallel)$

Even though the SQUID is a very precise technique the error the evaluation of M_s for nm-thick garnet films remains between 10 to 20 %. This error can be estimated from Figure VI-12(a): after saturation, the magnetic moment measured (coming from both the linear response of the substrate and the film) is of the order of $1.5 \cdot 10^{-6} \text{ A} \cdot \text{m}^2$, the error made on the linear fit is about 2% giving an uncertainty ΔM_s of $3 \cdot 10^{-8} \text{ A} \cdot \text{m}^2$. Such error is not negligible compared to the magnetic signal expected from thin film YIG: the typical value of M_s for YIG is 140 kA/m (see III.A.1.2) thus, a 50 nm thick YIG film on a $5 \times 5 \text{ mm}^2$ substrate gives a total magnetic moment $M_s = 1.8 \cdot 10^{-7} \text{ A} \cdot \text{m}^2$. The error is then about 10% on the M_s of YIG. Hence using SQUID magnetometry technique we can obtain the M_s of our sample within 15% error.

VI-B.4 Ferromagnetic resonance (FMR) measurement.

The FMR measurement is used to characterize the magnetic anisotropy and the dynamic of our films. We first describe the FMR set up, then the lock-in detection technique that is used for measuring the FMR signal and finally we present the ISHE measurement set up that is performed on the same machine.

VI.B.4.1 FMR set up

To excite the magnetic moment of the material we use an alternating rf field: $\mu_0 \mathbf{h}_{\text{rf}}$ with a fixed frequency and vary the static magnetic field $\mu_0 \mathbf{H}_{\text{stat}}$. The geometry of the set up is given by conditions for the precession of the magnetic moment (see Equation III-21) which requires: $\mathbf{h}_{\text{rf}} \perp \mathbf{H}_{\text{stat}}$.

The scheme of the setup is given in Figure VI-13: a RF source that can deliver from 1 to 30 GHz frequency is connected to a wave guide. The signal travels back and forth on a waveguide and collected in a reflection diode. The DC voltage from the diode is sent in a lock-in and measured after demodulation in a nanovoltmeter.

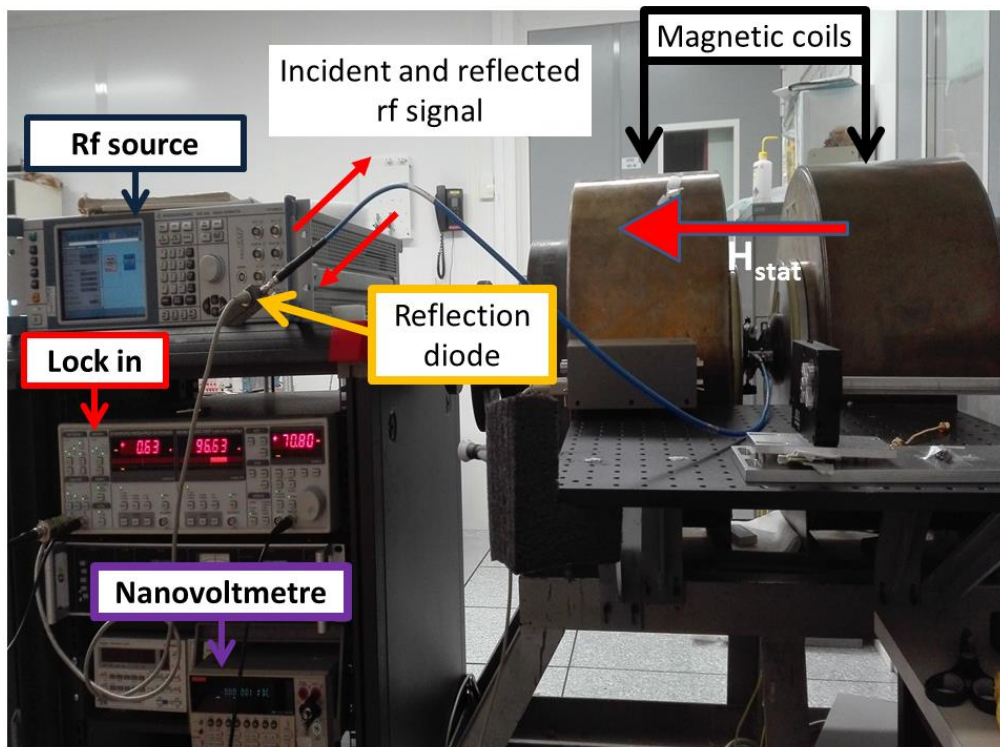


Figure VI-13 Overall scheme of the FMR set up

The symmetry of excitation is more detailed in the Figure VI-14.

The electromagnetic RF wave propagation (in red on the Figure VI-14) is fixed by the waveguide consequently the direction of \mathbf{h}_{rf} (in yellow on the Figure VI-14) as well. The sample lies directly on the waveguide (thin film face on the strip line to maximize the intensity of excitation \mathbf{h}_{rf}). The static magnetic field ($\mu_0 \mathbf{H}_{stat}$) intensity is swept in the direction perpendicular to \mathbf{h}_{rf} . The waveguide is open ended giving a full reflection of the RF power that is collected in the reflection diode.

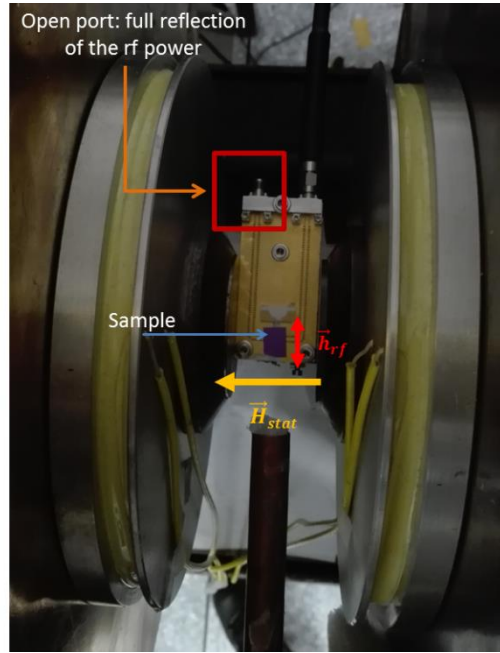


Figure VI-14 Direction of the different terms involved in the FMR set up

In the next section we will detail the demodulation of the signal using lock-in technique.

VI.B.4.2 Lock in detection technique.

To extract from the background signal of the overall measurement the FMR absorption signal corresponding to few nanometers of a MM we use a lock-in detection technique.

A small part of the static magnetic field is modulated at a low frequency ($f_0=73$ Hz) in comparison to the resonant frequency of the ferromagnetic material (\sim GHz). The static field is then written:

$$H_{stat} = H_0 + \delta H_0(f_0) \quad VI-10$$

where $\delta H_0(f_0)$ is modulated at the frequency f_0 . The total power detected by the diode is then:

$$P(H_{stat}) = P_{background} + P(H_0 + \delta H_0) \quad VI-11$$

the first term $P_{background}$ corresponds to the background contribution and is independent of the static field modulation, the second term $P(H_0 + \delta H_0)$ is related to the precession of the garnet magnetic moment and is dependent on the static field. The derivation of the absorbed power with respect to f_0 is written:

$$\frac{\partial P(H_{stat})}{\partial f_0} = \frac{\partial P_{background}}{\partial f_0} + \frac{\partial P(H_0 + \delta H_0)}{\partial f_0}$$

$$\frac{\partial P(H_{stat})}{\partial f_0} = 0 + \frac{\partial P(H_0 + \delta H_0)}{\partial H_0} \frac{\partial (H_0 + \delta H_0)}{\partial f_0}$$

$$\frac{\partial P(H_{stat})}{\partial f_0} = \frac{\partial P(H_0 + \delta H_0)}{\partial H_0} \delta H_0 \quad VI-12$$

We can then detect the derivative of the absorbed power and obtain FMR resonant curve similar to Figure VI-15(b).

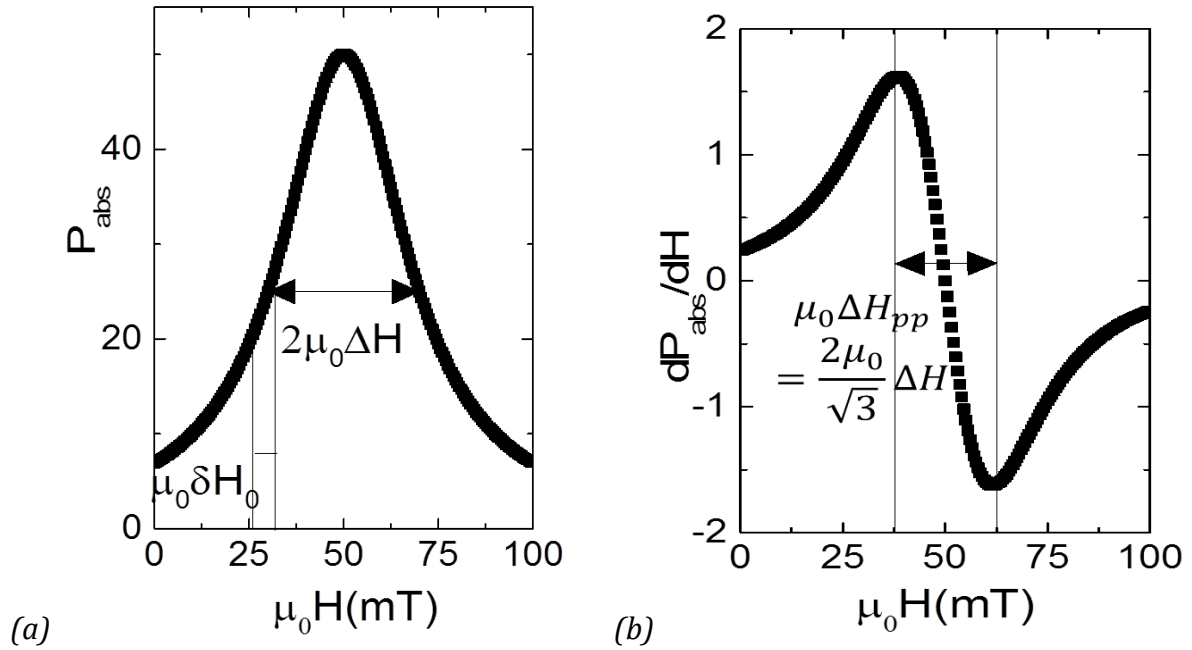


Figure VI-15 FMR absorption curve (a) of the characteristic lorentzian shape and its derivative (b) obtained after lock-in demodulation.

We need however to ensure that the amplitude of the modulated field is negligible small compared to the linewidth of the resonant peak: $\delta H_0 \ll \Delta H_{pp}$ as shown in Figure VI-15(a). The absorbed power due to FMR has a lorentzian shape (Figure VI-15(a)), hence after demodulation by the lock in the signal will have an anti-lorentzian shape (see Figure VI-15 (b)).

VI.B.4.3 ISHE measurement.

To prove the spin transparency of the interface we also measured ISHE voltage (V_{ISHE}) on SHE NM(Pt) /MI (BiYIG) bilayer using the same overall set up. In the FMR resonant conditions due to the transfer of spin angular momentum at the MI/NM SHE interface we can measure the ISHE induced voltage on the Pt top layer as illustrated in the Figure VI-16 (b).

For this measurement the RF field is modulated in amplitude. The Pt is connected via wire bonding on two metallic plates isolated from the strip line (blue line in Figure VI-16(a)) in order

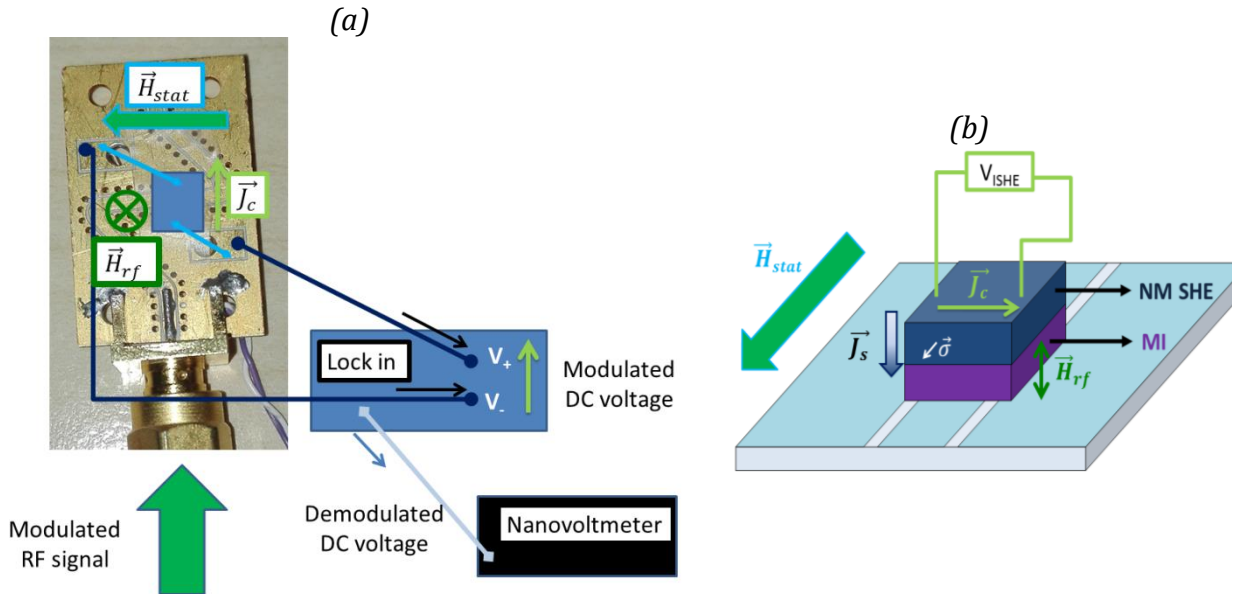


Figure VI-16 (a) Set up adapted to the ISHE measurement: silver wire bonding are connected to the top layer Pt to measure a voltage in the direction of the charge current J_c and (b) sketch of the representation of the different components involved in the ISHE

to measure a potential difference V_{ISHE} in the direction corresponding to J_c in the ISHE geometry (Figure VI-16(b)). A Lorentzian shape corresponding to the FMR induced spin current in Pt is measured on the nanovoltmeter (Figure VI-16(a)).

VI-B.5 Magnetoresistive effects.

Magnetoresistive effects (AHE and SMR) have been measured by JM George and Q Barbedienne in UMR CNRS Thales. The setup is shown in Figure VI-17(a) and the microscope image of a device used for those measurements (in Figure VI-17(b)).

The sample is mounted in chip holder and inserted into a cryostat. In this set up the sample holder can rotate over 360° in the three different planes and the direction of external field $\mu_0 H_{\text{ext}}$ is fixed (Figure VI-17(a)) and can vary in magnitude up to 5T.

The modulated voltage is then sent to the lock-in and after demodulation a DC voltage peak can be measured.

A DC current from few hundreds of μA to 1mA, the corresponding current density can be estimated $J_c \sim 10^9\text{-}10^{10}$ A/m² using the dimension of the device (2 μm wide strip) and the thickness of the Pt top layer (6 nm). This should not damage the Pt top layer. Depending on the observed magnetoresistive effect (SMR or AHE) the longitudinal (Figure VI-17(c)) or the transverse (Figure VI-17(b)) voltage is measured and the corresponding resistance is derived.

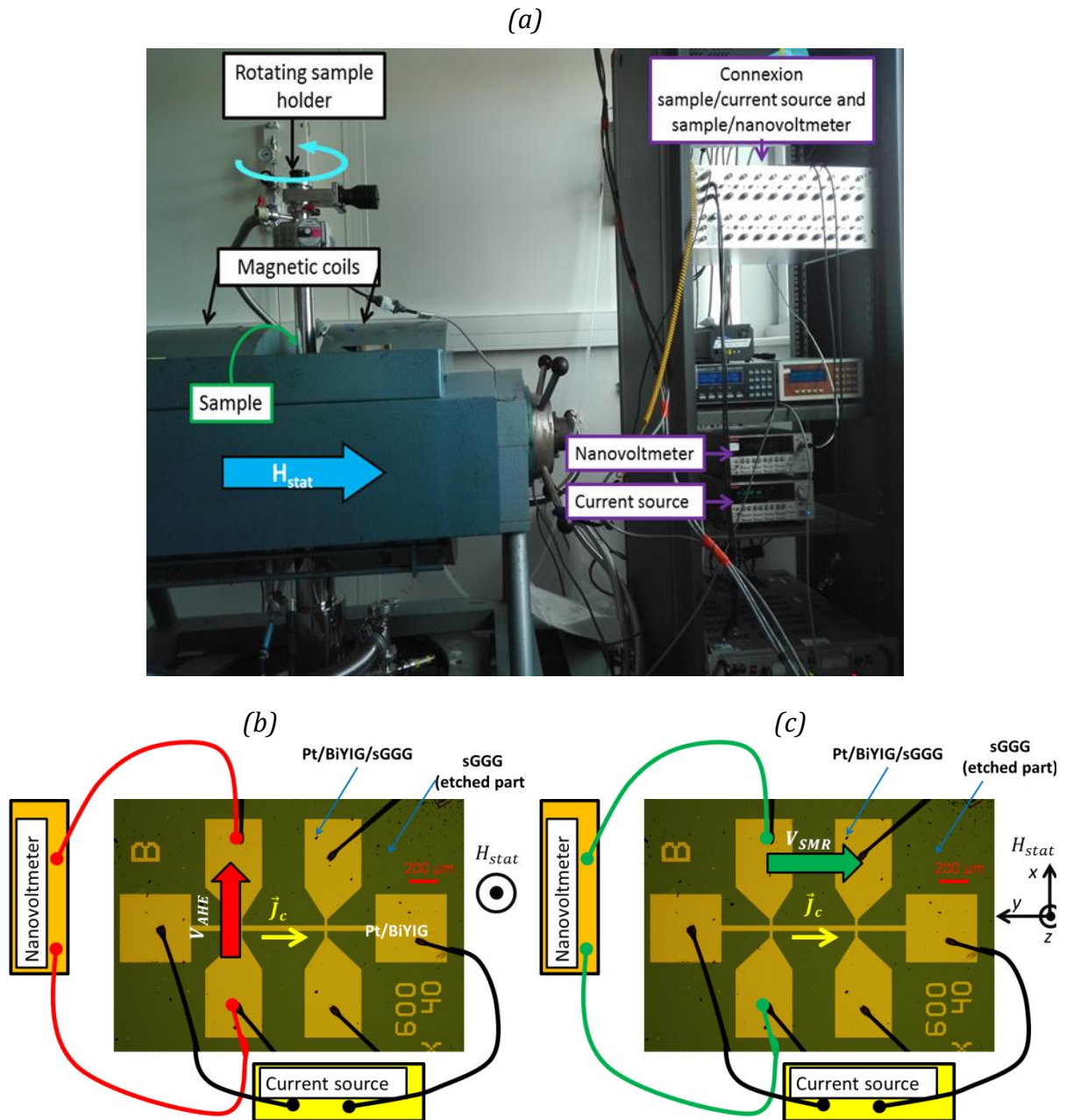


Figure VI-17 (a) Scheme of the SMR and AHE set up. Microscope image of the design and the geometry to measure AHE(b) and SMR(c). The yellowish part corresponds to Pt/BiYIG and the greenish part is the etched part of the sample (so only the sGGG substrate).

Devices used for the measurement are shown in Figure VI-17(b-c). After sputtering of 6 nm Pt on BiYIG the pattern is designed by optical lithography using a negative resist. We then perform ionic etching on the device to obtain the pattern of Figure VI-17(b-c) necessary to measure SMR or AHE.

VI-C Magneto-optical measurement.

Iron garnets and specially BiYIG are recognized for their magneto-optical properties at visible wavelength²⁰. For the characterization of our thin films we used two light based experimental techniques: Kerr microscopy and Faraday rotation measurement.

VI-C.1 Kerr microscopy.

The Kerr microscopy technique is based on the Kerr effect (see Section III.A.1.5.1.1). We use it in the polar geometry which corresponds to $\mathbf{k}_{light} \parallel \mathbf{n}$ (with \mathbf{n} the normal of the film surface) and \mathbf{M}_{film} oriented in the out-of-plane direction. This configuration provides the maximal signal and is the most suited for PMA materials.

The set up geometry is shown in Figure VI-18(a). The incident light is polarized perpendicularly to the static field $\mu_0 \mathbf{H}_{stat}$ and reflected on the magnetic sample. Depending on the direction of \mathbf{M}_{film} the polarization direction of the reflected light ($\mathbf{E}_{reflected}^r$) will rotate of θ_F due to the Kerr effect (i.e. Faraday effect for a reflected and not transmitted light). The reflected light passes through a polarizer and analyzer oriented along \mathbf{u}_{pol} , the intensity of the light detected by the CCD camera is then proportional to the scalar product $\mathbf{E}_{reflected}^r \cdot \mathbf{u}_{pol}$ (Figure VI-18(b)). The intensity of the light measured is then dependent on the polarization direction of $\mathbf{E}_{reflected}^r$ which can be related to \mathbf{M}_{film} (Figure VI-18(b)) due to the Kerr effect. The source is a linearly polarized white light.

Contrary to Faraday rotation or SQUID magnetometry measurements we can not obtain quantitative information on the magnetic moment or the magneto-optical activity of the film using Kerr microscopy. However for the case of BiYIG films because the magneto-optical coefficient of the film is considerably higher than the one of the paramagnetic substrate it is a very convenient way to obtain the magnetic anisotropy. Magneto-optical hysteresis curves of BiYIG//GGG and sGGG are well defined and most of the time no background subtraction is required.

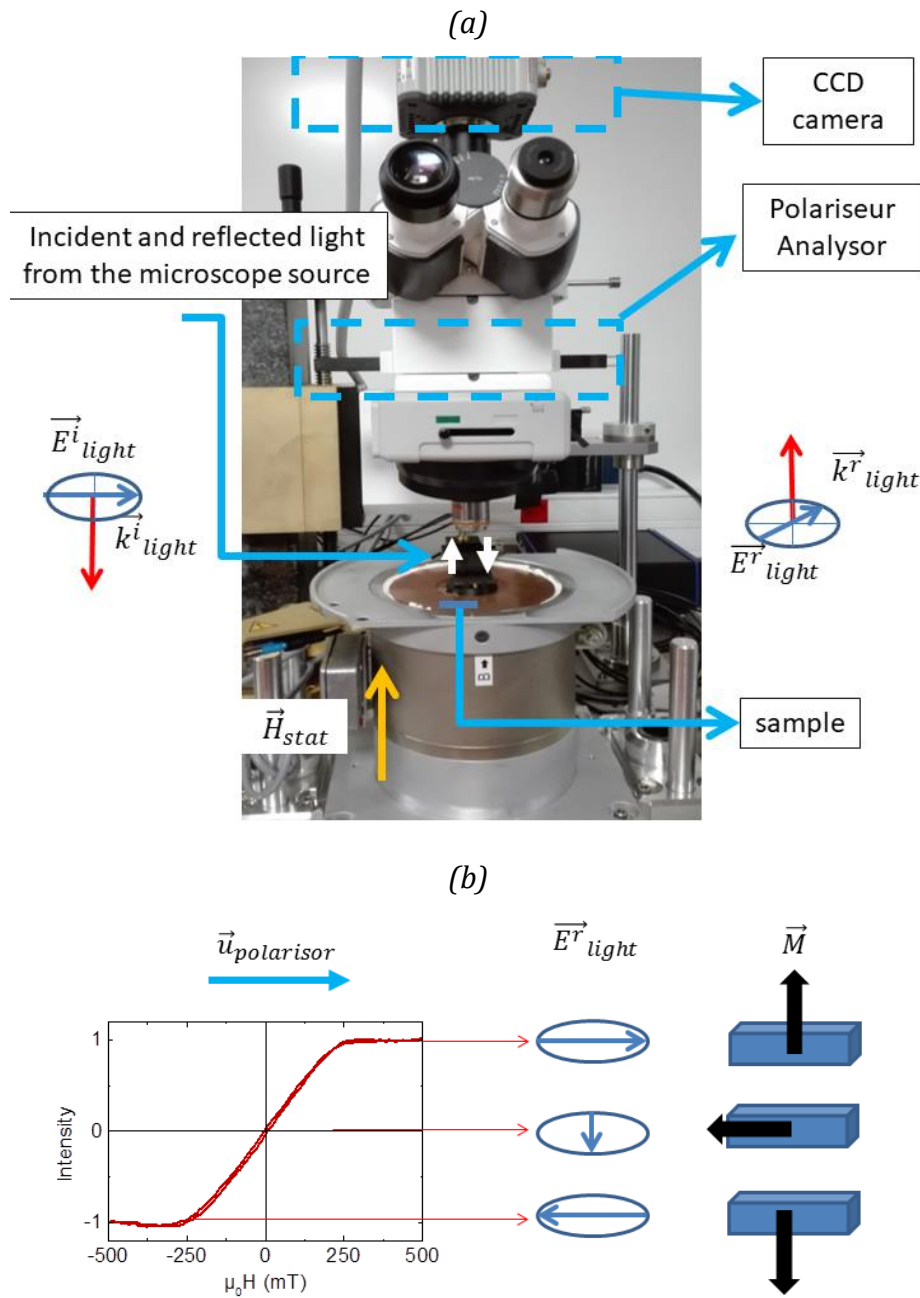


Figure VI-18(a) Kerr microscope in the polar mode configuration. The incident light ($\vec{E}^i_{light}, \vec{k}^i_{light}$) is polarized perpendicularly to the static field $\mu_0 \vec{H}_{stat}$. The polarisation of the reflected light is rotated of θ due to the FR of the sample. The intensity of the light collected by the CCD camera is proportional to the direction of the \vec{E}^r_{light} (and of \vec{M}) with respect to the polarisor (b).

The typical size of our magnetic domains is from tenth of micrometers to submicrometers and the spatial resolution of Kerr microscope images is, at most, 300nm. The size of the magnetic domains D_{width} can be derived using 2D Fast Fourier transform (FFT) on magnetic domains images of the thin film in the remanent state after demagnetization.

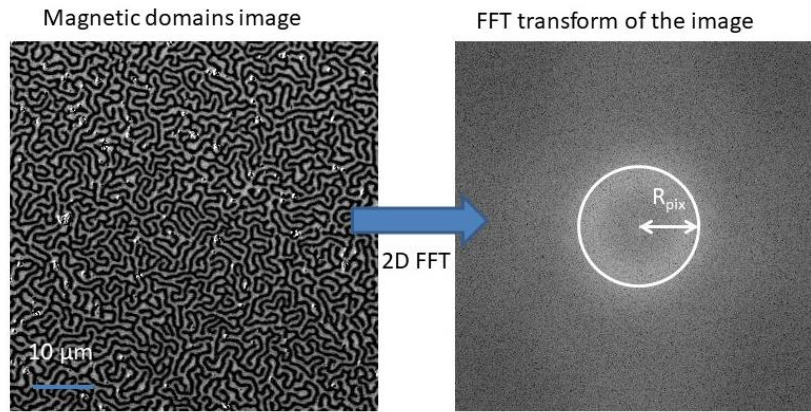


Figure VI-19 Magnetic domains image of a 30 nm thick BiYIG//sGGG and corresponding FFT transform of the image. From the radius R_{pix} of the circle we can obtain the domains width $D_{width} = 1\mu m$

The demagnetization is performed by applying an alternative out-of-plane external field with a decaying intensity down to zero. The frequency, decay time and the starting value for $\mu_0 H_{stat}$ need to be adjusted with respect to the magnetic characteristics of the sample since the validity of D_{width} obtained by FFT is defined by the 'quality' of the remanent state obtained after demagnetization. The error on the evaluation of D_{width} depends on the pixel size with respect to the domain size and the quality of the FFT, usually D_{width} is defined within $\pm 0.1\mu m$.

VI.C.1.1 Domain wall motion.

The propagation of magnetic domains requires a vectorial magnetic field: the in-plane field is required to fix the domains chirality and the out-of-plane field stabilizes the magnetic state and allow domains nucleation. For out-of-plane magnetized sample only tenth of mT are necessary to saturate the magnetic moment or to nucleate magnetic domains in the direction perpendicular to the film. On the vectorial field set up (Figure VI-20(a)), we mount a small coil (Figure VI-20(b)) that can reach 10mT.

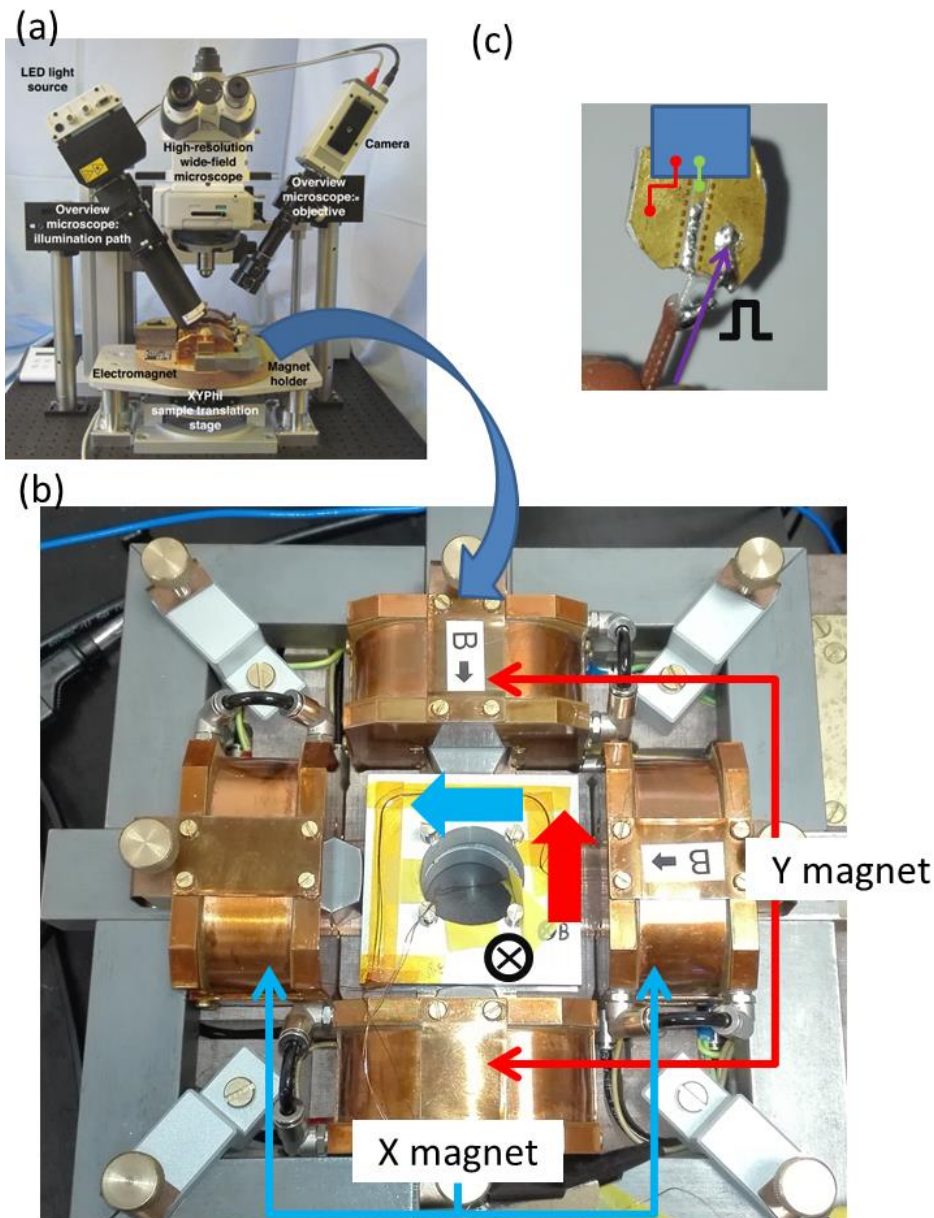


Figure VI-20 Set up of the Kerr microscope with a vectorial field (a), on the top of the X and Y magnets (up to 120 mT) a home made coil can generate a field (up to 10 mT) in the out-of-plane direction (b). For domain wall motion the sample is wired bonded to the ground and the signal of a strip line, the latter is connected to a pulse generator and we send μs width pulses of voltage (c).

To achieve current induced domain wall motion (CIDWM) using current pulses in a magnetic insulator it requires angular momentum transfer at an SHE metal/BiYIG interface, the SHE metal that was used is Pt. We sent short current pulses ($\sim 200\text{ns}$) in the Pt top (which is 5nm thick). Giving the lateral size ($\sim \mu\text{m}$) and the typical resistance of our devices ($\sim 5\text{k}\Omega$) high current densities are obtained in Pt ($\sim 10^{11} - 10^{12}\text{A}\cdot\text{m}^{-2}$) the short pulses of current are necessary to prevent damaging the Pt top layer. The current pulses source can deliver short pulses of 200 ns voltage up to 10 V. A coplanar wave guide is used to send those short time pulse (Figure VI-20(c)).

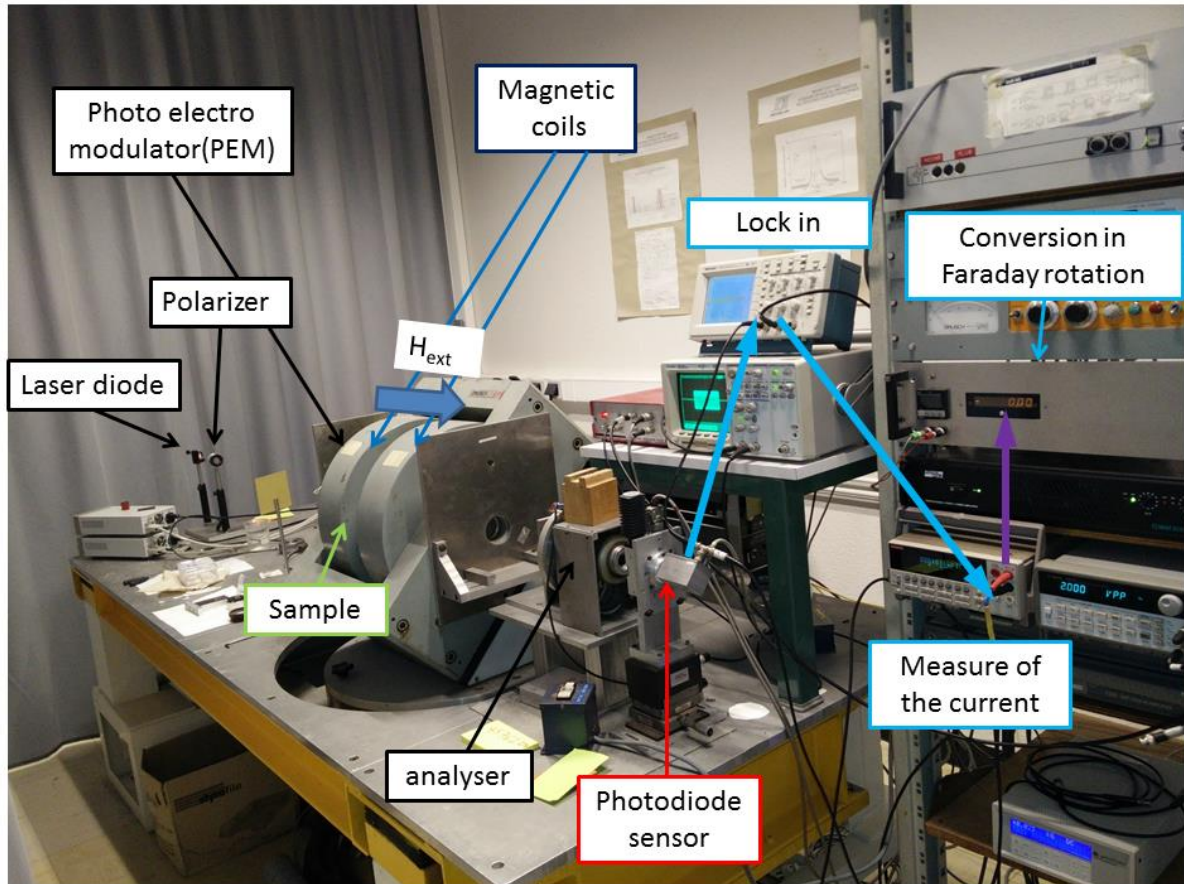
VI-C.2 Faraday rotation measurement.

The measurement of Faraday rotation has been performed at the LABSTICC in Brest on the experimental set up of N. Beaulieu. A scheme of the set-up is presented in the Figure VI-21. The incident laser goes first through a 45° polarizer and then through a Photoelectromodulator (PEM) that modulates the polarization of the laser beam at the frequency f_{PEM} ($f_{\text{PEM}}=50$ kHz). After the PEM a part of the modulated signal is taken as a reference: it is linearly polarized, converted it into an electrical signal and sent to a lock in set at f_{PEM} .

The other part of the laser beam passes through the magnetized sample and its polarization rotates of θ_F due to the Faraday effect. The external field $\mu_0 H_{\text{ext}}$ is applied perpendicularly to the magnetic film as shown in Figure VI-21(b). The linear component of the electric field from the light beam is extracted using the analyzer, converted into an electrical signal (via a photodiode) and sent to the lock-in.

The electrical signal corresponding to the beam that passed through the sample is subtracted from the reference one (taken just after the PEM) and demodulated. The DC voltage obtained is sent into a nanovoltmeter and corresponds then to the rotation of the light polarization.

(a)



(b)

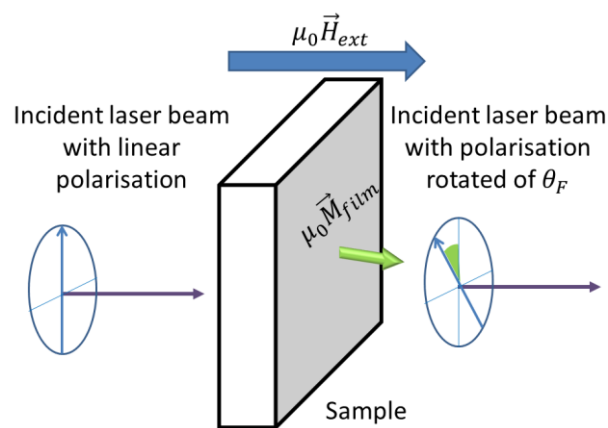


Figure VI-21-Scheme of the Faraday rotation measurement set up (a) and geometry of the light propagation vector, external field and the magnetic moment of the sample for measurement (b).

The modulation of the PEM is set to 50 kHz and the maximum value for $\mu_0 H_{ext}$ is 300mT. Therefore only sample with PMA or low saturation field in the out-of-plane direction could be characterized using Faraday rotation measurement.

VII Thin films characteristics.

In this part, we present the main characteristics of our films. We start with the feature relative to the growth itself. In a second part we present the structural and the magnetic properties of our films (both static and dynamic). Finally we relate the anisotropy to the structural properties of our films.

VII-A Growth conditions.

Here we present first structural characteristics (lattice parameter) of the different materials that will be used for the elaboration of our films (target and substrate). Those parameters will be useful in the following to understand structural and magnetic properties of the films. In the second part we give an example of the optimization of one growth parameter: the temperature and finally we present the growth conditions for our films.

VII-A.1 Generalities about the growth.

The two substrates that were used for the growth are garnets: $\text{Ga}_3\text{Gd}_5\text{O}_{12}$ (GGG) and substituted GGG (sGGG) oriented along the (111) direction. They have the same garnet cubic structure as the deposited materials which are $\text{Bi}_x\text{Y}_{3-x}\text{Fe}_5\text{O}_{12}$ ($\text{Bi}_x\text{Y}_{3-x}\text{IG}$).

Due to its lattice parameter which is very close to the one of bulk YIG the GGG substrate is traditionally used for the growth of YIG films^{46,101,130}, while because it has a larger lattice parameter the sGGG substrate is used for the growth of substituted YIG films where the Yttrium is replaced by a larger atom such as Bismuth, Dysprosium, Europium...^{20,26}. The choice of the substrate is essential to keep a good quality of the films: low lattice mismatch (<1%) between the bulk material and the substrate allow obtaining an epitaxial growth of films and decreases structural defaults density such as dislocations or local relaxation within the film¹³¹⁻¹³³.

VII.A.1.1 Derivation of the different lattice parameters and misfits

The lattice parameter of the substrate has to be compared with the one of the bulk phase. The lattice parameter of the polycrystalline target (a_{target}) used for the growth is taken as the reference.

This a_{target} can be obtained from out-of-plane ($2\theta - \omega$) XRD scans of the target. The relative intensity of each peaks corresponding to different grains' orientation can be calculated using the form factor of a centrosymmetric structure¹³⁴ (garnet structure belongs to the $\bar{1}\bar{a}3d$ space group), from the angular position of those peaks we obtain a_{target} . As an example, we display the XRD scan of the $\text{Bi}_1\text{Y}_2\text{IG}$ polycrystalline target (Figure VII-1) and labeled the most intense peaks to their respective atomic plane. It is then possible to obtain a_{target} from the angular position of those peaks.

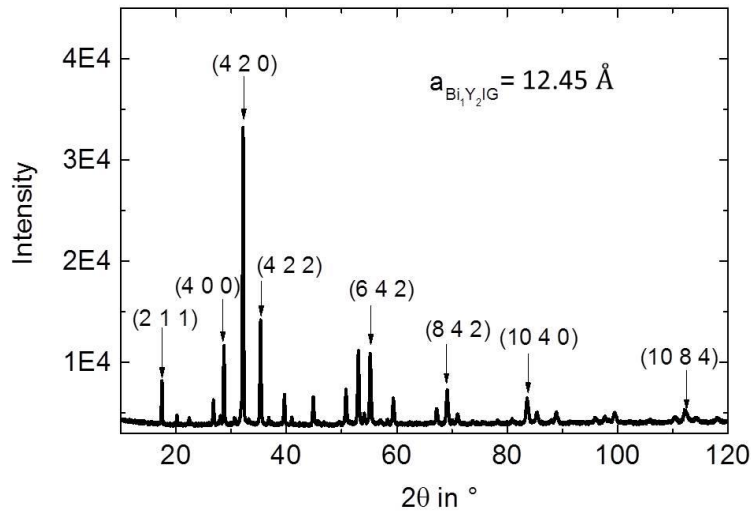


Figure VII-1 XRD scan of the polycrystalline Bi_1Y_2IG target: the position and the intensity of the different peaks allow to derive the lattice parameter : $a_{target} = 12.45\text{Å}$

In Table VII-1 we display the lattice parameter of each material (substrate, target) and the misfit $\frac{\Delta a}{a}$ for each substrate-target combination:

$$\frac{\Delta a}{a} = 100 \cdot \left(\frac{a_{target} - a_{substrate}}{a_{substrate}} \right) \quad VII-1$$

From the Table VII-1 we see that the misfit varies sign and magnitude allowing different type of strain, this point is discussed below.

	a_{YIG} = 12.38 Å	$a_{Bi0.7Y2.3IG}$ = 12.43 Å	$a_{Bi1Y2IG}$ = 12.45 Å	$a_{Bi1.5Y1.5IG}$ = 12.59 Å
a_{GGG} = 12.38 Å	<0.1%	0.4%	0.6%	1.7%
a_{sGGG} = 12.49 Å	-0.9%	-0.5%	-0.3%	0.8%

Table VII-1 Calculated mismatches between the different substrate and target used for the thin films growth

VII.A.1.2 Discussions about the different misfits.

Increasing the doping in Bi within the target leads to an increase of the lattice parameter, this is due to Bi^{3+} ionic radii being larger than the Y^{3+} one ($r_{Bi^{3+}} = 117 \text{ pm}$ and $r_{Y^{3+}} = 88 \text{ pm}$)¹³⁵. Depending on the substrate it leads to different situations:

- for GGG substrate the lattice parameter of the target is systematically bigger than the one of the substrate.
- for sGGG substrate at lower Bi content ($x < 1$) the lattice parameter of the target remains smaller than the one of the substrate. For the highest Bi content ($x = 1.5$) the lattice parameter of sGGG becomes smaller than the one of the substrate.

Using the same polycrystalline target, we can consequently have two different signs and magnitude of misfits depending on the substrate that is used for the growth. In the following of this Chapter we will see that this affects the films' properties.

VII-A.2 Growth conditions.

The growth parameters of YIG have been optimized previously by H. Molcepres and R. Bernard, and allow obtaining single crystalline ultrathin YIG films of excellent dynamical properties⁴⁶. For the growth of BiYIG it was however necessary to optimize the temperature of growth and the fluency of the laser in order to crystallize the desired garnet structure.

In the next part we present an example of optimization for one growth parameter: the temperature for thin films grown using the $\text{Bi}_{0.7}\text{Y}_{2.3}\text{IG}$ target. Similar optimization have been performed for the other Bi content in order to obtain the optimized growth condition for each Bi concentration.

VII.A.2.1 Optimization of the temperature growth parameter.

As a starting point we used the growth parameter of YIG which are presented in the first column of Table VII-3. Previous study on PLD growth of BiYIG reported an optimal growth temperature lower than for YIG¹³⁶. Hence we chose to decrease the growth temperature from the one of YIG and varied it from 650°C ($I=4.5$ A) to 400°C ($I=2$ A).

	PO_2	f_{laser}	E_{laser}	T_{growth} (measured on sGGG)	thickness
Film 1	0.25 mbar	2.5 Hz	1.3 J/cm ²	650°C ($I=4.5$ A)	32 nm
Film 2				570°C ($I=4$ A)	30 nm
Film 3				520°C($I=3.5$ A)	21 nm
Film 4				400°C($I=2$ A)	60 nm

Table VII-2 Sum up of the different growth conditions for the different $\text{Bi}_{0.7}\text{Y}_{2.3}\text{IG}$ films

The growth characteristics and the thickness of the different sample are presented in the Table VII-2 . The characterization of the different films necessary for the optimization is presented below.

VII.A.2.1.1 Roughness.

In the Figure VII-2 we show $5 \times 5 \mu\text{m}^2$ 2D AFM scans with the corresponding 3D image and the roughness measured on the 2D scans. Since films 2 and 3 presented similar characteristics we present only 3 out of the 4 different films (1,3 and 4).

The film 1, grown at the highest temperature, presents high density of surface defects and a roughness significantly higher (8 times larger!) than the two other films. The two other films (3 and 4) present a roughness below 2 nm with different profile of the surface. For the film 3 few 'big' (up to 7nm height) defects are increasing the overall roughness whereas the surface of the film 2 is quite homogeneous.

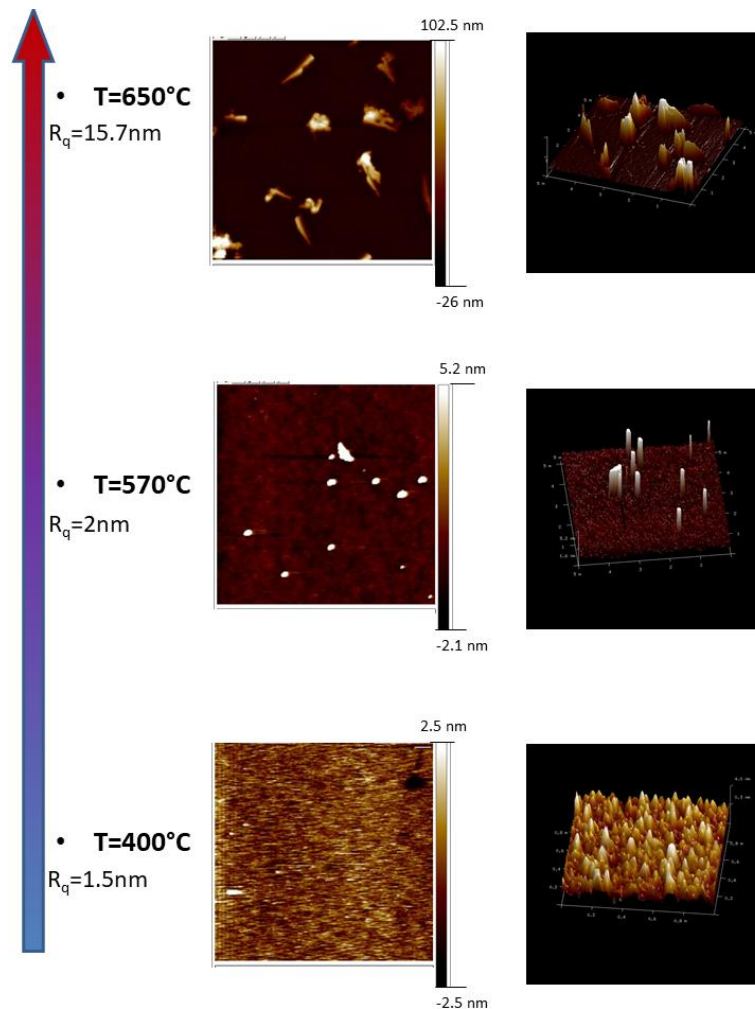


Figure VII-2 AFM scans of $5 \times 5 \mu\text{m}^2$ surfaces of films grown at 650, 570 and 400°C. The 2D (left) and corresponding 3D images (right) shows that the smoothness of the surface and the presence of defects are highly dependent upon the growth temperature.

This AFM study shows that high growth temperature is detrimental for the surface quality of the thin film and also that decreasing the growth temperature increases the surface homogeneity. The smoothest surface is observed for films grown at 400°C.

VII.A.2.1.2 XRD scans.

We compared structural properties of the different films using out-of-plane XRD scans along the (888) family of atomic plane in the Figure VII-3. Structural properties of films grown at 570 and 520°C were the same. Thus we only present the XRD scan of the film grown at 520 °C.

A diffraction peak corresponding to a single crystallized film is observed for thin films grown at 570°C (or 520°C) and 650°C. A small angular difference between the two peaks (labeled by arrows) is observed, it is however not significant enough to suggest a sizable difference of the structure between the two films. For a growth temperature of 400°C no diffraction peak corresponding to a crystalline structure is observed, however the thickness of the layer could be evaluated by XRR, therefore we conclude that the film is amorphous. No parasitic phases are detected on the overall scan (2θ varies from 5 to 120°)

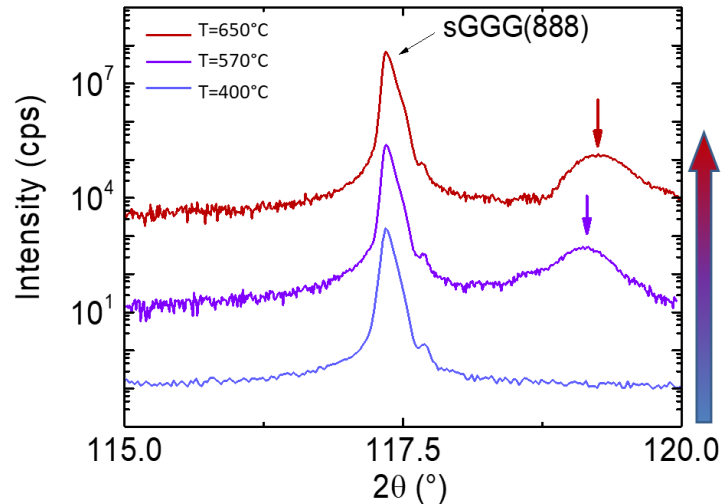


Figure VII-3 XRD scan along the (888) plane for BiYIG//sGGG grown at 3 different different temperature. For the lowest T_{growth} no cristalline structure of the film is observed.

From XRD characterization we can conclude that the lowest growth temperature of 400°C doesn't allow to crystallize a garnet structure.

VII.A.2.1.3 Kerr microscopy.

Finally we characterized the magneto-optical properties of those films by measuring polar hysteresis curve with Kerr microscope (the curve are normalized but there are no subtraction of the linear background) shown in the Figure VII-4(a).

In the case of the lowest growth temperature no magnetic signal but only the linear contribution of the substrate is observed (this coherent with the fact that there was no crystallization of the BiYIG). For sample grown at 520°C we see a strong PMA with a saturation at 25 mT, for a larger growth temperature (570 and 650°C) the out-of-plane field necessary to saturate the sample is increasing to 50mT. Magnetic domains imaging could be realized only on samples grown at 570 and 520°C (Figure VII-4(b)). No magnetic domains could be observed for $T_{growth}=650^{\circ}\text{C}$, either the size of magnetic domains was too small to be resolved with the Kerr microscope or the strength of the PMA was not enough to stabilize out-of-plane magnetic domains, however imaging of the surface show an high density of defects (which is coherent with previous AFM images) testifying of the bad surface quality. For thin films grown at 570°C we could also image magnetic domains however needles-like defaults are also observed, the density of these defaults is less important than for the case of the film grown at 650°C.

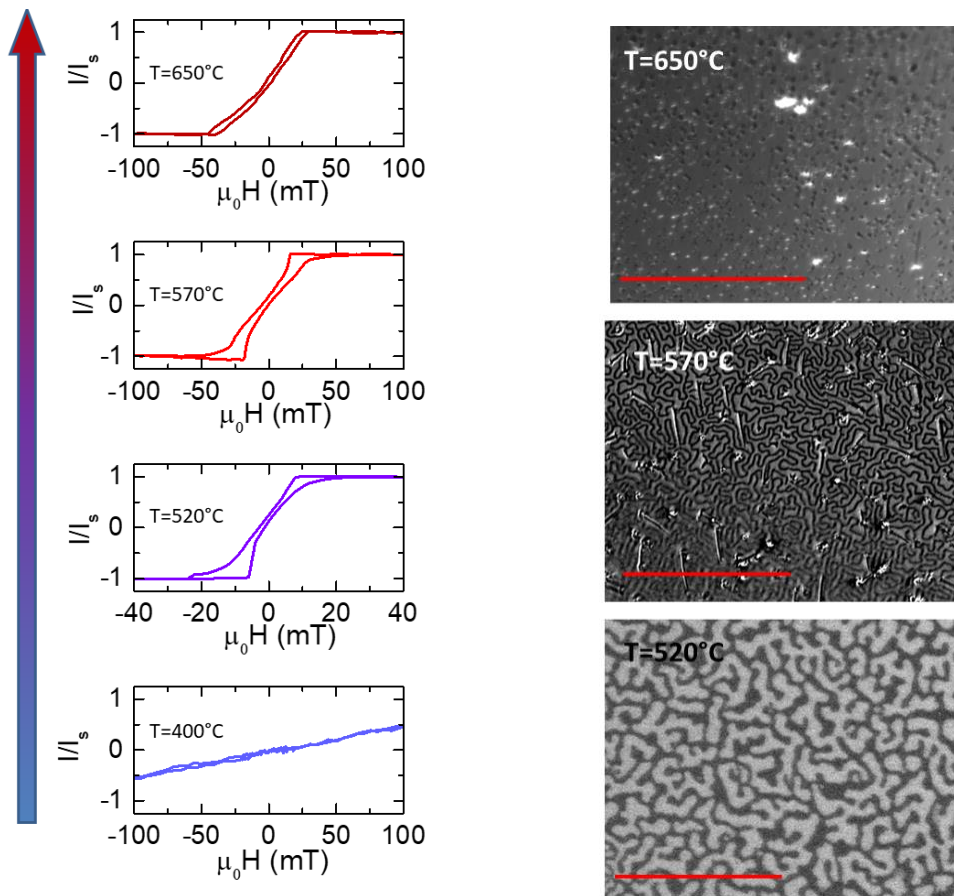


Figure VII-4 Kerr hysteresis curves and magnetic domains imaging of BiYIG//sGGG sample grown at 4 different temperatures. The magneto-optical quality of the thin film is highly dependent upon the growth temperature.

Sample grown at $T_{\text{growth}} = 400^\circ\text{C}$ showed magnetic domains structure and few defects on the surface. Kerr microscopy imaging allow to discriminate between the three different growth temperature since a strong PMA and low defect density are observed only for a growth temperature of 520°C .

Summing up AFM, XRD and Kerr microscopy data we conclude that the optimal growth temperature for our sample is 520°C . At this growth temperature the roughness is satisfying and we could crystallize a single BiYIG crystal. The material shows PMA, and out-of-plane magnetic domains with a reasonable density of defaults at the surface. This study illustrates the importance of one specific growth parameter: the substrate's temperature to obtain high quality single crystalline thin film.

VII.A.2.2 Optimized growth conditions

The optimized growth conditions for the different $\text{Bi}_x\text{Y}_{3-x}\text{IG}$ films are presented in the Table VII-3. Consistently with what has been reported^{24,136,137} the optimized growth temperature is decreasing with increasing the Bi content x due to higher volatility of the Bi atoms^{136,137}.

	YIG	Bi _{0.7}	Bi ₁	Bi _{1.5}
Oven temperature	650°C	520°C	500°C	450-500°C
Laser fluency	2.2mJ/mm ²	3.1mJ/mm ²	3.8mJ/mm ²	3.1mJ/mm ²
O ₂ pressure	0.25 mbar			
Laser repetition	2.5 Hz			
Distance target/substrate	44 mm			

Table VII-3 Optimized growth conditions for Bi_xY_{3-x}IG films.

Now that generalities concerning materials used for the growth and growth conditions have been presented we will focus on our films characteristics.

VII-B Structural properties.

Structural properties of our thin films are studied with XRD:

- $2\theta - \omega$ XRD scan along the (111) growth direction is used to obtain the distance between two atomic planes in the out-of-plane direction.
- RSM along the (642) oblique plane allows getting the substrate/film epitaxial relation in the $(20\bar{2})$ in-plane direction.

This information are necessary to determine the growth regime (strained or relaxed) of the film and to obtain the lattice parameter of the thin film in the different 'directions' (in-plane and out-of-plane) and (if they are grown under strain) the relaxed structure.

All different structural values derived within this Section will be summed up in the Table VII-4.

VII-B.1 Out-of-plane structure

Figure VII-5 displays $2\theta - \omega$ XRD scans of $\text{Bi}_x\text{Y}_{3-x}\text{IG}/\text{GGG}$ films centered on the (444) diffraction peak of the GGG substrate ($2\theta = 51.06^\circ$). The position of each films' diffraction peak as well as their thicknesses are labeled on the graph. From the angular position of those peaks we can make several observations:

- increasing the Bi content within the film leads to a shift of the (444) peak towards lower diffraction angle.
- the position of the (444) film's diffraction peak remains systematically at lower angle than the one of the substrate.

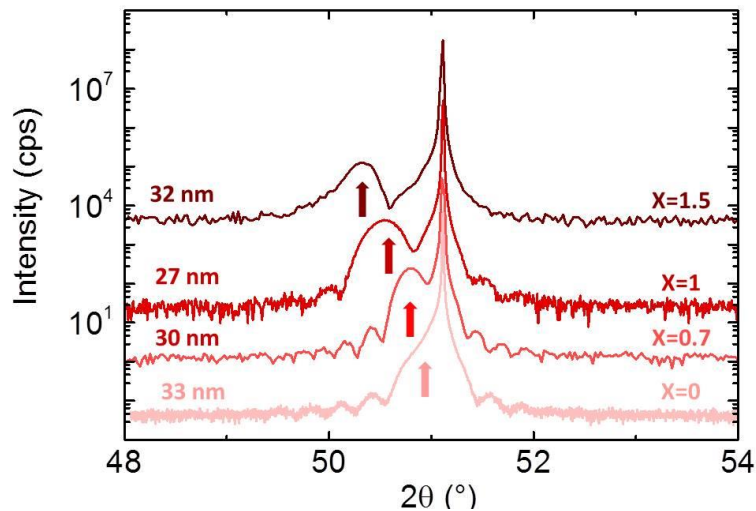


Figure VII-5 (444) Diffraction peaks of $\text{Bi}_x\text{Y}_{3-x}\text{IG}/\text{GGG}$ films for various Bi doping and thicknesses. The out-of-plane lattice spacing of the film (red arrow) is increasing with the Bi content.

Directly from the interatomic distance plane d_{444} in the out-of-plane direction we can derive the out-of-plane lattice parameter a^\perp which would corresponds to the lattice parameter of the film if its symmetry was cubic. The expression of a^\perp is then:

$$a^\perp = 4\sqrt{3}d_{444} \quad \text{VII-2}$$

As shown in the first column of Table VII-4 the term $a_{Bi_xY_{3-x}IG//GGG}^\perp$ increases with the Bi content of the target, this is consistent with the fact that the target lattice parameter increases with Bi content (Figure III-6).

Moreover the substrate-target misfit for the GGG substrate case is found to be always positive (Table VII-1), this is coherent with a film's peak position shifted at lower angle than the one of the substrate on the XRD scan (the lower the angle the higher the lattice parameter): in the out-of-plane direction $a_{Bi_xY_{3-x}IG//GGG}^\perp > a_{GGG}$.

In the Figure VII-6 we display the same type of XRD scan for the case of $Bi_xY_{3-x}IG$ films grown on sGGG substrate. The angular position of the sGGG (444) diffraction peak is: $2\theta = 50.59^\circ$ ($a_{sGGG} > a_{GGG}$). From the angular position of the $Bi_xY_{3-x}IG//sGGG$ (444) diffraction peaks (labeled with a blue arrow) we can conclude that:

- increasing the Bi rate within the film leads to a shift of the thin film (444) peak towards lower diffraction angle.
- the position of the film's diffraction peak remains at lower angle than the one of the substrate only for 1.5 Bi doping, for lower Bi content (from 0 to 1) the angular position of the film's diffraction peak is at higher angle than the one of the substrate.

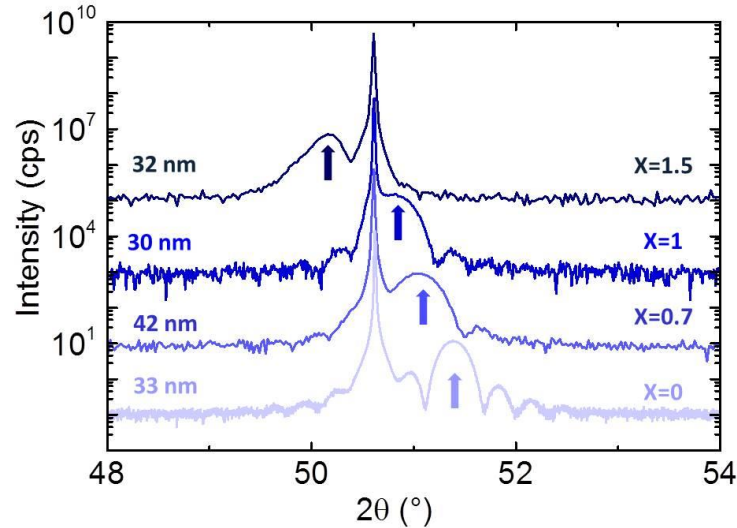


Figure VII-6 (444) Diffraction peaks of $Bi_xY_{3-x}IG//sGGG$ films for various Bi doping. The out-of-plane lattice spacing of the film (blue arrow) is increasing with the Bi content until it exceeds the one of the substrate ($Bi=1.5$).

Once again the increase of Bi content within the film leads to an increase of $a_{Bi_xY_{3-x}IG//sGGG}^\perp$ (first column of Table VII-4). Moreover we observe that for a Bi doping $x < 1.5$ we have $a_{Bi_xY_{3-x}IG//sGGG}^\perp < a_{sGGG}$ and that $a_{Bi_{1.5}Y_{1.5}IG//GGG}^\perp > a_{sGGG}$ this is consistent with the sign of the misfit target/substrate derived in Table VII-1 (negative except for $x=1.5$).

Structural information that have been derived from XRD scan in the out-of-plane direction are following the prediction of the Table VII-1: $a_{Bi_xY_{3-x}IG}^\perp$ increases with x and the sign of the out-of-plane film/substrate misfit is the same as the one of the target/substrate.

VII-B.2 In-plane structure.

We characterized the in-plane structure of our thin films by XRD diffraction (RSM). Complementary, Transmission Electron Microscopy (TEM) has been performed in Madrid at the Instituto de Ciencia de Materiales de Madrid (CSIC) allowing to obtain information at the atomic scale in our sample.

VII.B.2.1 RSM mapping.

Information on the in-plane lattice parameter of the film (a^{\parallel}) are obtained from RSM scan along the (642) oblique plane for $\text{Bi}_x\text{Y}_{3-x}\text{IG}/\text{GGG}$ films (Figure VII-7) and $\text{Bi}_x\text{Y}_{3-x}\text{IG}/\text{sGGG}$ (Figure VII-8).

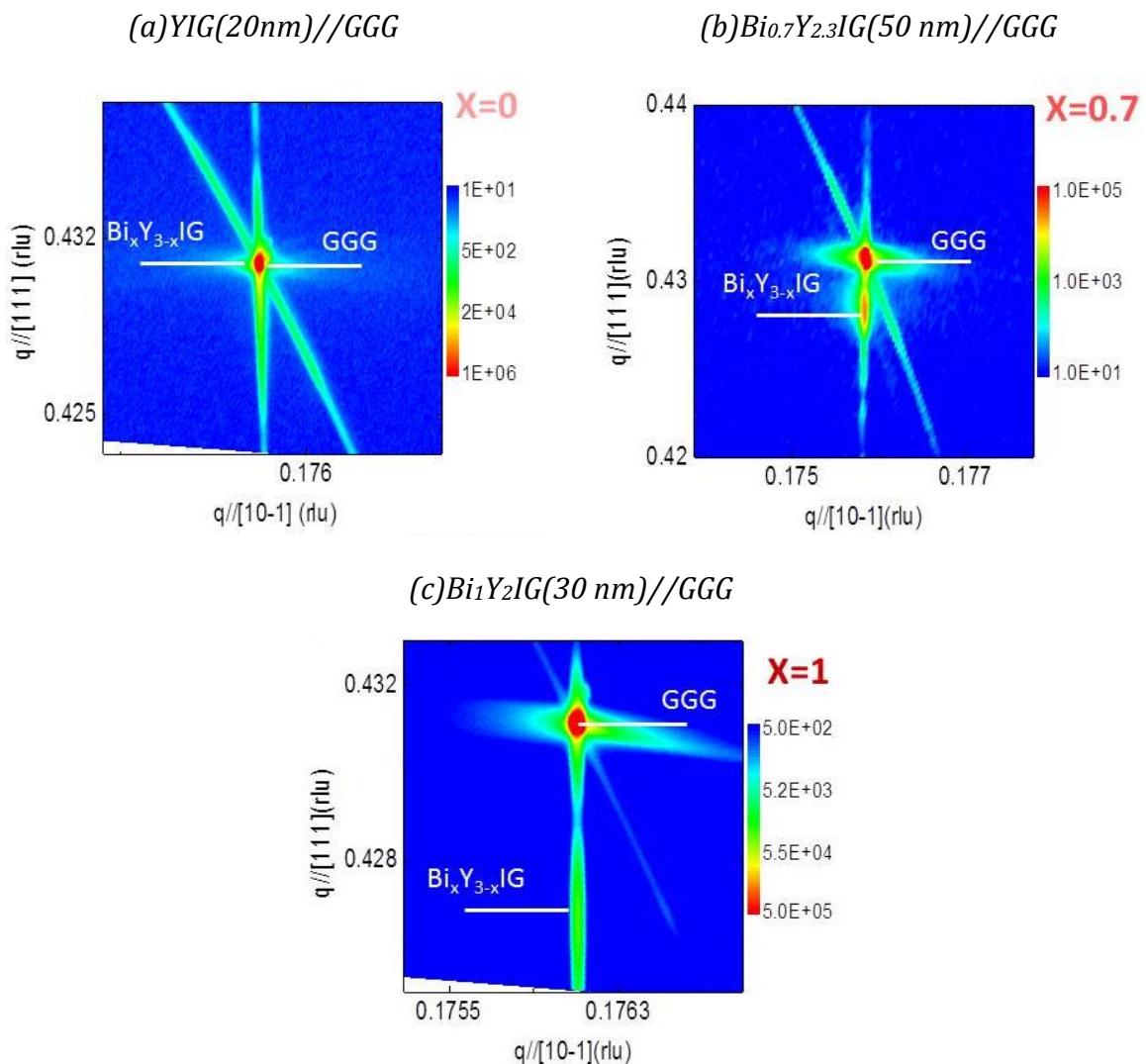


Figure VII-7 RSM along the (642) plane for $\text{Bi}_x\text{Y}_{3-x}\text{IG}/\text{GGG}$ films of different thicknesses and concentration x : alignment of the substrate and thin film peaks along the q_{\parallel} attests of the pseudomorphic growth of the film.

Except for the YIG//GGG films, plots of the 2D maps in the reciprocal space shows that films are fully strained: the diffraction peak of the GGG substrate and the one of the film are aligned along the q_{\parallel} direction (which corresponds to the $[10\bar{1}]$ in-plane direction).

For YIG//GGG sample the absence of the film diffraction pattern on the 2D RSM scans can be explained by the fact that our angular resolution was not enough along the (642) plane to distinguish the peak of the substrate from the one of the film. This is not surprising considering the misfit was already very small (0.16%) in the out-of-plane direction.

To confirm that there is an epitaxial strain in the other in-plane direction ($[11\bar{2}]$) we also performed a scan along the (682) plane ($[444]+[24\bar{2}]$) (in the substrate cubic structure $[24\bar{2}]$ and $[11\bar{2}]$ are equivalent) on $\text{Bi}_1\text{Y}_2\text{IG}/\text{sGGG}$ films: we observe the same alignment of the sGGG and thin film peak along the q_{\parallel} axis was observed.

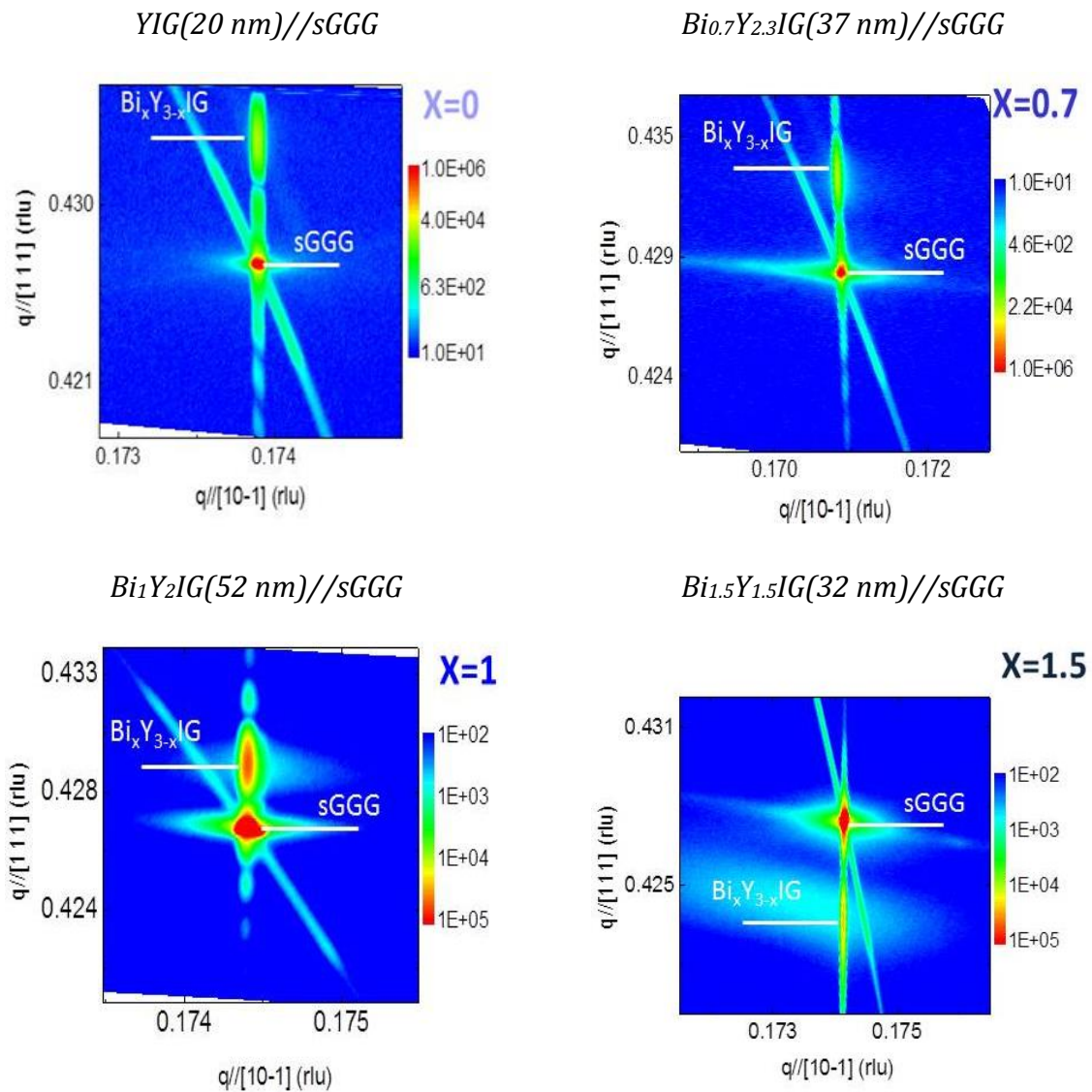


Figure VII-8 RSM along the (642) plane for BiYIG/sGGG films: the alignment of the substrate and thin film peaks along the q_{\parallel} testify of the pseudomorphic growth of the film

From the RSM scans we conclude that our films are grown under epitaxial strain and have the same lattice parameter that the substrate along the in-plane direction. RSM scans have been

performed for films from 20 to 50 nm thicknesses: the structure remains strained even for the thickest films.

VII.B.2.2 TEM analysis.

The in-plane epitaxial strain evidenced by XRD could further confirmed by TEM imaging of BiYIG//sGGG interface. TEM imaging along the $\langle 0-11 \rangle$ direction has been performed by J. Grandal and M. Varela (CSIC, Madrid) on a $\text{Bi}_{0.7}\text{Y}_{2.3}\text{IG}(15\text{nm})//\text{sGGG}$ sample. The BiYIG surface the sample is capped with 50 nm of Pt for protection.

TEM image of the BiYIG/sGGG interface shown in Figure VII-9(a) reveals that the film is strained on the substrate and atomically sharp interface with the substrate. This confirms the pseudomorphic growth of the film and the matching between the substrate and the film lattice parameter in the in-plane direction (100). In the Figure VII-9(b) the TEM image of the BiYIG film only is displayed: no relaxation can be observed which confirms that films are fully strained over the all thicknesses and that no local defects or relaxation (which would not be observable with XRD) are present.

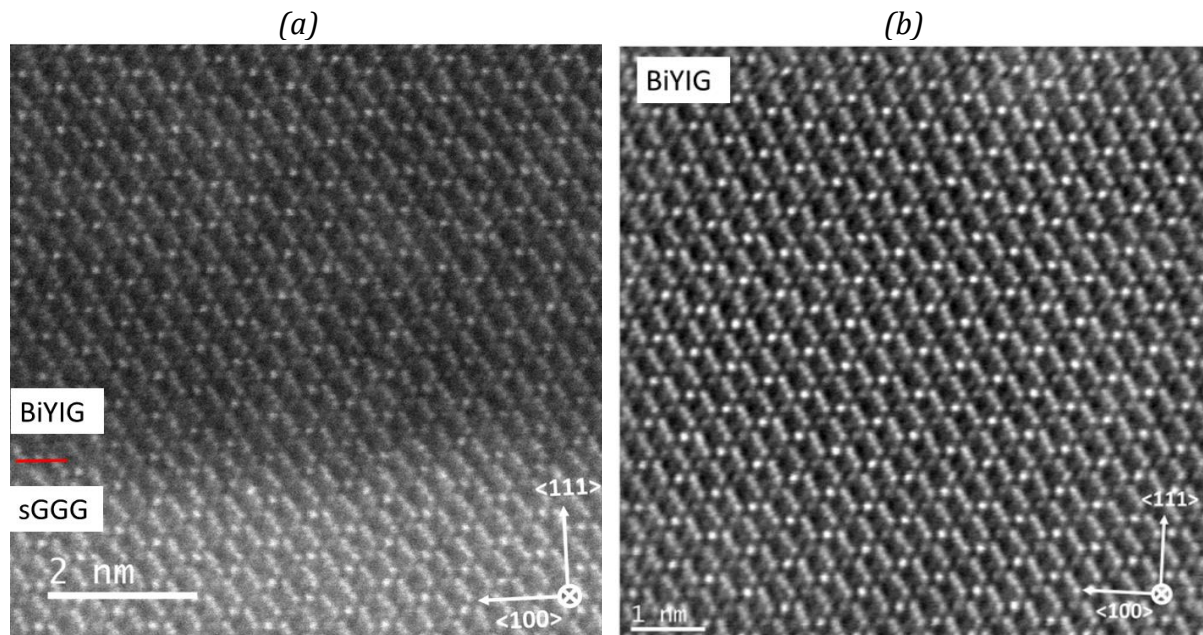


Figure VII-9-TEM image of the BiYIG//sGGG interface (a) and BiYIG film only (b). The first image reveals no structural defects at the interface such as dislocations which confirms the pseudomorphic growth. The second image confirms that the BiYIG structure is fully strained along the entire film's thickness. No relaxation is observed.

TEM imaging is confirming the previous XRD analysis and reveals a fully strained structure over the all film thickness. Combining XRD analysis and TEM imaging we evidence that the film is uniformly strained with no local defaults.

VII-B.3 Discussion.

Using the derived values of the in-plane and out-of-plane lattice parameter we can derive the one of the relaxed structure of the films by assuming that:

- the in-plane strain is isotropic.

- the material is under an elastic deformation (see Annexe I.B).
- the relaxed structure of the material is assumed to be cubic (as it is for garnet structure).

The lattice parameter of the relaxed structure a_0 can be derived using Equation III-9. As in many other works^{20,33,137} we assume that mechanical properties of the garnet are not changed with Bi doping (E and μ are the same than for YIG).

To be fully exact in the derivation of the relaxed lattice parameter we should consider a biaxial strain indeed $\sigma_{\parallel[1-10]} \neq \sigma_{\parallel[2-1-1]}$ ¹⁰⁷ and the Equation III-9 can be refined using the elastic stiffness constant of the YIG⁹⁸. The value obtained for a_0 with this second model varies of 0.2% maximum compared to the one obtained with the isotropic model. This difference remains in the error bar of the XRD measurement, thus we will use the simpler isotropic model to derive a_0 .

The different values of a_0 derived using this relation are found in the Table VII-4. The trend of increasing of a_0 with Bi content in the film is confirmed: a relative increase of 0.6% (0.8%) for $a_{Bi_xY_{3-x}IG//GGG}^{\perp}$ ($a_{Bi_xY_{3-x}IG//sGGG}^{\perp}$) is observed between films with $x=0$ to $x=1.5$. Reference values of a_{target} obtained from XRD analysis varies by 0.9% when comparing YIG and $Bi_{1.5}Y_{1.5}IG$ (Table VII-1). This increase of a_0 ($BiYIG$) with the Bi content is about the same as the one of the target which suggests a good stoichiometry and a successful Bi transfer from the target to the film during the growth.

	$a_{film}^{\perp}(\text{Å})$	$a_{film}^{\parallel}(\text{Å})$	$a_0(\text{Å})$	$\frac{\Delta a^{\parallel}}{a_0} \cdot 100$
GGG			12.38	
YIG//GGG	12.42	12.38	12.40	-0.18%
$Bi_{0.7}Y_{2.3}IG//GGG$	12.47	12.38	12.43	-0.40%
$Bi_1Y_2IG//GGG$	12.50	12.38	12.45	-0.53%
$Bi_{1.5}Y_{1.5}IG//GGG$	12.56	12.38	12.48	-0.79%
sGGG			12.49	
YIG//sGGG	12.32	12.49	12.40	0.75%
$Bi_{0.7}Y_{2.3}IG//sGGG$	12.38	12.49	12.43	0.49%
$Bi_1Y_2IG//sGGG$	12.43	12.49	12.46	0.27%
$Bi_{1.5}Y_{1.5}IG//sGGG$	12.61	12.49	12.56	-0.53%

Table VII-4 Sum up of the different structural characteristics of $Bi_xY_{3-x}IG$ films depending on their growth substrate. As a reminder the lattice parameters of the two substrates (GGG and sGGG) are also displayed

In Section III.A.1.4, III.A.2.4.2 and III.A.3.2 we mentioned the magneto elastic anisotropy term that is related to the strain. In our thin films the strain is imposed in the plane of the film and is given by: $\frac{\Delta a^{\parallel}}{a_0} = \frac{-a_0 + a_{film}^{\parallel}}{a_0}$. It is given in % in the last column of Table VII-4, and we observe that both the sign and the magnitude of this term varies depending on the substrate or the Bi content of the film, consequently the contribution of the magneto elastic anisotropy term will depend on those two parameters.

In this part we presented the different structural characteristics of our films. We saw that depending on the substrate and the doping in Bi different strain can arise (positive or negative). As the strain is related to some anisotropy term we expect different magnetic behaviors depending on this strain. In the next part we focus on those magnetic properties.

VII-C Magnetic properties.

This section presents magnetic characteristics of our thin films and is divided in three different parts:

- the first one details the static magnetic properties of our films: we define the magnetic moment M_s and the magnetic easy axis.
- the second part presents magneto-optical measurements of our BiYIG films as BiYIG is recognized for its high magneto-optical activity^{20,37,138,139}.
- the last part focuses on the dynamical characteristics of our films and we distinguish the case of thin films with in-plane magnetic anisotropy to the one of out-of-plane magnetized films.

VII-C.1 Determination of the magnetic anisotropy.

The magnetic moment per unit volume: M_s is obtained using SQUID magnetometry (see Section VI-B.3): after subtraction of the substrate contribution using a linear fit and division by the volume of the thin film we obtain M_s within $\pm 10\%$. To have a better accuracy when doing the linear fit M_s vs $\mu_0 H$ measurements were performed along the direction of the magnetic easy axis.

In the second row of Table VII-5 we see that the M_s value remains the same within the error bar: neither the doping in Bi nor the change of substrate has significant effect on M_s . These results are coherent with previous observations of Hansen et al²¹ on garnet ferrite (see III.A.2.2) showing that M_s for YIG and BiYIG remains the same at room temperature.

The magnetic anisotropy H_{Ku} is evaluated using in-plane FMR measurements (see Section VI-B.4) from the Kittel law fit of f_{res} vs $\mu_0 H_{res}$ for thin films :

$$f_{res} = \frac{g_l \mu_b}{h} \mu_0 \sqrt{H_{res} \cdot (H_{res} + M_{eff})} = \frac{\gamma \mu_0}{2\pi} \sqrt{H_{res} \cdot (H_{res} + M_s - H_{Ku})}. \quad VII-3$$

In our convention a positive value for the magnetic anisotropy H_{Ku} will favor an out-of-plane anisotropy.

In the Figure VII-10 we show the f_{res}^2 vs $\mu_0 H_{res}$ for $\mu_0 H_{stat}$ applied in the in-plane direction of the film for a 14 nm thick YIG//sGGG film. No dependance of $\mu_0 H_{res}$ with respect to the different in-plane cristalline axis could be measured, thus the in-plane field was not applied along a specific orientation. For each frequency f_{res} the in-plane static field $\mu_0 H_{stat}$ is swept, for $\mu_0 H_{stat} = \mu_0 H_{res}$ the measured signal can be fitted by an anti-lorentzian (see Section VI.B.4.2 and inset of Figure VII-10). From this fit we obtain $\mu_0 H_{res}$ for each f_{res} (square in Figure VII-10). Those experimental points are then fitted using the Kittel equation (dotted line in Figure VII-10) in order to obtain H_{Ku} .

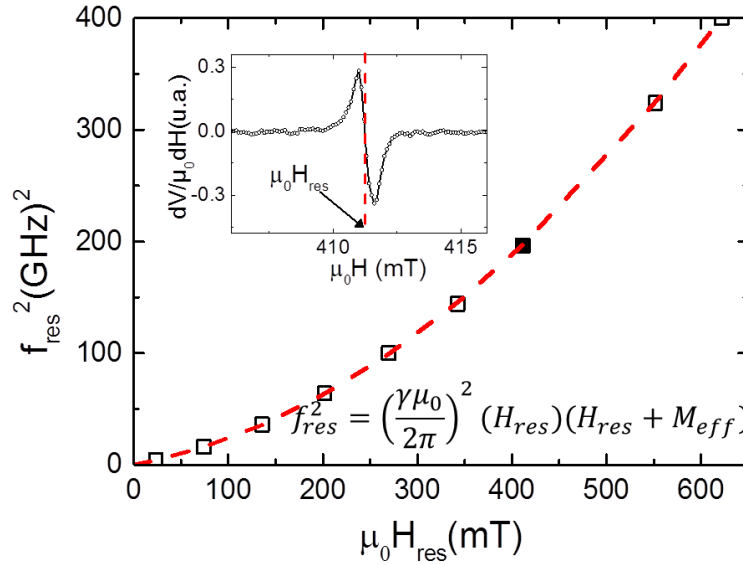


Figure VII-10 f_{res}^2 vs $\mu_0 H_{res}$ obtained for 14 nm YIG//sGGG from in-plane FMR experiment (squares) fitted with the Kittel law (dotted red line). From the fit it is possible to extract M_{eff} (bottom right equation). In top left we display a typical FMR resonant curve (corresponding to the black square) used to obtain H_{res} .

In the Table VII-5 we present values of M_{eff} obtained from FMR measurements and the anisotropy field H_{Ku} (derived from M_{eff} using M_s)

As shown in the Table VII-5 H_{Ku} changes sign depending on the substrate of growth and the Bi content:

- for $\text{Bi}_x\text{Y}_{3-x}\text{IG//sGGG}$ films with $x=0.7$ and 1 we observe positive values of H_{Ku} favoring PMA. Moreover because $H_{Ku} > M_s$ the magnetic anisotropy in those films is out-of-plane (the demagnetization term is compensated by H_{Ku}).
- for all other cases (GGG substrate and 1.5 Bi doping on sGGG substrate) H_{Ku} is negative and favors in-plane magnetic anisotropy or is not enough to compensate the shape anisotropy term. In those films we observe an in-plane easy magnetic axis.

To confirm the presence of PMA we will use Kerr microscopy in the polar mode, rather than the SQUID, and take advantage of the high BiYIG magneto-optical activity (see III.A.2.5). For the case of our BiYIG thin films, in which we consider only the uniaxial and shape anisotropy, the out-of-plane saturation field is written as:

$$H_{sat}^\perp = M_s - H_{Ku} \quad \text{VII-4}$$

Where H_{sat}^\perp the saturation field in the out-of-plane direction. The case of $H_{Ku} > M_s$ corresponds to thin films with PMA, a precise determination of H_{Ku} is not possible and H_{sat}^\perp corresponds to the coercive field only. For in-plane magnetized sample it is possible to estimate numerically H_{Ku} from H_{sat}^\perp .

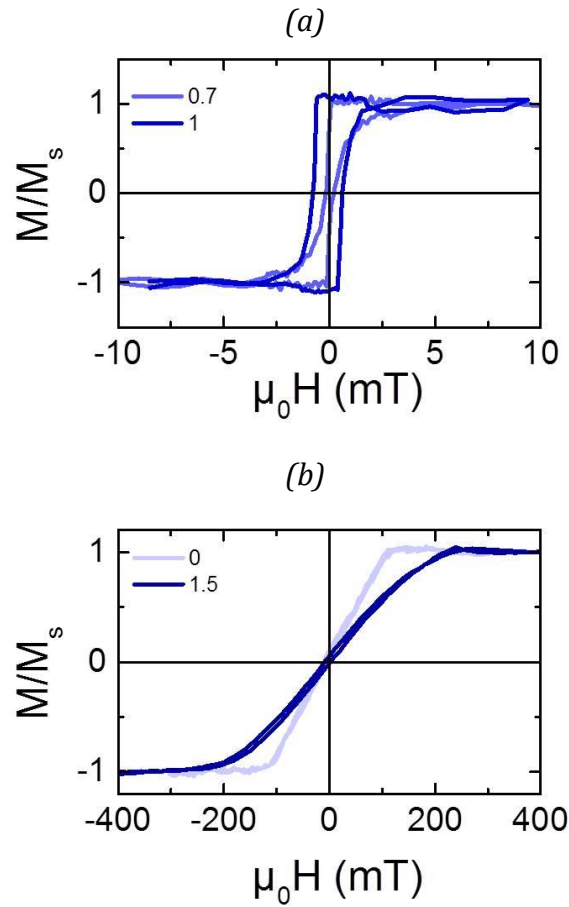


Figure VII-11 Hysteresis curves performed with Kerr microscope in the polar mode on $\text{Bi}_x\text{Y}_{3-x}\text{IG//sGGG}$ films. PMA, characterized by low saturation field and square shape hysteresis curve is observed for 0.7 and 1 Bi doping rate (a). For 1.5 or 0 doping rate in Bi sample are in plane magnetized and high field is required to saturate the sample in the out-of-plane direction(b).

The Figure VII-11 displays polar Kerr hysteresis curves results for sample grown on sGGG substrates. To have a clearer insight of the different anisotropies we divided it in two graphs:

- Figure VII-11(a) presents Kerr hysteresis curve for films with PMA observed on $\text{Bi}_x\text{Y}_{3-x}\text{IG//sGGG}$ films with $x=0.7$ and $x=1$. The saturation field below 10 mT corresponds to the coercive field of the sample. The presence of PMA in those films is coherent with data from Table VII-5 where $H_{Ku} > M_s$.
- Figure VII-11(b) shows Kerr hysteresis curves for YIG//sGGG and $\text{Bi}_{1.5}\text{Y}_{1.5}\text{IG//sGGG}$: for both cases the large value of $\mu_0 H_{sat}^\perp$ are characteristics of an in-plane magnetic anisotropy. For YIG//sGGG we observe that $\mu_0 H_{sat}^\perp (\sim 100\text{mT}) < \mu_0 M_s (\sim 170\text{mT})$ this is consistent the positive value of $\mu_0 H_{Ku} \approx 60\text{mT}$ obtained from FMR measurements in Table VII-5. For $\text{Bi}_{1.5}\text{Y}_{1.5}\text{IG//sGGG}$ H_{Ku} extracted from FMR measurements is negative, this is coherent with the values obtained from Kerr hysteresis curve: $\mu_0 H_{sat}^\perp (\sim 210\text{mT}) > \mu_0 M_s$.

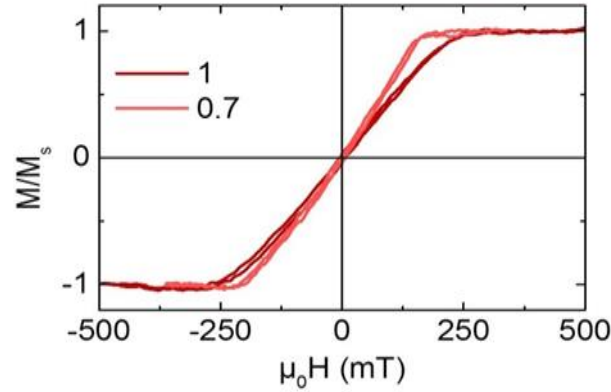


Figure VII-12 Hysteresis curves performed on Kerr microscope on $\text{Bi}_x\text{Y}_{3-x}\text{IG//GGG}$ films. In-plane magnetic anisotropy is observed for the Bi content $x=0.7$ and 1. The saturation field (so the strength of the in-plane magnetic anisotropy) is decreasing slightly with increasing Bi content.

For the case of BiYIG//GGG the Figure VII-12 shows that all samples are in-plane magnetized. The saturation field remains above $\mu_0 M_s$ and increases slightly with Bi content. This is coherent with $\mu_0 H_{Ku}$ values obtained from FMR measurements in Table VII-5 which are negative and increasing (in absolute value) with the Bi content. For YIG//GGG due to both easy in-plane magnetic axis and the low θ_F (compared to BiYIG) no hysteresis curve with Kerr polar mode could be performed.

Another proof of PMA is the presence of magnetic domains oriented in the out-of-plane direction for the remanent state.

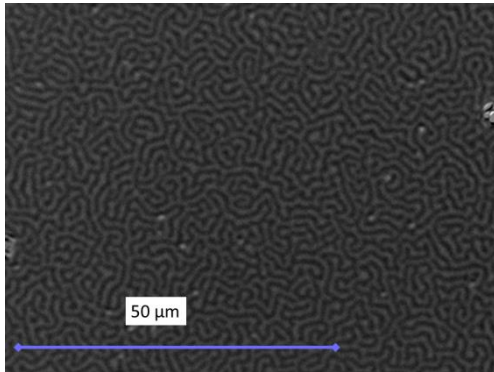
In the Figure VII-13 we present Kerr microscope images of magnetic domains present in BiYIG films with PMA (so $\text{Bi}_{0.7}$ and $\text{Bi}_1\text{YIG//sGGG}$). Those domains are μm -wide and can therefore be resolved with Kerr microscope.

It is possible to derive the domain wall energy σ from the domains width D_{width} using the Kooy et Heinz model¹⁴⁰. With nm-thick BiYIG films we are in the ultrathin film limit, defined by $\frac{t_{films}}{D_{width}} \ll 1$ (t_{film} being the thin film thickness), for which the model can be simplified to the one of ref¹⁴¹ (detailed in the Annexe I.C). In this ultrathin film regime D_{width} is predicted to be exponentially dependent on σ (and therefore on $\sqrt{K_u}$ due to Equation III-2) which makes D_{width} a very sensitive parameter to any variation of H_{Ku} . We now analyze the magnetic domains images with the help of the theory developed in ref¹⁴¹.

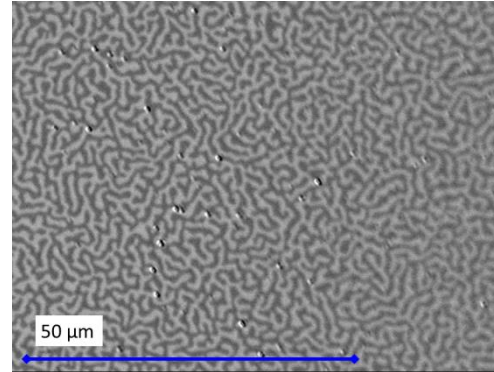
The Figure VII-13 shows the evolution of the magnetic domains width after demagnetization on $\text{Bi}_{0.7}\text{Y}_{2.3}\text{IG}$ and $\text{Bi}_1\text{Y}_2\text{IG}$ for different thin film thickness. We observe that:

- increasing the thin film thickness t_{film} leads to a decrease of D_{width} . For instance by decreasing the film thickness by a factor of 2 for $\text{Bi}_{0.7}\text{Y}_{2.3}\text{IG//sGGG}$ we multiply D_{width} by a factor of 6 (Figure VII-13(d-e)).
- For a given thickness D_{width} of the film is not the same depending on the Bi doping x . The trend observed is that for a given thickness $D_{width}^{x=0.7} > D_{width}^{x=1}$.

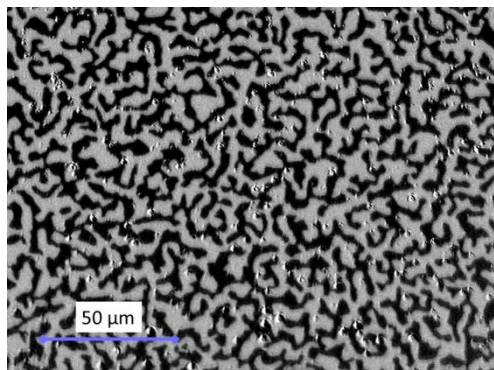
(a) $\text{Bi}_{0.7}\text{Y}_{2.3}\text{IG}/\text{sGGG}$
 $t_{\text{film}}=48 \text{ nm}$ $D_{\text{width}}=0.8\mu\text{m}$



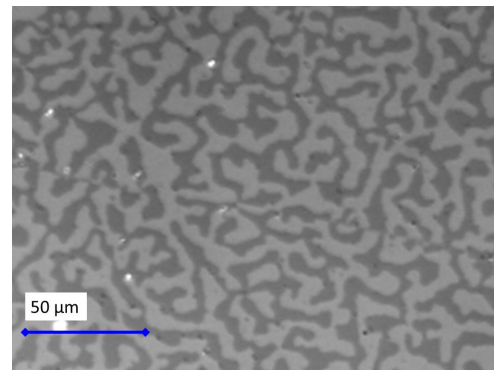
(d) $\text{Bi}_1\text{Y}_2\text{IG}/\text{sGGG}$
 $t_{\text{film}}=29 \text{ nm}$ $D_{\text{width}}=0.74\mu\text{m}$



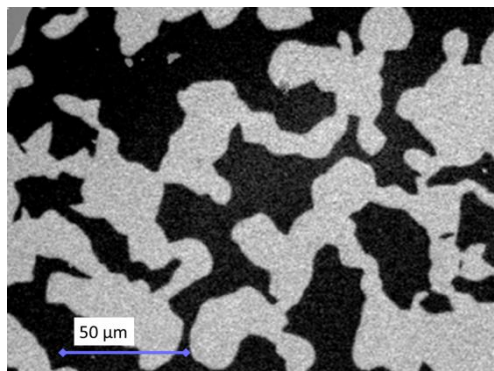
(b) $\text{Bi}_{0.7}\text{Y}_{2.3}\text{IG}/\text{sGGG}$
 $t_{\text{film}}=21 \text{ nm}$ $D_{\text{width}}=3.6\mu\text{m}$



(e) $\text{Bi}_1\text{Y}_2\text{IG}/\text{sGGG}$
 $t_{\text{film}}=16 \text{ nm}$ $D_{\text{width}}=4.2\mu\text{m}$



(c) $\text{Bi}_{0.7}\text{Y}_{2.3}\text{IG}/\text{sGGG}$
 $t_{\text{film}}=10 \text{ nm}$ $D_{\text{width}}>20\mu\text{m}$



(f) $\text{Bi}_1\text{Y}_2\text{IG}/\text{sGGG}$
 $t_{\text{film}}=15 \text{ nm}$ $D_{\text{width}}\sim 20\mu\text{m}$

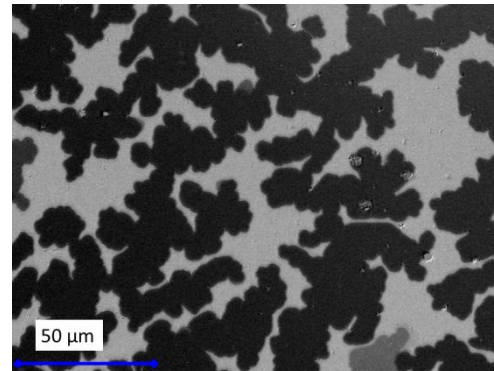


Figure VII-13 Evolution of D_{width} for different t_{film} of $\text{Bi}_x\text{Y}_{3-x}\text{IG}/\text{sGGG}$ films ($x=0.7$ (a-c) and 1(d-f)). D_{width} is reduced with increasing t_{film} as expected from the Kaplan and

Gehring model¹⁴¹ (presented in Annexe I.C). Moreover for $D_{width}^{x=0.7} \sim D_{width}^{x=1}$ (a-d)(b-e) we have $t_{film}^{x=0.7} > t_{film}^{x=1}$ due to a difference in anisotropy between the two doping rate.

The first observation is coherent with the model¹⁴¹ that predicts for ultrathin films: $D_{width} \propto \frac{1}{e^{t_{film}}}$ (see in Annexe I.C).

The second observation could be related to the difference in anisotropy between $Bi_{0.7}Y_{2.3}IG$ and Bi_1Y_2IG films found from FMR measurements. The Equation 0-9 in Annexe I.C shows that if both M_s and the exchange constant A does not depend on the Bi ratio for the same thickness of the film the inequality $D_{width}^{x=1} < D_{width}^{x=0.7}$ would imply that $K_{eff}^{x=1} < K_{eff}^{x=0.7}$.

If the magnetization has been measured to be unaffected by the Bi content x BLS measurements showed that it is not the case of the exchange stiffness which increases with increasing x ²⁸. Thus we can not relate certainly relate this observation with the variation of anisotropy measured from FMR.

It is however possible to give a rough estimation of the anisotropy field corresponding to the value of σ_{DW} derived for the two different Bi content ($x=0.7$ and 1) from the evolution of D_{width} with t_{film} (see the Annexe I.C). Combining Equation III-2 and III-6 it is possible to relate the absolute value of $\mu_0 H_{Ku}^\sigma$ to σ_{DW} if the exchange constant D_{ex} is known with the following formula:

$$\mu_0 H_{Ku}^\sigma = \frac{2K_{eff}}{M_s} = \frac{\sigma_{DW}^2}{8AM_s} = \frac{\sigma_{DW}^2}{4D_{ex}M_s^2} \quad VII-5$$

The literature provides measured values of D_{ex} for $Bi_xY_{3-x}IG$ of different Bi content x ($x=0.92, 0.54, 0.36, 0.14$ and $x=0$)²⁸. Those values present a quite linear evolution with the Bi content x thus, we infer the value of $D_{ex} = 7.44$ and $8.24 \cdot 10^{-17} \text{ T}\cdot\text{m}^2$ for $x=0.7$ and 1 respectively. The M_s value used corresponds to ours SQUID measurements (cf Table VII-5).

The value of $\mu_0 H_{Ku}^\sigma$ calculated from σ_{DW} are displayed in the last column of Table VII-5 and can be compared to the one obtained from FMR measurements (second column of Table VII-5).

We note that the evolution of $\mu_0 H_{Ku}^\sigma$ with the Bi content are in qualitative agreement with the FMR measurements meaning that : $\mu_0 H_{Ku}^\sigma(Bi_{0.7}Y_{2.3}IG) > \mu_0 H_{Ku}^\sigma(Bi_1Y_2IG)$. However the value of $\mu_0 H_{Ku}^\sigma$ is under estimated of about 50% compared to FMR measurements. This can be attributed to an overestimated value of D_{ex} and to the two different error sources coming from the experimental measurements. In Equation VII-5 the two error sources are:

- the error on σ_{DW} which is $\pm 10\%$ (see Annexe I.C).
- the error on M_s which is (at least) $\pm 10\%$.

The total error on $\mu_0 H_{Ku}^\sigma$ evaluated from σ_{DW} is about 30%. Thus the major error source leading to about 50% of difference between values estimated from FMR and from σ_{DW} seems to be related to the determination of D_{ex} in $BiYIG$ which is not surprising as two values for D_{ex} varying of about 50% can be found in the literature for the YIG (see Section III.A.1.3).

For thin films with PMA we could confirm the presence of PMA by a numerical estimation of the anisotropy field from FMR characterization and Kerr microscopy imaging of out-of-plane magnetic domains. However the absolute value does not converge the qualitative decrease in anisotropy with increasing Bi content can be observed in both cases.

	$\mu_0 M_s (mT)$	$\mu_0 M_{eff} (mT)$	$\mu_0 H_{Ku} (mT)$	$\sigma \left(\frac{mJ}{m^2} \right)$	$\parallel \mu_0 H_{Ku}^\sigma \parallel (mT)$ From VII-5
YIG//GGG	163	218	-56		
Bi _{0.7} Y _{2.3} IG//GGG	172	213	-41		
Bi ₁ Y ₂ IG//GGG	160	237	-78		
YIG//sGGG	163	102	61		
Bi _{0.7} Y _{2.3} IG//sGGG	179	-115	324	0.86	244
Bi ₁ Y ₂ IG//sGGG	173	-29	202	0.65	134
Bi _{1.5} Y _{1.5} IG//sGGG	162	245	-66		

Table VII-5 Sum up of the static magnetic parameters for Bi_xY_{3-x}IG films grown on different substrates. The M_s , M_{eff} , $\mu_0 H_{Ku}$ are obtained from SQUID and FMR measurements. The σ is derived from the domain width vs thickness evolution from the Kaplan and Gehring model and $\mu_0 H_{Ku}^\sigma (mT)$ is obtained from the equation VII-5) using σ

In this part we characterized the static magnetic properties of our samples and concluded that:

- the total magnetic moment is not modified by the doping in Bismuth or by the substrate of growth.
- in-plane or out-of-plane magnetic anisotropy can be observed in our films depending on the substrate of growth or the Bismuth concentration.

In the following part we focus on the magneto-optical properties of BiYIG films with PMA using Faraday rotation characterization.

VII-C.2 Magneto-optical properties.

Doping of YIG by Bismuth enhances the Faraday rotation (FR) and for the growth of Bi_xY_{3-x}IG epitaxial films by PLD¹³⁷ and LPE^{20,21} a linear increase of θ_F with Bi content x at 630 nm has been measured of:

- $\frac{\theta_F}{x} = -1.9^\circ/\mu m$ for PLD grown films.
- $\frac{\theta_F}{x} = -2.54^\circ/\mu m$ for LPE grown films.

Measurements of θ_F in Orsay performed at the LPS with J. Sampaio at 630 nm for our films grown on sGGG with $x=0.7$ and 1 Bi content showed an increase of: $\frac{\theta_F}{x} = -0.9^\circ/\mu m$.

Other measurements have been realized in Brest at the LABSTICC with Nathan Beaulieu, due to very low thickness of our films, the sensitivity of the FR measurement set up allow to extract θ_F in our films only at lower wavelength of $\lambda = 520nm$. Indeed in the IR-far UV wavelength range the FR of BiYIG is higher with decreasing λ ²⁰.

The Figure VII-14 presents the dependence of $-\theta_F$ $\lambda=520nm$ (FR of BiYIG is negative) to the film thickness ($t_{Bi_xY_{3-x}IG}$). The FR coefficient is normalized to the expected Bi content of the film (so the one of the target) for all $Bi_xY_{3-x}IG$ films ($x>0$) grown on the two different substrates.

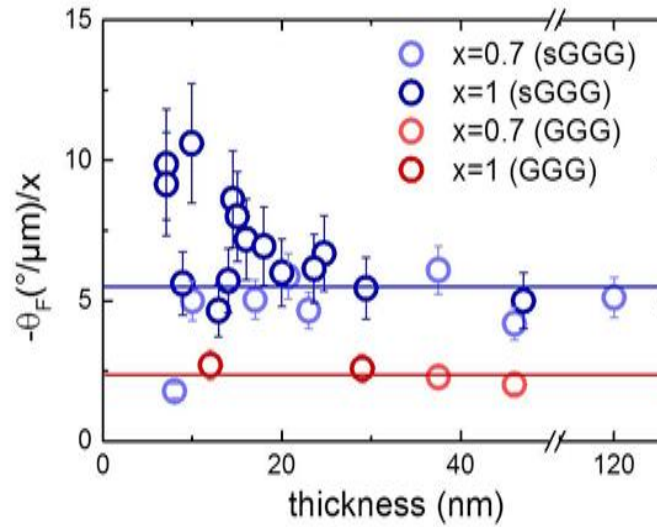


Figure VII-14 $-\theta_F$ $\lambda=520nm$ ($^{\circ}/\mu m$) per Bi content x in $Bi_xY_{3-x}IG$ films vs the film thickness. The solid line corresponds to the mean value obtained of $-\theta_F$ $\lambda=520nm$ for films grown on sGGG (blue) and GGG (red) substrate. The error bar is estimated to 20% on the value of θ_F .

We note that for films grown on the same substrate θ_F $\lambda=520nm$ normalized to the Bi content remains approximately the same within the error bar.

At 520 nm wavelength the averaged values of θ_F ($Bi_xY_{3-x}IG//sGGG$) and θ_F ($Bi_xY_{3-x}IG//GGG$) normalized to the Bi content x of the target (blue and red continuous line) are respectively $5.5 \frac{deg}{\mu m \cdot x}$ and $2.35 \frac{deg}{\mu m \cdot x}$.

The increase of θ_F with the nominal Bi content x suggests a rather efficient transfer of Bismuth from the target to the films which seems to be substrate dependent. This substrate dependency of θ_F could be due to the positive misfit substrate/target for the GGG substrate which could be less favorable than a negative misfit (case of sGGG) to include Bi within the unit cell. This FR characterization suggests that the Bi content within our films is increasing with the one of the target. This is coherent with our structural analysis that showed an increase of the film's lattice parameter a_0 with the Bi content of the target (Table VII-4). However from structural characterization only it is not possible to determine the origin of the increase in the lattice parameter which could be due also to the presence cation or oxygen off-stoichiometry⁹⁸. The FR characterization allows now to correlate the increase of a_0 with a higher Bi content^{16,20,33,37}.

VII-C.3 Dynamical magnetic properties.

Dynamical magnetic properties and magnetic losses (ΔH_0 and α) of the film can be extracted from FMR measurements using the broadening of the FMR peak (Equation III-40 and Section III.B.1.3).

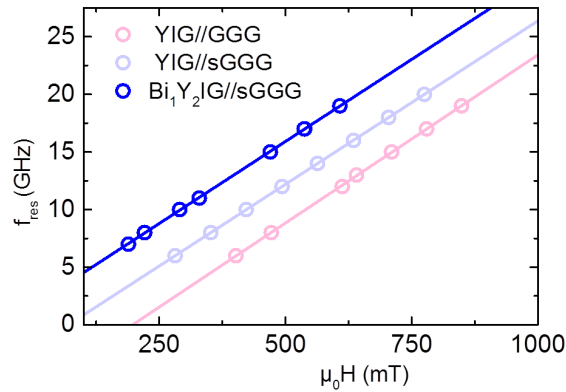
VII.C.3.1 Derivation of the Landé factor.

In Equation III-40 we need to determine the gyromagnetic constant $\gamma = \frac{g_L \mu_B}{\hbar}$ in which all variables are known except the Landé factor g_L which is related to the angular momentum of the electron. In the YIG magnetic Fe^{3+} ions involved in the resonant process have their orbital momentum quenched, thus the orbital momentum is zero and g_L used for YIG FMR experiments is the one of the free electron $g_L = g_{free\ electron} = 2.023$ ¹⁴². To guarantee that our FMR characterizations are correct it is essential to confirm that the value of $g_L = g_{free\ electron}$ remains valid for nm-thick BiYIG films.

To obtain g_L (from γ) we use out-of-plane FMR measurement ($H_{stat} \perp$ plane of the film) for which the Kittel law is written as:

$$f_{res} = \mu_0 \gamma (H_{res} - M_{eff}) \quad \text{VII-6}$$

(a)



(b)

	M_{eff} (kA/m)	$g_L (\pm 1\%)$
YIG//sGGG	50	2.03
YIG//GGG	156	2.08
Bi ₁ Y ₂ IG//sGGG	-46	2.04

Figure VII-15 (a) Out-of-plane FMR measurements on Bi₁Y₂IG//sGGG, YIG//GGG and YIG//sGGG to determine the g_L parameter using Equation VII-6. Two parameters are obtained from the fit: M_{eff} and g_L (b). The error bar corresponds to the one obtained from the fit.

The Figure VII-15(a) shows a linear dependence of f_{res} vs $\mu_0 H_{res}$ expected for out-of-plane FMR measurements for 20 nm thick YIG//GGG, YIG//sGGG, and BiYIG//sGGG films (Figure VII-15(a)). Using the linear fit we obtain γ and derive g_L (Figure VII-15(b)) using $\mu_B = 9.274 \cdot 10^{-24} \text{ J}\cdot\text{T}^{-1}$ and $\hbar = 6.626 \cdot 10^{-34} \text{ J}\cdot\text{s}$ ¹⁴².

The results obtained for g_L are differing at the maximum of 4% compared to the theoretical value of $g_L = 2.023$ which allow to use the theoretical value of $g_L = 2.0$ in the following FMR analysis of our films.

VII.C.3.2 FMR characterization for in-plane magnetized thin films.

The dynamical characterization of thin films presenting in-plane anisotropy ($\text{Bi}_x\text{Y}_{3-x}\text{IG//GGG}$ with $x=0, 0.7$ or 1 and $\text{Bi}_x\text{Y}_{3-x}\text{IG//sGGG}$ with $x=0$ and 1.5 .) is performed with in-plane FMR measurements ($H_{stat} \parallel$ film plane). At each excitation frequency f_{res} the FMR resonant curve is fitted with an anti-lorentian curve (red line in Figure VII-16) in order to extract the peak to peak linewidth $\mu_0\Delta H_{pp}$. From a linear fit of $\mu_0\Delta H_{pp}$ vs f_{res} (see Equation III-40) we obtain α and $\mu_0\Delta H_0$ for the case of in-plane magnetized films.

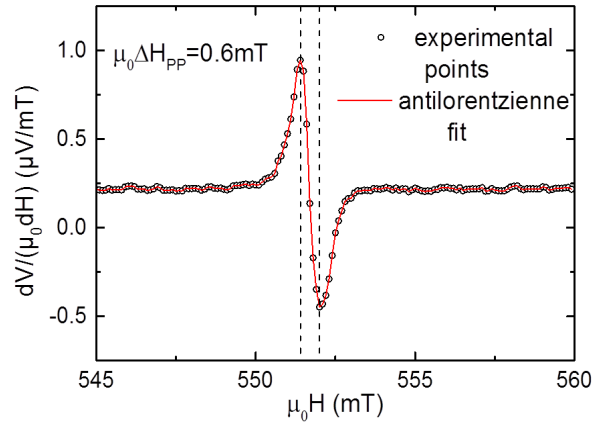


Figure VII-16 FMR absorption curve of 14 nm thick YIG//sGGG @ 20GHz. From experimental points (dots) we use an anti-lorentzienne fit (red line) to obtain the peak to peak linewidth $\mu_0\Delta H_{pp}$.

Experimental values and linear fit of $\mu_0\Delta H_{pp}$ vs f_{res} are shown in Figure VII-17 and the dynamical characteristics (α and $\mu_0\Delta H_0$) extracted from the fit are summed up in the Table VII-6.

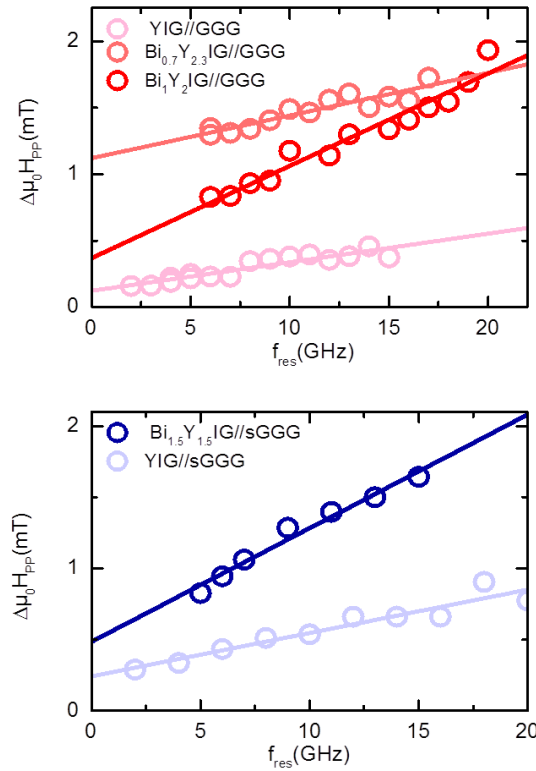


Figure VII-17 $\mu_0 \Delta H_{pp}$ vs f_{res} for in-plane magnetized BIYIG sample. Fitting the experimental point with the equation III-40 allows obtaining the Gilbert damping α and the inhomogeneous broadening $\mu_0 \Delta H_0$ (reported in Table VII-6).

Magnetic losses in our YIG//GGG thin films ($\alpha = 5 \cdot 10^{-4}$ and $\mu_0 \Delta H_0 = 0.12 \text{ mT}$) are comparable to the one obtained in thin films used to propagate spin wave or to induce auto oscillation^{103,112} (for instance the dynamical characteristics of thin films used for auto oscillators are: $\alpha = 2.3 \cdot 10^{-4}$ and $\mu_0 \Delta H_0 = 0.14 \text{ mT}$ ⁴⁶). These results indicate that our films are suitable for spintronic applications.

For YIG//sGGG dynamical properties (both α and ΔH_0) are not as good as the one of YIG//GGG (see Table VII-6). This increase of magnetic losses for YIG//sGGG could be due to the higher substrate/target misfit value for YIG//sGGG. This can favor impurities or defects formation and act as an extrinsic channel for magnetic relaxation¹⁴³ (see III-B.2).

As mentioned in the Section V.A.3.2, few attempts for PLD grown YIG films on different substrate have been made^{98,104–106,131}. Our results can be compared to the one reported in those studies. Over all different garnet substrate used instead of GGG (YAG^{104,131}, NdGG¹⁰⁶, SmGG¹⁰⁵) for the growth of YIG, the best dynamical properties are obtained for YIG//sGGG. Best values reported in the literature for those YIG//sGGG thin films are: $\alpha = 8.3 \cdot 10^{-4}$ and $\mu_0 \Delta H_0 = 1.26 \text{ mT}$ ¹⁰⁶, this remains higher than what is measured in our YIG//sGGG films ($\alpha = 7.4 \cdot 10^{-4}$ $\mu_0 \Delta H_0 = 0.24 \text{ mT}$). Thus even though changing the substrate of growth affects the dynamical quality of our films compared to growth on sGGG our values of damping are still below what was reported so far.

When the material is doped with Bismuth we observe an increase of both the Gilbert damping parameter and the inhomogeneous broadening term (see Table VII-6) and the increase of α follows the increase of Bi rate in the film. Even though dynamical losses are enhanced in our Bi doped films compared to the YIG one the values of $\mu_0 \Delta H_{pp}$ measured in our films remain

lower than the one reported in the literature for PLD grown or sputtered doped garnet (at 9 GHz $\mu_0\Delta H_{pp} = 10$ mT for sputtered TmIG¹⁴⁴, $\mu_0\Delta H_{pp} = 3$ mT for PLD grown MnYIG¹¹⁰, $\mu_0\Delta H_{pp} = 60$ mT for PLD grown BiIG²⁴).

The enhancement of the magnetic losses for Bi substituted films could be explained by different mechanisms. First, the doping in Bismuth is known to induce SOC (which is the reason of the increase of $\|\theta_F\|$ compared to the one of YIG for $\lambda = 0.5$ to $1\mu\text{m}$)^{16,40,145} due to overlapping of the Bi $6p$ and $6s$ orbitals with the Fe $3d$ and O $2p$. This hybridization can be demonstrated and derived from first principle calculation⁴⁰. Hybridization between those two orbitals is coupling the spin of electrons involved in the resonant process ($3d$ Fe electrons) to the orbital moment of the Bismuth and increases the SOC^{16,40}. This opens a new relaxation channel for the magnetic moment, that could enhance both extrinsic and intrinsic relaxation mechanisms (see Section III-B.3). Secondly, the misfit substrate/film is also increasing with the Bi content (especially for BiYIG on GGG substrate) this can contribute to extrinsic relaxation processes (in a similar way as for the case of YIG//sGGG).

	α	$\mu_0 \Delta H_0$ (mT)
YIG//GGG	$5 \cdot 10^{-4}$	0.12
Bi _{0.7} Y _{2.3} IG//GGG	$7.8 \cdot 10^{-4}$	1.1
Bi ₁ Y ₂ IG//GGG	$1.7 \cdot 10^{-3}$	0.37
YIG//sGGG	$7.4 \cdot 10^{-4}$	0.24
Bi _{1.5} Y _{1.5} IG//sGGG	$1.9 \cdot 10^{-3}$	0.48

Table VII-6 Dynamical parameters of in-plane magnetized Bi_xY_{3-x}IG films. Values are extracted from the fit of ΔH_{pp} vs f_{res} (obtained with in-plane FMR) using Equation III-40

We showed previously that changing the substrate or the Bi rate can change the magnetic anisotropy in the material making it more flexible for different applications, the figure of merit for a magnetic insulator in spintronic and magnonics is however the magnetic damping α . We characterized here dynamical properties of in-plane magnetized thin films presenting various anisotropies and showed that a change in anisotropy is leading to an increase of the magnetic losses in our films. Nevertheless they are better than what is reported in the literature and are therefore still suitable for spintronics and magnonics applications.

We present then the FMR characterization for thin films with PMA for which in-plane FMR can not be used to obtain a quantitative information on the magnetic damping.

VII.C.3.3 FMR characterization for out-of-plane magnetized thin films.

VII.C.3.3.1 In-plane FMR.

For thin films with PMA in-plane FMR is not suitable to obtain the Gilbert damping α . As displayed in the Figure VII-18 ΔH_{pp} does not follow the linear frequency dependence expected from Equation III-34, therefore the Gilbert damping cannot be extracted.

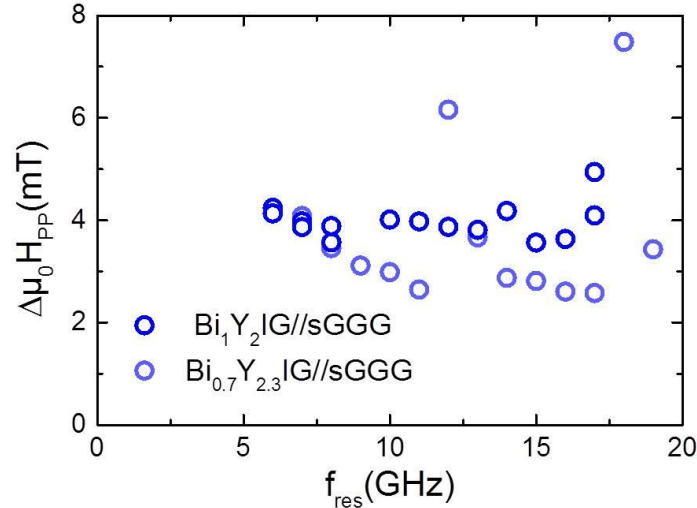


Figure VII-18 $\mu_0 \Delta H_{pp}$ vs f_{res} obtained from in-plane FMR for $\text{Bi}_{0.7}\text{Y}_{2.3}\text{IG}/\text{sGGG}$ (23 nm) and $\text{Bi}_1\text{Y}_2\text{IG}/\text{sGGG}$ (30 nm) with PMA. No linear dependence of $\mu_0 \Delta H_{pp}$ with the frequency is observed.

The two terms involved in the expression of the linewidth ΔH_{pp} are :

- the inhomogeneous contribution ΔH_0^{pp} .
- the Gilbert damping contribution which goes linearly with frequency.

If ΔH_{pp} is not frequency dependent this suggests that the term ΔH_0^{pp} is dominant over the Gilbert contribution for this geometry of excitation ($\mathbf{H}_{stat} \parallel \text{film plane}$). We need then to vary the geometry of excitation to eventually decrease the contribution of ΔH_0^{pp} in the linewidth.

VII.C.3.3.2 Investigation of ΔH_0^{pp}

To vary ΔH_0^{pp} and keep the damping contribution constant, we fix the excitation frequency at 8 GHz and vary the out-of-plane angle of the static FMR field on a 30 nm thick $\text{Bi}_1\text{Y}_2\text{IG}/\text{sGGG}$ presenting PMA.

The Figure VII-19(a) shows the variation of $\mu_0 \Delta H_{pp}$ vs θ at $f_{res} = 8$ GHz in this film. The magnitude of $\mu_0 H_{sat}$ necessary to induce resonance in those films is typically from 200 to 300 mT, which is enough to ensure that $\mathbf{M} \parallel \mathbf{H}_{stat}$.

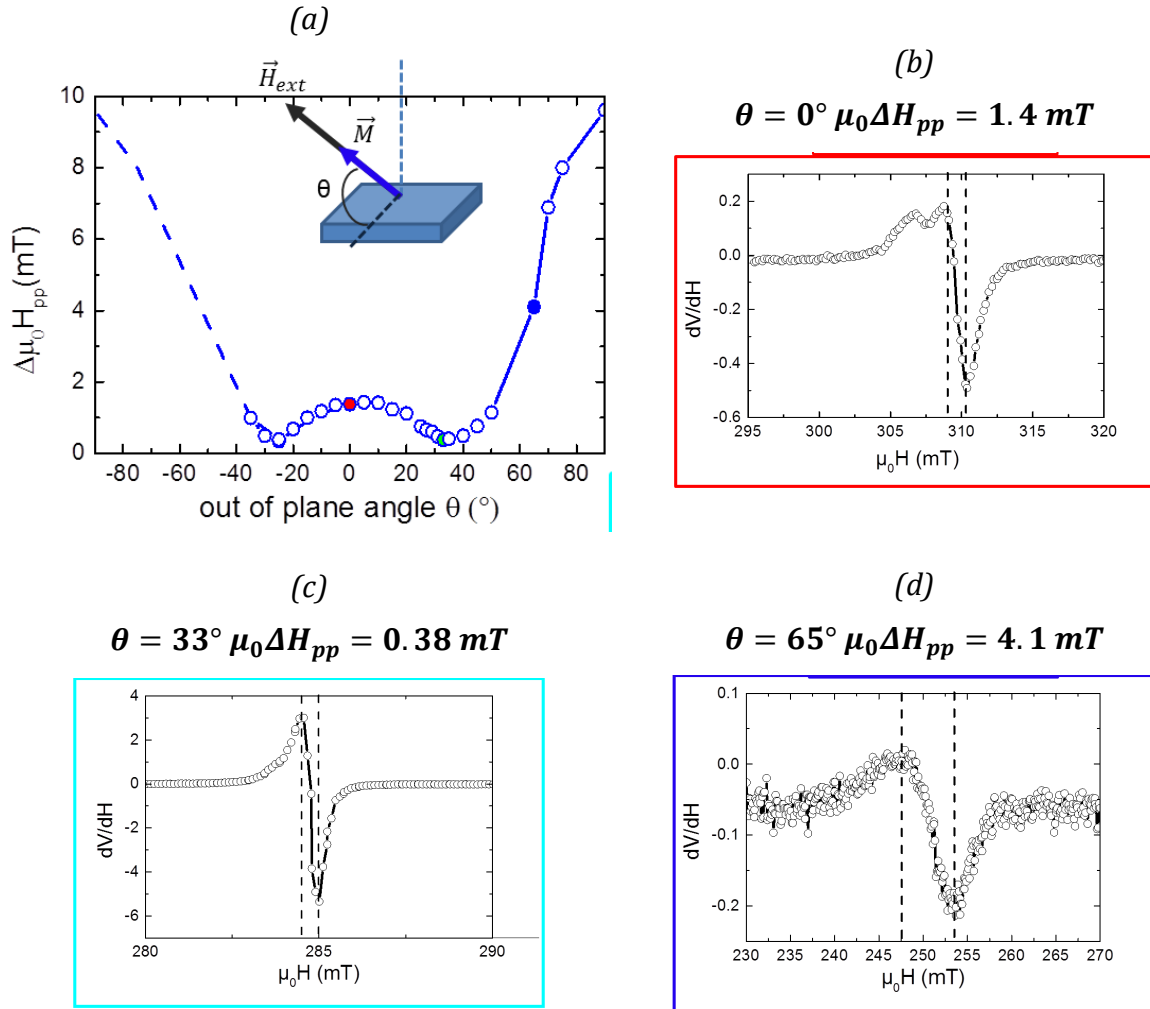


Figure VII-19 (a) Evolution of $\mu_0 \Delta H_{pp}$ vs θ for an excitation frequency of 8 GHz (see top sketch for the geometrical definition of θ), (b-d) FMR absorption curve for different values of θ (colored in the graph) with the respective values of $\mu_0 \Delta H_{pp}$. A clear dependence of $\mu_0 \Delta H_{pp}$ due to the inhomogeneous contribution with θ is observed

The plot of Figure VII-19(a) evidences a large angular dependence of the magnetic losses in the sample: $\mu_0 \Delta H_{pp}$ can be multiplied by more than 10 (Figure VII-19(b and d)) depending on the excitation geometry. For an out-of-plane angle $\theta_{min} = 33^\circ$, $\mu_0 \Delta H_{pp}$ is minimal and equal to 0.38 mT (Figure VII-19(c)). As the frequency of excitation is fixed the damping contribution part in the linewidth is fixed as well and the discrepancy in $\mu_0 \Delta H_{pp}$ is coming from the inhomogeneous broadening term $\mu_0 \Delta H_0^{pp}$, only. This suggests that depending on the excitation geometry the contribution of the term $\mu_0 \Delta H_0^{pp}$ in the overall linewidth will be different and that it will eventually dominate over the damping contribution.

After evidencing the angular dependence of $\mu_0 \Delta H_0^{pp}$ contribution we investigate its frequency dependence. Thus, for different frequencies of excitation, we varied θ of 30° around the value of $\theta_{min} = 33^\circ$ (minimizing $\mu_0 \Delta H_{pp}$ at 8 GHz) and measured the evolution of $\mu_0 \Delta H_{pp}$ with θ . This variation of $\mu_0 \Delta H_{pp}$ vs θ at 8, 9, 12, 13 and 14 GHz is shown in Figure VII-20.

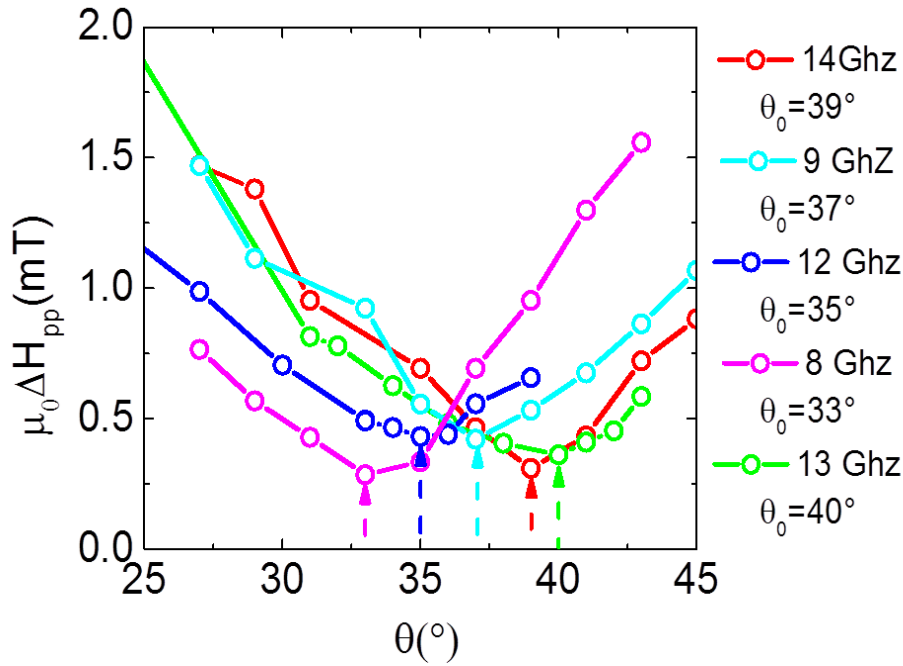


Figure VII-20 Evolution of the linewidth with θ for different frequencies of excitation. The angle giving the minimum value for $\mu_0\Delta H_{pp}$ (written in the legend below the corresponding excitation frequency) is labelled with an arrow on the graph.

The smallest linewidth $\mu_0\Delta H_{pp}^{min}$ at each frequency is labeled with an arrow and the corresponding angle θ_0 is given in the legend below each frequency. We note that those angles are different for each frequency: the inhomogeneous contribution is both angular and frequency dependent.

Now we evidenced that the magnitude of ΔH_0^{pp} has both an angular and a frequency dependence we can determine the value of the magnetic damping α .

VII.C.3.3.3 Damping calculation.

We first evidenced that the magnitude of the ΔH_0^{pp} term is detrimental to obtain the damping parameter for in-plane FMR. Then we experimentally demonstrated that the magnitude of this inhomogeneous broadening term is both angular and frequency dependent: $\Delta H_0^{pp} = \Delta H_0^{pp}(\theta, f)$.

We just say few words on the ΔH_0^{pp} frequency dependence which is contradictory with the expression of the damping equation (see Equation III-40) where it appears as a constant term. However it contains at least on frequency related relaxation process: the two magnon scattering which explains why we can express it $\Delta H_0^{pp}(f)$. But this dependence is quite complex (involving the spin wave dispersion relation and spin wave density of states) it can therefore not be explicitly written and is omitted in the linewidth expression. In our case it is necessary to take this frequency dependence to be completely accurate.

As we know which are the two parameters necessary to minimize the inhomogeneous broadening contribution we can determine the Gilbert damping: $\Delta H_\alpha^{pp} = \frac{2}{\sqrt{3}} \frac{\alpha 2\pi f}{\gamma \mu_0}$. This can be done using measurements of Figure VII-20 : we select for each frequency ΔH_{pp}^{min} which corresponds to a minimized contribution of the ΔH_0^{pp} parameter. In these conditions the

damping contribution is likely to be dominant over ΔH_0^{pp} and it should then be possible to extract its value. The expression of the linewidth is:

$$\Delta H_{pp}^{min}(\theta_0) = \Delta H_0^{pp}(\theta_0) + \frac{2}{\sqrt{3}} \frac{2\pi\alpha f}{\gamma} \quad \text{VII-7}$$

With $\Delta H_0^{pp}(\theta_0)$ the inhomogeneous contribution in the minimized geometry of excitation corresponding to the frequency f .

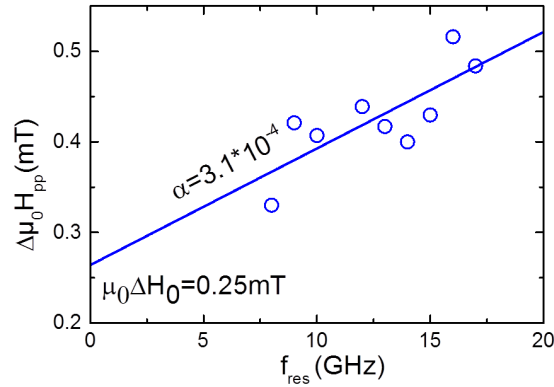


Figure VII-21 Evolution of $\Delta H_{pp}(\theta_0)$ vs frequency with θ_0 being the angle that minimizes the linewidth. In this case we observe the linear dependence of the linewidth with the frequency of excitation and using Equation III-40 it is possible to obtain the Gilbert damping and the minimal value of the inhomogeneous broadening term $\Delta H_0(\theta_0)$.

The plot $\mu_0\Delta H_{pp}(\theta_0)$ vs f is displayed in Figure VII-21 and magnetic losses of the film can be derived from this plot:

- The Gilbert damping α derived from the linear fit is $\alpha=3.1\cdot 10^{-4}$. It is comparable (and even better!) to what is measured for our YIG//GGG films(see Table VII-6).
- The inhomogeneous broadening term corresponds to the average of $\Delta H_0^{pp}(\theta_0)$ over the different frequency. We obtain $\mu_0\Delta H_0^{pp}=0.25\text{mT}$ which is comparable to values obtained for YIG//GGG thin films.

This study shows that even though in the in-plane geometry of excitation $\mu_0\Delta H_{pp}$ in those PMA films is quite high ($\sim 4\text{mT}$) the intrinsic magnetic losses corresponding to Gilbert contribution are comparable to the one of undoped YIG films.

VII.C.3.3.4 Discussion on the inhomogeneous contribution for films with PMA.

In the section III.A.1.6 we mentioned that the inhomogeneous broadening contribution can have different origins which are:

- a spread of the magnetic properties
- the scattering of the FMR mode on magnetic inhomogeneities.

These two contributions are giving rise to the strong anisotropic behavior of $\mu_0\Delta H_0^{146-150}$.

The spread of the magnetic properties (first origin) within the film modifies the effective magnetic moment $\mu_0 M_{eff}$ which is then written $\mu_0(M_{eff} + \Delta M_{eff})$. FMR curves presented in the Figure VII-20(b-d) shows clearly that the shape of $\mu_0\Delta H_{pp}$ varies strongly with the out-of-plane excitation angle, for certain angle of excitation we can even distinguish two resonant

peaks (Figure VII-20 (b)) which evidences the spread in the magnetic properties ΔM_{eff} giving rise to two different values of the resonant field.

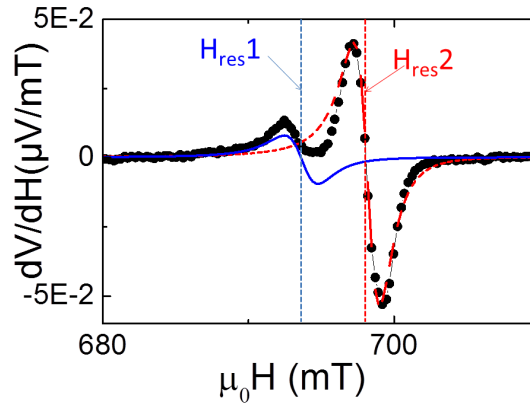


Figure VII-22 FMR curve fitted with two resonant condition for $f_{res}=20\text{GHz}$ for in-plane FMR. Two resonant field H_{res} can be obtained

To estimate the spread ΔM_{eff} we used in-plane geometry of excitation for which it is possible to fit separately two resonant peaks with two different resonant conditions H_{res1} and H_{res2} as shown in the Figure VII-22

We repeat this 'double fitting' procedure for different frequencies with $H_{stat} \parallel$ film (in-plane FMR). For each frequency we obtain then two different resonant conditions: H_{res1} and H_{res2} . We note that the difference in field between H_{res1} and H_{res2} is frequency dependent (Figure VII-23).

We then can fit separately H_{res1} vs f_{res} and H_{res2} vs f_{res} using the in-plane Kittel law fit and we obtain M_{eff1} and M_{eff2} (see Figure VII-23). The spread in magnetic properties of the sample in terms of effective magnetic moment is then:

$$\mu_0 \Delta M_{eff} = \mu_0 (M_{eff1} - M_{eff2}) = 6\text{mT}.$$

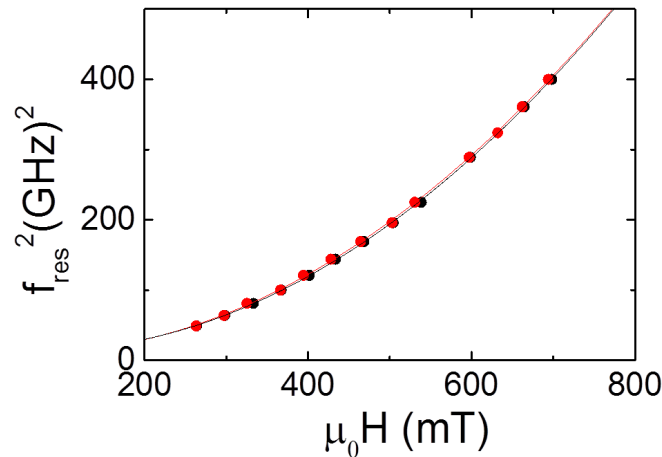


Figure VII-23 Fit of the two resonant field $\mu_0 H_{res1}$ and $\mu_0 H_{res2}$ using the in-plane Kittel law.

The contribution of the magnetic inhomogeneities in the linewidth is written¹⁴⁷:

$$\Delta H_0^{inhomo} = \frac{\partial H_{res}}{\partial M_{eff}} \Delta M_{eff} \quad \text{VII-8}$$

For the special case of in-plane excitation geometry it can be shown (see Annexe I.D) that ΔH_0^{inhomo} is frequency independent: $\mu_0 \Delta H_0^{inhomo} \sim \mu_0 \frac{\Delta M_{eff}}{2} = 3\text{mT}$. This corresponds typically to the order of magnitude $\mu_0 \Delta H_{pp}$ measured from in-plane FMR for thin films with PMA (Figure VII-18). This confirms that, for in-plane FMR excitation, the constant value of ΔH_{pp} is due to the inhomogeneous contribution ΔH_0^{inhomo} . We note that this value is about 10 times larger than the smallest obtained linewidth for out-of-plane angle of the static field $\theta \sim 30^\circ$ considering the difference in magnitude it is not surprising that we could not extract the damping contribution in this geometry of excitation.

We demonstrated that a proper geometry of excitation is necessary to obtain α due to magnetic inhomogeneities in the sample and that the observation of the Section VII.C.3.3.1 are due to the strong contribution of ΔH_0^{inhomo} for in-plane geometry of excitation.

VII-D Discussion on the magnetic anisotropy in BiYIG films.

In this part we will discuss on the origin of the magnetic anisotropy within our films.

VII-D.1 Anisotropy terms.

We first review the different anisotropy terms and how they are determined.

The effective magnetic anisotropy (K_{eff}) defines the easy magnetic axis within the sample it is determined from FMR measurement. A positive (negative) effective anisotropy corresponds to out-of-plane (in-plane) direction for the easy magnetic axis.

If we neglect the cubic term due to the magnetocrystalline anisotropy (which is small compared to the other uniaxial term in ultrathin films of BiYIG and YIG as we saw in the part III.A.1.4, III.A.2.3 and III.A.3.2) K_{eff} is written:

$$K_{eff} = K_u + K_{shape} \quad VII-9$$

With K_u the uniaxial magnetic anisotropy and $K_{shape} = \frac{-\mu_0 M_s^2}{2}$ the shape anisotropy term for thin films (see Section III.A.3.2).

The term K_{shape} is derived from SQUID measurements; it is therefore defined within at least 20% (due to the SQUID uncertainty). The term K_u is the total uniaxial anisotropy and is obtained from K_{eff} and K_{shape} .

For YIG and BiYIG films under epitaxial strain we saw (in Sections III.A.1.4, III.A.2.3 and III.A.3.2) that the total uniaxial anisotropy is the sum of two contributions : K_{growth} and K_{MO} .

- the magneto elastic term K_{MO} is due to epitaxial strain
- the growth induced anisotropy term K_{growth} is due to preferential ordering of certain ions within the different sites in the structure.

The magneto elastic contribution K_{MO} can be derived from Equation III-3 and III-13. For a strain along the [111] crystalline axis it is written:

$$K_{MO} = \frac{3}{2} \lambda_{111}(Bi_x Y_{3-x} IG) \left(\frac{E}{1-\mu} \right) \left(\frac{(a_0 - a_{substrate})}{a_0} \right) \quad VII-10$$

with $\lambda_{111}(Bi_x Y_{3-x} IG) = -2.89 * 10^{-6} (1 + 0.75x) \frac{J}{m^3}$ the magnetostriction constant along the (111) axis for $Bi_x Y_{3-x} IG$ epitaxial films⁴⁵ (which is slightly different than for the bulk) and a_0 the lattice parameter of the relaxed structure (can be found in Table VII-4). Values of K_{MO} derived from structural data of Table VII-4 using the Equation VII-10 are found in Table VII-7.

The rest of the uniaxial anisotropy contribution is attributed to the growth induced anisotropy term: $K_{growth} = K_u - K_{MO}$. Thus, it is defined with the same error range as K_u : 20% and is also shown in Table VII-7.

Values of the different anisotropy terms in Table VII-7 are also gathered in the chart of the Figure VII-24 in order to compare the magnitude.

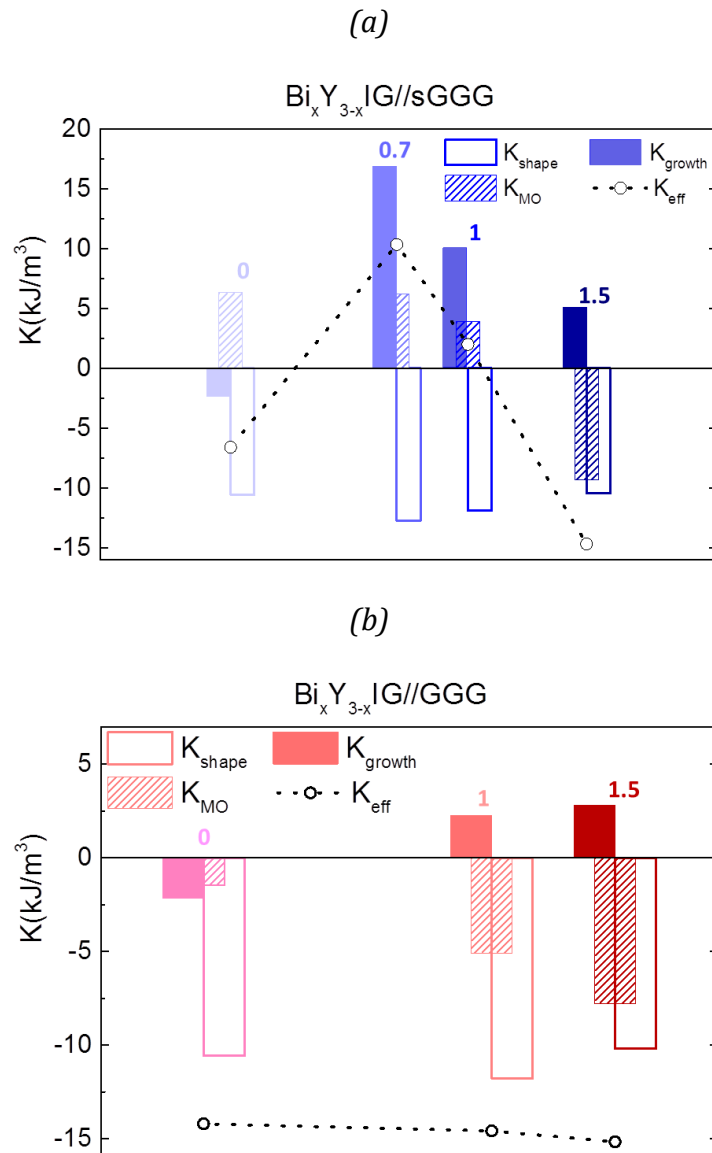


Figure VII-24 Different anisotropies contributions for $\text{Bi}_x\text{Y}_{3-x}\text{IG}$ films on sGGG (a) and GGG(b) substrates. The Bi content x is displayed on the top of each chart.

Now all different anisotropy terms are defined we discuss their origin, their magnitude and their dependences on the structure and the Bi content within the film.

VII-D.2 Origin of the different anisotropy in our films .

In all our thin films the overall magnetization is roughly the same which makes the value of K_{shape} almost constant. As we observed different anisotropy in our BiYIG films the two terms, K_{growth} and K_{MO} , defining the uniaxial anisotropy, have to be dependent either on the Bi content or the substrate of growth.

VII.D.2.1 Role of the magneto elastic contribution.

The magneto-elastic term is related to the epitaxial strain in our thin films. As a consequence it can be either positive or negative depending on the sign of $a_{substrate} - a_0$.

For thin films grown under compressive strain $a_{substrate} - a_0 < 0$ the magneto elastic contribution (K_{MO}) will favor in-plane magnetic anisotropy and will add to the shape anisotropy term K_{shape} .

For thin films grown under tensile strain ($a_{substrate} - a_0 > 0$). K_{MO} becomes positive and favors PMA. However if we compare the value of K_{shape} and K_{MO} in the Table VII-7 (3rd and 1st column) we see that the magnitude of K_{MO} is not sufficient to fully compensate K_{shape} (K_{MO} is at most 36% of K_{shape}) even when observe PMA.

Due to the latter observations we conclude that K_{growth} has to play a predominant role in the determination of PMA in our thin films. We discuss this term below.

VII.D.2.2 Growth induced anisotropy.

In the Table VII-7, we notice that K_{growth} has different signs and magnitude depending on whether the material is doped or not in Bismuth. For Bi doped films: $K_{growth} > 0$ and for undoped films YIG: $K_{growth} < 0$.

For the case of YIG films the presence of K_{growth} seems surprising as there are no doping (the origin of K_{growth} for the case of BiYIG films detailed in the part III.A.2.4.1). The presence of growth induced anisotropy in PLD grown YIG has already been reported by Manuilov et al¹⁵¹. This negative value for K_{growth} have been attributed to a Fe^{3+} deficiency electrically compensated by O^{2-} . In that case the chemical formula of the non-stoichiometric YIG structure is written:



Here the deficiency in Fe^{3+} can be considered as a substitution by O^{2-} diamagnetic ions and the growth induced anisotropy comes from preferential ordering of those vacancies.

In that case the value of K_{growth} does not depend on the growth substrate (the difference between $K_{growth}^{YIG//GGG}$ and $K_{growth}^{YIG//sGGG}$ is within the 20% of uncertainty in K_{growth} due to SQUID error), it is not dependant on the strain within the material. As it is negative it will stabilize the in-plane anisotropy which is already present for thin films.

For the case of BiYIG a positive K_{growth} is observed varying from 1 to 16 kJ/m³ depending on the substrate of growth, both magnitude and sign are coherent with what was previously observed in LPE grown BiYIG films (see III.A.2.4.1). Contrary to the case of YIG thin films the strain (tensile or compressive) seems to play an important role in the magnitude:

- for the case of growth under compressive strain $K_{growth} < 2$ kJ/m³.
- for the case of growth under tensile strain $K_{growth} > 10$ kJ/m³.

Such dependence could be explained by the fact that the type of deformation within the film will favor or not a preferential ordering of the Bi^{3+} ions (which is at the origin of K_{growth}). This assumption could be confirmed using atomic resolved structural analysis (TEM, EELS).

As we presented now how the different uniaxial anisotropy terms (K_{MO} and K_{growth}) vary with the strain and the Bi doping we can now conclude on the origin of the two different anisotropies present in our films.

VII-D.3 Conclusion on the origin of the anisotropy.

We define here the origin of the anisotropy and determine the relevant parameters to play on if we want to stabilize PMA or in-plane magnetic anisotropy.

For YIG thin films we observe only in-plane magnetic anisotropy. Indeed the combination of a negative K_{growth} with a magneto elastic term that will not compensate K_{shape} can not lead to PMA. Due to the negative sign of K_{growth} (which is set by the type of atoms that are substituted and the growth direction³⁰) the value of K_{eff} for the YIG thin films will always be negative and the term K_{MO} can slightly tune K_{eff} by being positive or negative but will never bring PMA. For YIG films we can estimate the value of the misfit necessary to obtain PMA with K_{MO} only using the Equation VII-10 and the values of Table VII-7 to estimate the different contribution:

- $K_{shape} \sim -10 \text{ kJ}\cdot\text{m}^{-3}$
- $K_{shape} \sim -3.7 \text{ kJ}\cdot\text{m}^{-3}$

The misfit to obtain compensation of both terms with epitaxial strain would then be $\sim -1.4\%$. This would require the use of a garnet substrate with lattice parameter of at least 12.55 \AA and no garnet substrates with such high lattice parameters are available. Moreover such high misfit values would favor even more defects and would eventually increase the growth induced contribution making the compensation even harder.

For BiYIG films the sign of K_{growth} will always favor PMA however to stabilize this PMA the magnitude of the growth induced term is important. We note that for thin films with the same nominal Bi rate thin films grown under compressive strain present a K_{growth} which is 5 to 8 times smaller than for films grown under tensile strain. As it is not possible to obtain PMA with too small values of K_{growth} the strain plays a major role to obtain PMA.

In YIG films we conclude that anisotropy is in-plane, and slightly tunable with epitaxial strain. The magnetic anisotropy in Bi doped ultrathin films is defined by the strain through the magneto elastic term and by the preferential ordering of Bi atoms through the growth induced term. The magnitude of this latter seems to be somehow related to the type of strain and high values of K_{growth} necessary to obtain PMA requires a growth under tensile strain. Therefore in our BiYIG films the anisotropy can be defined by the strain and the Bi doping rate through the growth induced term mostly. Interestingly the PMA in BiYIG films comes from the contribution of two terms does not requires too high values of misfits (that would be necessary if only K_{MO} would contribute). This allows obtaining PMA in low doped YIG films and to crystallize a material which has dynamical properties as good as the one of the undoped one.

	Thickness (nm)	$K_{MO}(\frac{kJ}{m^3})$	$K_u(\frac{kJ}{m^3})$	$K_{shape}(\frac{kJ}{m^3})$	$K_{growth}(\frac{kJ}{m^3})$	$\frac{K_{MO}}{K_{shape}}(\%)$
YIG//GGG	20	-1.48	-3.63	-10.57	-2.15	
Bi _{0.7} Y _{2.3} I _G //GGG	42	-5.08	-2.81	-11.77	2.27	
Bi ₁ Y ₂ I _G //GGG	30	-7.77	-4.97	-10.19	2.80	
YIG//sGGG	20	6.31	3.96	-10.57	-2.35	48
Bi _{0.7} Y _{2.3} I _G //sGGG	42	6.21	23.08	-12.75	16.87	36
Bi ₁ Y ₂ I _G //sGGG	30	3.88	13.90	-11.91	10.02	15
Bi _{1.5} Y _{1.5} I _G //sGGG	22	-9.35	-4.25	-10.44	5.10	

Table VII-7 Sum up of the different anisotropy contribution within the different films

VIII Spintronic applications with BiYIG.

Using PLD it is possible to elaborate a magnetic insulator with tunable anisotropy and low magnetic damping. The next step for BiYIG films is then to be used in magnon-spintronic devices on the same fashion as the YIG.

In this section we present Pt/BiYIG bilayers in the context of spintronic applications. First of all the effect of Pt deposition on the magnetic properties of BiYIG thin films is discussed. Then we present different spintronic phenomena observed in those bilayers :

- Spin Hall Effect on Pt/Bi_{1.5}Y_{1.5}IG/sGGG.
- Spin Hall Magnetoresistance on Pt/Bi₁Y₂IG/sGGG.
- Anomalous Hall Effect on Pt/Bi₁Y₂IG/sGGG.

Those effects are demonstrating the presence of a spin current flowing at the interface between the two materials and proving that BiYIG is a suitable MI for spintronic applications. In the last part we present charge current generated auto-oscillations in Pt/BiYIG and show that it is also possible to generate spin waves from auto-oscillations.

VIII-A Effect of Pt on the magnetic characteristics of BiYIG films.

Before we present spintronic measurements, it is important to evaluate if the presence of Pt modifies the BiYIG's structural or magnetic properties in Pt/BiYIG bilayers.

VIII-A.1 Magnetic anisotropy with Pt on in-plane magnetized sample.

Magnetic properties of in-plane magnetized thin films with and without Pt top layer are determined using FMR in the in-plane geometry. Using the Kittel law (Equation VII-3), we obtain the effective magnetization M_{eff} . Figure VIII-1 presents results of FMR on Bi_{1.5}Y_{1.5}IG(20 nm)//sGGG with and without 6 nm Pt top layer deposited by sputtering. The two different values of M_{eff} , extracted from the Kittel law fit (continuous line), shows that in presence of Pt top layer the effective field is increased of 33 kA/m.

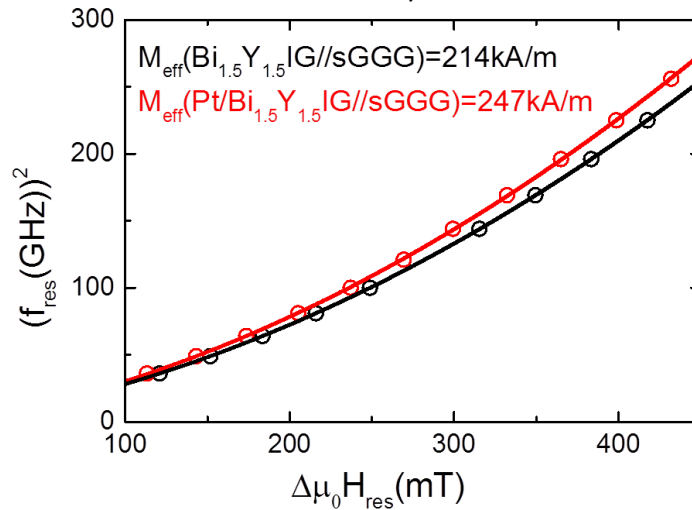


Figure VIII-1-(a) In-plane FMR for Pt/Bi_{1.5}Y_{1.5}IG//sGGG (23 nm), M_{eff} values extracted from the Kittel law fitting. Continuous line represent the Kittel law fit and dots are the experimental points.

The increase in M_{eff} can be attributed to a modification of either M_s or H_{Ku} . No modification in the M_s (within the 10% error bar) has been measured with SQUID for the case of sample with Pt top layer, thus the modification in M_{eff} is attributed to a change in anisotropy. This modification corresponds however to only 15% of the initial effective field $\mu_0 M_{eff}(\text{Bi}_{1.5}\text{Y}_{1.5}\text{IG})$ moreover it is a positive term which strengthen the initial in-plane easy magnetic axis in Bi_{1.5}Y_{1.5}IG//sGGG.

From in-plane FMR characterisation it is possible to estimate a decrease of anisotropy by 40 mT when Pt is deposited on in-plane magnetized thin films. This effect does not lead to a significant change in the magnetic behavior of the sample (in-plane easy axis is preserved). We will now see how the Pt affects thin films with positive H_{Ku} and PMA.

VIII-A.2 Effect of Pt on BiYIG films with PMA.

For thin films with PMA it is possible to quantify a change in magnetic anisotropy due to Pt with Kerr microscopy technique and magnetic domains imaging. As mentioned in Section VII-C.1, and detailed in the Annexe I.C, in the case of ultrathin films the size of magnetic domains in the film at remanance (D_{width}) depends exponentially on $\sqrt{K_{eff}}$ (see Equation 0-10). As for the case of BiYIG with different doping level we will quantify the potential change in anisotropy induced by the Pt top layer using D_{width}

The Figure VIII-2 (a-c) displays a Kerr microscopy image of a 16 nm thick Bi₁Y₂IG//sGGG sample at remanance on which 3 nm thick Pt has been deposited. From Figure VIII-2 (a) and (c) we see a clear decrease of D_{width} when Pt is deposited. This decrease of D_{width} when the sample is covered with Pt is even more striking on the Figure VIII-2 (b) where we can see both the Pt covered and uncovered part (half of the sample was protected during the sputtering).

In the table of Figure VIII-2(d) are displayed the value of :

- D_{width} obtained from 2D FFT on the Kerr microscope images
- the parameter σ derived using the model of Annexe I.C
- the effective anisotropy field $\mu_0 H_{eff} = \frac{2K_{eff}}{M_s}$ calculated from σ with the Equation III-2.

The evaluation of D_{width} by FFT confirms the drastic decrease of the domains size for Pt covered sample (divided by almost a factor of 2) which corresponds to a diminution of 20% for σ_{DW} .

This decrease of σ can be attributed to :

- a modification of K_{eff} (Equation III-2).
- the presence of an interfacial Dzyaloshinskii-Moriya Interaction (DMI) term (see Annexe I.E).

By performing k wave vector resolved BLS measurements in Paris 13 (presented in the Annexe I.E) the presence of DMI could be excluded. Hence the modification of σ_{DW} is attributed to a change in K_{eff} (via $\mu_0 H_{Ku}$ and not the M_s as mentioned in the Section above). The change in terms of anisotropy field is estimated of $\Delta\mu_0 H_{Ku}^{Pt} \sim 30$ mT.

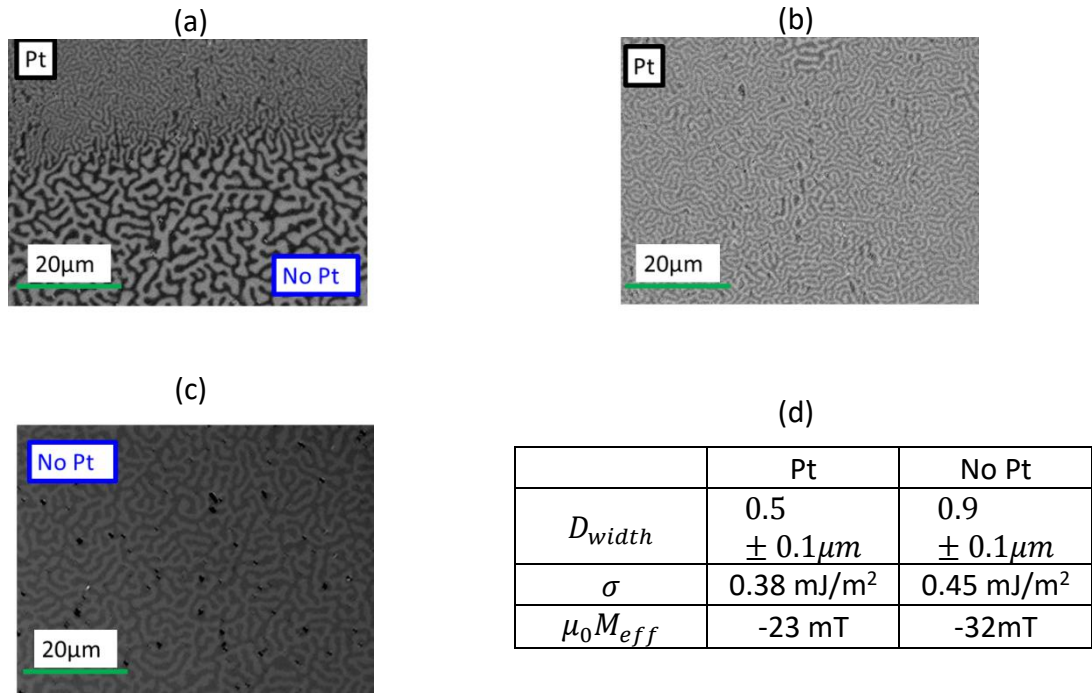


Figure VIII-2-Magnetic domain image of $Bi_1Y_2IG(20nm)//sGGG$ with and without Pt in the remanant state

For the case of sample with PMA D_{width} is strongly affected after sputtering of Pt. The decrease in $\mu_0 H_{Ku}$ is 50% lower than the one observed for in-plane magnetized sample however for PMA films it corresponds to a higher variation (30%) of K_{eff} (which is smaller for PMA films). For some films in which the PMA was barely stabilized and $K_{eff} \sim 0 \text{ J/m}^3$ the deposition of Pt lead to in-plane magnetic anisotropy. The decrease in anisotropy with Pt is then not negligible for thin films with PMA. The potential origin of this magnetic anisotropy due to Pt is discussed in the next section.

VIII-A.3 Discussion on the origin of the change in anisotropy.

First of all it is important to highlight the fact that Pt deposition did not systematically affect the anisotropy in our sample:

- No change in anisotropy has been observed for Pt deposition on $Bi_{0.7}Y_{2.3}IG//sGGG$ whatever the thickness of the film.
- No change in anisotropy has been observed with Kerr microscopy for Pt deposition on $Bi_1Y_2IG//sGGG$ for thicknesses lower than 15 nm.
- The change of magnetic anisotropy was not always observed for Pt deposition on $Bi_1Y_2IG//sGGG$ for thicker than 15 nm.
- The magnitude of change in anisotropy estimated from Kerr microscopy was not related to the thickness of the Pt or the BiYIG layer.

From the three last observations, it is possible to exclude a surface induced anisotropy origin (K_s) which would be inversely proportional in magnitude to the thickness of the BiYIG layer. Another possibility would be that Pt could modify the intrinsic value of the H_{Ku} in BiYIG. This would mean that the Pt top layer would modify the atomic arrangement within the BiYIG (and

modify K_{growth}) which would be highly unlikely. The other possibility is that a strain would be induced at the Pt/BiYIG interface on the first atomic layers of BiYIG (which would modify K_{MO}). Such effect could be due to intermixing between BiYIG and Pt. Therefore a TEM analysis of the Pt/BiYIG interface has been performed on the same sample of the one presented in Section VII.B.2.2.

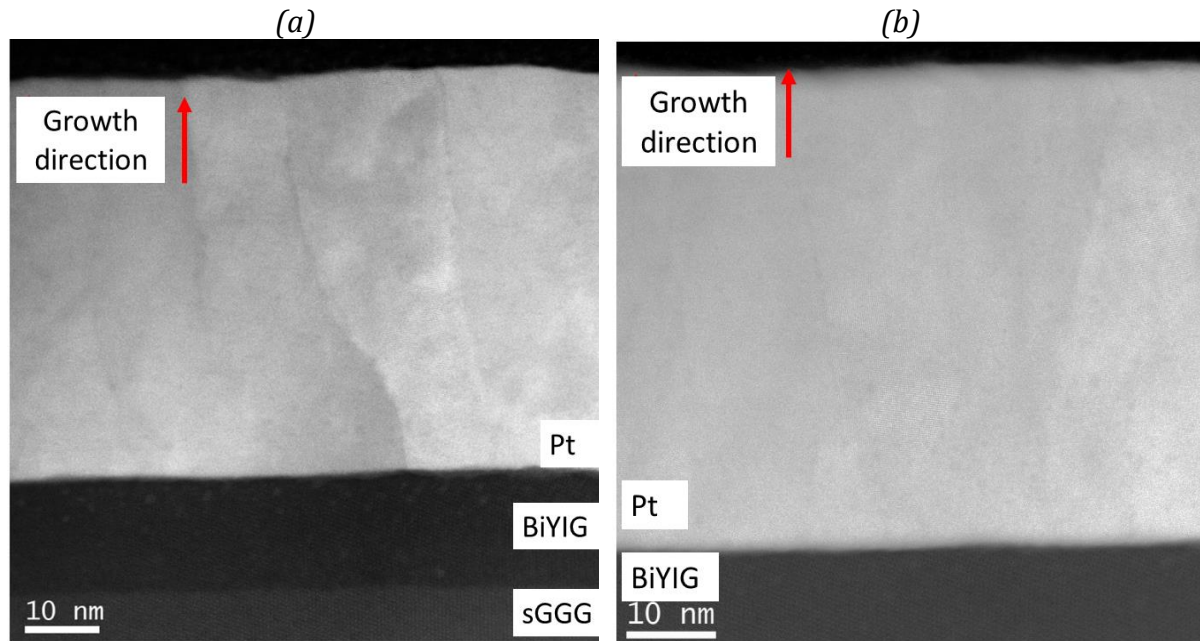


Figure VIII-3 TEM image of the Pt/BiYIG/sGGG stack (a) and zoom on the Pt/BiYIG interface (b). Grain boundaries are observed on the Pt due to polycrystallinity and the Pt/BiYIG interface is abruptly defined and shows no intermixing.

The TEM image shows grain boundaries in Pt due to polycrystalline growth, and the Pt/BiYIG interface is abruptly defined. This excludes any modification of BiYIG anisotropy due to intermixing with the Pt top layer.

It is then possible that either the sputtering deposition method or the plasma etching process (that is used to clean the sample) would affect the chemistry of the BiYIG surface via oxidation which could explain the modification of anisotropy. Therefore we investigated the effect of the cleaning procedure and the deposition mechanism on the magnetic anisotropy of BiYIG. To do so we used a 20 nm thick Bi₁Y₂IG//sGGG sample on which a part of sample was protected by a resist and the other part was not (using optical lithography) and performed:

- Plasma etching only.
- Plasma etching and Pt deposition by sputtering.
- Pt deposition using evaporation after etching.

After the deposition the resist was removed with acetone.

As previously, the change in anisotropy between the two regions (protected by the resist and unprotected) was evaluated by Kerr microscopy from D_{width} and Kerr images of the different procedure with D_{width} evaluated from FFT in the different region for each image are presented in Figure VIII-4(a-c) and (d).

When the sample is etched in the unprotected region a slight modification in D_{width} between the etched and unetched region is observable on the Kerr image (Figure VIII-4(c)). However

the difference in D_{width} from the two regions evaluated by FFT remains within the error bar (Figure VIII-4(c) and (d)).

When the sample is etched and 5 nm Pt was deposited in the unprotected region (Figure VIII-4(a)) D_{width} is notably modified and reduced by approximately a factor of two (Figure VIII-4(d)).

When Pt has been deposited by e-beam evaporation technique after the same etching procedure (Figure VIII-4(c)), no modifications on the domains width is observed. E-beam evaporated Pt atoms have less kinetic energy than sputtered one when they arrive on the BiYIG surface.

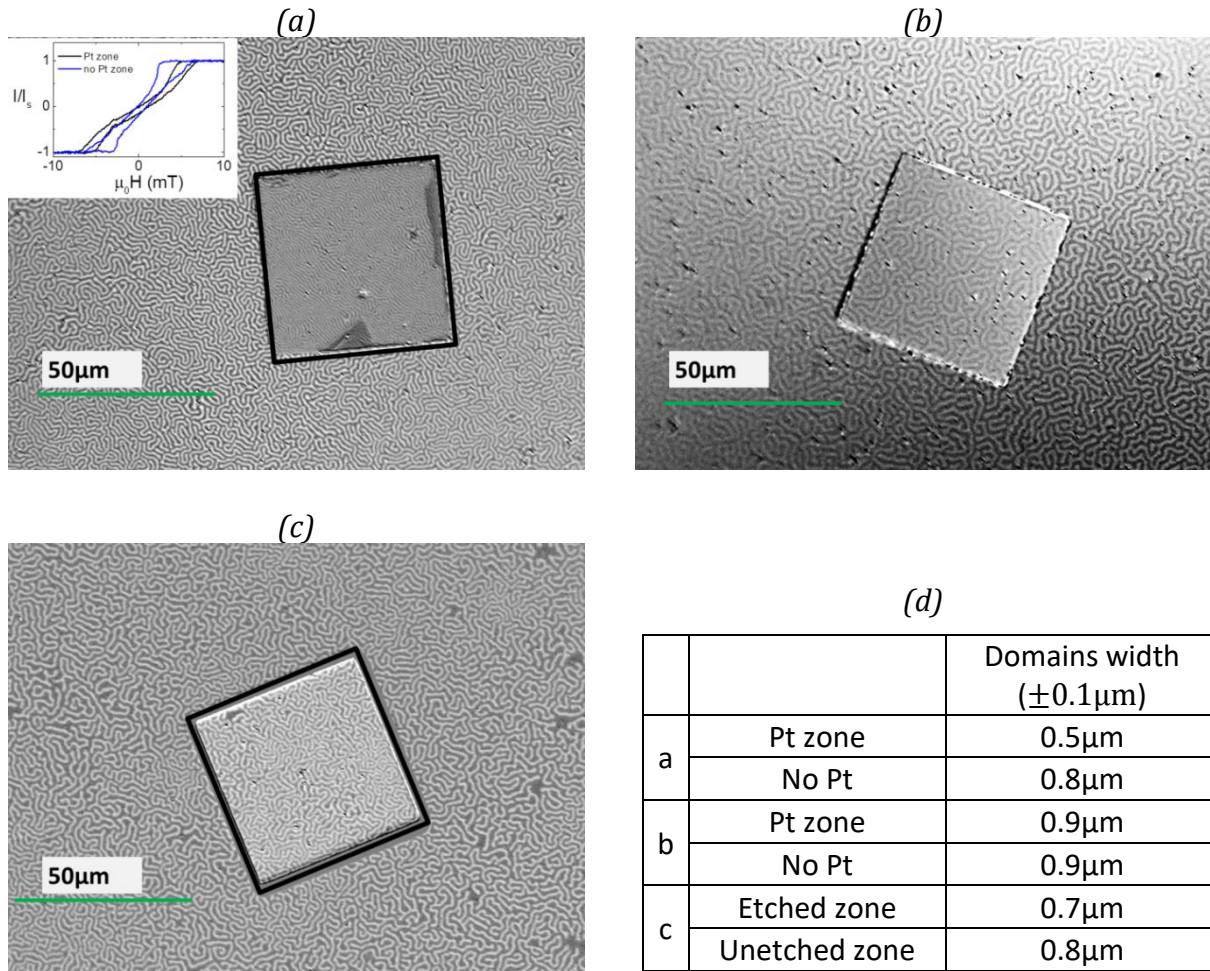


Figure VIII-4 Kerr microscope image for 20 nm thick of $\text{Bi}_1\text{Y}_2\text{IG}/\text{sGGG}$ at remanant state for: (a) etching and 5 nm Pt sputtered (and inset of the hysteresis curve with Pt and no Pt zone) (b) etching 5 nm Pt evaporated (c) only etching. (d) Sum up table with the domains width for each image extracted from FFT

These observations are supporting the hypothesis that the change in anisotropy when Pt is deposited is coming from the deposition method and not from the surface preparation or from the material deposited.

In the literature we found that a similar effect has been reported for Pt deposited on 18 nm thick LPE grown YIG films⁹⁴. They observed a decrease of the uniaxial anisotropy field of 8 mT

for YIG with a Pt top layer. This effect was attributed to an ‘interfacial mechanism of spin orbit coupling origin’.

In our thin films the SOC of Pt does not seem to play a major role as Pt deposited by evaporation is not affecting H_{Ku} in BiYIG films. Moreover we deposited Au by sputtering on some Bi₁Y₂IG//sGGG and, as for the case of Pt it led to a non-systematic change in D_{width} . Au is known for its low SOC which is another proof of the fact that in our case the change in H_{Ku} is not related to SOC in Pt.

We could not establish the precise origin of the change in H_{Ku} for thin films with Pt top layer but it seems that the deposition method of the top layer plays a major role. Eventhough those effects were not systematic and not properly understood but they should however be mentioned. In the following we will present magnons-spintronic phenomena involving Pt/BiYIG layer.

VIII-B Inverse Spin Hall Effect measurement.

To confirm the flow of angular momentum from BiYIG to the Pt top layer ISHE measurements are performed Pt/BiYIG bilayer (6 nm of Pt are sputtered on the top of 20 nm Bi_{1.5}Y_{1.5}IG//sGGG sample after a plasma etching procedure). Bi_{1.5}Y_{1.5}IG//sGGG presents in-plane magnetic anisotropy which is the most adapted geometry for ISHE measurements (see Section IV-D.2).

VIII-B.1 Spin pumping.

The first evidence of angular momentum transfer between Pt and BiYIG is the increase of the Gilbert damping in BiYIG after deposition of Pt due to spin pumping (see Section IV-B.1). Spin pumping is measured using characterization of magnetic losses in Bi_{1.5}Y_{1.5}IG//sGGG with and without Pt top layer.

The Figure VIII-5(a) presents the evolution of $\mu_0\Delta H_{pp}$ with f_{res} for Pt/Bi_{1.5}Y_{1.5}IG//sGGG and Bi_{1.5}Y_{1.5}IG//sGGG. Values of magnetic losses: $\mu_0\Delta H_0$ and α obtained from the linear fit are reported in the Figure VIII-5(b). Due to spin angular momentum transfer in the Pt top layer Pt sputtering increases the magnetic losses of $\Delta\alpha_{sp} = \alpha_{Pt} - \alpha_{No Pt} = 12 \cdot 10^{-4}$ (Figure VIII-5(b)) ($\Delta\alpha_{sp}$ corresponds to part of angular momentum of BiYIG transferred in Pt). The spin mixing conductance $G_{\uparrow\downarrow}$, characteristic of the interface spin transparency is also derived using Equation IV-22 and displayed in the Figure VIII-5(b).

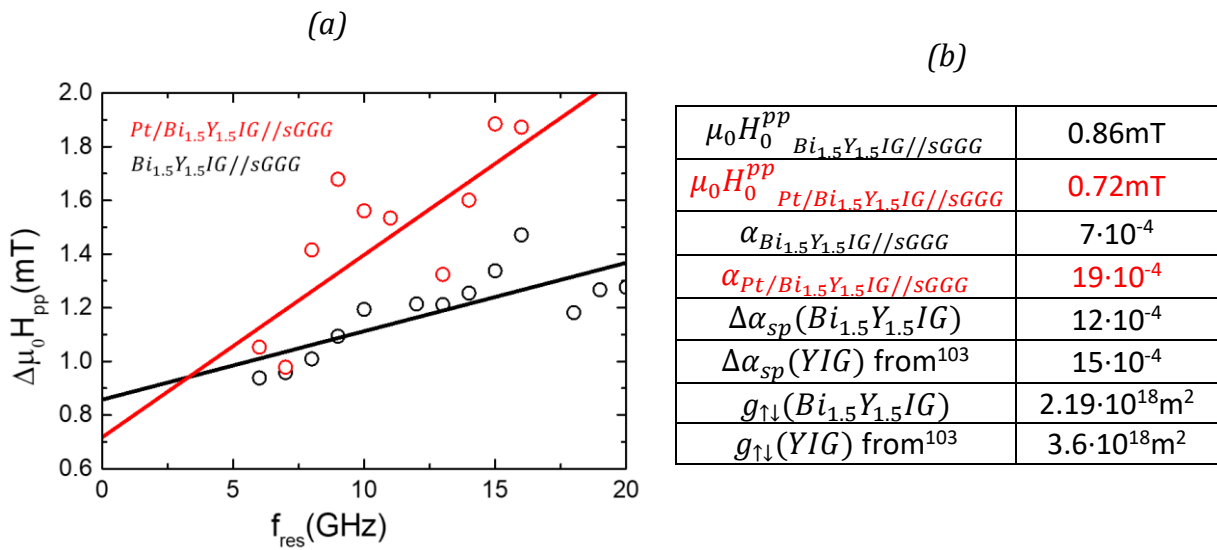


Figure VIII-5(a) $\mu_0\Delta H_{pp}$ vs f_{res} for Bi_{1.5}Y_{1.5}IG//sGGG and Pt/Bi_{1.5}Y_{1.5}IG//sGGG and (b) values of the extrinsic contribution and the Gilbert damping obtained from the linear fit, calculated values of the damping, spin pumping and the spin mixing conductance for Bi_{1.5}Y_{1.5}IG and YIG films

The comparison between BiYIG and YIG PLD grown films in terms of spin transparency is done from values of Figure VIII-5(b). The increase of magnetic losses due to spin pumping and the $G_{\uparrow\downarrow}$ for Pt/Bi_{1.5}Y_{1.5}IG//sGGG is comparable to what is obtained for Pt/YIG//GGG (Figure VIII-5(b)) which suggests that the doping of Bismuth doesn't affect the spin transparency of

the Pt/Iron Garnet interface and that BiYIG PLD grown films can be used on the same fashion as the YIG ones for spintronic applications.

Now that from spin pumping characterisation BiYIG films seems as efficient as the YIG ones for spintronic applications, ISHE measurement are performed to prove that spin current can be transferred from BiYIG to Pt.

VIII-B.2 ISHE.

In the FMR resonant conditions the out of equilibrium magnon accumulation at the BiYIG/Pt interface is transferred as spin angular momentum in Pt and induces a spin current \mathbf{J}_s polarised along σ flowing from BiYIG to Pt. Due to SHE in Pt \mathbf{J}_s can be electrically detected (see Figure VIII-6(a) for the geometry). ISHE is a proof of an effective spin angular momentum transfer from BiYIG to Pt and will confirm observations of the previous Section.

The experimental set up and the geometry of the ISHE measurements are presented the Section VI.B.4.3 and the Figure VIII-6(a) respectively. The RF excitation frequency applied to the Pt/Bi_{1.5}Y_{1.5}IG//sGGG sample is 6GHz and the in-plane static field $\mu_0 H_{stat}$ varies from 130 to -130 mT.

In the FMR resonant condition the precession of the Bi_{1.5}Y_{1.5}IG//sGGG magnetic moment absorbs RF power: an anti-Lorentzian shape like curve (Figure VIII-6(b) inset) is detected via the lock in. In the same experimental conditions ($\mu_0 H_{stat}$ /RF excitation) a Lorentzian shape like curve is electrically detected in the Pt top layer (Figure VIII-6(c)).

Worth to note that in Figure VIII-6(b) the sign of the ISHE voltage peak depends on the sign of $\mu_0 H_{stat}$. This confirms the SHE origin of the detected voltage: since σ induced in Pt is \parallel to $\mu_0 H_{stat}$ reversing the polarity of σ reverses the sign of \mathbf{J}_c due to the SHE cross product.

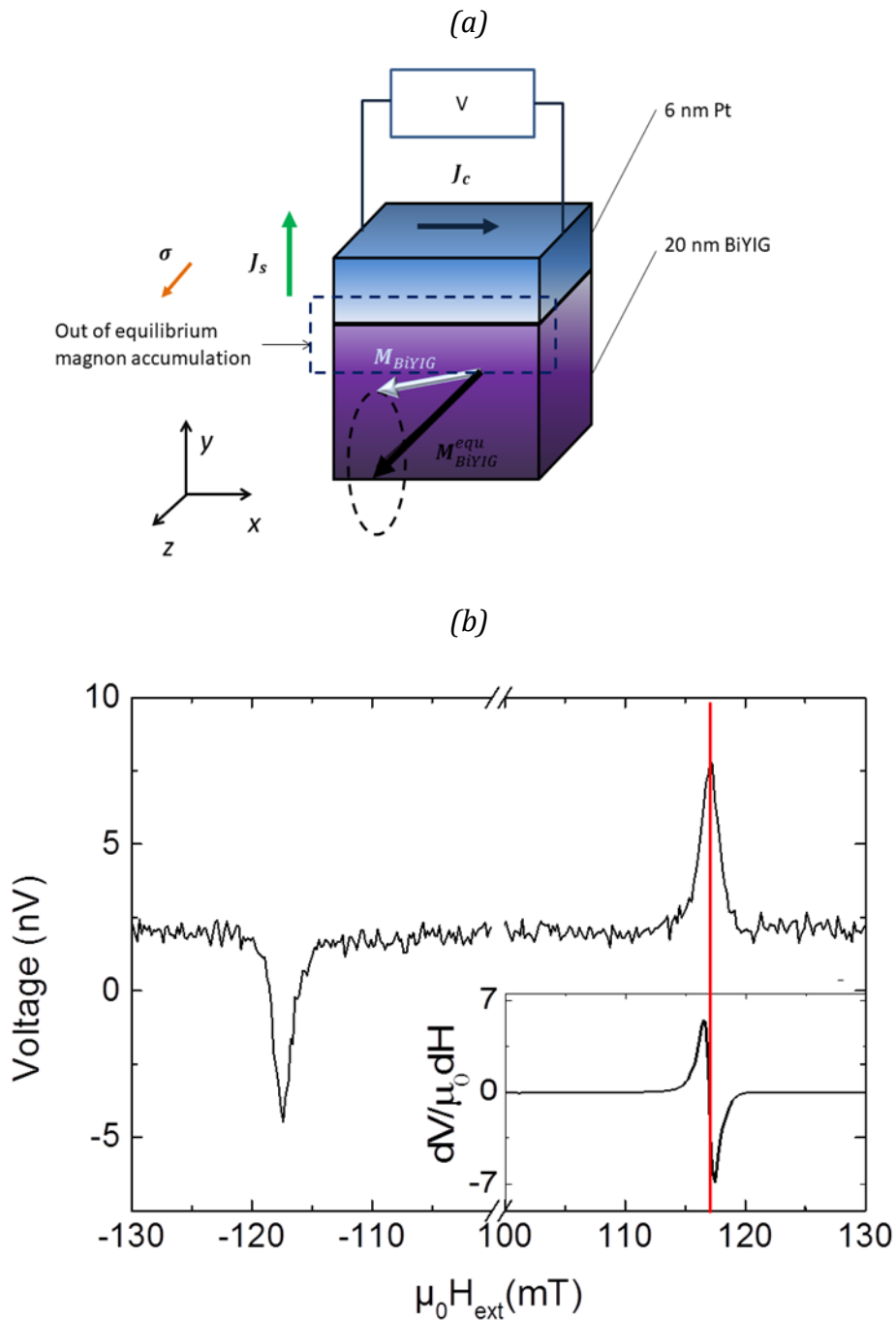


Figure VIII-6(a) Geometry of the ISHE measurement set up and (b) detection of a voltage variation in the Pt top layer in the FMR resonant condition for the Pt/Bi_{1.5}Y_{1.5}IG//sGGG (inset)

This ISHE measurement confirms the spin pumping measurements and proves that a spin current can flow from Bi_{1.5}Y_{1.5}IG to Pt in the FMR resonant conditions.

As we prove that spin angular momentum can be transferred from BiYIG to Pt we will now show that the reverse process can also be observed by performing SMR and AHE measurements in BiYIG films presenting PMA.

VIII-C SMR measurements.

SMR measurements are realised on a Hall cross bar of $2\mu\text{m}$ wide and $100\mu\text{m}$ long patterned by ionic etching in a Pt(6nm)/Bi₁Y₂IG(15nm)//sGGG sample. To improve the quality of electrical contacts Au (200nm)//Ti (20 nm) pads are deposited by evaporation. The microfabrication has been realised by Q. Barbedienne and the final device is the one described in Figure VI-17(c). The experimental set up used for measurements is the one of Section VI-B.5.

The Figure VIII-7 presents a sketch of the measurement geometry: a constant current $I=1\text{mA}$ is applied in the x direction in the Pt strip, an external field $\mu_0 H_{ext} = 500 \text{ mT}$ varies angularly in the three different planes (x,y) , (x,z) and (y,z) (the variation in each plane corresponds to an angle defined in Figure VIII-7). The magnitude of $\mu_0 H_{ext}$ is sufficient to ensure that $M_{BiYIG} \parallel H_{ext}$ for all directions of H_{ext} . The voltage V_{xx} is measured along the direction of the charge current J_c (and the resistance is deduced from $R_{xx} = \frac{V_{xx}}{I}$). Depending on the current/magnetization direction geometry different magnetoresistive effects can be observed:

- If the Pt layer becomes magnetized due to proximity induced magnetization Anisotropic Magnetoresistance (AMR) can be measured. AMR corresponds to a spin dependence transport phenomena it is observed in FM and depends on the angle between the charge current I and the magnetization M_{FM} of the FM (in our case if Pt would be polarized by BiYIG: $M_{Pt} \parallel H_{ext}$). The dependence of the resistivity in Pt due to AMR effect ρ_{Pt}^{AMR} is written¹⁵²:

$$\rho_{Pt}^{AMR} = \rho_0^{AMR} + \Delta\rho^{AMR} \cos^2(I, M) \quad \text{VIII-1}$$

$$\text{with } \Delta\rho^{AMR} = \frac{(-\rho_{M\parallel I} + \rho_{M\perp I})}{\rho_0^{AMR}}$$

- If spin torque is absorbed or reflected at the BiYIG-Pt interface SMR effect can be observed. It is possible to differentiate SMR from AMR effect because SMR is dependent upon the polarisation of the interfacial spin accumulation in Pt induced by SHE: σ (see IV-D.1). Due to the SHE cross product $\perp I$. The dependence in resistivity due SMR is then written¹²²:

$$\rho_{Pt}^{SMR} = \rho_0^{SMR} + \Delta\rho^{SMR} \sin^2(\sigma, M) \quad \text{VIII-2}$$

$$\text{with } \Delta\rho^{SMR} = \frac{(-\rho_{\sigma\parallel I} + \rho_{\sigma\perp I})}{\rho_0^{SMR}}$$

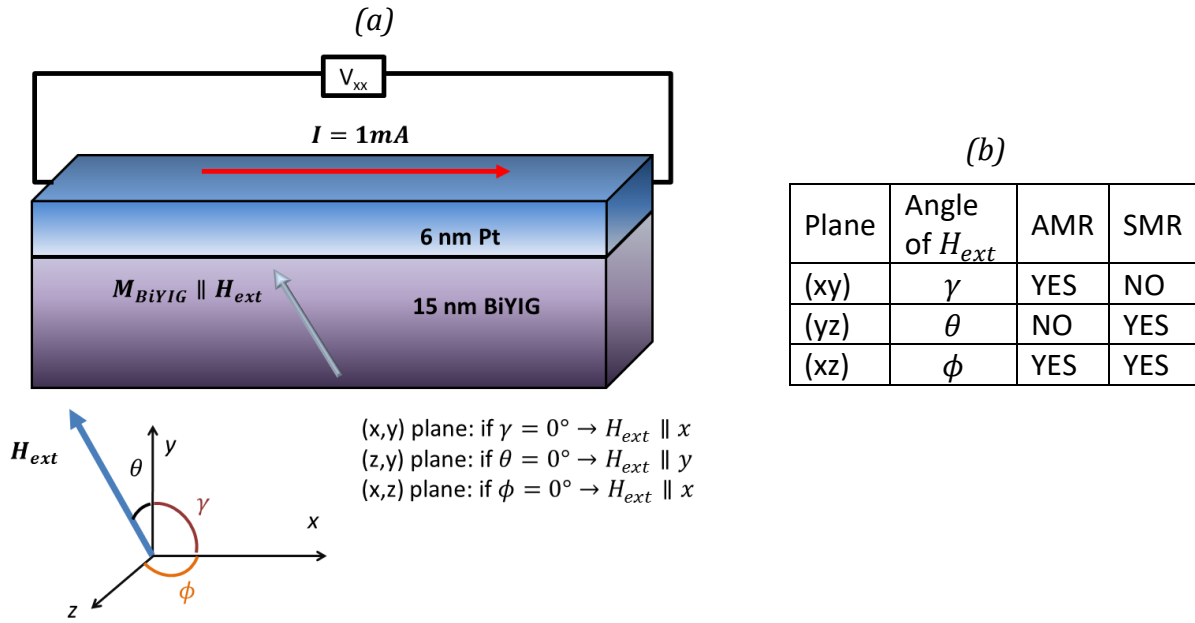


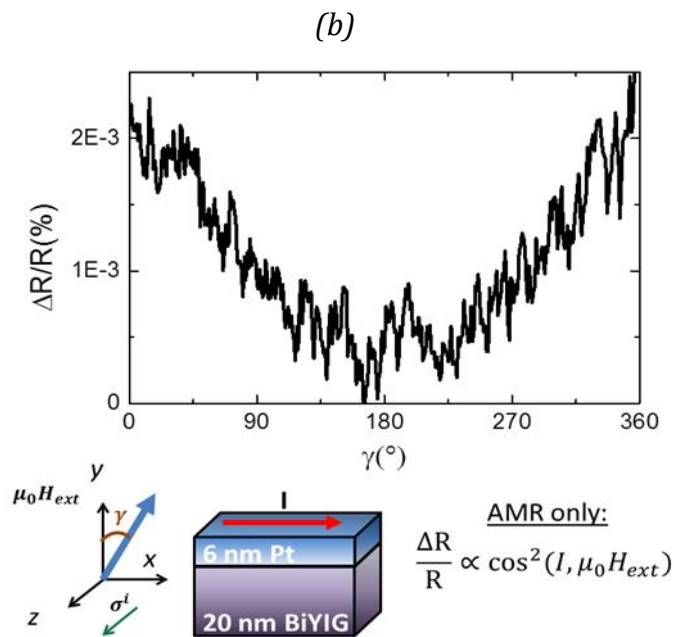
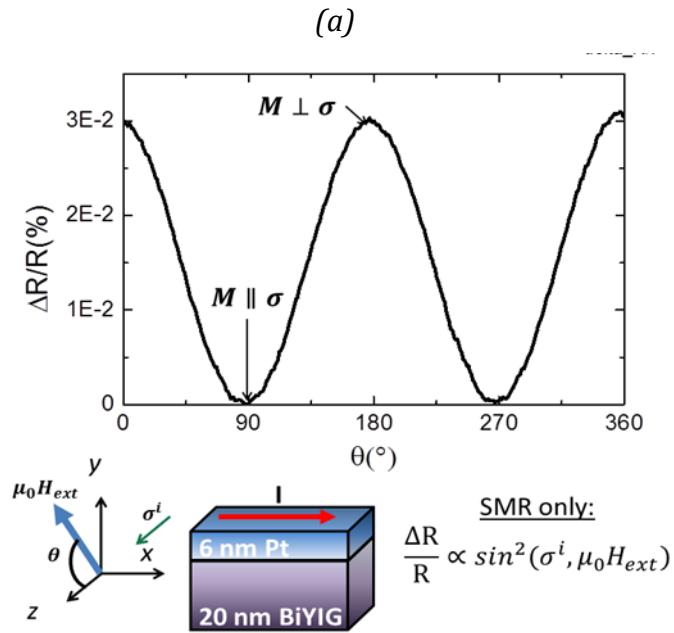
Figure VIII-7 (a) Sketch of the geometry used for SMR experiment. The external field applied in the three possible planes is sufficient to ensure that $\mathbf{M}_{BiYIG} \parallel \mathbf{H}_{ext}$. Depending on the geometry it is possible to observe or not AMR and SMR as depicted in the Table(b)

The Table of Figure VIII-7(b) sums up all the different expected effects depending on the plane of variation of H_{ext} .

The Figure VIII-8 displays the variation in $\frac{\Delta R}{R} = \frac{2\Delta R_{xx}}{R_{xx}^{min} + R_{xx}^{max}}$ with respect to H_{ext} . All three different orientation are considered and the measurement have been performed at room temperature:

- In the Figure VIII-8(a) H_{ext} varies in the plane perpendicular to the direction of I (y,z). In this geometry SMR effect only should be observable: a variation of $\frac{\Delta R}{R}$ is due to spin current reflection or absorption (depending on the orientation of \mathbf{M}_{BiYIG}) at the Pt/BiYIG interface. As expected from SMR signal $\frac{\Delta R}{R}$ is π - periodic (see Equation VIII-2) and presents minimum when $\mathbf{M}_{BiYIG} \parallel \boldsymbol{\sigma}^i$ (total reflection of the spin current at the interface)
- In the Figure VIII-8(b) H_{ext} varies in the plane perpendicular to $\boldsymbol{\sigma}^i$ (polarization of spin current in Pt due to SHE). In this geometry only AMR effect should be observable (if Pt is spin polarized by the BiYIG). We note that the curve is noisy and that a 2π - periodicity of $\frac{\Delta R}{R}$ instead of the π - periodicity expected (see Equation VIII-1) is observed. Moreover the variation in amplitude of $\frac{\Delta R}{R}$ for the AMR effect ($\sim 2 \cdot 10^{-3}\%$) is one order of magnitude below the effect related to SMR ($\sim 3 \cdot 10^{-2}\%$). The 2π periodicity is attributed to low intensity of the AMR contribution compared to the noise. The π periodic AMR signal could be observed at 11 K on another sample with one order of magnitude variation of $\frac{\Delta R}{R}$ compared to SMR measurements. The AMR effect is considerably less important in magnitude than the SMR one.
- In the Figure VIII-8(c) AMR and SMR signal should contribute as $\mu_0 H_{ext}$ varies in a plane containing both $\boldsymbol{\sigma}$ and \mathbf{I} . The variation of $\frac{\Delta R}{R}$ is π -periodic with a $\sin^2(\boldsymbol{\sigma}, \mathbf{M}_{BiYIG})$

dependence (characteristic of the SMR contribution). The amplitude of variation is the same as the SMR in Figure VIII-7(a) which confirms that this effect is the dominant one over the AMR effect.



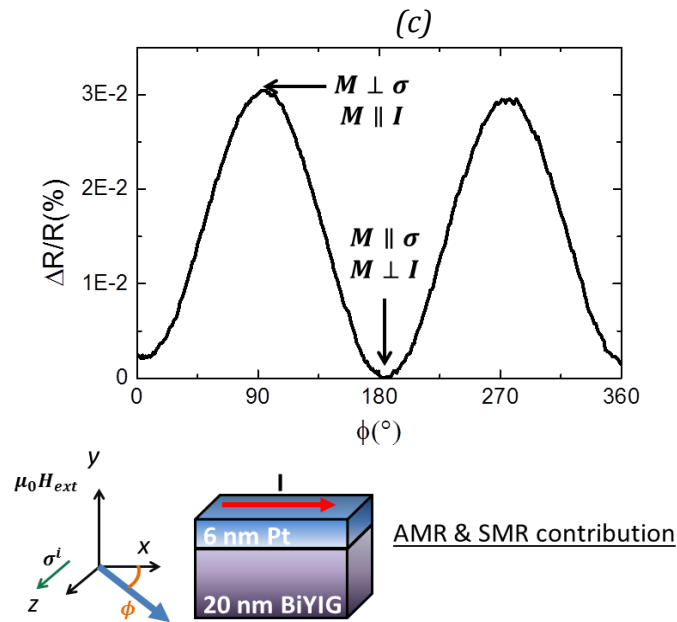


Figure VIII-8-Resistance variation vs the angular position of the external field. Depending on the plane of the field variation different effects are expected: (a) SMR only, (b) AMR only and (c) SMR+AMR

These measurements evidenced the presence of SMR in Pt/BiYIG and excluded that the measured signal could be attributed to AMR only. The relative variation in resistance $\frac{\Delta R_{max}}{R_0}$ due to SMR in Pt/BiYIG is comparable to what has been reported in Pt/YIG ($\frac{\Delta R_{max}}{R_0} = 7 \cdot 10^{-4}$ for PLD grown YIG¹⁵³).

Using AMR-SMR measurements we evidenced the reflection and the absorption of spin current in Pt/BiYIG. This measure is complementary with the ISHE one as the SMR is related to a spin flow from Pt to BiYIG. In the following Section we evidenced another effect related to reflection and transmission of spin current from Pt: AHE, this phenomenon is more convenient to observe on PMA materials (see Section V.C.1.1). Thus AHE has been measured on Pt/BiYIG films presenting PMA.

VIII-D Anomalous Hall Effect in Pt/BiYIG.

AHE measurements are realized on a 15 nm thick Bi₁Y₂IG//sGGG sample presenting strong PMA on which 6 nm Pt has been sputtered. Since sputtering of Pt can affect H_{Ku} Kerr hysteresis in the out-of-plane direction of the sample before and after sputtering are shown in Figure VIII-9. Even though the BiYIG remains out-of-plane with Pt top layer the hysteresis loop is affected after deposition of Pt and $\mu_0 H_{sat}^\perp$ is increased of 5mT. This magnetic characterization leads to the conclusion that this Pt(6 nm)/Bi₁Y₂IG(15 nm)//sGGG sample remains out-of-plane and is still suitable for AHE measurements.

After deposition the same microfabrication as the one for the SMR device has been realised, the measurement of the AHE is realised in the configuration presented in Figure VI-17(c), the experimental set up is the same as the one used for SMR measurements.

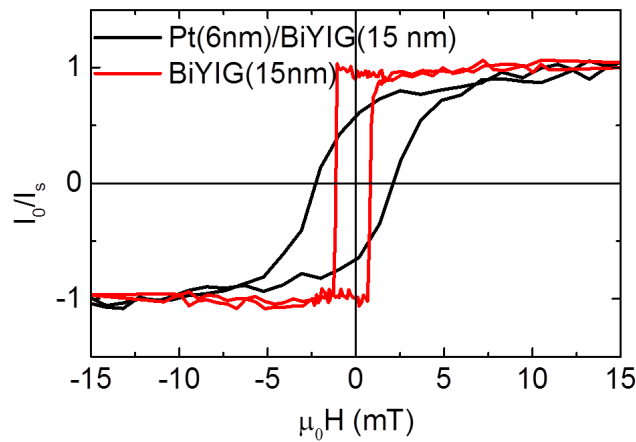


Figure VIII-9-Kerr hysteresis loop performed on BiYIG before and after sputtering of Pt.

The AHE experiment is performed by applying a constant current of $I_c=1$ mA into the $4\mu\text{m}$ width and $45\mu\text{m}$ long Pt/Bi₁Y₂IG//sGGG track, the transverse resistance of Pt (R_{xy}) is measured as shown in the Figure VI-17(c). The Figure VIII-10 (a) presents the evolution of R_{xy} with respect to the field $\mu_0 H$ applied in the out-of-plane direction: at low field (~ 10 mT) a jump in R_{xy} , corresponding to the alignment of M_{BiYIG} with $\mu_0 H$, is measured. This variation in resistance corresponds to the AHE resistance R_{AHE} . After saturation of M_{BiYIG} the R_{xy} becomes linearly dependant on $\mu_0 H$, this corresponds to the Ordinary Hall Effect (OHE) in Pt. In order to obtain the AHE contribution only the linear contribution of the OHE has to be subtracted from Figure VIII-10 (a). The linear fit of the OHE contribution in Pt/BiYIG gives $R_{OHE}=-0.24\cdot 10^{-10}\frac{\Omega\text{m}}{\text{T}}$, considering the dimension of the device and the Pt thickness it is close to the value obtained for bulk Pt¹⁵⁴ ($-0.23\cdot 10^{-10}\frac{\Omega\text{m}}{\text{T}}$).

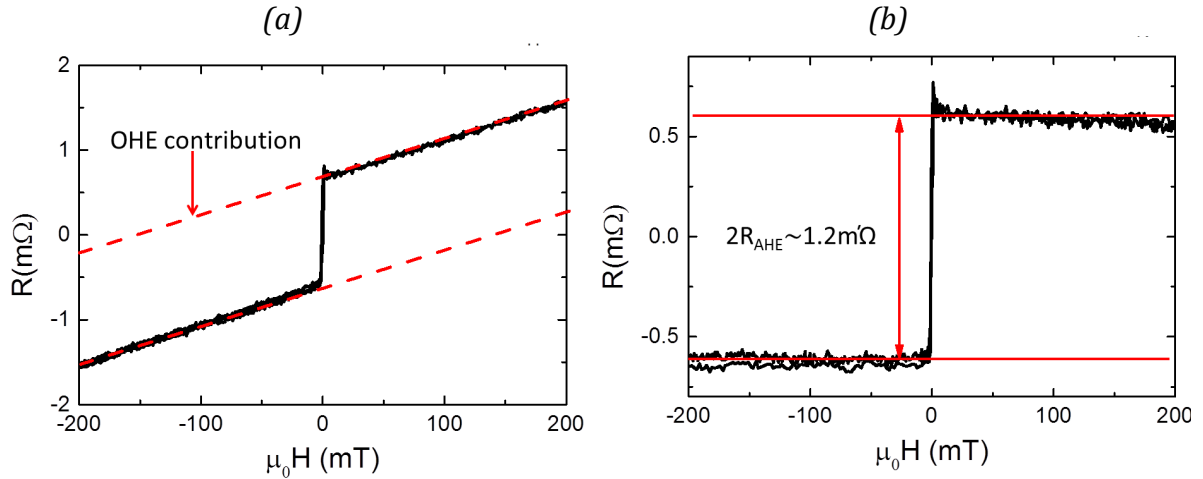


Figure VIII-10-AHE measured in Pt(6nm)/BiYIG(15nm)/sGGG bilayer with (a) and without (b) the Ordinary Hall Effect contribution.

R_{AHE} is obtained from the curve of Figure VIII-10 (b) in which the OHE contribution is removed and an offset is applied to compensate from the electrodes misalignment. The Table VIII-1 sums up different values of R_{AHE} reported for Pt/Iron Garnet bilayers and the one of Pt/BiYIG measured in this study. The value of R_{AHE} in Pt/BiYIG remains within the same range of magnitude as what is reported for Iron Garnet materials.

	Pt/YIG ⁶²	Pt/TmIG(sputtering) ⁶³	Pt/BiYIG	Pt/TmIG(PLD) ¹⁵⁵
R_{AHE}	$-6 \cdot 10^{-12} \Omega m$	$\approx -3 \cdot 10^{-12} \Omega m$	$3.4 \cdot 10^{-12} \Omega m$	$-1.1 \cdot 10^{-12} \Omega m$

Table VIII-1- SMR conductivity and AHE resistance for different Pt/Garnet materials.

In this section another spintronic phenomena: the AHE has been measured which is a further confirmation that BiYIG are a suitable platform for spintronic.

The spin current flow from BiYIG to Pt and from Pt to BiYIG is now confirmed by several spintronic phenomena. So far we did not take profit of the extremely good dynamical properties of BiYIG which should make it an ideal platform for the propagation of spin wave or the generation of autooscillations. Magnon-spintronics applications in BiYIG are presented in the next Section.

VIII-E Spin wave emission using a charge current.

Experiments presented in this Section have been realized in the team of V. Demidov and S. Demokritov at Muenster University. They used μ -focused BLS technique (details of BLS are provided in the Annexe I.E) on a Pt(6 nm)/Bi₁Y₂I₉(20 nm)//sGGG in which they applied a charge current I in order to: first generate auto-oscillations in BiYIG and then investigate the spin wave properties of a low losses MI with PMA.

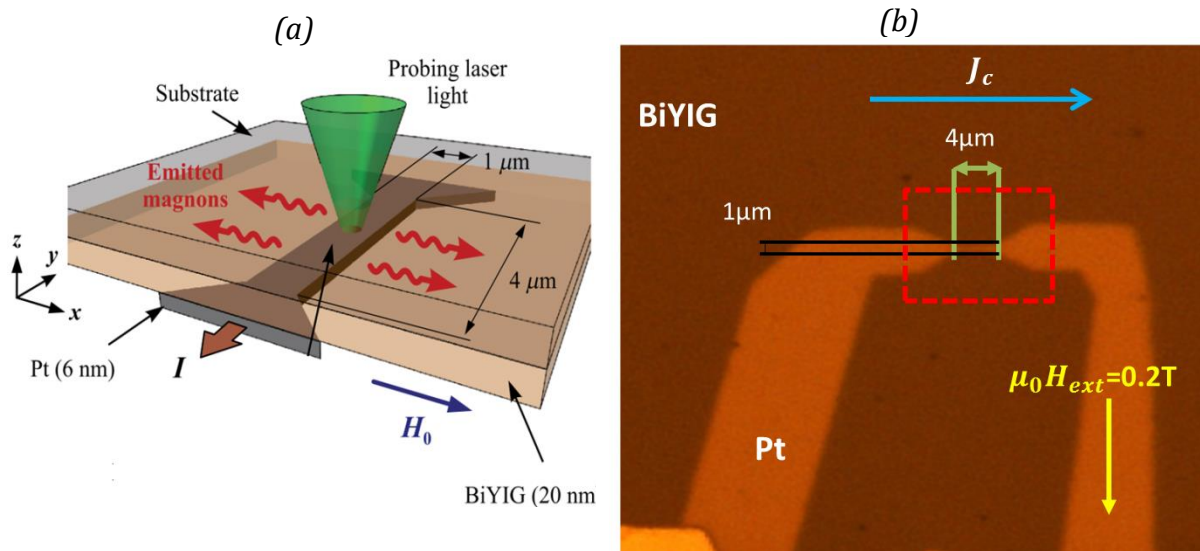


Figure VIII-11-Scheme of the BLS observation set up (a) and picture of the real device (b). The zone surrounded in red corresponds to the one observed by BLS.

A microscope image of the device used for this experiment is presented in the Figure VIII-11(b): a 1 μm wide, 4 μm long strip of Pt has been deposited on the BiYIG sample. Contrary to the SMR and AHE Hall Cross the BiYIG part is not etched. As sketched in Figure VIII-11(a) the BLS spot is focused on the strip Pt part (which corresponds to part within the red rectangle in Figure VIII-11(b)) in order to image magnons in this area. To satisfy the condition of auto-oscillation generation the external field $\mu_0 H_{ext}$ is applied \perp to the charge current J_c

VIII-E.1 Auto-oscillation observation.

In Pt/BiYIG the auto-oscillation regime corresponds to the compensation of the magnetic losses by a current induced STT τ_{STT} (see Section IV-B.2) in Pt. To maximize the efficiency of the spin transfer torque (τ_{STT}) the polarisation σ of the SHE induced spin current J_s from the initially applied charge current J_c has to be perpendicular to \mathbf{m}_{BiYIG} (see Equation IV-23). Here the \mathbf{m}_{BiYIG} term corresponds to a component transverse to the static magnetization arising from thermal fluctuation of the BiYIG magnetic moment and is perpendicular to the static magnetic moment of the BiYIG $M_{BiYIG}^0 (\parallel H_{ext})$. This explains why the geometry of Figure VIII-11(b): $J_c \perp H_{ext}$ (or equally $\sigma \perp \mathbf{m}_{BiYIG}$) is the one used to generate auto-oscillations^{56,57,103}.

Auto oscillations are obtained when the magnitude of τ_{STT} is sufficient to compensate the magnetic losses which corresponds in term of applied charge current J_c to⁴⁶:

$$J_c^{crit} = \frac{t_{BiYIG} e \alpha f_a M_s}{\theta_{SHE} \gamma \hbar}$$

VIII-3

where f_a is the auto-oscillation frequency.

Since the BLS intensity is proportional to the magnon density in the region of interest, the damping compensation regime corresponds to an increase of the BLS intensity taken at $f = f_a$. This corresponds to the observation of Figure VIII-12 :

- for $f = f_a$ the BLS intensity increases when the applied current I_c exceeds the critical current: $I_c^{crit} = 1,8$ mA (Figure VIII-12(b))(corresponding to a current density of $3 \cdot 10^{11}$ A/m²)
- for an applied current above the critical current the BLS intensity at the frequency of auto-oscillation $f_a = 5.56$ GHz is maximal (Figure VIII-12(a)).

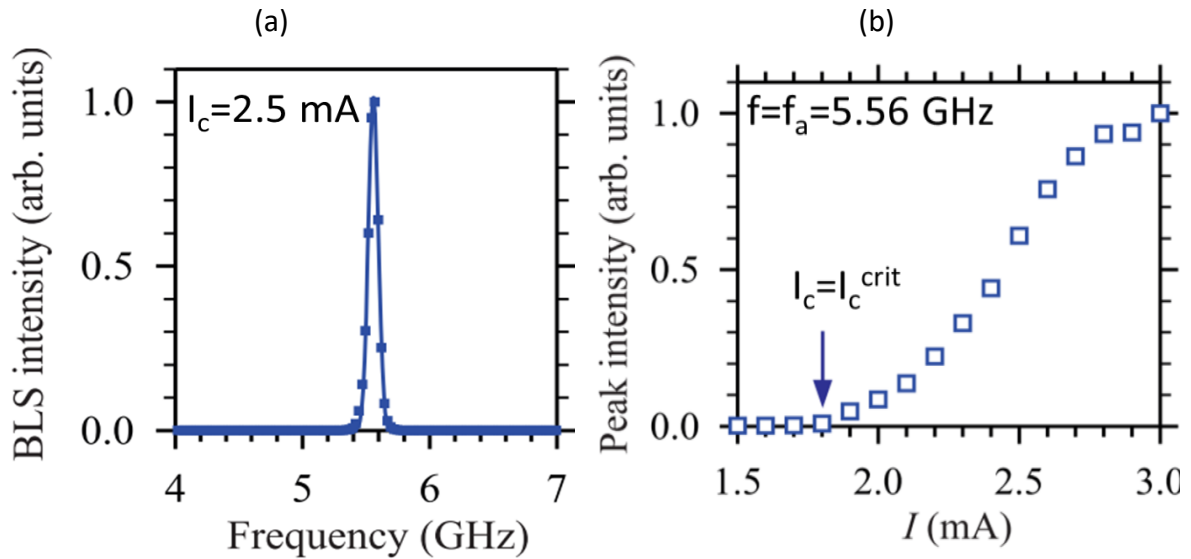


Figure VIII-12 (a) BLS intensity measured by placing the ROI in the middle of the Pt line and applying a constant charge current of 2.5 mA ($> I_c^{crit} = 1.8$ mA). High BLS intensity is observed for the auto-oscillation frequency $f_a = 5.56$ GHz. Variation of the BLS intensity signal probed in the same ROI with the applied charge current for the fixed frequency $f_a = 5.56$ GHz. The onset of auto-oscillations is characterised by an increase of the BLS intensity for $I > I_c^{crit}$ (b)

The current density necessary to induce auto-oscillation (related to the magnetic damping as seen in Equation VIII-3) in Pt/BiYIG films is comparable to the one required for Pt/YIG//GGG of comparable thicknesses¹⁰³. As we saw that the magnetic moment is not considerably changed for BiYIG compared to YIG this suggests that BiYIG and YIG are comparable in terms of dynamical properties.

Now BLS mapping evidenced auto-oscillation of M_{BiYIG} in the Pt/BiYIG stripe region the map is extended outside the stripe to see how the auto-oscillation excite propagating magnons in the BiYIG region that is not covered with Pt.

VIII-E.2 Spin wave emission from auto oscillation.

The BLS mapping is now extended outside the Pt covered region. The applied current 2.5 mA is sufficient to induce auto-oscillations.

The BLS map of the sample in the extended zone is displayed in the Figure VIII-13. Contrary to what has been reported for the case of YIG thin films in the auto oscillation regime¹⁰³ the high intensity BLS signal is not confined in the Pt excitation zone only but extends over few μm length. This evidences the presence of magnons with frequency f_a in the surrounding of the Pt stripe. In other words auto oscillations generated in Pt/BiYIG induce propagating spin wave in BiYIG which is not what is observed in YIG where they remain localised. To explain this phenomena it is necessary to understand the origin of the auto oscillation localisation in YIG.

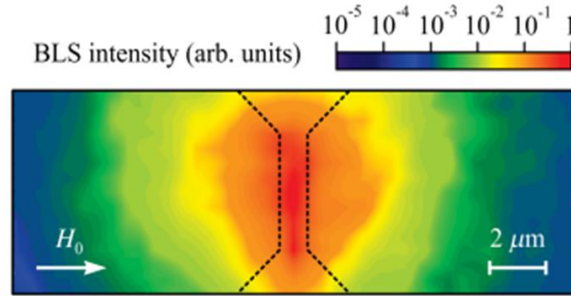


Figure VIII-13-BLS intensity of the sample in the area surrounding the Pt stripe performed at the auto-oscillation frequency for fixed external field value $\mu_0 H_{ext} = 0.2\text{mT}$. High intensity of BLS signal indicates high magnon density outside the auto-oscillation area.

The self-localization of auto-oscillations in YIG ultrathin films is attributed to a nonlinear shift of the auto-oscillation frequency compared to original FMR frequency. This shift is attributed to different factors:

- A local decrease of M_s due to Joules heating in the Pt zone where DC-current is applied. This modifies locally M_{eff} (due to a decrease of the demagnetization term) and diminish f_{res} .
- The Oersted field due to the DC current which modifies the field felt by the YIG in the Pt region ($H_{Pt/YIG} = H_{ext} + H_{Oe}$)

For those reasons $f_a < f_{res}^{YIG}$ which prevents auto-oscillation mode to couple to other spin wave mode in the YIG film.

The Figure VIII-14 gives more insights about the SW behaviour in the BiYIG sample studied. It shows the SW dispersion relation (for SW propagating in the plane of the film and the angle $\phi = (\mathbf{k}_{SW}, \mathbf{I}_c)$) as well as the FMR resonant frequency in the BiYIG without Pt region (f_{res}^{BiYIG}) and the auto oscillation frequency f_a in the Pt/BiYIG area. From the Figure VIII-14 we note that $f_a > f_{res}^{BiYIG}$ and f_a crosses the dispersion curve of SW in BiYIG, this allows the generation of SW from autooscillation. The auto oscillation frequency is also the one of a magnon that can propagate in BiYIG with a $\mathbf{k} \neq \mathbf{0}$ propagation vector. This explains the presence of magnons in the surrounding area of the Pt stripe.

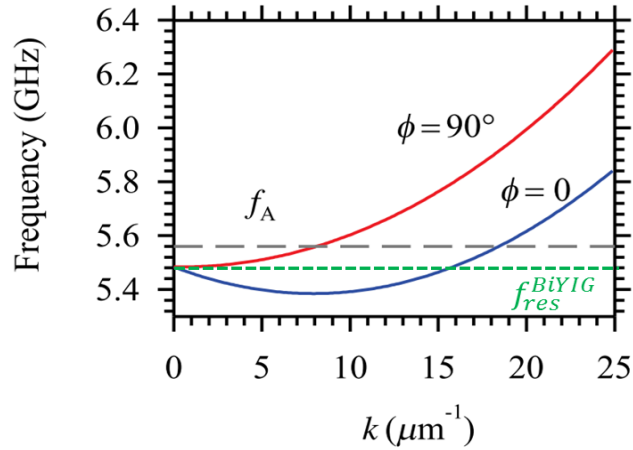


Figure VIII-14 Spin wave dispersion relation of the BiYIG films for SW propagating \parallel (red) or \perp (blue) to $\mathbf{M}_{\text{BiYIG}}$. The frequency of the auto-oscillation f_a corresponding to an external field $\mu_0 H_{\text{ext}} = 0.2 \text{ mT}$ in the Pt/BiYIG region is drawn in the dotted line.

The slight increase of f_a compared to $f_{\text{res}}^{\text{BiYIG}}$ is attributed to two reasons:

- In the BiYIG sample of study $M_{\text{eff}} \sim 0 \text{ kA/m}$ and the anisotropy term H_{Ku} compensate the demagnetizing field. Hence the modification of the demagnetizing field value due to Joule heating is not modifying $f_{\text{res}}^{\text{Pt/BiYIG}}$ from $f_{\text{res}}^{\text{BiYIG}}$.
- The presence of Pt top layer on BiYIG decreases H_{Ku} contribution as detailed in the Part VIII-A. Hence in the Pt covered region for a given external field $\mu_0 H_{\text{ext}}$: $f_{\text{res}}^{\text{Pt/BiYIG}} > f_{\text{res}}^{\text{BiYIG}}$.

Thus auto-oscillation can generate SW propagating in all direction (ϕ from 0 to 90°) that can propagate over μm distance. The observed attenuation length is about $4 \mu\text{m}$. This experimental value is the expected one considering for $k \sim 18 \mu\text{m}^{-1}$ for $\phi = 0$.

In this part a new phenomena observable thanks to PMA is presented which is the generation of magnetostatic SW from STT induced auto-oscillation. BiYIG films with PMA allow solving the localization problem of auto-oscillation attributed to non linear shift of the auto oscillation frequency. Moreover the low magnetic damping in our films allow to observe SW propagation over few μm distance.

To sum up this Section focused on applications of BiYIG we showed that it is suitable to observe spintronic phenomena and allows transfer of angular momentum to a NM SHE top layer. Moreover we showed that the PMA coupled to low magnetic losses allow in these material to generate from current induced auto-oscillation coherent SW. This material presents itself as a new platform for magnons-spintronic applications which offers new possibilities for the field.

IX Conclusion and Outlook.

We can now draw the main conclusions about this Ph.D. work and present outlooks that this work is opening.

IX-A Conclusion.

This PhD manuscript deals with two fields of physics: materials science and spintronic applications. In a first work we elaborated and characterized a new ultrathin magnetic insulator: the Bismuth doped YIG. We could evidence interesting properties in this material making it relevant for magnon-spintronic applications. In a second time we performed several magnon-spintronic experiments and confirmed that it was a suitable material for those applications. We could observe both well-established spintronic phenomenon that did not specially exploit the new characteristics of the material and new magnon-spintronics ones that relied on the new properties of this material.

We first in the Section V evidenced that ultrathin MI could be used for magnon-spintronic applications and highlighted the main added values of those materials compared to metallic one: their low magnetic losses. This property makes them interesting especially for magnon-spintronic applications. We presented recent advances in terms of material science and showed that both PMA and in-plane magnetized ultrathin MI could be elaborated. However one missing brick remains: an ultrathin MI combining both good dynamical properties and PMA which was, so far, not reported. This would complete the panel of materials available for magnon-spintronics applications and allow broadening the horizon of phenomena that could be observed.

After evidencing the need within the magnon-spintronics community of a low magnetic losses PMA MI we presented in the Chapter VII the elaboration and characterization of a new ultrathin MI: the Bismuth doped YIG. Ultrathin films of single crystal BiYIG of various doping in Bi have been grown on two different kinds of substrate sGGG and GGG. Structural characterization evidenced an epitaxially strained structure in our films, this strain was either tensile or compressive and lead to two types of deformations of the BiYIG cubic unit cell. Magnetic characterization showed that the magnetization within those films remained approximately the same but that depending on the Bi doping rate and the substrate of growth different anisotropies could be observed. We showed that structural and magnetic properties could be related and that the magnetic anisotropy within our films was defined by two terms: the growth induced and strain induced anisotropy. We evidenced that the anisotropy could be tuned by epitaxial strain. Magneto-optical characterisation evidenced an high Faraday Rotation coefficient (characteristic of BiYIG) in our films making it suitable for light based detection technique such as Kerr microscopy or BLS. Dynamical properties of our films were probed using FMR experiments and allow to evidence ultra-low magnetic losses which is one important criteria for magnon-spintronics applications. Interestingly even BiYIG with PMA presented damping values comparable to the one observed on state of the art ultrathin MI. At the end of this Chapter we could present a new ultrathin MI with PMA and low magnetic losses which could potentially feel the need rose in the Chapter V.

In the Chapter VIII it was necessary to confirm that this material was suitable for magnon-spintronics applications. Therefore we were interested in Pt/BiYIG bilayers. We first characterized our thin films after the Pt deposition and reported that Pt could modify (decrease) the magnetic anisotropy in our films of a constant value ($\sim 40\text{mT}$). We attributed this effect to the deposition method. Then we evidenced for in-plane magnetized BiYIG films

that a transfer of spin angular momentum is possible from the BiYIG to a NM SHE (Pt) by performing spin pumping and ISHE measurements. Then we could observe in BiYIG with PMA that a spin current from Pt to BiYIG could be absorbed or reflected by performing SMR measurements. Finally, taking advantage of the PMA, we also easily could observe AHE. All characteristics values of the different spintronic effects have been compared to the one of reported for ultrathin MI. It was shown that our films were as efficient as MI used for spintronics from previous reports. Finally low damping PMA BiYIG films have been used to observe electrical generation of coherent spinwave from auto-oscillations. This new phenomena could be achieved thanks to:

- the low magnetic damping that allow propagation of spinwave.
- PMA that allow auto-oscillation to couple with propagating spin wave modes.

This last observation evidences the relevance of BiYIG for magnon-spintronics community. It is however not the only effect that we expect to observe in BiYIG with PMA and low losses.

IX-B Outlook.

The BiYIG showed new properties and allow fulfilling the panel of available materials for spintronic applications as now both in-plane and out-of-plane magnetized low losses MI can be elaborated. Outlooks for the material within the community are multiple.

IX-B.1 Magnon-spintronics applications.

The next step in our films with PMA is to observe SOT assisted magnetic switching as it has been realised on TmIG^{108,155}. Using Kerr microscopy technique we could also image the current induced magnetization switching.

From a practical point of view as spin wave dispersion relation is tuned by the magnetic anisotropy the PMA would also be an advantage for magnonic applications. It would for instance allow observing the propagation of forward volume waves in the material without a large bias magnetic field.

BiYIG could also be a suitable material for spin wave filter or magnonic crystals patterning. Thanks to the high FR BLS imaging techniques would be easy to use in order to image the spin wave propagation within those magnonic devices.

Taking profit of the large magneto-optical activity in BiYIG innovative schemes for on-chip magnon-light coupler could be now developed, bridging the field of magnonics to the one of photonics.

IX-B.2 New magnetic insulators for spintronics.

Now we evidence that different magnetic anisotropy could be observed in our films an even more fine tuning of those properties would be desirable. This could be achieved using stacks of BiYIG and YIG multilayers with different thicknesses, taking profit of the interfacial anisotropy. Moreover coupling of those different layers could maybe give rise to SOC based phenomena such as DMI.

Finally the field of PMA MI for magnon-spintronics application is not limited to the Iron Garnet and other materials with very strong uniaxial anisotropy such as hexaferrite could be used for magnon-spintronics applications which would allow generation of THz range spin wave and broaden the spectrum of magnonic applications

Annexe

A. Commutation rules for the spin dynamic equation.

The commutator $[\mathbf{S}, \mathcal{H}_t]$ is written:

$$[\mathbf{S}, \mathcal{H}_t] = \mu_0 \frac{g\mu_B}{\hbar} [\mathbf{S}, \mathbf{S} \cdot \mathbf{H}] = \mu_0 \frac{g\mu_B}{\hbar} [\mathbf{S}, S_x H_x] + [\mathbf{S}, S_y H_y] + [\mathbf{S}, S_z H_z]$$

For the z component of the spin this gives :

$$\begin{aligned} [S_z, \mathcal{H}_t] &= [S_z, S_z H_z] + [S_z, S_y H_y] + [S_z, S_x H_x] \\ &= S_z \cdot (S_z H_z) - (S_z H_z) \cdot S_z + S_z \cdot (S_x H_x) - (S_x H_x) \cdot S_z + S_z \cdot (S_y H_y) - (S_y H_y) \cdot S_z \\ &= S_z \cdot (S_z H_z) - (H_z S_z) \cdot S_z + S_z \cdot (S_x H_x) - (H_x S_x) \cdot S_z + S_z \cdot (S_y H_y) - (H_y S_y) \cdot S_z \\ &= \mathbf{H}_z [S_z, S_z] - H_x [S_x, S_z] + H_y [S_y, S_z] \\ &= i\hbar (H_x S_y - H_y S_x) \\ &= i\hbar (\mathbf{H} \times \mathbf{S}) \cdot \mathbf{z} \end{aligned}$$

Similar calculation along the other y and x axis gives the final result

$$[\mathbf{S}, \mathcal{H}_t] = \mu_0 \frac{g\mu_B}{\hbar} i\mathbf{H} \times \mathbf{S}$$

B. Calculation of the relaxed structure lattice parameter with a uniform and homogeneous strain model.

In order to obtain the relaxed lattice parameter a_0 from XRD scans of a strained structure some assumptions are necessary. In our case those are the following :

- The substrate has a cubic structure.
- The relaxed structure is cubic: $a_0^\perp = a_0^\parallel$, which is characteristic of a garnet structure.
- The same BiYIG target can (and does) lead to different lattice parameter if grown on different substrate: $a_0^{BiYIG//sGGG} \neq a_0^{BiYIG//GGG}$.
- The strain is isotropic in the plane of the material.
- There is no strain in the out-of-plane direction.

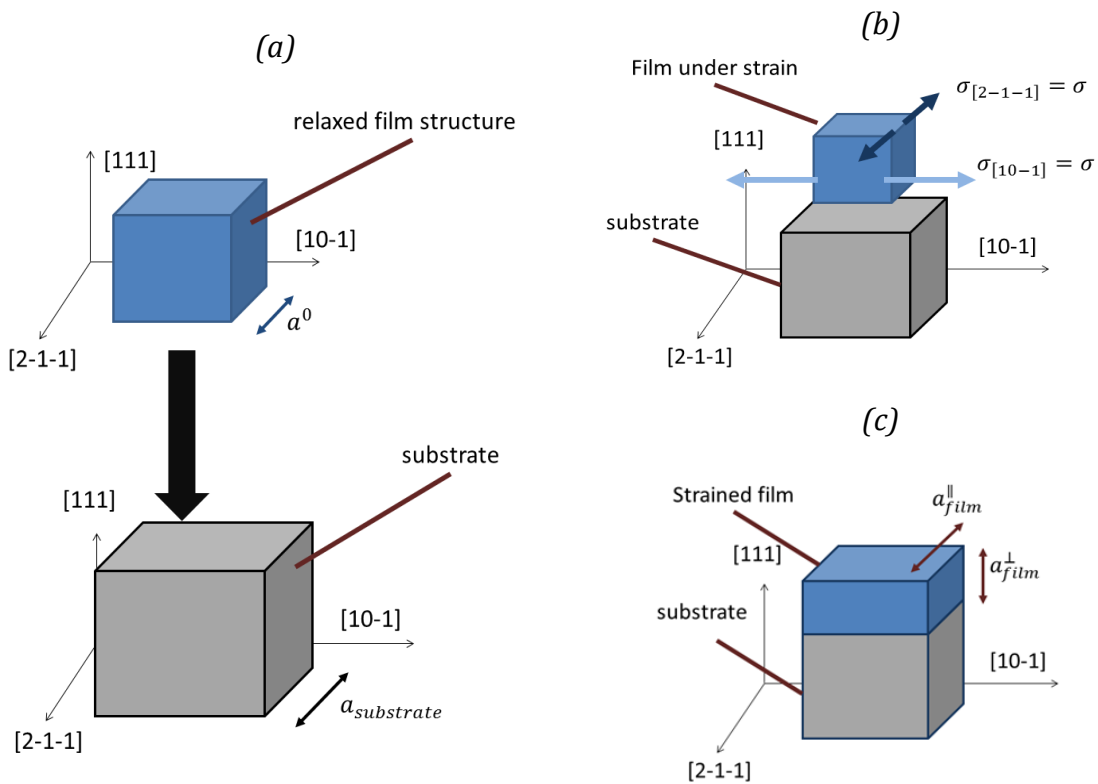


Figure 0-1 Scheme of the growth under strain. The cubic relaxed structure is deposited on a cubic substrate with a positive misfit (a) a uniform in-plane strain is applied by the substrate on the relaxed structure in the two in-plane directions (b) and deforms the original lattice unit cell (c).

The situation of the growth under strain is illustrated in the Figure 0-1. We point that the sketch is simplified: a cubic structure oriented in [111] out-of-plane should have a tetragonal shape and not a cubic one.

Within the elastic theory the deformation tensor and the strain in the three crystallographic directions are related by:

$$\epsilon = \begin{bmatrix} \epsilon_{[10-1]} \\ \epsilon_{[2-1-1]} \\ \epsilon_{[111]} \end{bmatrix} = \frac{1}{E} \begin{bmatrix} 1 & -\mu & -\mu \\ -\mu & 1 & -\mu \\ -\mu & -\mu & 1 \end{bmatrix} \begin{bmatrix} \sigma_{[10-1]} \\ \sigma_{[2-1-1]} \\ \sigma_{[111]} \end{bmatrix} \quad 0-1$$

Where $\epsilon_{[111]}$, $\sigma_{[111]}$, E and μ are respectively the deformation and the strain along the [111] crystallographic axis, the Young modulus (in $\text{kg.m}^{-1}\text{s}^{-1}$) and the Poisson coefficient (unit less). The 4th assumption concerning in-plane strain leads to $\sigma_{[10-1]} = \sigma_{[2-1-1]} = \sigma$ and $\sigma_{[111]} = 0$. Hence, the Equation 0-1 becomes:

$$\epsilon = \frac{1}{E} \begin{bmatrix} 1 & -\mu & -\mu \\ -\mu & 1 & -\mu \\ -\mu & -\mu & 1 \end{bmatrix} \begin{bmatrix} \sigma \\ \sigma \\ 0 \end{bmatrix} = \frac{1}{E} \begin{bmatrix} \sigma(1-\mu) \\ \sigma(1-\mu) \\ -2\mu\sigma \end{bmatrix} \quad 0-2$$

The in-plane deformation is the same along the two crystallographic axis $\epsilon_{[10-1]} = \epsilon_{[2-1-1]} = \epsilon_{\parallel}$ (which is not surprising for a cubic material under an uniform strain). The ratio between the in-plane and out-of-plane deformation is then written:

$$\frac{\epsilon_{\parallel}}{\epsilon_{\perp}} = \frac{a_{film}^{\parallel} - a_0}{a_{film}^{\perp} - a_0} = \frac{\mu - 1}{2\mu} \quad 0-3$$

Hence a_0 can be written in terms of the material constant and parameters of the strained structure:

$$a_0 = \frac{(a_{film}^{\perp} - a_{film}^{\parallel})(1 - \mu)}{1 + \mu} + a_{film}^{\parallel} \quad 0-4$$

- The in-plane lattice parameter of the film is obtained from RSM scans and due to epitaxial strain $a_{film}^{\parallel} = a_{substrate}$.
- The out-of-plane lattice parameter corresponds to the interatomic distance in the out-of-plane direction $d_{[444]}$ which can be obtained for XRD scan along the (111) direction, $a_{film}^{\perp} = 4\sqrt{3}d_{[444]}$ if we assume that the film structure is cubic (not the case due to strain deformation) the film lattice parameter would be a_{film}^{\perp} .

The strain parameter σ can be also expressed in terms of deformation ϵ_{\perp} or ϵ_{\parallel} using the Equation 0-3.

$$\sigma = -\frac{E}{2\mu} \epsilon_{\perp} = \frac{(-a_{film}^{\perp} + a_0) E}{a_0} \frac{E}{2\mu} \quad 0-5$$

$$\sigma = -\frac{E}{\mu - 1} \epsilon_{\parallel} = \frac{(-a_{film}^{\parallel} + a_0) E}{a_0} \frac{E}{\mu - 1} \quad 0-6$$

C. Derivation of the domain wall energy from the Kaplan et Gehring model.

An analytical model to obtain the dependence of the magnetic domains width (D_{width}) with respect to the thin film thickness (t_{film}) have been developed first by Kooy et Enz¹⁴⁰. This model has been simplified in a paper of Kaplan et Gerhing¹⁴¹ for the case of $D_{width} \gg t_{film}$ (ultrathin film regime). In this limit the expression of D_{width} with respect to t_{film} is:

$$D_{width} = t_{film} e^{\frac{\pi b}{2} + 1} e^{\frac{\pi D_0}{2 t_{film}}} \quad 0-7$$

With b a parameter that depends on the shape of magnetic domains ($b=-0.666$ for stripes pattern) and D_0 the dipolar length which is related to the domain wall energy (σ_{DW}) and the magnetization of the film (M_S).

$$D_0 = \frac{2\sigma_{DW}}{\mu_0 M_S^2} \quad 0-8$$

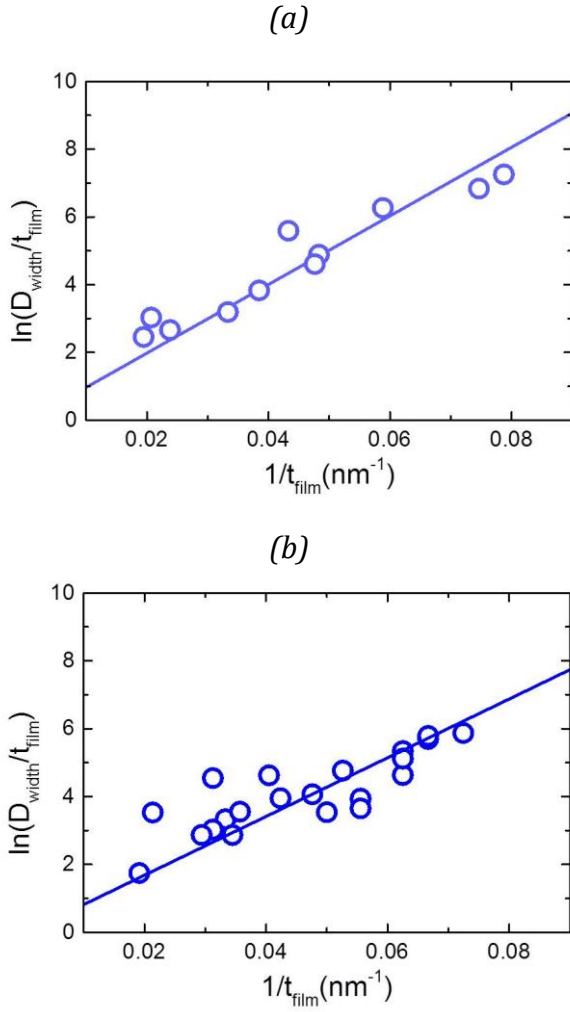
Moreover σ_{DW} can be expressed in terms of effective anisotropy K_{eff} (Equation III-2) which allows relating D_{width} to K_{eff} :

$$D_{width} = t_{film} e^{\frac{\pi b}{2} + 1} e^{\frac{4\pi \sqrt{AK_{eff}}}{t_{film} \mu_0 M_S^2}} \quad 0-9$$

In order to obtain σ_{DW} from D_{width} the dependence of $\ln\left(\frac{D_{width}}{t_{film}}\right)$ with $\frac{1}{t_{film}}$ can be linearly fitted:

$$\ln\left(\frac{D_{width}}{t_{film}}\right) = \frac{\pi}{2} b + 1 + \frac{\pi D_0}{2 t_{film}} = \frac{\pi}{2} b + 1 + \frac{\pi \sigma}{\mu_0 M_S^2 t_{film}} \quad 0-10$$

The Figure 0-2 presents the linear fit of $\ln\left(\frac{D_{width}}{t_{film}}\right)$ with $\frac{1}{t_{film}}$ for PMA Bi_xY_{3-x}IG//sGGG ($x=0.7$ in Figure 0-2(a) and $x=1$ in Figure 0-2(b)) with the values of σ and D_0 derived from the fit (Figure 0-2(c)).



(c)

Doping in Bi	σ (mJ/m ²)	D ₀ (nm)
X=0.7	0.86	59 nm
X=1	0.65	53 nm

Figure 0-2 $\ln\left(\frac{D_{width}}{t_{film}}\right)$ vs $\frac{1}{t_{film}}$ for (a) $Bi_{0.7}Y_{2.3}IG$ and (b) $Bi_1Y_2IG //sGGG$ thin films, values extracted from the fit are the domain wall energy and the dipolar length (c)

In order to compare the value of σ for two different Bi concentration it is necessary to give the relative error: $\frac{\Delta\sigma}{\sigma}$. This error has two origins: the fit uncertainty and the error made on the evaluation of M_s by the SQUID.

The fit uncertainty gives the error on the dipolar length ΔD_0 from the differentiations of the Equation 0-10:

$$\Delta\left(\ln\left(\frac{D_{width}}{t_{film}}\right)\right) = \frac{\Delta D_0}{2t_{film}} \quad 0-11$$

And the error made on the dipolar length ΔD_0 is linked with the dipolar length error:

$$\frac{\Delta\sigma}{\sigma} = \frac{\Delta D_0}{D_0} + 2\left(\frac{\Delta M_s}{M_s}\right) \quad 0-12$$

The error on the fit is 10% and the error on M_s is 10%. The total error on σ is then 30%.

D. Derivation of ΔH_0^{inhomo} for in-plane FMR.

The expression of $\Delta H_0^{inhomo} = \frac{\partial H_{res}}{\partial M_{eff}} \Delta M_{eff}$ can be found for the case of in-plane FMR excitation by using the in-plane Kittel law:

$$\frac{(2\pi f)^2}{\gamma^2} = \mu_0^2 H_{res} (H_{res} + M_{eff}) \quad 0-13$$

Due to magnetic inhomogeneities $M_{eff} \rightarrow M_{eff}^0 + \Delta M_{eff}$. Deriving the expression above with respect to M_{eff} gives:

$$\begin{aligned} \frac{4\pi^2 f_{res}}{\gamma^2} \frac{2\partial f}{\partial M_{eff}} \Delta M_{eff} = \\ \mu_0^2 \left(\left(\frac{\partial H_{res}}{\partial M_{eff}} \Delta M_{eff} \right) (H_{res} + M_{eff}) + H_{res} \left(\frac{\partial H_{res}}{\partial M_{eff}} \Delta M_{eff} + \Delta M_{eff} \right) \right) \end{aligned} \quad 0-14$$

In our experiment the f_{res} is fixed and does not depend on any variation of M_{eff} thus:

$\frac{2\partial f}{\partial M_{eff}} = 0$. From the expression 0-10 it is then possible to express $\frac{\partial H_{res}}{\partial M_{eff}}$ in terms of M_{eff} and H_{res} :

$$\left(\frac{\partial H_{res}}{\partial M_{eff}} \Delta M_{eff} \right) = \left(\frac{H_{res} \Delta M_{eff}}{2H_{res} + M_{eff}} \right) \quad 0-15$$

To ensure that $M_{BiYIG} \parallel H_{ext}$ f_{res} has been chosen to satisfy $H_{res} \gg M_{eff}$. The parameter ΔH_0^{inhomo} for in-plane FMR excitation is then written:

$$(\Delta H_0^{inhomo}) = \left(\frac{H_{res} \Delta M_{eff}}{2H_{res} + M_{eff}} \right) \approx \frac{1}{2} \Delta M_{eff} \quad 0-16$$

E. Brillouin Light Scattering (BLS) **characterisation of BIYIG with and without Pt** **capping.**

BLS measurements have been performed in Paris 13, in order to investigate the reason for the change in the domains width (D_{width}) for thin films partly covered with Pt. The purpose of BLS measurements was to determine the origin of the change in σ when a Pt top layer was sputtered on our films.

In the presence of Dzyaloshinskii-Moriya interaction (DMI) the domain wall energy σ has to be modified from the one of Equation III-2 and is written:

$$\sigma = 4 \sqrt{K_{eff}A - \pi D_{DMI}} \quad 0-17$$

With D_{DMI} is the DMI parameter in in J/m^2 .

In this conditions a modification of σ can be due to a change of D_{DMI} or K_{eff} . A way to estimate the DMI term is BLS measurements^{156,157}

The BLS technique is a light based detection technique where a laser beam of a fixed wavelength ($\lambda = 532$ nm in this experiment) is sent on a magnetic material under an external magnetic field ($\mu_0 H_{ext}$). Depending on the direction and the intensity of $\mu_0 H_{ext}$ the photons of the laser can scatter on thermal magnon and create (or annihilate) a magnon of frequency f_{sw} .

The out-of-plane angle of $\mu_0 H_{ext}$ will fix the \mathbf{k} vector of the magnon. The presence of DMI would show as a non-reciprocity of the magnon dispersion relation i.e the two magnons \mathbf{k} and $-\mathbf{k}$ would have different frequencies.

A typical BLS spectrum is shown in Figure 0-3. Peaks labeled $M^+(M^-)$ (in blue) corresponds the annihilation (creation) of the magnon corresponding to $f_{sw}(M^+)$ (or $f_{sw}(M^-)$). The frequency $f_{sw}(M^+)$ ($f_{sw}(M^-)$) is called Stokes (anti Stokes) frequency.

The value of f depends on $\mu_0 H_{ext}$ direction and intensity and gives information on the anisotropy of the sample. The difference $f_{sw}(M^+) - f_{sw}(M^-)$ is related to the presence of a DMI term^{156,157}.

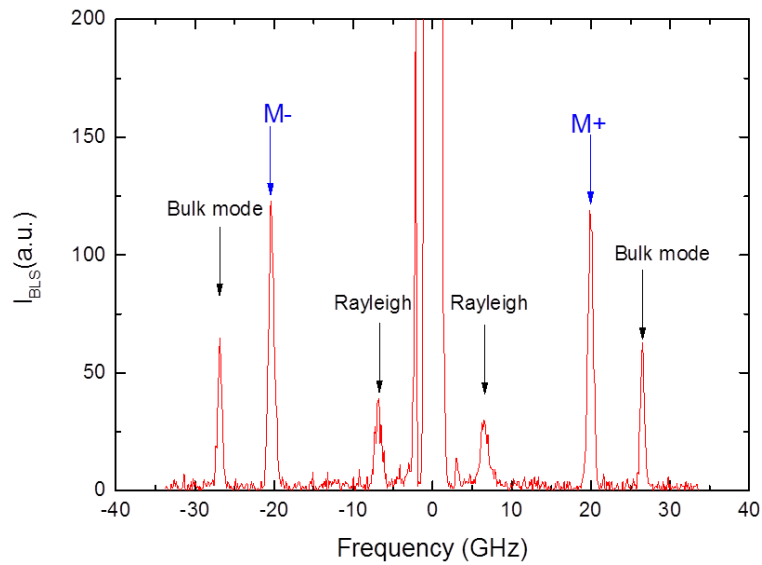


Figure 0-3. Typical BLS spectrum obtained on Pt(5nm)/BiYIG(16nm)//sGGG sample with $\mu_0 H_{ext} = 0.6T$ oriented at 30° in the out-of-plane direction.

The team of M. Ben Sherif performed measurements on samples covered on one side only with Pt.

We display here measurements performed on a 16 nm thick Bi₁Y₂IG//sGGG sample for which the Kerr microscopy image was showing a clear change in D_{width} depending on the region (Pt or No Pt) as shown in Figure 0-4(a). The variation in D_{width} is about 50%: $D_{width}^{Pt} = 0.8\mu m$ (Figure 0-4 (c)) and $D_{width}^{No Pt} = 1.7\mu m$ (Figure 0-4(b)) which corresponds to a variation of σ due to Pt top layer (using Equation 0-8 and 0-9) of $\Delta\sigma_{Pt} = 0.1 \text{ mJ/m}^2$. If the change would be only due to anisotropy variation it would correspond to a field of $\Delta\mu_0 H_{Ku}^{Pt} = 0.04 \text{ mT}$ (Equation VII-5).

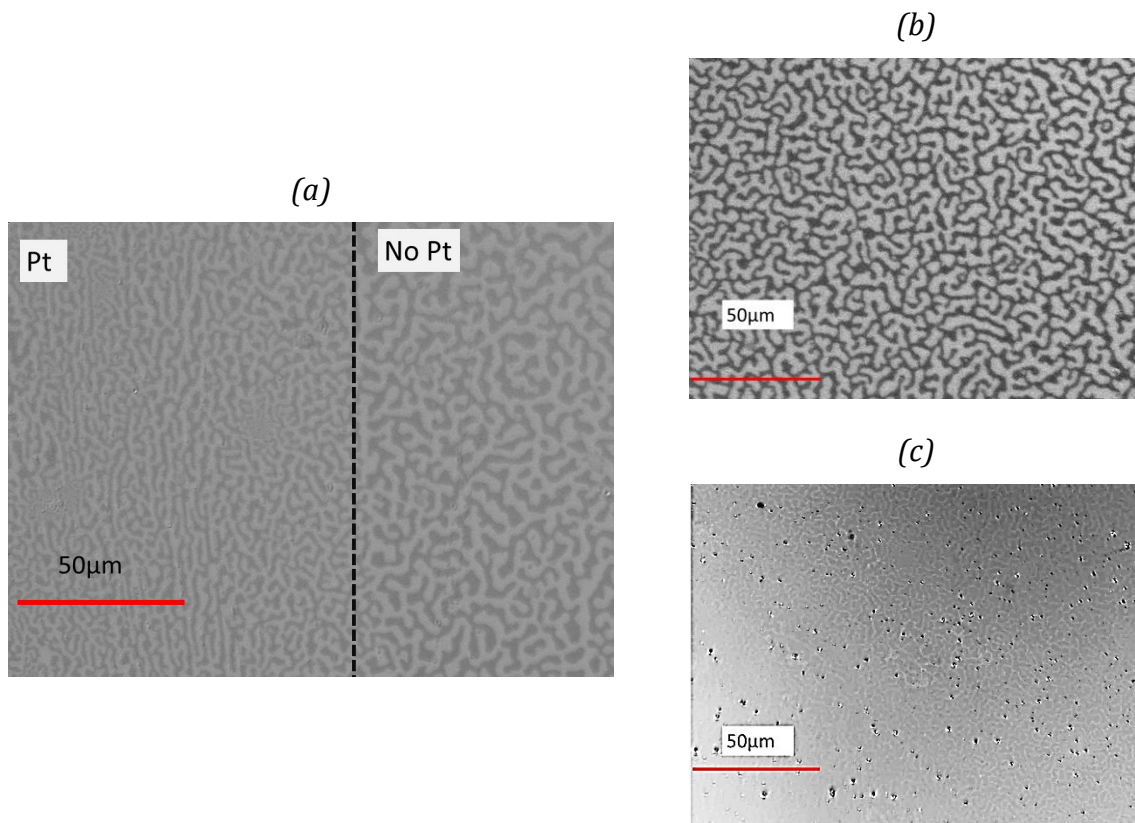


Figure 0-4 (a) Kerr microscopy image of BiYIG(16 nm)/sGGG sample covered with 3 nm Pt at the boundary between the Pt and not Pt covered zone, in the non-covered zone and in the Pt covered zone only.

The Figure 0-3 displays a BLS spectrum for the sample capped with Pt, $\mu_0 H_{ext}$ is oriented at 30° from the sample surface. The difference between the Stokes and Anti Stokes frequency remains in the error bar which suggests the absence of DMI in our films.

The Figure 0-5 presents the field dependence of the Stokes and Anti Stokes frequencies for the region covered with Pt or not. This corresponds to a spin wave dispersion curve from which it is possible to extract $\mu_0 H_{Ku}$. There is a measurable difference in the dispersion relation if the region has or not a top Pt layer corresponding to a modification of $\mu_0 H_{Ku}$ and not of D_{DMI} . The variation of $\mu_0 H_{Ku}^{Pt}$ in Pt is estimated of 40mT from the difference between the anisotropy values extracted from the spin wave dispersion relation: $\mu_0 H_{Ku}^{Pt/BiYIG} = 160\text{mT}$ and $\mu_0 H_{Ku}^{BiYIG} = 200\text{mT}$. This value is coherent with value derived using the variation of σ (see above).

BLS measurements allow to conclude that in Pt/BiYIG the variation in σ is due to anisotropy change and not to a Pt induced DMI term.

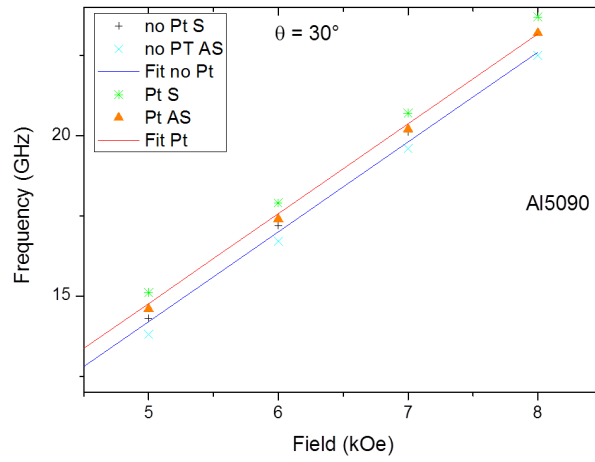


Figure 0-5-Spin wave dispersion relation for region covered (in red) and not covered (in blue) with Pt

X Résumé en français.

Cette partie présente un bref résumé de la thèse en français.

X-A Introduction.

Cette thèse porte sur la croissance, la caractérisation et les applications magnon-spintronique de films ultrafins (quelques dizaines de nanomètres) de grenats magnétiques. Ces grenats sont des isolants connus depuis les années 60 pour leurs faibles pertes magnétiques. Pour cette raison ils ont été largement utilisés pour des applications dans le domaine de l'électronique radio fréquence. Parmi ces grenats le matériau de référence en terme de pertes magnétiques est le grenat de fer Yttrium³ ($\text{Y}^3\text{Fe}^5\text{O}_{12}$ ou YIG) qui, sous sa forme massive, possède l'amortissement de Gilbert (α) le plus faible: $\alpha_{\text{YIG}} = 2 \cdot 10^{-5}$.

Jusqu'à la dernière décennie détecter, manipuler et générer une dynamique d'aimantation dans des isolants nécessitait l'utilisation de méthodes inductives (antennes) énergivores et encombrantes. En 2010 il a été mis en évidence qu'un transfert de courant de spin entre un isolant magnétique et un métal est possible⁹⁰. Depuis lors, de nombreux travaux impliquant des isolants magnétiques et des matériaux conducteurs ont été menés et il est possible d'utiliser le transport de charge afin de modifier ou détecter l'aimantation dans un isolant^{46,55,122,128}. C'est le domaine de la magnon-spintronique. Ces effets magnon spintronique peuvent être observés dans des bicouches métal/isolant magnétique. Un terme de transfert de spin s'ajoute à l'équation de la dynamique d'aimantation de l'isolant magnétique. Ce couple additionnel est noté τ_{STT} . L'effet de ce couple sur la dynamique d'aimantation de l'isolant est inversement proportionnel aux pertes magnétiques de Gilbert et l'épaisseur de la couche magnétique. Ainsi, pour la magnon-spintronique, il est souhaitable d'avoir des films de faible épaisseur et ayant un faible amortissement magnétique.

Au cours des cinq dernières années l'ablation laser pulsée a permis d'obtenir des films ultrafins (quelques dizaines de nanomètres d'épaisseur) de YIG à faible amortissement de Gilbert ($\alpha = 2 \cdot 10^{-4}$)⁴⁶ dans lesquels il est possible d'induire des autos oscillations magnétiques via un courant de charge¹⁰³ mais aussi d'y propager des ondes de spins (générées par des méthodes inductives) sur des distances micrométriques¹¹². Cependant les applications pour ces films ultrafins de YIG sont limitées par l'anisotropie magnétique de ceux-ci: dans ces films la direction préférentielle d'aimantation dans ces films est planaire. La motivation de cette thèse est de répondre au besoin en terme matériau pour la magnon-spintronique et d'élaborer un matériau magnétique ultrafin, à faibles pertes magnétiques et à anisotropie magnétique perpendiculaire.

Au cours des années 70, les études sur des films micrométriques de grenat dopés ont permis de mettre en évidence que le grenat de fer Yttrium substitué au Bismuth (BiYIG) possédait une anisotropie perpendiculaire²⁰. De plus, le BiYIG est reconnu pour sa forte rotation Faraday dans le visible³⁷, ce qui le rend intéressant pour les méthodes expérimentales reposant sur l'interaction photon/magnons (Diffusion de Brillouin, Microscopie Kerr...)largement utilisées dans le domaine de la magnon-spintronique. Peu d'études sur la dynamique d'aimantation de ce matériau ont été menées. Cette thèse présente la croissance par ablation laser pulsée de films de $\text{Bi}_x\text{Y}_{3-x}\text{IG}$ ultrafins. Nous avons étudié quatre compositions $x=0, 0.7, 1$ et 1.5 . Des films de 7 à 120 nm de BiYIG monocristallins, sans phases parasites ont été élaborés. Dans un premier temps le manuscrit présente la caractérisation des propriétés dynamiques, structurales et magnéto optiques de ces films. Dans un second temps on s'intéresse aux applications de ces films pour la magnon-spintronique.

X-B Caractérisation.

La croissance par ablation laser pulsée de ces films a été réalisée sur deux substrats différents qui sont le Grenat de Gallium Gadolinium (GGG) et le GGG substitué. Ces deux substrats sont des grenats paramagnétiques à la structure cubique (similaire à celle du BiYIG). Ils présentent deux paramètres de maille légèrement différents. Pour obtenir des films trois cibles polycristallines de BiYIG et une de YIG ont été utilisées. Le paramètre de maille du BiYIG augmente avec la concentration en Bismuth (Figure X-1(a)). Ainsi en jouant sur le type de substrat ou le type de cible utilisée il est possible d'induire des écarts de paramètre de maille cible/substrat de signe et de magnitude différents comme illustré dans la Figure X-1. Ces différences de paramètres de mailles sont à l'origine de contraintes épitaxiales et de déformations dans les films.

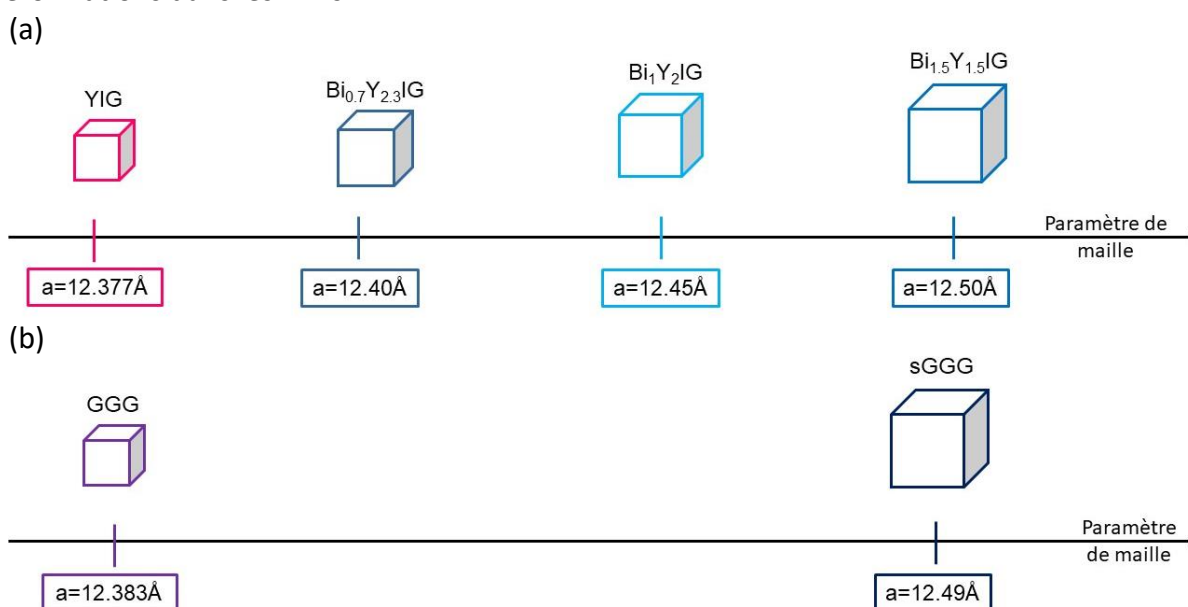


Figure X-1 Illustration de l'évolution et valeur du paramètre de maille des différentes cibles de BiYIG et de YIG (a) et des différents substrats (b) utilisés pour la réalisation des films ultra fins.

La caractérisation structurale des films a été effectuée par diffraction de rayons X (DRX). Il est possible à partir des scans $2\theta/\omega$ en configuration symétrique et à partir des cartes de réseau réciproque (RSM) d'extraire le paramètre de maille des films hors du plan et dans le plan. La Figure X-2 (a-d) présente les caractéristiques structurales des films de BiYIG élaborés sur GGG et la Figure X-2 (e-j) présente les caractéristiques structurales des films de BiYIG élaborés sur sGGG. Les scans de RSM montrent un alignement du pic de diffraction du substrat et celui du film selon l'axe q_{\parallel} . Ceci traduit le fait que dans le plan les films de BiYIG ont le même paramètre de maille que celui du substrat (Figure X-2 (c,i)). Les scans de rayons en configuration symétrique permettent de distinguer le pic de diffraction du substrat et celui du film. Hors du plan le paramètre de maille du substrat et du film sont différents ((Figure X-2 (b,h)). La maille initialement cubique du BiYIG se déforme tetragonalement sous la contrainte épitaxiale du substrat. Cette déformation induit une structure tetragonale du film qui dépend de l'écart entre le paramètre de maille du substrat et de la cible ((Figure X-2 (d, j)). Selon le taux de Bismuth ou le substrat utilise différentes déformations peuvent être observées.

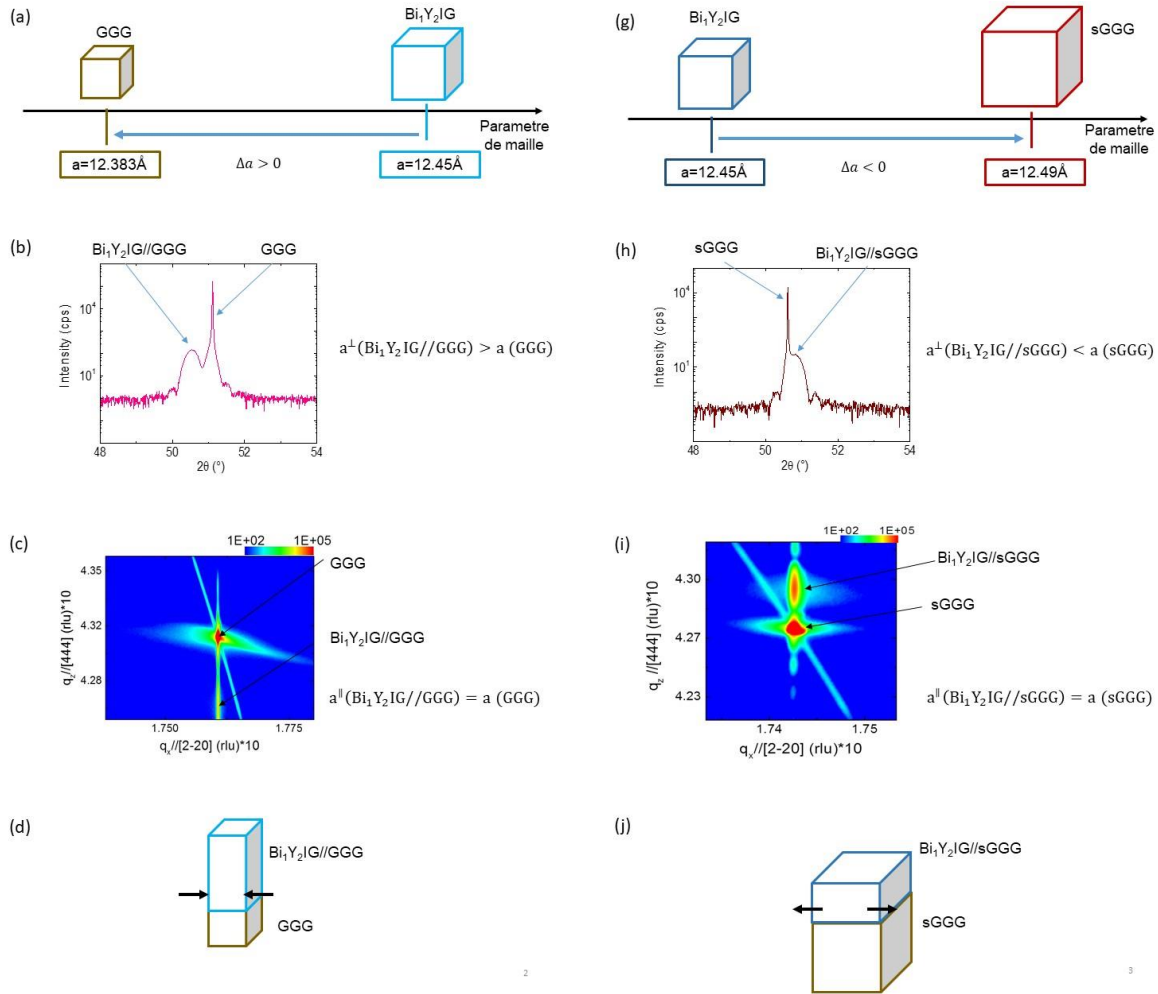


Figure X-2. DRX dans la direction hors du plan (444) (a-h) et carte de réseau réciproque dans la direction oblique (642) pour du BiYIG//GGG et BiYIG//sGGG respectivement. Due à la contrainte induite dans le plan par le substrat la maille unitaire cubique du BiYIG (a-g) se déforme (d-j). Cette déformation est mise en évidence par la DRX.

Grâce à la théorie magnéto élastique il est possible de calculer le paramètre de maille de la structure relaxée à partir du paramètre de maille dans le plan et hors du plan:

$$a_0 = a_{film}^{\parallel} - \frac{\mu - 1}{1 + \mu} (a_{film}^{\perp} - a_{film}^{\parallel}) \quad X-1$$

Dans cette expression a_0 , a_{film}^{\perp} et a_{film}^{\parallel} sont les paramètres de maille des matériaux relaxé, et du film selon la direction hors du plan et dans le plan. a_0 Est calculé grâce au coefficient de Poisson μ à partir des données de DRX.

La déformation induite par la contrainte donne lieu à un terme d'anisotropie appelé magnéto élastique K_{MO} . Le signe et l'amplitude de ce terme dépendent de la déformation du matériau Δa :

$$K_{MO} = -\frac{3}{2} \sigma \lambda_{hkl} = \frac{(a_{film}^{\parallel} - a_0)}{a_0} \cdot \frac{E}{\mu - 1} \cdot \frac{3}{2} \lambda_{111} \quad X-2$$

Dans cette expression λ_{111} et E sont respectivement le coefficient magnétostrictif et le module de Young du matériau. La contrainte σ est proportionnelle à la déformation du matériau. Ce terme magnéto élastique étant relié à l'écart entre le paramètre de maille du matériau relaxé et celui du substrat il est possible de modifier l'amplitude et le signe de ce

terme d'anisotropie en choisissant le substrat et le dopage en Bismuth adéquat. Pour une contrainte extensive (paramètre de maille du substrat plus grand que celui de la cible) le terme magnéto élastique favorise une direction préférentielle d'aimantation hors du plan et inversement pour une contrainte compressive.

La microscopie Kerr hors plan permet d'obtenir facilement l'anisotropie magnétique dans nos films grâce à la forte rotation Faraday induite par le dopage en Bismuth. Comme illustre dans la Figure X-3 la direction préférentielle d'aimantation dépend du signe de l'écart de paramètre de maille entre le substrat et le film (et donc de la contrainte induite par le substrat). Une contrainte compressive (BiYIG//GGG et Bi_{1.5}Y_{1.5}IG//sGGG) résulte en une anisotropie planaire des films tandis qu'une contrainte extensive (Bi₁Y₂IG//sGGG et Bi_{0.7}Y₂IG//sGGG) correspond à une anisotropie perpendiculaire comme illustre dans la Figure X-3. Le signe du terme magnéto élastique donne la direction préférentielle d'aimantation dans les films de BiYIG.

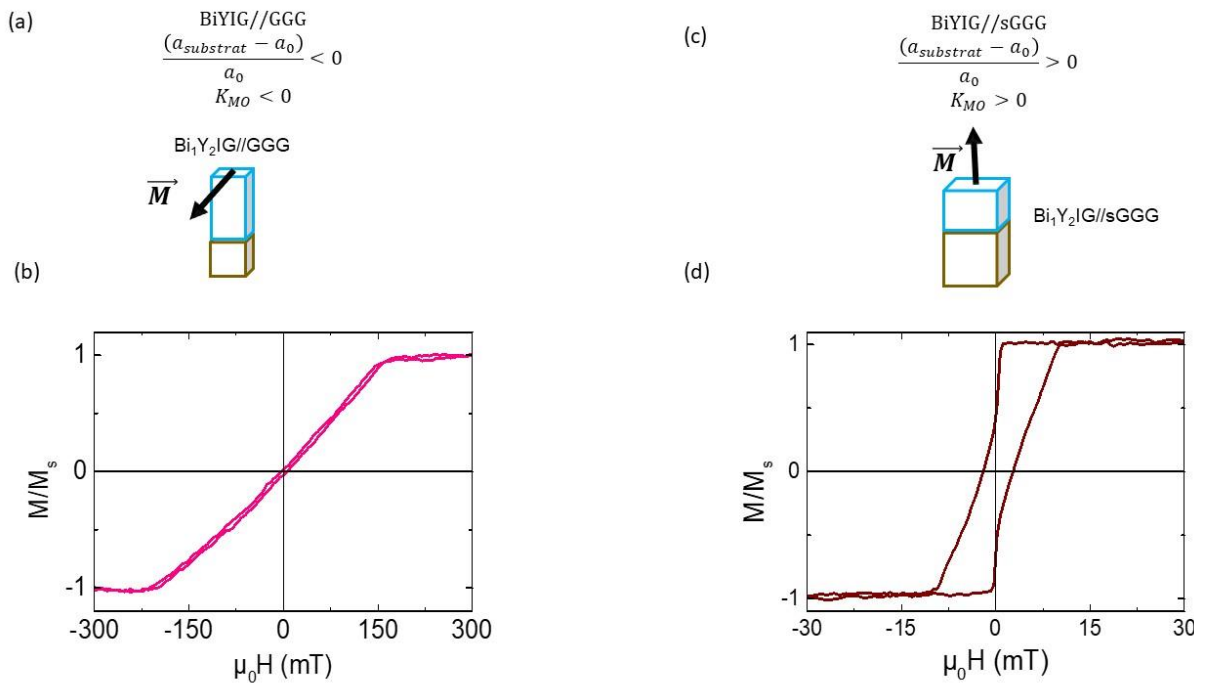


Figure X-3(b-d) Courbe d'hystérésis réalisées par microscopie Kerr pour des films de BiYIG soumis à deux types de contrainte différentes. Pour le cas d'une contrainte compressive (a) l'anisotropie est planaire, pour une contrainte extensive (c) l'anisotropie est perpendiculaire.

Dans les films à anisotropie perpendiculaire il est possible d'observer des domaines magnétiques de largeur micrométrique. Comme illustre dans la Figure X-4 leur largeur décroît exponentiellement en augmentant l'épaisseur du film. Ceci est attendu pour des films magnétiques dont la largeur des domaines est très grande devant l'épaisseur des films (modélé Kaplan et Gerhing)¹⁴¹.

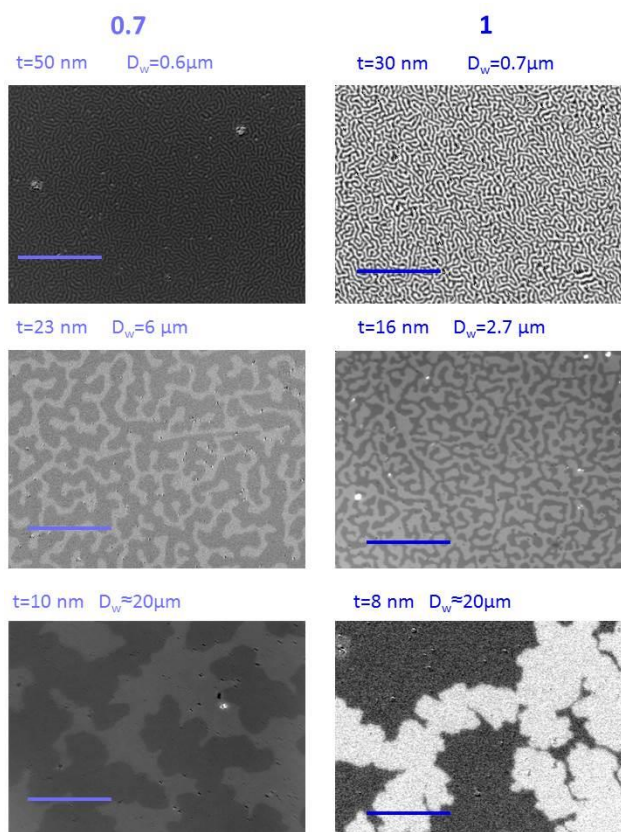


Figure X-4 Evolution de la taille des domaines magnétiques à rémanence pour les films de BiYIG à différent dopage et différentes épaisseurs. La largeur des domaines croît exponentiellement à mesure que l'épaisseur du film décroît, comme prévu par le modèle de Kaplan et Gerhing¹⁴¹

Stabiliser une anisotropie magnétique hors plan nécessite toutefois de compenser complètement le champ démagnétisant avec un terme uni-axial positif. Ce dernier est mesuré dans nos films en utilisant la technique de la résonance ferromagnétique (FMR) en géométrie plane. En comparant ce terme à l'anisotropie magnéto élastique calculée à partir des données de DRX on constate que le terme magnéto élastique n'est pas suffisant pour expliquer la direction d'aimantation dans nos films. Un terme supplémentaire d'anisotropie positif : l'anisotropie de croissance est nécessaire. Ce terme a été observé dans des films micrométriques de BiYIG élaborés par épitaxie en phase liquide²⁰. Pour obtenir des informations sur la dynamique d'aimantation la technique de FMR est utilisée. Dans les films à direction d'aimantation facile dans le plan des mesures en géométrie plane sont suffisantes pour obtenir l'amortissement de Gilbert. Le paramètre α mesuré dans ces films est un peu plus important que celui des meilleurs films de YIG. Pour les films à aimantation perpendiculaire la largeur de raie mesurée en FMR en configuration plane reste constante quel que soit la fréquence d'excitation et ne permet donc pas d'extraire les pertes magnétiques à partir de la formule de Gilbert :

$$\mu_0 \Delta H = \mu_0 \Delta H_0 + \frac{\alpha 2\pi f_{res}}{\gamma} \quad X-3$$

Dans cette formule ΔH est la largeur de raie mesurée pour la fréquence d'excitation f_{res} , le terme γ est le facteur gyromagnétique. Les deux termes α et ΔH_0 sont l'amortissement de Gilbert et le deuxième est la largeur de raie inhomogène. Le terme de Gilbert correspond aux pertes intrinsèques du matériau. Le terme inhomogène est lié aux pertes extrinsèques et

notamment aux inhomogénéités magnétiques au sein du matériau. L'amplitude de ce terme dépend de la fréquence et de la géométrie d'excitation FMR. Pour des films à anisotropie perpendiculaire en configuration planaire ce terme est dominant par rapport au terme intrinsèque α et la largeur de raie ne dépend pas linéairement de la fréquence d'excitation comme illustré dans la Figure X-5(a). Nous avons donc minimisé le terme inhomogène en modifiant la géométrie d'excitation FMR, on retrouve ainsi la dépendance linéaire de la largeur de raie à la fréquence d'excitation permettant d'obtenir l'amortissement magnétique. Comme illustre dans la Figure X-5 (b) l'amortissement magnétique des films à aimantation perpendiculaire est comparable à celui des films de YIG non dopés dans lesquels il était possible d'observer des autos oscillations.

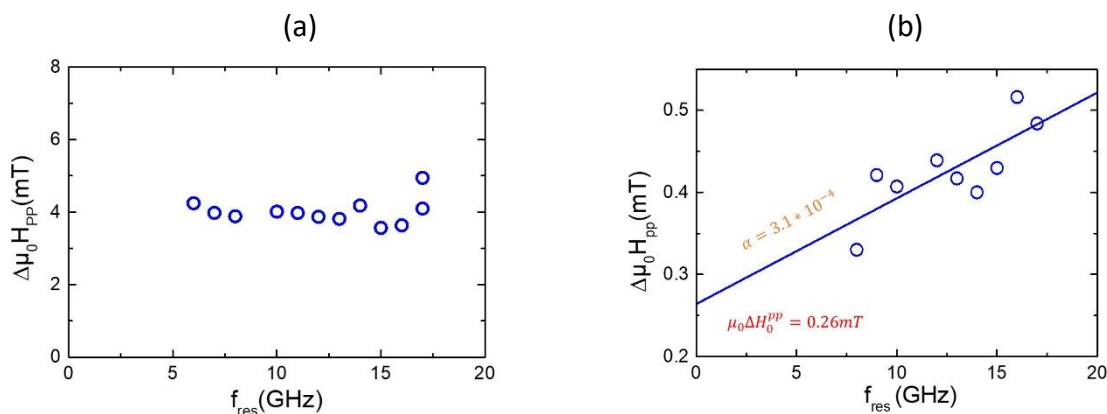


Figure X-5. Evolution de la largeur de raie vs la fréquence de résonance pour des films à aimantation perpendiculaire pour (a) la géométrie d'excitation planaire et (b) la géométrie minimisant le terme inhomogène

Ainsi, les films de YIG dopés au Bismuth d'une dizaine de nanomètre d'épaisseur ont été élaborés par ablation laser pulsée, en combinant l'anisotropie de croissance et l'anisotropie de contrainte il est possible de stabiliser une anisotropie perpendiculaire dans ces films. Les caractérisations magnétiques montrent que ces films ont un amortissement de Gilbert similaire aux films de YIG non dopés. Ces films peuvent donc être utilisés pour des applications magnons spintroniques comme les films de YIG.

X-C Applications.

En combinant ces films de BiYIG avec une couche de Platine il est possible d'observer différents effets spintroniques mettant en évidence un transfert de courant de spin entre le Platine et le BiYIG. Ces phénomènes sont l'effet Hall de spin inverse, la magnétorésistance de spin ou l'effet Hall anormal.

Grâce au faible amortissement de Gilbert dans ces films il est également possible d'observer des auto oscillations induites par le courant (Figure X-6). Dans la zone d'excitation une forte intensité de diffusion de Brillouin est observée due à la génération d'auto oscillations par courant dans le Platine, de plus la zone de forte intensité s'étend au-delà de la zone couverte par le Platine.

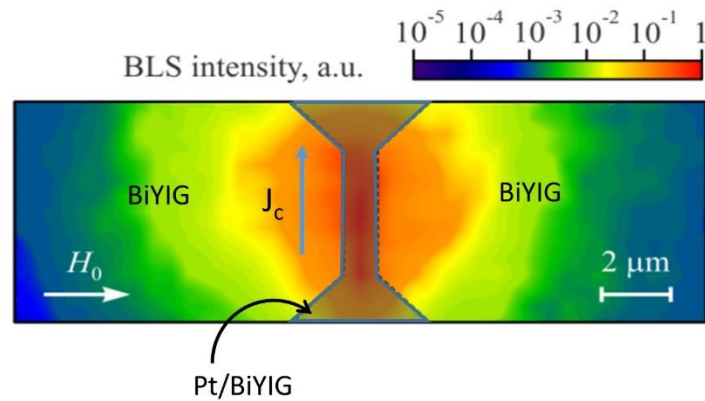


Figure X-6 Auto oscillations observées par diffusion de Brillouin sur un film de BiYIG//sGGG à anisotropie perpendiculaire

Cette extension en dehors de la zone où le courant est envoyé correspond à des ondes de spin qui sont générées à partir des auto-oscillations dans le BiYIG. Ce couplage entre l'auto-oscillation et les ondes de spin propagatives n'est possible que grâce à l'anisotropie perpendiculaire des films et n'a jamais pu être observé dans le YIG ultrafin. Les films de BiYIG à faible amortissement de Gilbert et à anisotropie perpendiculaire représentent un intérêt pour la magnon spintronique puisqu'il est maintenant possible de générer des ondes de spin grâce à des courants de charge dans un isolant magnétique. Grâce au faible amortissement de Gilbert ces ondes se propagent sur des distances micrométriques.

X-D Conclusion et perspectives.

À l'issue de cette thèse un nouveau matériau ultra fin a pu être élaboré pour lequel il est possible d'y contrôler l'anisotropie sans augmenter les pertes magnétiques. Grâce à ses propriétés uniques il est possible d'y observer des phénomènes inédits comme la génération d'ondes de spin cohérentes à partir d'un courant de charge.

Pour la suite ces films de BiYIG constituent un nouveau matériau prometteur pour la magnon spintronique et ouvrent de nombreuses possibilités dans le domaine. Ces films peuvent être utilisés pour la fabrication de composants magnoniques (filtres d'ondes de spin, guide d'onde...) mais aussi pour l'observation de phénomènes spintronique comme le retournement d'aimantation par courant de charge ou la propagation de domaines magnétiques...

Pour la suite il est possible d'envisager la croissance de bi ou tri couches de BiYIG à différents dopages pour obtenir de nouvelles propriétés et d'assurer un meilleur contrôle de l'anisotropie.

References

1. Bertaut, F., Forrat, F., Herpin, A. & Mériel, P. Etude par diffraction de neutrons du grenat ferrimagnétique Y₃Fe₅O₁₂. *Comptes Rendus Hebdomadaires des Seances l'Academie des Sci.* **243**, 898–901 (1956).
2. Sparks, M., Loudon, R. & Kittel, C. Ferromagnetic relaxation. I. Theory of the relaxation of the uniform precession and the degenerate spectrum in insulators at low temperatures. *Phys. Rev.* **122**, 791–803 (1961).
3. Sparks, M. & Kittel, C. Ferromagnetic relaxation mechanism for M_z in yttrium iron garnet. *Phys. Rev. Lett.* **4**, 232–234 (1960).
4. Geller, S. & Gilleo, M. A. The crystal structure and ferrimagnetism of yttrium-iron garnet, Y₃Fe₂(FeO₄)₃. *J. Phys. Chem. Solids* **3**, 30–36 (1957).
5. Néel, M. Louis. Propriétés magnétiques des ferrites ; ferrimagnétisme et antiferromagnétisme. *Ann. Phys.* **12**, 137–198 (1948).
6. Anderson, E. E. Molecular field model and the magnetization of YIG. *Phys. Rev.* **134**, (1964).
7. Edmonds, D. T. & Petersen, R. G. Effective Exchange Constant in Yttrium Iron Garnet. *Phys. Rev. Lett.* **4**, 92–92 (1960).
8. Klingler, S. *et al.* Measurements of the exchange stiffness of YIG films using broadband ferromagnetic resonance techniques. *J. Phys. D. Appl. Phys.* **48**, 015001 (2015).
9. Darby, M. I. & Isaac, E. D. Magnetocrystalline nisotropy of ferro- and ferrimagnetics. *IEEE Trans. Magn.* **10**, 259–304 (1974).
10. Hansen, P. Anisotropy and magnetostriction of gallium-substituted yttrium iron garnet. *J. Appl. Phys.* **45**, 3638–3642 (1974).
11. Clark, A. E. & Belson, H. S. Giant room-temperature magnetostrictions in TbFe₂ and DyFe₂. *Phys. Rev. B* **5**, 3642–3644 (1972).
12. Hubert, A. & Schäfer, R. *Magnetic Domains*. (Springer Berlin Heidelberg, 1998). doi:10.1007/978-3-540-85054-0
13. Kahl, S. Bismuth iron garnet films for magneto-optical photonic crystals. (Mikroelektronik och informationsteknik, 2004).
14. Hamrle, J. Magneto-optical Kerr effect (MOKE) Photon-photon spectroscopies (absorption) I : (2014).
15. Deltronic Crystal Isowave. Deltronic Crystal Isowave - Yttrium Iron Garnet. (2013). Available at: deltroniccrystalindustries.com/node/27/pdf.
16. Robertson, J. M., Wittekoek, S., Popma, T. J. A. & Bongers, P. F. Preparation and optical properties of single crystal thin films of bismuth substituted iron garnets for magneto-optic applications. *Appl. Phys.* (1973).
17. Wittekoek, S., Popma, T. J. A., Robertson, J. M. & Bongers, P. F. Magneto-optic spectra and the dielectric tensor elements of bismuth-substituted iron garnets at photon energies between 2.2-5.2 eV. *Phys. Rev. B* **12**, 2777–2788 (1975).
18. Cooper, R. W., Crossley, W. A., Page, J. L. & Pearson, R. F. Faraday rotation in YIG and TbIG. *J. Appl. Phys.* **39**, 565–567 (1968).
19. Hansen, P., Tolksdorf, W., Witter, K. & Robertson, J. Recent advances of bismuth

- garnet materials research for bubble and magneto-optical applications. *IEEE Trans. Magn.* **20**, 1099–1104 (1984).
20. Hansen, P. & Krumme, J.-P. Magnetic and magneto-optical properties of garnet films. *Thin Solid Films* **114**, 69–107 (1984).
 21. Hansen, P., Klages, C. -P. & Witter, K. Magnetic and magneto-optic properties of praseodymium- and bismuth-substituted yttrium iron garnet films. *J. Appl. Phys.* **60**, 721–727 (1986).
 22. Gurskii, L. I., Telesh, E. V., Kalanda, M. A., Paulenka, A. A. & Ukhov, V. A. Formation of Bi substituted Yttrium Iron Garnet Nanosized films. *Physics, Chem. Appl. Nanostructures* 511–514 (2009).
 23. Tepper, T. & Ross, C. A. Pulsed laser deposition and refractive index measurement of fully substituted bismuth iron garnet films. *J. Cryst. Growth* **255**, 324–331 (2003).
 24. Popova, E. *et al.* Magnetic anisotropies in ultrathin bismuth iron garnet films. *J. Magn. Magn. Mater.* **335**, 139–143 (2013).
 25. Kahl, S. & Grishin, A. M. Evolution of properties of epitaxial bismuth iron garnet films with increasing thickness. *J. Magn. Magn. Mater.* **278**, 244–255 (2004).
 26. Hansen, P., Klages, C. -P. & Witter, K. Magnetic and magneto-optic properties of praseodymium- and bismuth-substituted yttrium iron garnet films. *J. Appl. Phys.* **60**, 721–727 (1986).
 27. Strocka, B., Holst, P. & Tolksdorf, W. EMPIRICAL FORMULA FOR THE CALCULATION OF LATTICE CONSTANTS OF OXIDE GARNETS BASED ON SUBSTITUTED YTTRIUM- AND GADOLINIUM-IRON GARNETS. *Philips J. Res.* **33**, 186–202 (1978).
 28. Siu, G. G., Lee, C. M. & Liu, Y. Magnons and acoustic phonons in Y₃-xBi_xFe₅O₁₂. *Phys. Rev. B* **64**, 094421 (2001).
 29. Scott, G. B. & Lacklison, D. E. Magneto-optic Properties and Applications of Bismuth Substituted Iron Garnets. *IEEE Trans. Magn.* **12**, 292–311 (1976).
 30. Callen, H. GROWTH-INDUCED ANISOTROPY BY PREFERENTIAL SITE ORDERING IN GARNET CRYSTALS. *Appl. Phys. Lett.* **18**, 311–313 (1971).
 31. Callen, H. On growth-induced anisotropy in garnet crystals. *Mater. Res. Bull.* **6**, 931–938 (1971).
 32. Wolfe, R., LeCraw, R. C., Blank, S. L. & Pierce, R. D. Growth-Induced Anisotropy in Bubble Garnet Films Containing Calcium. in *AIP Conf. Proc* **34**, 172–174 (1976).
 33. Hansen, P., Klages, C.-P., Schuldt, J. & Witter, K. Magnetic and magneto-optical properties of bismuth-substituted lutetium iron garnet films. *Phys. Rev. B* **31**, 5858–5864 (1985).
 34. Fratello, V. J., Slusky, S. E. G., Brandle, C. D. & Norelli, M. P. Growth-induced anisotropy in bismuth: Rare-earth iron garnets. *J. Appl. Phys.* **60**, 2488–2497 (1986).
 35. Gyorgy, E. M., Rosencwaig, A., Blount, E. I., Tabor, W. J. & Lines, M. E. GENERAL CONDITIONS FOR GROWTH-INDUCED ANISOTROPY IN GARNETS. *Appl. Phys. Lett.* **18**, 479–480 (1971).
 36. Hansen, P., Witter, K. & Tolksdorf, W. Magnetic and magneto-optic properties of lead- and bismuth-substituted yttrium iron garnet films. *Phys. Rev. B* **27**, 6608–6625 (1983).
 37. Matsumoto, K. *et al.* Enhancement of magneto-optical Faraday rotation by bismuth substitution in bismuth and aluminum substituted yttrium–iron–garnet single-crystal films grown by coating gels. *J. Appl. Phys.* **71**, (1992).
 38. Bi, L. *et al.* On-chip optical isolation in monolithically integrated non-reciprocal optical resonators. *Nat. Photonics* **5**, 758–762 (2011).

39. Magdenko, L. *et al.* Microelectronic Engineering Wafer-scale fabrication of magneto-photonic structures in Bismuth Iron Garnet thin film. *Microelectron. Eng.* **87**, 2437–2442 (2010).
40. Oikawa, T., Suzuki, S. & Nakao, K. First-principles study of spin-orbit interactions in bismuth iron garnet. *J. Phys. Soc. Japan* **74**, 401–404 (2005).
41. Mizumoto, T., Stadler, B. J. H. & Mizumoto, T. Integrated Magneto-Optical Materials and Isolators : A Review Integrated Magneto-Optical Materials and Isolators : A Review. *IEEE Photonics J.* **6**, 1–15 (2014).
42. Vittoria, C., Lubitz, P., Hansen, P. & Tolksdorf, W. FMR linewidth measurements in bismuth-substituted YIG. *J. Appl. Phys.* **57**, 3699–3700 (1985).
43. LeCraw, R. C., Luther, L. C. & Gyorgy, E. M. Growth-induced anisotropy and damping versus temperature in narrow linewidth, 1- μ m YIG(Bi, Ca, Si) bubble films. *J. Appl. Phys.* **53**, 2481–2482 (1982).
44. Tamada, H., Kaneko, K. & Okamoto, T. Bi-Substituted LPE Garnet Films with FMR Linewidth as Small as YIG. *IEEE Transl. J. Magn. Japan* **3**, 98–103 (1988).
45. Ben Youssef, J., Legall, H. & U. P. et M. C. Characterisation and physical study of bismuth substituted thin garnet films grown by liquid phase epitaxy (LPE). (1989).
46. d’Allivy Kelly, O. *et al.* Inverse spin Hall effect in nanometer-thick yttrium iron garnet/Pt system. *Appl. Phys. Lett.* **103**, 082408 (2013).
47. Gurevich, A. G. & Melkov, G. A. *Magnetization Oscillations and Waves*. (Taylor & Francis, 1996).
48. Kasuya, T. & LeCraw, R. C. Relaxation Mechanisms in Ferromagnetic Resonance. *Phys. Rev. Lett.* **6**, 223–225 (1961).
49. Collet, M. Dynamique d’ondes de spin dans des microstructures à base de films de YIG ultra-minces : vers des dispositifs magnoniques radiofréquences. (Université Paris-Saclay, 2018).
50. Valet, T. & Fert, A. Theory of the perpendicular magnetoresistance in magnetic multilayers. *Phys. Rev. B* **48**, 7099–7113 (1993).
51. Takahashi, R. *et al.* Electrical determination of spin mixing conductance at metal/insulator interface using inverse spin Hall effect. in *Journal of Applied Physics* **111**, 07C307 (2012).
52. Wang, H. L. *et al.* Scaling of spin hall angle in 3d, 4d, and 5d metals from Y₃Fe₅O₁₂/metal spin pumping. *Phys. Rev. Lett.* (2014). doi:10.1103/PhysRevLett.112.197201
53. Chen, Y.-T. *et al.* Theory of spin Hall magnetoresistance. *Phys. Rev. B* **87**, 144411 (2013).
54. Garello, K. *et al.* Ultrafast magnetization switching by spin-orbit torques. *Appl. Phys. Lett.* **105**, 2–6 (2014).
55. Hamadeh, A. *et al.* Full Control of the Spin-Wave Damping in a Magnetic Insulator Using Spin-Orbit Torque. *Phys. Rev. Lett.* **113**, 197203 (2014).
56. Evelt, M. *et al.* Spin Hall-induced auto-oscillations in ultrathin YIG grown on Pt. *Sci. Rep.* **8**, 1–7 (2018).
57. Safranski, C. *et al.* Spin caloritronic nano-oscillator. *Nat. Commun.* **8**, 117 (2017).
58. Xiao, J. & Bauer, G. E. W. Spin-Wave Excitation in Magnetic Insulators by Spin-Transfer Torque. *Phys. Rev. Lett.* **108**, 217204 (2012).
59. Dyakonov, M. I. A .F. Ioffe Physico-Technical Institute of the Academy of Sciences of the USSR, Leningrad, USSR. **35**, 1–2 (1971).
60. Kimura, T., Otani, Y., Sato, T., Takahashi, S. & Maekawa, S. Room-temperature

- reversible spin hall effect. *Phys. Rev. Lett.* **98**, 1–4 (2007).
61. Seki, T. *et al.* Giant spin hall effect in perpendicularly spin-polarized FePt/Au devices. *Nat. Mater.* **7**, 125–129 (2008).
 62. Meyer, S. *et al.* Anomalous Hall effect in YIG|Pt bilayers. *Appl. Phys. Lett.* **106**, (2015).
 63. Tang, C. *et al.* Anomalous Hall hysteresis in Tm₃Fe₅O₁₂/Pt with strain-induced perpendicular magnetic anisotropy. *Phys. Rev. B* **94**, 1–5 (2016).
 64. Zhou, X. *et al.* Tuning magnetotransport in PdPt/Y₃Fe₅O₁₂: Effects of magnetic proximity and spin-orbit coupling. *Appl. Phys. Lett.* **105**, (2014).
 65. Zhang, S. S.-L. & Vignale, G. Nonlocal Anomalous Hall Effect. *Phys. Rev. Lett.* **116**, 136601 (2016).
 66. Dushenko, S. *et al.* Gate-Tunable Spin-Charge Conversion and the Role of Spin-Orbit Interaction in Graphene. *Phys. Rev. Lett.* **116**, 1–6 (2016).
 67. Rojas-Sánchez, J.-C. *et al.* Spin Pumping and Inverse Spin Hall Effect in Platinum: The Essential Role of Spin-Memory Loss at Metallic Interfaces. *Phys. Rev. Lett.* **112**, 106602 (2014).
 68. Sánchez, J. C. R. *et al.* Spin-to-charge conversion using Rashba coupling at the interface between non-magnetic materials. *Nat. Commun.* **4**, 2944 (2013).
 69. Jia, X., Liu, K., Xia, K. & Bauer, G. E. W. Spin transfer torque on magnetic insulators. *EPL (Europhysics Lett.)* **96**, 17005 (2011).
 70. Scheck, C., Cheng, L. & Bailey, W. E. Low damping in epitaxial sputtered iron films. *Appl. Phys. Lett.* **88**, 7–10 (2006).
 71. Prinz, G. A., Jonker, B. T., Krebs, J. J., Ferrari, J. M. & Kovanic, F. Growth of single crystal bcc α -Fe on ZnSe via molecular beam epitaxy. *Appl. Phys. Lett.* **48**, 1756–1758 (1986).
 72. Scheck, C., Cheng, L., Barsukov, I., Frait, Z. & Bailey, W. E. Low relaxation rate in epitaxial vanadium-doped ultrathin iron films. *Phys. Rev. Lett.* **98**, 1–4 (2007).
 73. Kubota, T. *et al.* Half-metallicity and Gilbert damping constant in Co₂Fe_xMn_{1-x}Si Heusler alloys depending on the film composition. *Appl. Phys. Lett.* **94**, 1–4 (2009).
 74. Liu, C., Mewes, C. K. A., Chshiev, M., Mewes, T. & Butler, W. H. Origin of low Gilbert damping in half metals. *Appl. Phys. Lett.* **95**, (2009).
 75. Shaw, J. M. *et al.* Magnetic damping in sputter-deposited Co₂MnGe Heusler compounds with A₂B₂ and L₂₁ orders: Experiment and theory. *Phys. Rev. B* **97**, 1–12 (2018).
 76. Oogane, M. *et al.* Gilbert magnetic damping constant of epitaxially grown Co-based Heusler alloy thin films. *Appl. Phys. Lett.* **96**, 1–4 (2010).
 77. Oogane, M., Kubota, T., Naganuma, H. & Ando, Y. Magnetic damping constant in Co-based full heusler alloy epitaxial films. *J. Phys. D: Appl. Phys.* **48**, (2015).
 78. Schoen, M. A. W. *et al.* Ultra-low magnetic damping of a metallic ferromagnet. *Nat. Phys.* **12**, 839–842 (2016).
 79. Schreiber, F., Pflaum, J., Frait, Z., Mühge, T. & Pelzl, J. Gilbert damping and g-factor in Fe_xCo_{1-x} alloy films. *Solid State Commun.* **93**, 965–968 (1995).
 80. Lee, A. J. *et al.* Metallic ferromagnetic films with magnetic damping under 1.4×10^{-3} . *Nat. Commun.* **8**, 1–6 (2017).
 81. Liu, T. *et al.* Ferromagnetic resonance of sputtered yttrium iron garnet nanometer films. *J. Appl. Phys.* **115**, 17A501 (2014).
 82. Onbasli, M. C. *et al.* Pulsed laser deposition of epitaxial yttrium iron garnet films with low Gilbert damping and bulk-like magnetization Pulsed laser deposition of epitaxial

- yttrium iron garnet films with low Gilbert damping and bulk-like magnetization. **106102**, (2014).
83. Park, J.-H. *et al.* Co/Pt multilayer based magnetic tunnel junctions using perpendicular magnetic anisotropy. *J. Appl. Phys.* **103**, 07A917 (2008).
 84. Yamanouchi, M. *et al.* Domain Structure in CoFeB Thin Films With Perpendicular Magnetic Anisotropy. *IEEE Magn. Lett.* **2**, 3000304–3000304 (2011).
 85. Devolder, T. *et al.* Damping of $\text{Co}_x\text{Fe}_{80-x}\text{B}_{20}$ ultrathin films with perpendicular magnetic anisotropy. *Appl. Phys. Lett.* **102**, 022407 (2013).
 86. Rantschler, J. O. *et al.* Effect of 3d, 4d, and 5d transition metal doping on damping in permalloy thin films. *J. Appl. Phys.* **101**, (2007).
 87. Wu, H. *et al.* Magnon Valve Effect between Two Magnetic Insulators. *Phys. Rev. Lett.* **120**, 1–6 (2018).
 88. Shang, T. *et al.* Effect of NiO inserted layer on spin-Hall magnetoresistance in Pt/NiO/YIG heterostructures. *Appl. Phys. Lett.* **109**, 032410 (2016).
 89. Zhou, H. *et al.* Spin pumping in the nonlinear dynamic regime of a Pt/Y₃Fe₅O₁₂ heterostructure. *Appl. Phys. Lett.* **108**, (2016).
 90. Kajiwara, Y. *et al.* Transmission of electrical signals by spin-wave interconversion in a magnetic insulator. *Nature* **464**, 262–266 (2010).
 91. Rao, Y.-H. *et al.* Liquid phase epitaxy magnetic garnet films and their applications. *Chinese Phys. B* **27**, 086701 (2018).
 92. Dubs, C. *et al.* Sub-micrometer yttrium iron garnet LPE films with low ferromagnetic resonance losses. *J. Phys. D: Appl. Phys.* **50**, (2017).
 93. Mendes, J. B. S. *et al.* Spin-Current to Charge-Current Conversion and Magnetoresistance in a Hybrid Structure of Graphene and Yttrium Iron Garnet. *Phys. Rev. Lett.* **115**, 1–5 (2015).
 94. Beaulieu, N. *et al.* Temperature Dependence of Magnetic Properties of an 18-nm-thick YIG Film Grown by Liquid Phase Epitaxy: Effect of a Pt Overlayer. (arXiv:1808.05785v2 [cond-mat.mtrl-sci] UPDATED).
 95. Wang, H., Du, C., Hammel, P. C. & Yang, F. Spin transport in antiferromagnetic insulators mediated by magnetic correlations. *Phys. Rev. B - Condens. Matter Mater. Phys.* (2015). doi:10.1103/PhysRevB.91.220410
 96. Du, C., Wang, H., Hammel, P. C. & Yang, F. Y₃Fe₅O₁₂ spin pumping for quantitative understanding of pure spin transport and spin Hall effect in a broad range of materials (invited). *J. Appl. Phys.* **117**, (2015).
 97. Bhoi, B. *et al.* Stress-induced magnetic properties of PLD-grown high-quality ultrathin YIG films. *J. Appl. Phys.* **123**, (2018).
 98. Kubota, M. *et al.* Systematic control of stress-induced anisotropy in pseudomorphic iron garnet thin films. *J. Magn. Magn. Mater.* **339**, 63–70 (2013).
 99. Jungfleisch, M. B. *et al.* Thickness and power dependence of the spin-pumping effect in $\langle \text{mrow} \langle \text{msub} \langle \text{mi mathvariant="normal"} \rangle \langle \text{mn} \rangle 3 \langle \text{mn} \rangle \langle \text{msub} \rangle \langle \text{msub} \langle \text{mi} \rangle \text{Fe} \langle \text{mn} \rangle 5 \langle \text{mn} \rangle \langle \text{msub} \rangle \langle \text{msub} \langle \text{mi} \rangle \text{mathvariant="normal"} \rangle \text{O} \langle \text{mn} \rangle 12 \langle \text{mn} \rangle \langle \text{msub} \rangle \langle \text{mrow} \rangle \langle \text{math} \rangle \rangle \rangle$ /Pt heter. *Phys. Rev. B* **91**, 134407 (2015).
 100. Sposito, A., May-Smith, T. C., Stenning, G. B. G., de Groot, P. A. J. & Eason, R. W. Pulsed laser deposition of high-quality μm -thick YIG films on YAG. *Opt. Mater. Express* **3**, 624 (2013).
 101. Manuilov, S. A. & Grishin, A. M. Pulsed laser deposited Y₃Fe₅O₁₂ films: Nature of

- magnetic anisotropy II. *J. Appl. Phys.* **108**, (2010).
102. Hauser, C. *et al.* Yttrium Iron Garnet Thin Films with Very Low Damping Obtained by Recrystallization of Amorphous Material. *arXiv:1502.06724v2* 1–13 (2016). doi:10.1038/srep20827
 103. Collet, M. *et al.* Generation of coherent spin-wave modes in yttrium iron garnet microdiscs by spin–orbit torque. *Nat. Commun.* **7**, 10377 (2016).
 104. Wang, H., Du, C., Hammel, C. & Yang, F. Strain-Tunable Magnetocrystalline Anisotropy in Epitaxial Y₃Fe₅O₁₂ Thin Films. *Phys. Rev. B* **89**, 134404 (2013).
 105. Fu, J. *et al.* Epitaxial growth of Y₃Fe₅O₁₂ thin films with perpendicular magnetic anisotropy. *Appl. Phys. Lett.* **110**, 202403 (2017).
 106. Yoshimoto, T. *et al.* Static and Dynamic Magnetic Properties of Single-Crystalline Yttrium Iron Garnet Films Epitaxially Grown on Three Garnet Substrates. *Adv. Electron. Mater.* **1800106**, 1–8 (2018).
 107. Kubota, M. *et al.* Stress-induced perpendicular magnetization in epitaxial iron garnet thin films. *Appl. Phys. Express* **5**, 4–6 (2012).
 108. Quindeau, A. *et al.* Tm₃Fe₅O₁₂/Pt Heterostructures with Perpendicular Magnetic Anisotropy for Spintronic Applications. doi:10.1002/aelm.201600376
 109. Wu, C. N. *et al.* High-quality single-crystal thulium iron garnet films with perpendicular magnetic anisotropy by off-axis sputtering. *Cit. AIP Adv.* **8**, (2018).
 110. Wang, C. T. *et al.* Controlling the magnetic anisotropy in epitaxial Y₃Fe₅O₁₂ films by manganese doping. *Phys. Rev. B* **96**, 224403 (2017).
 111. Li, P. *et al.* Spin-orbit torque-assisted switching in magnetic insulator thin films with perpendicular magnetic anisotropy. *Nat. Commun.* **7**, 12688 (2016).
 112. Collet, M. *et al.* Spin-wave propagation in ultra-thin YIG based waveguides. *Appl. Phys. Lett.* **110**, (2017).
 113. Chudo, H. *et al.* Spin pumping efficiency from half metallic Co₂MnSi. *J. Appl. Phys.* **109**, (2011).
 114. Pirro, P. *et al.* Spin-wave excitation and propagation in microstructured waveguides of yttrium iron garnet/Pt bilayers. *Appl. Phys. Lett.* **104**, 1–5 (2014).
 115. Wesenberg, D., Liu, T., Balzar, D., Wu, M. & Zink, B. L. Long-distance spin transport in a disordered magnetic insulator. *Nat. Phys.* (2017). doi:10.1038/nphys4175
 116. Chumak, A. V., Serga, A. A. & Hillebrands, B. Magnonic crystals for data processing. *J. Phys. D: Appl. Phys.* **50**, (2017).
 117. Karenowska, A. D., Chumak, A. V., Serga, A. A. & Hillebrands, B. Magnon spintronics. in *Handbook of Spintronics* (2015). doi:10.1007/978-94-007-6892-5_53
 118. Lauer, V., Neb, R., Chumak, A. & Hillebrands, B. Improvement of the Yttrium Iron Garnet/Platinum Interface for Spin Pumping-Based Applications.
 119. Chumak, A. V., Serga, A. A., Hillebrands, B. & Kostylev, M. P. Scattering of backward spin waves in a one-dimensional magnonic crystal. **022508**, 1–4 (2014).
 120. Fischer, T. *et al.* Experimental prototype of a spin-wave majority gate. *Appl. Phys. Lett.* **110**, 1–5 (2017).
 121. Heinrich, B. *et al.* Spin Pumping at the Magnetic Insulator (YIG)/Normal Metal (Au) Interfaces. *Phys. Rev. Lett.* **107**, 066604 (2011).
 122. Hahn, C. *et al.* Comparative measurements of inverse spin Hall effects and magnetoresistance in YIG/Pt and YIG/Ta. *Phys. Rev. B* **87**, 174417 (2013).
 123. Pai, C. F., Ou, Y., Vilela-Leão, L. H., Ralph, D. C. & Buhrman, R. A. Dependence of the efficiency of spin Hall torque on the transparency of Pt/ferromagnetic layer interfaces.

- Phys. Rev. B - Condens. Matter Mater. Phys.* **92**, (2015).
124. Shang, T. *et al.* Effect of NiO inserted layer on spin-Hall magnetoresistance in Pt/NiO/YIG heterostructures. *Appl. Phys. Lett.* **109**, (2016).
 125. Padrón-Hernández, E., Azevedo, A. & Rezende, S. M. Amplification of Spin Waves by Thermal Spin-Transfer Torque. *Phys. Rev. Lett.* **107**, 197203 (2011).
 126. Aldosary, M. *et al.* Platinum/yttrium iron garnet inverted structures for spin current transport. *Appl. Phys. Lett.* **108**, 242401 (2016).
 127. Li, J. *et al.* Observation of magnon-mediated current drag in Pt/yttrium iron garnet/Pt(Ta) trilayers. *Nat. Commun.* **7**, 1–6 (2016).
 128. Avci, C. O. *et al.* Fast switching and signature of efficient domain wall motion driven by spin-orbit torques in a perpendicular anisotropy magnetic insulator/Pt bilayer. *Appl. Phys. Lett.* **111**, (2017).
 129. Wunderlich, J. Current-switched magnetic insulator. *Nat. Mater.* **16**, 284–285 (2017).
 130. Buhay, H. *et al.* Thick Yttrium-Iron-Garnet (YIG) Films Produced by Pulsed Laser Deposition (PLD) for Integration Applications. *IEEE Trans. Magn.* **31**, 3832–3834 (1995).
 131. Sposito, a *et al.* Pulsed laser deposition of high-quality μm -thick YIG films on YAG. *Opt. Mater. Express* **3**, 624–632 (2013).
 132. Lagomarsino, S. & Tucciarone, A. Structural properties of magnetic garnet films. *Thin Solid Films* **114**, 45–67 (1984).
 133. Makino, H., Hibiya, T. & Matsumi, K. Misfit Strain in LPE (Y , Eu) 3 (Fe , Ga) 5 O 12 Garnet Films. in *MAGNETISM AND MAGNETIC MATERIALS — 1973: Nineteenth Annual Conference* **803**, 80–84 (ASCE, 1974).
 134. Cubic crystal system. Available at: https://en.wikipedia.org/wiki/Cubic_crystal_system.
 135. Ovsyankin, V. V. & Feofilov, P. P. VISUAL EXHIBITION OF IONIC RADIUS Re Os. *Jetp Lett.* **4**, 317 (1966).
 136. Sposito, A., Gregory, S. A., de Groot, P. A. J. & Eason, R. W. Combinatorial pulsed laser deposition of doped yttrium iron garnet films on yttrium aluminium garnet. *J. Appl. Phys.* **115**, 053102 (2014).
 137. Chern, M.-Y. & Liaw, J.-S. Study of $\text{Bi}_x\text{Y}_{3-x}\text{Fe}_5\text{O}_{12}$ Thin Films Grown by Pulsed Laser Deposition. *Jpn. J. Appl. Phys.* **36**, 1049 (1997).
 138. Takeuchi, H., Ito, S. I., Mikami, I. & Taniguchi, S. Faraday rotation and optical absorption of a single crystal of bismuth-substituted gadolinium iron garnet. *J. Appl. Phys.* **44**, 4789–4790 (1973).
 139. Helseth, L. E., Hansen, R. W., Il'yashenko, E. I., Baziljevich, M. & Johansen, T. H. Faraday rotation spectra of bismuth-substituted ferrite garnet films with in-plane magnetization. *Phys. Rev. B* **64**, 174406 (2001).
 140. KooyEnz
ExperimentalAndTheoreticalStudyOfDomainConfigurationInThinLayersBaFeO.pdf.
 141. Kaplan, B. & Gehring, G. A. The domain structure in ultrathin magnetic films. *J. Magn. Mater.* **128**, 111–116 (1993).
 142. Cohen, E. R. & Taylor, B. N. The 1986 CODATA Recommended Values of the Fundamental Physical Constants. *J. Phys. Chem. Ref. Data* **17**, 1795–1803 (1988).
 143. Hurben, M. J. & Patton, C. E. Theory of two magnon scattering microwave relaxation and ferromagnetic resonance linewidth in magnetic thin films. *J. Appl. Phys.* **83**, 4344–4365 (1998).

144. Wu, C. N. *et al.* High-quality single-crystal thulium iron garnet films with perpendicular magnetic anisotropy by off-axis sputtering. *AIP Adv.* **8**, 055904 (2018).
145. Dionne, G. F. & Allen, G. A. Spectral origins of giant Faraday rotation and ellipticity in Bi-substituted magnetic garnets. *J. Appl. Phys.* **73**, 6127–6129 (1993).
146. Patton, C. E. Linewidth and relaxation processes for the main resonance in the spin-wave spectra of Ni-Fe Alloy Films. *J. Appl. Phys.* **39**, 3060–3068 (1968).
147. Mo, N. *et al.* Origins of the damping in perpendicular media: Three component ferromagnetic resonance linewidth in Co-Cr-Pt alloy films. *Appl. Phys. Lett.* **92**, (2008).
148. Chappert, C., Dang, K. Le, Beauvillain, P., Hurdequint, H. & Renard, D. Ferromagnetic resonance studies of very thin cobalt films on a gold substrate. *Phys. Rev. B* **34**, 3192–3197 (1986).
149. Purcell, S. T., Van Kesteren, H. W., Cosman, E. C., Zeper, W. B. & Hoving, W. Magnetic properties of ultrathin epitaxial Co films on a Pd (111) single crystal. *J. Appl. Phys.* **69**, 5640–5642 (1991).
150. Zakeri, K. *et al.* Spin dynamics in ferromagnets: Gilbert damping and two-magnon scattering. *Phys. Rev. B* **76**, 104416 (2007).
151. Manuilov, S. Ferromagnetic resonance in films with growth induced anisotropy. (KTH Royal Institute of Technology, 2011).
152. Chen, Y. T. *et al.* Theory of spin Hall magnetoresistance (SMR) and related phenomena. *J. Phys. Condens. Matter* **28**, (2016).
153. Meyer, S. *et al.* Temperature dependent spin transport properties of platinum inferred from spin Hall magnetoresistance measurements. *Appl. Phys. Lett.* **104**, (2014).
154. M. Hurd, C. *The Hall Effect in Metals and Alloys.* (1972).
155. Avci, C. O. *et al.* Current-induced switching in a magnetic insulator. *Nat. Mater.* **16**, 309–314 (2017).
156. Belmeguenai, M. *et al.* Interfacial Dzyaloshinskii-Moriya interaction in perpendicularly magnetized Pt/Co/AlO_x ultrathin films measured by Brillouin light spectroscopy. *Phys. Rev. B* **91**, 180405 (2015).
157. Chaurasiya, A. K. *et al.* Direct Observation of Interfacial Dzyaloshinskii-Moriya Interaction from Asymmetric Spin-wave Propagation in W/CoFeB/SiO₂ Heterostructures Down to Sub-nanometer CoFeB Thickness. *Sci. Rep.* **6**, 32592 (2016).

Summary in English:

Title : Pulsed laser deposition of substituted thin garnet films for magnonic applications.

Key words : Garnets thin films, Pulsed laser deposition, magnetic insulators, magnetization dynamics, magneto-optical properties, magnonics

This PhD work focuses on the Pulsed Laser Deposition (PLD) growth of Bismuth doped Iron Garnet nanometer thick films. Those films are characterised and used for magnon-spintronics applications. This PhD has two main focuses : material science and magnon-spintronics applications.

The aim of this PhD is to fill up the need in the magnon-spintronics community of an ultrathin magnetic material combining low magnetic losses and tunable magnetic anisotropy. Indeed the recent breakthrough in the domain was the ability of generating magnetic auto-oscillations from a charge current in a magnetic insulator. This result has been obtained by using an 20 nm thick film of Yttrium Iron Garnet (YIG) with low magnetic losses ($\alpha = 2 \cdot 10^{-4}$). Those ultrafin films of YIG can also be used for spin waves propagation over micrometeter distances. However the easy magnetic axis in those films is set to in plane due to the shape anisotropy and it is not a tunable parameter. To go further in terms of magnon-spintronics applications a perpendicularly easy magnetized low losses ultra-thin magnetic material would be desirable.

Liquid Phase Epitaxy growth of micrometer thick doped YIG during the 70's evidenced that the magnetic anisotropy could be modified by doping or substitution. Especially the substitution of Yttrium atoms by Bismuth ones on the dodecaedric atomic sites allows to stabilise out of plane magnetic anisotropy. Moreover the BiYIG is also known to posses high magneto optical activity. This PhD presents the growth by Pulsed Laser Deposition of ultrathin BiYIG films (7 to 50 nm thick). In those films the uniaxial magnetic anisotropy has two main origins : the magneto elastic and the growth induced anisotropy. Using the strain in those films it is possible to obtain both out of plane and in plane magnetic anisotropy. The dynamical characterisation shows that magnetic losses in the perpendicular easy magnetized films are comparable to the one of YIG ultrathin films. The high magneto optical activity in those films makes the BiYIG ultrathin films suitable for lighth based detection technics involving lighth/magnetism interaction.

By sputtering a Pt sublayer on the top of BiYIG ultra thin films we could observ different spintronic phenomena evidencing the transfer of spin current from the metal to the insulator. Low losses and nanometer thickness in perpendicularly easy magnetized BiYIG films allow to observ current induced magnetic auto oscillation in the same fashion as what was previously done with ultrathin YIG. The perpendicular magnetic anisotropy allows however to couple those auto oscillation to spin waves, which was not possible for in plane magnetized YIG fims. This new phenomena is related to the unique properties of the ultrathin BiYIG.

BiYIG ultrathin films are thus opening new perspectives in the magnon spintronic commnutiy due to their low thickness and tunable magnetic anisotropy.

Résumé en français:

Titre : Croissance par ablation laser de films ultrafins de grenats substitués pour les applications magnoniques.

Mots clés : Grenats ultra fins, ablation laser pulsée, isolants magnétiques, dynamique d'aimantation, propriétés magnéto-optiques, magnonique.

Ce travail de doctorat porte sur la croissance par ablation laser pulsée de films ultrafins de Grenat de Fer et d'Yttrium dopés au Bismuth (BiYIG). Ces films d'épaisseur nanométriques sont caractérisés puis utilisés pour des applications magnon-spintroniques. Cette thèse englobe deux thématiques différentes de la physique : la science des matériaux et les applications magnon-spintroniques.

La motivation de cette thèse repose sur le besoin, venant de la communauté magnon-spintronique, d'un nouveau matériau magnétique ultrafin à anisotropie ajustable. En effet, au cours des dernières années, une avancée majeure dans le domaine a été l'obtention d'auto-oscillations magnétiques induites par un courant de charge dans un isolant magnétique. Ce résultat a été rendu possible grâce à l'utilisation d'un film ultrafin (20 nm) de Grenat de Fer et d'Yttrium (YIG) possédant de très faibles pertes magnétiques. Ces films ultrafins de YIG sont également intéressants pour la magnonique puisqu'il est aussi possible d'y propager et de manipuler des ondes de spin sur de grandes distances. Cependant, la direction facile d'aimantation dans ces films est fixée par l'anisotropie de forme et n'est pas un paramètre ajustable. Pour pousser plus loin les possibilités dans le domaine de la magnon-spintronique un matériau ultrafin, présentant des pertes magnétiques similaires au YIG, dans lequel il serait possible de stabiliser une anisotropie perpendiculaire serait désirable.

La croissance par épitaxie en phase liquide de films de YIG substitués de plusieurs microns d'épaisseur a permis de mettre en évidence que l'anisotropie magnétique pouvait être modifiée par dopage. Notamment que la substitution des atomes d'Yttrium par les atomes de Bismuth sur les sites atomiques dodécédriques permet d'obtenir une direction facile d'aimantation hors du plan, le BiYIG est également reconnu pour sa forte activité magnéto-optique.

Cette thèse présente la croissance par ablation laser pulsée de films ultrafins (7 à 50 nm d'épaisseur) de BiYIG. Dans ces films l'anisotropie magnétique a deux origines : l'anisotropie de croissance et l'anisotropie de contrainte. Dans ces films grâce à la contrainte les deux types d'anisotropies magnétique (planaire ou perpendiculaire) peuvent être obtenues. La caractérisation dynamique des films montre que la substitution d'Yttrium par le Bismuth n'augmente pas les pertes magnétiques et que l'amortissement de Gilbert dans le BiYIG est comparable à celui du YIG. De plus l'augmentation de l'activité magnéto optique du BiYIG par rapport à celle du YIG rend ce nouveau matériau très intéressant pour des techniques expérimentales impliquant l'interaction lumière/ moment magnétique (BLS, Kerr microscope...).

Pour observer des phénomènes spintronique nous avons déposé une couche de Pt. Des mesures de transport comme la magnétoresistance Hall de spin, l'effet Hall de spin inverse ou l'effet Hall anormal témoignent d'un transfert de courant de spin à l'interface BiYIG-Pt. Grâce à l'anisotropie perpendiculaire, il est également possible d'observer de nouveaux phénomènes comme la génération d'onde de spin cohérent à partir d'auto-oscillations.

Ce nouvel isolant magnétique combinant une faible épaisseur, un faible amortissement magnétique et une anisotropie magnétique modifiable est donc un matériau prometteur pour des applications magnon-spintroniques et ouvre de nouvelles possibilités pour le domaine.